

PRIMARY PRODUCTIVITY AND BIOGEOCHEMICAL CARBON
CYCLING IN THE BEAUFORT AND CHUKCHI SEAS, ARCTIC OCEAN

A DISSERTATION
SUBMITTED TO THE DEPARTMENT OF
ENVIRONMENTAL EARTH SYSTEM SCIENCE
AND THE COMMITTEE ON GRADUATE STUDIES
OF STANFORD UNIVERSITY
IN PARTIAL FULFILLMENT OF THE REQUIREMENTS
FOR THE DEGREE OF
DOCTOR OF PHILOSOPHY

Molly Alyse Palmer

March 2013

© 2013 by Molly Alyse Palmer. All Rights Reserved.

Re-distributed by Stanford University under license with the author.



This work is licensed under a Creative Commons Attribution-Noncommercial 3.0 United States License.

<http://creativecommons.org/licenses/by-nc/3.0/us/>

This dissertation is online at: <http://purl.stanford.edu/dk725fp2129>

I certify that I have read this dissertation and that, in my opinion, it is fully adequate in scope and quality as a dissertation for the degree of Doctor of Philosophy.

Kevin Arrigo, Primary Adviser

I certify that I have read this dissertation and that, in my opinion, it is fully adequate in scope and quality as a dissertation for the degree of Doctor of Philosophy.

Robert Dunbar

I certify that I have read this dissertation and that, in my opinion, it is fully adequate in scope and quality as a dissertation for the degree of Doctor of Philosophy.

Leif Thomas

Approved for the Stanford University Committee on Graduate Studies.

Patricia J. Gumport, Vice Provost Graduate Education

This signature page was generated electronically upon submission of this dissertation in electronic format. An original signed hard copy of the signature page is on file in University Archives.

ABSTRACT

The Arctic Ocean has undergone unprecedented changes in sea ice extent and thickness in recent years, including record-setting sea ice minimums in 2007 and 2012. These changes are predicted to affect Arctic marine primary productivity (the photosynthetic fixation of carbon dioxide by tiny algae called phytoplankton) because the timing and intensity of the summer phytoplankton bloom are strongly controlled by the dynamics of sea ice and water column stabilization. Satellite-based estimates indicate that primary production in ice-free waters has increased dramatically over the last few decades as a result of the increases in open water and length of the growing season associated with the thinning ice cover. In addition, climate models predict that the Arctic will experience greater and more rapid warming than other areas of the planet over the next century, suggesting that these changes may become even more prevalent in the future.

The thinning sea ice has already had a dramatic impact on regional biogeochemistry: in 2011, we observed one of the most massive phytoplankton blooms ever recorded *under the sea ice* in the Chukchi Sea, an area traditionally thought of as too dark and too cold for massive blooms to occur. In the Chukchi, melt-ponds on the ice surface have proliferated to an extent that, in combination with the thinning ice cover, light penetration through the ice to surface waters is now sufficient for net photosynthesis to occur. The bloom we witnessed in 2011 extended for over 100 km into the >1 m thick ice pack, and was characterized by extraordinarily high diatom biomass and rates of production.

These changes represent a marked shift in our conception of Arctic marine ecosystems and have potential global-scale implications due to feedbacks relating to sea ice albedo, global atmospheric and ocean circulation patterns, and natural greenhouse gas exchanges between the atmosphere and ocean. Chapter 1 presents an overall introduction to the Arctic and discusses the causes and consequences of this changing seasonal cycle of productivity. Chapter 2 presents results from field work performed in the Beaufort Sea in the summer of 2008 exploring the spatial and temporal variability of phytoplankton photosynthesis in the ice-associated region of

the flaw-lead polynya (area of perennially open water that rings the Arctic Ocean between land-fast ice and the central Arctic ice pack; it can be used somewhat as an analog for future open-water and ice-edged based productivity).

Continuing with this theme of exploring primary productivity and biogeochemical cycles in the changing Arctic, Chapter 3 details the results from photophysiological experiments performed during the summer of 2010-2011 that highlight the unique features allowing Arctic phytoplankton to reach high levels of biomass in the extreme environment under the ice. In Chapter 4, I present data from recent 1-D modeling efforts that utilize the light and nutrient-controlled responses of phytoplankton growing under the ice to explore the consequences and implications of this shifting bloom cycle on regional biogeochemical processes.

ACKNOWLEDGMENTS

First and foremost, I would like to thank my advisor, Kevin Arrigo. Kevin has been an excellent role model over the years, teaching my invaluable lessons from how to formulate research questions and how to balance science with life. I admire and respect Kevin for all he has accomplished, and have benefitted so much from his wisdom, guidance, and brilliance as a scientist.

I would like to thank my committee members, Rob Dunbar, Leif Thomas, and Karen Casciotti, for their positive support, sharing their expertise with me, and for our many enlightening discussions. In particular, they have all been the best role models a young scientist could ask for, and have shown me the type of scientist I would one day like to become. In addition, I would like to thank my defense chair, Stephen Monismith, for giving his time and attention to this project. Also at Stanford, I would like to thank Peter Vitousek for his guidance during my Masters degree, which trained me how to be a scientist, how to write a technical paper, how to present and discuss research, and how to conduct field work in remote locations. I received invaluable support and council – and was inspired to become a scientist – during my early years in the Earth Systems Program from Julie Kennedy, Deana Fabbro-Johnson, Scott Fendorf, Anne Egger, and of course Peter and Kevin.

I would like to thank the Arrigo lab, past and present, for providing many fruitful discussions on research, helping to expand my scientific mind, and serving as delightful colleagues and comrades-in-arms. Matt Mills and Anne-Carlijn Alderkamp have both served as key examples of how to achieve success as a hard-working research scientist, and I thank them both for our endless science discussions and for sharing many laughs. Gert van Dijken has provided crucial technical support to the lab over the years, and I am sure is one of the main reasons we have accomplished all that we have. Lindsey Kropuenske Artman and Ben Saenz were outstanding role models, both in science and in life, and helped keep me motivated and engaged during the early years of my time in the Arrigo lab. Zach Brown has been a great friend and conspiring scientist, and I thank him for our countless discussions on the formation of subsurface chlorophyll maxima in the Arctic, the endless memories and laughs we've

shared, and of course his can-do personality and hard-working attitude. I would especially also like to thank Kate Lowry for her positive and cheerful attitude, kind listening ears, and for helping us both survive the 2010 ICESCAPE cruise. She was always there with a bright smile, ready and willing to go above and beyond her duties each and every day. I have the utmost respect for Kate, and can't thank her enough for all the wonderful moments we've shared that have helped me grow both personally and academically. And to the new students, Aaron Strong, Casey Smith, and Kate Lewis, thanks for bringing in energy and spirit to the lab in the last few months.

Many colleagues have aided me in my research through the years, and I would like to joyfully and gratefully thank and acknowledge CJ Mundy, Michel Gosselin, David Barber, Yves Gratton, Andrea Rossnagel, Roxanne Maranger, Jean-Eric Tremblay, Johannie Martin, Jens Ehn, Atsushi Matsuoka, Greg Mitchell, Colleen Kellogg, Christine Michel, Tasha Reddy, David Holland, Sam Laney, Karen Frey, Brian Seegers, and many others for providing scientific guidance and research aid.

I would be remiss not to acknowledge some of my friends who have helped get me through these years at Stanford, including Sarah Truebe, Jeremy Brown, Chris Leader, Liz Cassel, Josie Nevitt and of course the Friday beer/volleyball/tailgate/IM crew Solomon, Owen, Libby, Tom, Mike O., Jeremy C., Mike S., Mandy, Dana T., Maggie, Jesse, Justine, Sharmini, Sverre, Cynthia, Lida, and many others. You all have been a great source of fun and entertainment through the years. Thanks also to all my Clearwater Daughters out there, past, present and future, for helping me grow, learn, live, de-stress, have fun, and experience Club Minocqua; friends who have camped together shall never again divide. Special thanks to Grandma Sunny, for providing mentorship and love, and for setting an extraordinary life example. Thanks also to my Stanford rugby teammates; the determination, grit, and integrity we learned together has helped me be the strong woman I am today.

I am forever grateful for meeting my fiancé and best friend Marshal on the *Healy* in 2010. We have shared and grown so much in the past few years, and he has been my preferred hang-out buddy and partner-in-crime in these last two and a half years of my research. Marshal is the best company after a long day of work, and a

constant source of support and encouragement. Our weekends spent hunting, fishing, and camping, or just relaxing at home, have played a key role in helping me stay positive, calm, and determined in the last few years.

Finally, I would like to thank my family: my dad Bill, my mom Grace, and my sisters Laura and Katie. My parents taught me the strength, humor, integrity, and brilliance that are all key parts of the scientist I have become, and I would not have made it through any of this without their support, guidance, encouragement, wisdom, love, visits, and phone chats. In particular, the sage and witty advice and guidance from my dad, and the kind words and diverting stories from my mom, have played an important role in getting me through this part of my life. My little sister Laura has been a close friend and I admire her for her strength, wittiness, cleverness, and outgoing personality. She listened and was there for me throughout this whole process, and we share a bond that has helped keep me grounded and strong. Her encouragement and amazing strength in particular – in addition to her kind feedback and witty discourse – has been a refreshing and wonderful part of my life, and has helped me get to where I am today. Katie, Chris, and little Daniel have been a source of joy this past year, and I value the discussions on research and life that Katie and I have shared. This thesis is dedicated to my family.

This work was made possible through a NASA Earth and Space Science Fellowship to Molly A. Palmer, and NSF grant to Kevin Arrigo and David Holland. Part of this work is a contribution to the NASA ICESCAPE project, which was sponsored by the Ocean Biology and Biogeochemistry and Cryospheric Sciences programs at NASA. Another part of this work is a contribution to the International Polar Year – Circumpolar Flaw Lead System Study, funded by multiple international organizations. This research was aided in great part from the hard work and dedication of the men and woman of the USCGC *Healy* and the CCGS *Amundsen*.

TABLE OF CONTENTS

ABSTRACT	iv
ACKNOWLEDGMENTS	vi
TABLE OF CONTENTS	ix
LIST OF TABLES	xv
LIST OF FIGURES	xvii
Chapter 1: Introduction	1
1. The changing Arctic	2
2. Causes and consequences of sea ice loss in the Arctic Ocean	4
3. The seasonal cycle of Arctic marine primary productivity	5
4. The impact of recent changes on Arctic Ocean primary productivity	7
5. An experimental approach for exploring spatial and temporal variability in primary productivity in the Chukchi and Beaufort Seas	9
6. References	12
Chapter 2: Spatial and temporal variation of photosynthetic parameters in natural phytoplankton assemblages in the Beaufort Sea, Canadian Arctic	26
1. Title page	27
2. Reprint request	28
a. Request letter	28
b. Permissions letter	29
3. Abstract	31
4. Introduction	32
5. Materials and Methods	34
a. Study area	34
b. Sampling protocols	35

c. Nutrients, DIC, and extracted Chl <i>a</i>	36
d. Pigment analysis	37
e. Calculation of spectral absorption coefficients	37
f. Photosynthesis-irradiance (P-E) measurements	38
g. Statistical analysis	39
6. Results	40
a. General open water (OW) and under ice (UI) physical, chemical, and biological conditions	40
b. Phytoplankton pigment analysis	41
c. Phytoplankton spectral absorption characteristics	42
d. Summary of P-E parameters for OW and UI sites	43
e. Effect of environmental factors on P-E parameters	43
f. Spatial variability in P-E parameters: Franklin Bay	44
g. Temporal variability in P-E parameters: Darnley Bay	45
7. Discussion	46
8. Acknowledgments	51
9. References	52

**Chapter 3: Light and nutrient control of photosynthesis in natural
phytoplankton populations from the Chukchi and Beaufort Seas,**

Arctic Ocean	67
1. Title page	68
2. Abstract	69
3. Introduction	70
4. Materials and Methods	74
a. Study area	74
b. General sampling	75
c. %PAR, MLD, and sea ice concentration	75
d. P-E measurements	76
e. Absorption coefficients and quantum yields	77

f. Statistics	77
g. Summary of analyses conducted	78
5. Results	79
a. Site description	79
b. Differences between the surface and subsurface	80
i. Environmental conditions, Chl <i>a</i> , nutrients, and DIC	80
ii. Photosynthetic parameters	81
c. Differences between surface and subsurface in open water and under ice areas	82
i. Open water areas: surface vs. subsurface	82
1. Environmental conditions, Chl <i>a</i> , nutrients, and DIC	82
2. Photosynthetic parameters	83
ii. Under ice areas: surface vs. subsurface	84
1. Environmental conditions, Chl <i>a</i> , nutrients, and DIC	84
2. Photosynthetic parameters	85
iii. Open water and under-ice areas at the same depth)	85
1. Environmental conditions, Chl <i>a</i> , nutrients, and DIC	85
2. Photosynthetic parameters	86
d. Temporal variability in P-E parameters: Chukchi North Transect	87
i. Open water (oldest bloom type sampled)	88
1. Physical and chemical environment	88
2. Photosynthetic parameters	88
ii. Ice edge (mid-to-late bloom)	89
1. Physical and chemical environment	89
2. Photosynthetic parameters	89
iii. Under ice (earliest bloom type sampled)	90

1. Physical and chemical environment	90
2. Photosynthetic parameters	91
e. Regression analysis	91
6. Discussion	92
a. Light and nutrient control of P-E parameters during ICESCAPE	94
i. Under the sea ice	95
ii. Open water	96
iii. Temperature	97
b. Ecological implications of variability in P-E parameters	98
c. A new paradigm of primary productivity in the Chukchi Sea ...	100
7. Conclusions	101
8. Acknowledgements	103
9. References	104

Chapter 4: Modeling primary productivity and biogeochemical carbon cycling in the Chukchi Sea, Arctic Ocean: Impacts of sea ice retreat, thinning, and melt-pond proliferation on the summer phytoplankton bloom	125
1. Introduction	126
2. Background	130
a. Seasonal sea ice, snow, and pond cycle	130
b. Data details for ice and snow inputs	131
i. Ice advance and retreat	131
ii. Temperature and salinity profiles in the ice and snow ..	132
iii. Transition periods: dry to wet snow and pond formation	132
c. Impacts of ultraviolet radiation	133
d. Phytoplankton in the Chukchi and Beaufort Seas	136
e. Bacteria in the Chukchi and Beaufort Seas	137
3. Methods	137

a.	Model Domain	138
b.	Model inputs	138
c.	Solar irradiance and radiative transfer model	140
i.	Solar irradiance: ultraviolet radiation data	140
ii.	Solar irradiance: atmospheric radiative transfer model	140
iii.	Solar irradiance: sea ice, snow, and water radiative transfer model	141
d.	Computation and time stepping	142
e.	Biological response to UVR	142
f.	Biological model	143
i.	Phytoplankton	145
ii.	Bacteria	147
iii.	Zooplankton	148
iv.	Particulate and dissolved organic pools	149
v.	Inorganic N pools	149
4.	Results and discussion	150
a.	Standard model run	150
i.	Ice, snow, and melt pond cycle	150
ii.	Light transmittance	151
iii.	NO ₃	153
iv.	Phytoplankton and Chlorophyll <i>a</i>	154
v.	Zooplankton	156
vi.	Detritus, DON, NH ₄ , and Bacteria	157
vii.	Net primary productivity	158
b.	Growth limitation terms	160
c.	Model experiments	161
i.	Effect of varying pond cover on under ice and annual NPP	161
1.	10% Pond coverage vs. standard run.....	161

2.	50% Pond coverage vs. standard run	163
3.	No melt pond coverage vs. standard run	163
ii.	Effect of UVR inhibition on NPP	164
iii.	Effect of zooplankton grazing on NPP	166
iv.	Variable timing of ice retreat and ice thickness	166
1.	Early first year ice break-up and pond formation	166
2.	Multi-year ice	168
3.	No sea ice	168
5.	Conclusions	169
a.	What can the model tell us about the controls on NPP?	169
b.	Importance of the SCM	172
c.	Future changes	173
d.	Conclusions and future research directions	173
6.	Acknowledgements	175
7.	References	175

LIST OF TABLES

Chapter 2

Table 1. Physical and hydrological information in chronological order for 2008
CFL P-E curve data58

Table 2. Chl *a* (mg m⁻³) and Chl *a*-normalized HPLC-derived pigment concentrations (mg m⁻³ pigment per mg m⁻³ Chl *a*) for P-E curve samples (mean ± standard deviation)59

Table 3. Photosynthetic parameters in OW SCM, UI SCM (shaded), and UISW samples for large size cells (>5 µm) and total communities (>0.7 µm) (except \bar{a}^* and Φ_m , which are not size fractionated)60

Table 4. Time series data from Darnley Bay taken at the same station (DB7) under ice cover over the course of a large phytoplankton bloom61

Chapter 3

Table 1. Environmental data (**A**: physical and biological data; **B**: chemical data) and P-E parameters (**C**) from 2010-2011 ICESCAPE cruise, divided by depth class (shaded: surface; unshaded: subsurface)111

Table 2. P-E and related data from 2010-2011 ICESCAPE cruise, divided by ice class (top rows: open water; bottom rows: under sea ice) and depth class (shaded rows: surface; unshaded rows: subsurface). Shown are: (**A**) physical and biological data for P-E samples; (**B**) chemical data for P-E parameters; and (**C**) P-E parameters112

Table 3. Amount of irradiance ($E_{d,z,PAR}$) at two depths in different ICESCAPE habitats and environments: under bare ice and under ponded ice (top) and in open water (bottom), with differing incident surface irradiance ($E_{d,0,PAR}$), percent of incident above-surface irradiance transmitted to depth and bloom conditions115

Table 4. Results from multiple stepwise regression analysis. Shown are standardized regression coefficients (beta), plus their individual significance as well as the details of the overall regression fit 116

Table 5. Correlation matrix using the nonparametric Spearman rank test for P-E parameters and associated variables. Bold indicates significance ($p < 0.05$) 117

Chapter 4

Table 1. Description model runs of snow, ice, and pond thickness and development 185

Table 2. Biological weighting functions and wavelengths used in UVR inhibition model 186

Table 3. Model parameters and variables for the biological model 187

Table 4. References for comparison of model results for primary production 190

Table 5. Model results for light transmittance through the standard model run 191

Table 6. Model details for comparison of nitrate and chlorophyll data as shown in Figs. 9 and 10 192

Table 7. Results from model showing annual NPP compared to the standard model run (FYI 30% pond, shown in first column Table 1) 193

Table 8. Results from model showing annual NPP in various model runs where ice cover was modified from the standard model run 194

LIST OF FIGURES

Chapter 1

Figure 1. Average monthly Arctic sea ice extent for September 1979-2012	18
Figure 2. Monthly Arctic sea ice extent for September 2012	19
Figure 3. Arctic sea ice age, September 2007 vs. 2012	20
Figure 4. Estimated extent of Arctic sea ice based on age classes	21
Figure 5. Map showing hydrography and currents of the Arctic Ocean	22
Figure 6. Differences in annual primary productivity in the Arctic Ocean between 2007 and 2006 compared to the difference in the length of the growing season	23
Figure 7. Increases in open water area and annual primary production in the Arctic Ocean between 1998 and 2009, based on satellite data	24
Figure 8. Impact of ice loss on underwater light field, melt ponds vs. bare ice	25

Chapter 2

Figure 1. Map of Beaufort Sea study region	62
Figure 2. Spectral downwelling irradiance in Darnley Bay	63
Figure 3. Phytoplankton specific absorption spectrum for under ice communities	64
Figure 4. Photosynthetic parameters in Franklin Bay	65

Figure 5. Vertical profiles of temperature, fluorescence, and % PAR transmitted under sea ice during a phytoplankton bloom in Darnley Bay	66
--	----

Chapter 3

Figure legends	118
-----------------------------	-----

Figure 1. Map showing the location of all 2010 and 2011 ICESCAPE stations ...	120
--	-----

Figure 2. Spatial plots of ICESCAPE environmental variables in the surface and subsurface, separated by year (2010 and 2011)	121
---	-----

Figure 3. Spatial plots of ICESCAPE photosynthetic variables in the surface and subsurface, separated by year (2010 and 2011)	122
--	-----

Figure 4. Environmental (left) and photosynthetic (right) variables along the 2010 Chukchi North transect vs. depth, sampled July 6-7, 2010	123
--	-----

Figure 5. Environmental (left) and photosynthetic (right) variables along the 2011 Chukchi North transect vs. depth, sampled July 3-7, 2011	124
--	-----

Chapter 4

Figure 1a. Mean ice thickness taken 72°N, -125°W in the Canadian Beaufort Sea from 1972-1992.....	195
--	-----

Figure 1b. Mean snow thickness taken 72°N, -125°W in the Canadian Beaufort Sea from 1972-1992	196
--	-----

Figure 1c. Data showing varying sea ice and snow and pond thickness at four sites in Mould Bay, Arctic Ocean	197
Figure 1d. Pond fraction and pond depth at the SHEBA site	198
Figure 2a. Air temperatures, snow and ice depths, and sea level measured 300 m offshore in the Chukchi Sea near Barrow, AK in 2008	199
Figure 2b. Air temperatures, snow and ice depths, and sea level measured 1000 m offshore near Barrow, AK in 2008	200
Figure 2c. Data from the SHEBA experiment showing sea ice and snow thicknesses in MYI over the seasonal cycle	201
Figure 2d. Data from the SHEBA experiment showing sea ice, snow, and pond thicknesses in FYI over the seasonal cycle	202
Figure 2e. Data from the SHEBA experiment showing air temperatures, ice temperatures, and water temperatures in a FYI site	203
Figure 3. Plot showing modeling ice, snow, and pond thicknesses over time for the standard model runs described in Table 1	204
Figure 4a. Modeled daily cycle of integrated incident surface PAR and UVR irradiance, in $\mu\text{Ein m}^{-2} \text{ s}^{-1}$ for the dates shown in the year 2003	205
Figure 4b. Model output showing the annual cycle of daily incident surface PAR (integrated from 400-700nm) used in the model runs	206

Figure 5. Biological weighting functions in units reciprocal ($\mu\text{Ein m}^{-2} \text{s}^{-1}$) ⁻¹ for instantaneous irradiance exposure curve	207
Figure 6. Phytoplankton spectral absorption coefficient, $a^*(\lambda)$, used in model runs	208
Figure 7. Conceptual diagram representing main fluxes and flows of biological model	209
Figure 8. Modeled vs. measured PAR (400-700 nm) under bare and ponded ice covers	210
Figure 9. Measured vs. modeled nitrate (NO_3 , mmol m^{-3}) in the water column during the standard model run	211
Figure 10. Measured vs. modeled chlorophyll a (Chl a , mg m^{-3}) in the water column during the standard model run	212
Figure 11. Daily net primary production ($\text{mg C m}^{-2} \text{d}^{-1}$) shown over the seasonal cycle for the standard model run	213
Figure 12. Model output from standard model run, showing all model state variables	214
Figure 13. Results from standard model run showing state variables small (top) and large (bottom) phytoplankton in Chl a units	215
Figure 14. Model output from standard model run, showing model limitation terms	216

Figure 15. Daily net primary production ($\text{mg C m}^{-2} \text{d}^{-1}$) shown over the seasonal cycle for other model runs (not the standard run, which is shown here in grey)217

Figure 16. Annual net primary production ($\text{g C m}^{-2} \text{yr}^{-1}$) shown for the major model runs, as compared to measured and modeled data in other studies218

CHAPTER 1:
INTRODUCTION

Introduction

By Molly A. Palmer

Department of Environmental Earth System Science, Stanford University

The changing Arctic

The Arctic Ocean is in a rapid and unprecedented state of change. In recent decades, rising global temperatures have been linked to complex and interconnected changes in land, ocean, and atmospheric processes (Loeng et al. 2006). One of the most dramatic changes is the pervasive and extreme loss of sea ice throughout the entire Arctic Ocean (Maslanik et al. 2011). Not only has the bulk of the Arctic ice pack diminished in areal extent (Figs. 1 and 2), the volume of sea ice has decreased through the extreme reduction in overall ice thickness (Figs. 3 and 4) (Loeng et al. 2006; Maslanik et al. 2011). This includes a 30% reduction in the extent of the ice pack (Fig. 3; Comiso et al. 2008; Stroeve et al. 2008) and >40% reduction in average ice thickness (Fig. 4; Lindsay and Zhang 2005; Kwok and Rothrock 2009), a phenomenon recorded in nearly every regional Arctic sea as well as in land-fast ice all through the Arctic basin (Figs. 3 and 4; Douglas 2010).

Other changes have also been observed: over the last century, temperatures have risen by 0.09°C/decade, totaling 1-3°C and up to 4°C in winter over the past 50 years, and precipitation has increased by 8% (Loeng et al. 2006). Furthermore, these changes have been accelerating in recent years (Comiso 2006), with temperatures rising at increased rates (0.4°C/decade, four times greater than the average for the 20th century; Loeng et al. 2006) and culminating in the record-setting loss of sea ice witnessed in 2007 and 2012. The September 2012 sea ice minimum (Figs. 1 and 2) was 45% below the 30-year average (1981-2010), far exceeding the previous minimum that was reached in 2007 (Fig. 1), despite relatively average surface air temperature conditions in 2012 (NSIDC 2012). Compared to the 1979-2000 average sea ice conditions in the Arctic, the sea ice extent in 2012 represents a 49% reduction in the area of the Arctic that is covered by sea ice (NSIDC 2012).

Importantly, the majority consensus from the best climate models suggest that these sorts of changes, especially with regard to sea ice loss, will continue (and likely continue to accelerate) in the next few years to decades as global temperatures continue to rise (Loeng et al. 2006). Some projected changes include temperature increases of 3-5°C over land and up to 7°C over the Arctic Ocean by the end of the century (more than twice the global average) and a 10-20% increase in precipitation (up to 10°C warming and 30% increase in precipitation in autumn and winter) (Loeng et al. 2006). Sea ice extent is predicted to decrease by 10-50%, with potentially all summer sea ice disappearing by 2050 (Stroeve et al. 2007). In fact, most models predict that the Arctic region will experience greater and more rapid warming than other areas of the planet over the next century due to the multitude of feedbacks between the global earth system and the Arctic (e.g., sea ice-albedo, the hydrologic cycle, etc.; see Loeng et al. 2006 for a full description).

One of the most important questions facing Arctic marine scientists is how the changing sea ice cover and environmental conditions will impact marine primary productivity (PP), the photosynthetic fixation of carbon dioxide by tiny, single-celled algae called phytoplankton. These phytoplankton form the base of the marine food web and thus play a critical role in sustaining the upper trophic levels that are economically, spiritually, and strategically important in the world today, from fish and polar bears to seals and seabirds (Loeng et al. 2006). In the Arctic Ocean, sea-ice exerts the strongest control on biological populations and their distributions by providing habitat and surfaces for higher trophic levels (mammals, birds, etc.), facilitating ice-edge upwelling, supporting ice algal production, as well as by limiting light and vertical mixing in the under ice environment (Carmack and Macdonald 2002). Any changes in sea ice extent will no doubt have profound implications and consequences for the marine food web, and it has been hypothesized that the increase in open water area will enhance productivity by extending the period of time when there are light conditions favorable for phytoplankton growth (Arrigo et al. 2008). In addition to the role of sea ice cover in regulating marine PP, nutrient distributions in the Arctic Ocean provide a strong secondary control on PP over the hugely productive

continental shelf regions (Carmack et al. 2004). Reduced sea ice cover is predicted to increase nutrient stocks through several processes, including allowing for more wind mixing, upwelling, and convection (Loeng et al. 2006).

In this dissertation, I explore several ways that changing Arctic environmental conditions have impacted phytoplankton photosynthesis and growth, including in under-ice and ice-associated habitats, and use these insights to model how various ice covers may impact PP now and in the future in the Beaufort and Chukchi Seas (Fig. 5 shows a map of the region). These areas of the Pacific sector of the Arctic Ocean have been suggested to be extremely prone to environmental change in coming years, since it is the site of one of the main inflows of ocean currents into the mostly-closed Arctic region via the Bering Strait (Fig. 5) and also has been a hot-spot of changes in sea ice and primary productivity in the past decade (Fig. 6) (Arrigo and van Dijken 2011).

Causes and consequences of sea ice loss in the Arctic Ocean

A decade ago, when sea ice loss in the Arctic was first coming to national attention, satellite records indicated that Arctic perennial sea ice cover had declined $8.9 \pm 2.0\%$ per decade since 1978, with the Beaufort and Chukchi Seas exhibiting some of the most pronounced losses of sea ice extent and thickness (Comiso 2002; Meier et al. 2007; Comiso et al. 2008). However, by 2012, this rate had increased to 13.0% per decade relative to the 1979-2000 average, representing a large and unexpected acceleration in sea ice loss (Fig. 1; NSIDC 2012). The present rate of sea ice loss is predicted to push the system outside of the envelope of glacial-interglacial cycles that have characterized the last 800,000 years within the time frame of a century or less, with ice-free summers—which haven't occurred in well over a million years—becoming a real possibility (Overpeck et al. 2005).

As mentioned above, not only has there been a reduction in sea ice areal extent, there has also been a large decline in the overall volume of sea ice in the Arctic. This loss can be explained by the large-scale replacement of thick, stable multiyear ice with thin, brittle first-year ice that is more susceptible to large, rapid reductions in ice extent and fractional coverage (Figs. 3 and 4; Nghiem et al. 2007;

Maslanik et al. 2011). The loss of multiyear ice and associated reduction in ice thickness have been explained by a variety of mechanisms (e.g., Serreze et al. 2007; Giles et al. 2008), most notably the cumulative effects of warming (Rothrock and Zhang 2005; Stroeve et al. 2007) and changes in atmospheric circulation patterns (Maslanik et al. 2007a; Nghiem et al. 2007), oceanic heat transport (Shimada et al. 2006), physical ice structure (Maslanik et al. 2007b; Giles et al. 2008), hydrologic patterns (Maslanik et al. 2007b), and multiple feedback processes (Perovich and Polashenski 2012). Regional and local variations in winds and sea level pressure strongly influence ice transport: even small displacements in atmospheric circulation can cause large changes in ice cover, for example, by increasing the number of cloud free days and by enhancing ice transport out of the Fram Strait (as occurred in 2007) (Rigor et al. 2002; Maslanik et al. 2007a, b; Nghiem et al. 2007; Stroeve et al. 2008). Models show that over half the reduction of sea ice extent can be attributed to greenhouse gas forcing, the influence of which has increased in recent years despite strong natural signals (Cavalieri et al. 1997; Stroeve et al. 2007).

However, none of these phenomena can readily be used to explain the ice loss in 2012: temperatures were only 1-3°C warmer than average (compared to 3-5°C warmer than average in 2007) over much of the Arctic Ocean, and winds/atmospheric pressure patterns were not as favorable in promoting ice loss as in 2007 (NSIDC 2012). Instead, much of the loss of sea ice in 2012 is attributable to the earlier initiation of the melt cycle (leading to earlier retreat of sea ice) as well as the continued impact of the loss of old, thick ice, which has greatly reduced the ability of the sea ice cover to survive summer melt and persist into the winter (Figs. 3 and 4; NSIDC 2012). Hence, we can expect the types of changes that have been witnessed in recent years to continue into the future, as little of the old, thick multiyear ice now remains in the Arctic Ocean.

The seasonal cycle of Arctic marine primary productivity

The key questions asked in this dissertation focus on how the multitude of environmental changes described above will affect marine PP and biogeochemical

carbon cycling in the Beaufort and Chukchi Seas, Arctic Ocean. In the Pacific sector of the Arctic, the timing and intensity of the summer phytoplankton bloom are strongly controlled by the dynamics of sea ice and water column stabilization (Arrigo and van Dijken 2004; Wang et al. 2005; Carmack et al. 2006). As such, PP in the Beaufort and Chukchi Seas exhibits strong seasonality and closely follows the pattern of sea ice retreat, with an intense bloom following the ice edge in spring and summer (Arrigo and van Dijken 2004; Wang et al. 2005); the bloom is controlled initially by irradiance and then later by nutrient distributions (Hill and Cota 2005). The two main contributors to PP in the Beaufort Sea are phytoplankton (dominant, and thus the focus of this dissertation) and ice algae (<10% total production) (Horner and Schrader 1982; Gosselin et al. 1997; Loeng et al. 2006).

To understand how the changing physical environment impacts Arctic marine PP, it is important to consider the key controls limiting phytoplankton growth and photosynthesis in this region. At a fundamental level, the seasonal cycle of PP in the Arctic Ocean is controlled by the annual variability in incoming solar radiation (Sakshaug 2003). Long, dark winters gradually give way to mild springs, eventually leading to 24-hour-sunlit summers. This variation in solar radiation controls the seasonal cycle of sea ice melt and retreat, which in turn controls the physical environment of the ocean below it. Complex feedback loops between the sea ice, ocean, and atmosphere create a dynamic and ever-changing physical system in the surface Arctic Ocean, which in turn closely impacts the seasonal cycle of marine-based PP (Loeng et al. 2006).

Because of these changes in the seasonal cycle of solar insolation, little to no phytoplankton growth occurs in the winter, when very little light reaches the ocean surface. By late spring, however, light limitation gradually disappears as ice thins and melts and irradiance increases, creating a surface bloom in the waters adjacent to the ice edge; productivity typically decreases exponentially with depth in these areas, following the pattern in light availability (Carmack et al. 2004; Bates et al. 2005). This late spring/early summer phytoplankton bloom typically begins in surface waters adjacent to the ice edge where melting and retreating sea ice creates a shallow (10-20

m over the continental shelf), stable mixed layer that is conducive for phytoplankton growth (Hill and Cota 2005; Loeng et al. 2006; Perrette et al. 2011). This bloom grows rapidly, fueled by the ample summertime light and abundant nutrients. The nutrients fueling this spring/summer bloom have typically been remineralized either in place or carried in from outside the region during the long winter months (e.g., through the Bering Strait, Fig. 5; Cota et al. 1996; Codispoti et al. 2005, 2009). However, nitrate, the primary limiting nutrient, is quickly drawn down in the surface mixed layer to below detection levels during the initial bloom period, and thus phytoplankton eventually congregate in deeper waters adjacent to the nitracline later in the season (Martin et al. 2010). As a result, deep layers (30-70 m) of what are commonly called a subsurface chlorophyll *a* (Chl *a*) maximum (SCM), filled with phytoplankton that may reach high biomass and typically are relatively healthy, have been observed all over the Arctic Ocean (Martin et al. 2010; Palmer et al. 2011).

The impact of recent changes on Arctic Ocean primary productivity

With the longer growing season initiated by the loss and earlier melt of sea ice now present in the region, this spring-summer phytoplankton bloom now has not only much more area in which to grow, but also a much longer period of time in which to be productive. As a result, satellite-based estimates indicate that PP in ice-free waters of this region has increased dramatically over the last few decades (+20% in the whole Arctic; Figs. 6 and 7) as a result of the increases in open water (+27%) and the length of the growing season (+45 days) associated with the thinning ice cover (Figs. 6 and 7; Pabi et al. 2008; Arrigo et al. 2008; Arrigo and van Dijken 2011). This includes a 48% increase in annual primary production in the Chukchi Sea between 1997 and 2009, with even more dramatic increases elsewhere in the Arctic (Fig. 7; Arrigo and van Dijken 2011). If 2010-2012 are included in this analysis, the results show an increase of 40% for PP in the entire Arctic (Arrigo and van Dijken, *unpubl.*).

However, recent evidence suggests that this pattern of the seasonal cycle of marine PP may be changing as a result of the retreating and thinning sea ice cover. It is traditionally thought that phytoplankton growth in ice-covered areas of the Arctic is

minimal, and thus that most PP is concentrated in the marginal ice zone and/or open water regions (Sakshaug 2003; Grebmeier et al. 2006). The reason that phytoplankton are not thought to grow under the sea ice is because sea ice and snow strongly reflect and attenuate incoming solar radiation (Perovich 1998; Perovich and Polashenski 2012).

A number of field programs have explored the continental shelves and polynyas of the Beaufort and Chukchi Seas in recent years, most notably the Canadian Arctic Shelf Exchange Study (CASES) and Circumpolar Flaw Lead System Study (CFL) over the Mackenzie Shelf and the Shelf-Basin Interaction (SBI) and the Impacts of Climate on EcoSystems and Chemistry of the Arctic Pacific Environment (ICESCAPE) programs over the Alaskan Shelf. These projects in large part have focused on observing interactions between the shelves and deep-ocean basin, and also on observing the impact that changes in sea-ice cover have on biological productivity. Preliminary results have begun to illuminate the complexity and interconnectedness of the mechanisms and feedbacks controlling biogeochemical cycles in the region. However, because of the prevailing belief that little to no algae grow under the ice, and because of the difficulty in navigating ice-covered waters, these field campaigns to the region have focused largely on exploring open water and ice-edge based production (e.g., Codispoti 2005, 2009; Tremblay et al. 2006, 2008; Mundy et al. 2009, etc.).

In 2011, one of the most intense phytoplankton blooms ever recorded was observed during the ICESCAPE program *under the sea ice* in the Chukchi Sea, over the shelf region where bottom depths average 50 m (Arrigo et al. 2012; Arrigo et al. submitted). This bloom, composed primarily of pelagic diatoms of the genera *Thalassiosira*, *Chaetoceros*, and *Fragilariopsis* spp., reached biomass levels of 1291 mg m⁻² Chl *a* under 100% sea ice cover 0.8-1.2 m thick as far as 100 km into the main ice pack (Arrigo et al. 2012). Data from this field campaign indicate that the areas surveyed in open water south of the main ice edge likely had previously experienced an under ice bloom as well (Arrigo et al. submitted). These open water areas were largely characterized by completely depleted nitrate in the surface layers to 20-30 m,

and the presence of an SCM near the nitracline at depths ranging from 20-40 m (Arrigo et al. submitted).

Preliminary efforts towards understanding how and why phytoplankton were able to grow so rapidly and reach such high biomass levels under the ice in 2011 indicate that the thinning and changing sea ice cover likely plays a large role (Fig. 8; Frey et al. 2011; Arrigo et al. submitted). With thinner sea ice, not only can more light penetrate, but also melt ponds that are commonly found on the ice surface act as “windows” to the ocean below (Fig. 8; Frey et al. 2011). In 2011, this resulted in enhanced light penetration to the underlying water column, which was enough to surpass the threshold in light availability needed for shade-adapted Arctic phytoplankton communities to successfully photosynthesize and grow (Frey et al. 2011; Arrigo et al. 2012; Arrigo et al. submitted). No blooms used to develop in this region because these areas were historically covered by much thicker multi-year ice in the summer (~3-6 m thick), which lets through much less light (e.g., insufficient to surpass the threshold needed for photosynthesis; Frey et al. 2011). Studies showed that ice covered by melt ponds exhibited four-fold (13-59%) more light penetration than nearby unponded bare ice (Fig. 8; Arrigo et al. submitted; Frey et al. 2011; Arrigo et al. 2012). Thus, shade-adapted under-ice Arctic phytoplankton were likely able to achieve high biomass because they maintained relatively modest rates of photosynthesis with ample under-ice nutrients (Palmer et al. submitted).

An experimental approach for exploring spatial and temporal variability in primary productivity in the Chukchi and Beaufort Seas

In this dissertation, I explore some of the recent changes in the Arctic and relate them to changes in primary productivity and biogeochemical carbon cycling in the Beaufort and Chukchi Seas. Chapter 2 focuses on the flaw-lead polynya and ice-associated bloom in the Beaufort Sea, Canadian Arctic, as part of the 2007-2008 International Polar Year – Circumpolar Flaw Lead System Study (Palmer et al. 2011). The goal of this program was to explore how primary productivity and biogeochemical patterns in the perennially ice-free waters of the flaw polynya – the

area of open water that forms due to winds and other physical factors between the central Arctic ice pack and land-fast ice (Mundy et al. 2009). In this chapter, I describe the results of photosynthesis-irradiance (P-E) measurements performed on natural phytoplankton assemblages taken from the flaw polynya region, both in the open water and under the adjacent ice cover (Palmer et al. 2011). In these analyses, the physiological response of phytoplankton to a range of light levels is used to assess photoacclimation, photosynthetic efficiency, and maximum chlorophyll-a normalized rates of carbon (C) fixation. In order to be photosynthetically competent in areas of rapidly changing light and nutrient availability, phytoplankton acclimate through physiological adjustments that maximize C fixation while minimizing variations in growth rates and photodamage. Thus, the results of our experiments are intrinsically linked to environmental conditions, which in turn are controlled by physical parameters such as mixing and stratification. In addition, the flaw polynya can be used as a proxy for identifying changes that may occur if no sea ice is present in the region in the future, allowing us to predict future changes in biogeochemical cycling and primary productivity.

In Chapter 3, I describe results from more than 250 P-E measurements performed on natural phytoplankton assemblages from the Beaufort and Chukchi Seas during the 2010-2011 ICESCAPE project (Palmer et al. submitted). This comprises the largest P-E dataset for this region of the Arctic and represents a substantial and important contribution to the understanding of biogeochemical processes in this dynamic sea ice-ocean ecosystem. This is especially exciting given the recent discovery during ICESCAPE of an unprecedented massive phytoplankton bloom under the sea ice in the Chukchi Sea (Arrigo et al. 2012; Arrigo et al. submitted). To evaluate the environmental controls of photosynthesis across several habitat types, Chapter 3 focuses on the analysis on photophysiological differences between surface and subsurface populations, and between samples gathered in open water (OW; <25% ice) and under the sea ice (UI, >25% ice). Additionally, transects extending in the direction of ice retreat from OW to ~100 km into the ice pack (a proxy for the temporal evolution of a bloom) are used to explore changes in P-E parameters over

time and discuss the ecological implications of this change in regional productivity. In particular, Chapter 3 uses this photophysiological data to explore how algae may succeed in the under ice bloom, and describes a new paradigm for Arctic marine primary productivity that may become more prevalent in future years as ice continues to melt and retreat.

In Chapter 4, I present and discuss results from a new 1-D biological model of the Beaufort and Chukchi Seas, Arctic Ocean. Models are useful tools for synthesizing large datasets such as the ones presented in Chapters 2 and 3, and great for asking questions spanning long timescales. As such, one of the primary goals with the model was to explore the conditions that promote the development of under-ice phytoplankton blooms, such as those discussed in Chapters 2-3. The 1-D nitrogen-based biogeochemical model contains two phytoplankton groups, two zooplankton groups, bacteria, dissolved organic nitrogen, detritus, and inorganic nutrients (nitrate, ammonium, etc.). An important strength of the model is in the light component: the model is coupled to an atmospheric radiative transfer model that uses measured solar input data, and also contains realistic scattering and absorption of light through sea ice (including ultraviolet radiation). The formulations and parameterizations of the biological model incorporate many of the recent observations from the ICESCAPE program and uses the results from photophysiological experiments to parameterize under-ice phytoplankton growth. Clearly, the complex interactions between thinning sea ice cover, greatly enhanced melt-pond coverage, and accelerating rates of ice loss and retreat have resulted in dramatically different light and nutrient dynamics in the underwater marine habitat than historically have been present. One of the key questions is how these variables – sea ice and snow thickness; melt pond formation, persistence, and areal coverage; and changing dates of ice retreat/break-up; interact to initiate and control the magnitude of the spring and summer phytoplankton blooms in the Chukchi Sea, Arctic Ocean. Additionally, the model asks questions based on the observations of the 2011 Chukchi Sea bloom: what, if any, threshold in areal melt-pond coverage may be needed to allow for sufficient light penetration to the underlying water column to initiate an under-ice phytoplankton bloom? The overall

goal is simulate the under-ice bloom and investigate some of the various processes affecting bloom development and biogeochemical cycling in the region.

References

- Arrigo, K. R., and G. L. van Dijken. (2004) Annual cycles of sea ice and phytoplankton near Cape Bathurst, southeastern Beaufort Sea, Canadian Arctic. *Geophys. Res. Lett.* 31(8): L08304.
- Arrigo, K. R., G. L. van Dijken and S. Pabi. (2008) Impact of a shrinking Arctic ice cover on marine primary production. *Geophys. Res. Lett.* 35: L19606, [doi:10.1029/2008GL035028](https://doi.org/10.1029/2008GL035028).
- Arrigo, K. R. and G. L. van Dijken. (2011) Secular trends in Arctic Ocean net primary production. *J. Geophys. Res.* 116: C09011, [doi:10.1029/2011JC007151](https://doi.org/10.1029/2011JC007151)
- Arrigo, K. R., D. K. Perovich, R. S. Pickart, Z. W. Brown, G. L. van Dijken, K. E. Lowry, M. M. Mills, M. A. Palmer, W. M. Balch, F. Bahr, N. R. Bates, C. Benitez-Nelson, B. Bowler, E. Brownlee, J. K. Ehn, K. E. Frey, R. Garley, S. R. Laney, L. Lubelczyk, J. Mathis, A. Matsuoka, B. G. Mitchell, G. W. K. Moore, E. Ortega-Retuerta, S. Pal, C. M. Polashenski, R. A. Reynolds, B. Scheiber, H. M. Sosik, M. Stephens, and J. H. Swift. (2012) Massive phytoplankton blooms under Arctic sea ice. *Science* 336(6087): 1408, [doi:10.1126/science.1215065](https://doi.org/10.1126/science.1215065)
- Arrigo, K. R., D. K. Perovich, R. S. Pickart, Z. W. Brown, G. L. van Dijken, K. E. Lowry, M. M. Mills, M. A. Palmer, W. M. Balch, F. Bahr, N. R. Bates, C. Benitez-Nelson, E. Brownlee, K. E. Frey, S. R. Laney, J. Mathis, A. Matsuoka, B. G. Mitchell, G. W. K. Moore, R. A. Reynolds, H. M. Sosik, and J. H. Swift. (2012) Phytoplankton blooms beneath the sea ice in the Chukchi Sea. Submitted to *J. Geophys. Res. Oceans* 2 Nov. 2012.
- Bates, N. R., M. H. P. Best, D. A. Hansell. (2005) Spatio-temporal distribution of dissolved inorganic carbon and net community production in the Chukchi and Beaufort Seas. *Deep Sea Res. II* 54:3303-3323.

- Cavalieri, D. J., P. Gloersen, C. L. Parkinson, J. C. Comiso, and H. J. Zwally. (1997) Observed Hemispheric Asymmetry in Global Sea Ice Changes. *Science* 278(5340): 1104-1106.
- Carmack, E. C. and R. W. Macdonald. (2002) Oceanography of the Canadian Shelf of the Beaufort Sea: A Setting for Marine Life. *Arctic* 55:29-45.
- Carmack, E. C., R. W. Macdonald, and S. Jasper. (2004) Phytoplankton productivity on the Canadian Shelf of the Beaufort Sea. *Marine Ecology Progress Series* 277:37-50.
- Carmack, E. C., D. G. Barber, J. Christensen, R. Macdonald, B. Rudels, E. Sakshaug. (2006) Climate variability and physical forcing of the food webs and the carbon budget on panarctic shelves. *Progr. Oceanogr.* 71(2-4): 145-181.
- Codispoti, L. A., C. N. Flagg, and J. H. Swift. (2009) Hydrographic conditions during the 2004 SBI process experiments. *Deep Sea Res. II* 56: 1144-1163.
- Codispoti, L. A., C. N. Flagg, V. Kelly, and J. H. Swift. (2005) Hydrographic conditions during the 2002 SBI process experiments. *Deep Sea Res. II* 52: 3199-3226.
- Comiso, J. C. (2002) A rapidly declining perennial sea ice cover in the Arctic. *Geophys. Res. Lett.* 29:1956.
- Comiso, J. C. (2006) Abrupt decline in Arctic winter sea ice cover. *Geophys. Res. Lett.* 33(L18504).
- Comiso, J. C., C. L. Parkinson, R. Gersten, and L. Stock. (2008) Accelerated decline in the Arctic sea ice cover. *Geophys. Res. Lett.* 35: L01703.
- Cota, G. F., L. R. Pomeroy, W. G. Harrison, E. P. Jones, F. Peters, W. M. Sheldon Jr., and T. R. Weingartner. (1996) Nutrients, primary production and microbial heterotrophy in the southeastern Chukchi Sea: Arctic summer nutrient depletion and heterotrophy. *Geophys. Res. Lett.* 135: 247-258, doi:10.3354/meps135247
- Frey, K. E., D. K. Perovich, and B. Light. (2011) The spatial distribution of solar radiation under a melting Arctic sea ice cover. *Geophys. Res. Lett.*, 38, L22501, doi:10.1029/2011GL049421

- Giles, K. A., S. W. Laxon, and A. L. Ridout. (2008) Circumpolar thinning of Arctic sea ice following the 2007 record ice extent minimum. *Geophys. Res. Lett.* 35:L22502.
- Gosselin, M., M. Levasseur, P. A. Wheeler, R. A. Horner, and B. C. Booth. (1997) New measurements of phytoplankton and ice algal production in the Arctic Ocean. *Deep-Sea Res. Part II* 44(8): 1623-1644.
- Grebmeier, J. M., J. E. Overland, S. E. Moore, E. V. Farley, E. C. Carmack, L. E. Cooper, K. E. Frey, J. H. Helle, F. A. McLaughlin, and S. L. McNutt. (2006) A major ecosystem shift in the Northern Bering Sea. *Science* 311:1461-1464.
- Hill V., and G. Cota. (2005) Spatial patterns of primary production on the shelf, slope and basin of the Western Arctic in 2002. *Deep-Sea Res. II* 52: 3344-3354, [doi:10.1016/j.dsr2.2005.10.001](https://doi.org/10.1016/j.dsr2.2005.10.001)
- Horner, R. and G. C. Schrader. (1982) Relative contributions of ice algae, phytoplankton, and benthic microalgae to primary production in nearshore regions of the Beaufort Sea. *Arctic* 35(4):485-503.
- Kwok, R., and D. A. Rothrock (2009) Decline in Arctic sea ice thickness from submarine and ICESat records: 1958-2008, *Geophys. Res. Lett.*, 36.
- Lindsay, R. W. and J. Zhang. (2005) The thinning of Arctic sea ice, 1988-2003: have we passed a tipping point? *J. Climate* 18: 4879-4894.
- Loeng, H., K. Brander, E. Carmack, S. Denisenko, K. Drinkwater, B. Hansen, K. Kovacs, P. Livingston, F. McLaughlin, and E. Sakshaug. (2006) Marine Systems, p. 453-538 In: *Arctic Climate Impact Assessment: An Assessment of Consequences of Climate Variability and Change and the Effects of Increased UV in the Arctic Region*, Cambridge Univ. Press.
- Maslanik, J., S. Drobot, C. Fowler, W. Emery, and R. Barry. (2007a) On the Arctic climate paradox and the continuing role of atmospheric circulation in affecting sea ice conditions. *Geophys. Res. Lett.* 34:L03711.
- Maslanik, J. A., C. Fowler, J. Stroeve, S. Drobot, J. Zwally, D. Yi, and W. Emery. (2007b) A younger, thinner Arctic ice cover: Increased potential for rapid, extensive sea-ice loss. *Geophys. Res. Lett.* 34:L24501.

- Maslanik, J., J. Stroeve, C. Fowler, and W. Emery. (2011) Distribution and trends in Arctic sea ice age through spring 2011. *Geophys. Res. Lett.* 38(L13502), doi:10.1029/2011GL047735.
- Martin J., J.-È. Tremblay, J. Gagnon, G. Tremblay, A. Lapoussiere, C. Jose, M. Poulin, M. Gosselin, Y. Gratton, and C. Michel. (2010) Prevalence, structure and properties of subsurface chlorophyll maxima in Canadian Arctic waters. *Mar. Ecol. Prog. Ser.* 412: 69-84, doi:10.3354/meps08666.
- Meier, W. N., J. Stroeve, and F. Fetterer. (2007) Whither Arctic sea ice? A clear signal of decline regionally, seasonally and extending beyond the satellite record. *Annals of Glaciology* 46, 428-434.
- Mundy, C. J., M. Gosselin, J. Ehn, Y. Gratton, A. Rossnagel, D. G. Barber, J. Martin, J.-È. Tremblay, M. A. Palmer, K. R. Arrigo, G. Darnis, L. Fortier, B. Else, and T. Papakyriakou. (2009) Contribution of under-ice primary production to an ice-edge upwelling phytoplankton bloom in the Canadian Beaufort Sea. *Geophys. Res. Lett.* 36: L17601, doi:10.1029/2009GL038837
- National Snow and Ice Data Center (NSIDC) (2012). From the Arctic Sea Ice News Database. Accessed November 1, 2012 at <http://nsidc.org/arcticseaicenews>, National Snow and Ice Data Center, University of Colorado, Boulder, USA.
- Nghiem, S. V., I. G. Rigor, D. K. Perovich, P. Clemente-Colon, J. W. Weatherly, G. Neumann. (2007) Rapid reduction of Arctic perennial sea ice. *Geophys. Res. Lett.* 34: L19504.
- Overpeck, J. T., M. Sturm, J. A. Francis, D. K. Perovich, M. C. Serreze, R. Benner, E.C. Carmack, F. S. Chapin III, S. C. Gerlach, L. C. Hamilton, L. D. Hinzman, M. Holland, H. P. Huntington, J. R. Key, A. H. Lloyd, G. M. MacDonald, J. McFadden, D. Noone, T. D. Prowse, P. Schlosser, and C. Vorosmarty. (2005) Arctic System on Trajectory to New, Seasonally Ice-Free State. *EOS, Transactions American Geophysical Union* 86(34): 309-316.
- Pabi, S., G. L. van Dijken and K. R. Arrigo. (2008) Primary Production in the Arctic Ocean, 1998-2006. *J. Geophys. Res.* 113: C08005, doi:10.1029/2007JC004578

- Palmer, M. A., K. R. Arrigo, C. J. Mundy, J. K. Ehn, M. Gosselin, D. G. Barber, J. Martin, E. Alou, S. Roy, and J.-È. Tremblay. (2011) Spatial and temporal variation of photosynthetic parameters in natural phytoplankton assemblages in the Beaufort Sea, Canadian Arctic. *Polar Biol.* 34: 1915-1928, doi:10.1007/s00300-011-1050-x
- Perovich, D. K. (1998) *Physics of ice covered seas*, Volume 1, pp. 446. Univ. of Helsinki Press.
- Perovich, D. K., and C. Polashenski. (2012) Albedo evolution of seasonal Arctic sea ice. *Geophys. Res. Lett.* 39: L08501, doi:10.1029/2012GL051432
- Perrette M., A. Yool, G. D. Quartly, and E. E. Popova. (2011) Near-ubiquity of ice-edge blooms in the Arctic. *Biogeosciences* 8: 515-524.
- Rigor, I. G., J. M. Wallace, and R. L. Colony. (2002) Response of Sea Ice to the Arctic Oscillation. *J. Climate* 15:2648-2663.
- Rothrock, D. A. and J. Zhang. (2005) Arctic Ocean sea ice volume: What explains its recent depletion? *J. Geophys. Res.* 110:C01002.
- Sakshaug, E. (2003) Primary and secondary production in the Arctic Seas, in *The Organic Carbon Cycle in the Arctic Ocean*, edited by R. Stein and R. W. Macdonald, pp. 57–81, Springer-Verlag, Berlin.
- Serreze, M. C., M. M. Holland, and J. Stroeve. (2007) Perspectives on the Arctic's shrinking sea-ice cover. *Science* 315:1533-1536.
- Shimada, K., T. Kamoshida, M. Itoh, S. Nishino, E.C. Carmack, F. McLaughlin, S. Zimmerman, and A. Proshutinsky. (2006) Pacific Ocean Inflow: Influence on catastrophic reduction of sea ice cover in the Arctic Ocean. *Geophys. Res. Lett.* 22(L08605):1-4.
- Stroeve, J., M. M. Holland, W. Meier, T. Scambos, and M. Serreze. (2007) Arctic sea ice decline: Faster than forecast. *Geophys. Res. Lett.* 34:L09501.
- Stroeve, J., M. Serreze, S. Drobot, S. Gearheard, M. Holland, J. Maslanik, W. Meier, and T. Scambos. (2008) Arctic Sea Ice Extent Plummets in 2007. *EOS, Transactions American Geophysical Union* 89(2):13-14.

- Tremblay, J.-É., C. Michel, K. A. Hobson, M. Gosselin, and N. M. Price. (2006) Bloom dynamics in early opening waters of the Arctic Ocean. *Limnol. Oceanogr.* 51(2): 900-012.
- Tremblay, J.-É., K. Simpson, J. Martin, L. A. Miller, Y. Gratton, D. G. Barber, and N. M. Price. (2008) Vertical stability and the annual dynamics of nutrients and chlorophyll fluorescence in the coastal, southeast Beaufort Sea. *J. Geophys. Res.* 113: C07S90, doi:10.1029/2007JC004547
- Wang, J., G. F. Cota, and J. Comiso. (2005) Phytoplankton in the Beaufort and Chukchi Seas: distribution, dynamics, and environmental forcing. *Deep-Sea Res. II* 52: 3355-3368, [doi:10.1016/j.dsr2.2005.10.014](https://doi.org/10.1016/j.dsr2.2005.10.014)

Average Monthly Arctic Sea Ice Extent September 1979 - 2012

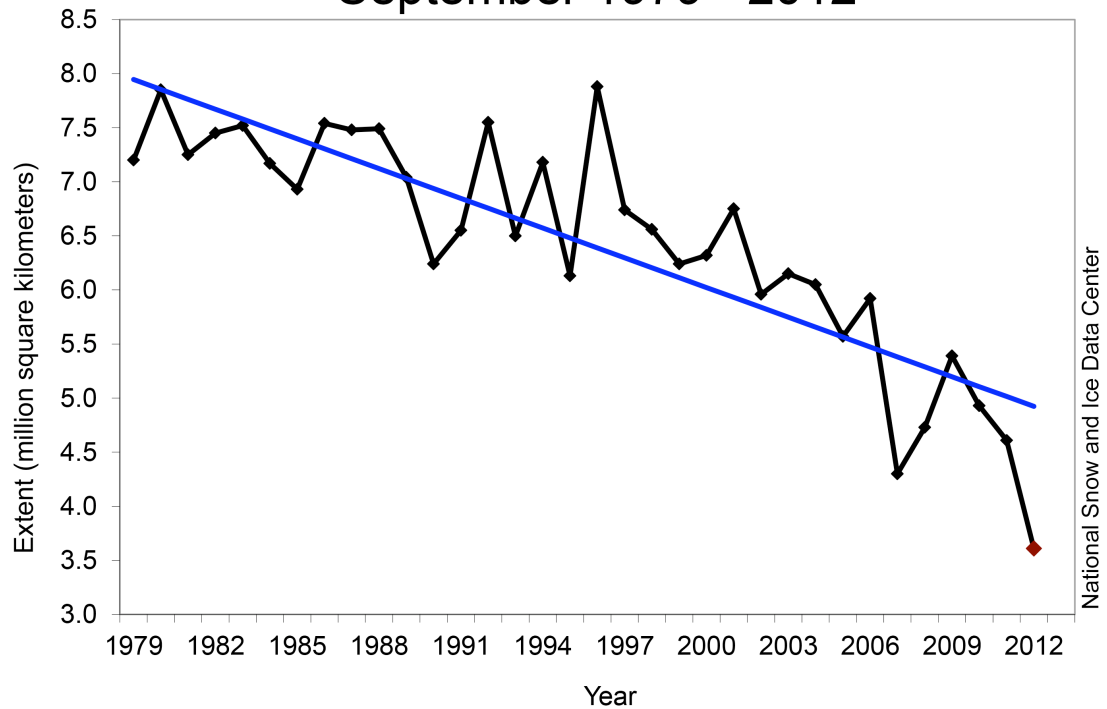


Figure 1. Average monthly sea ice extent in the Arctic Ocean for the September minimum (lowest average ice month) based on satellite data. Source: National Snow and Ice Data Center (NSIDC). In September 2012, the average sea ice extent in the Arctic was the lowest on satellite record, 16% below the previous September low that was reached in 2007.

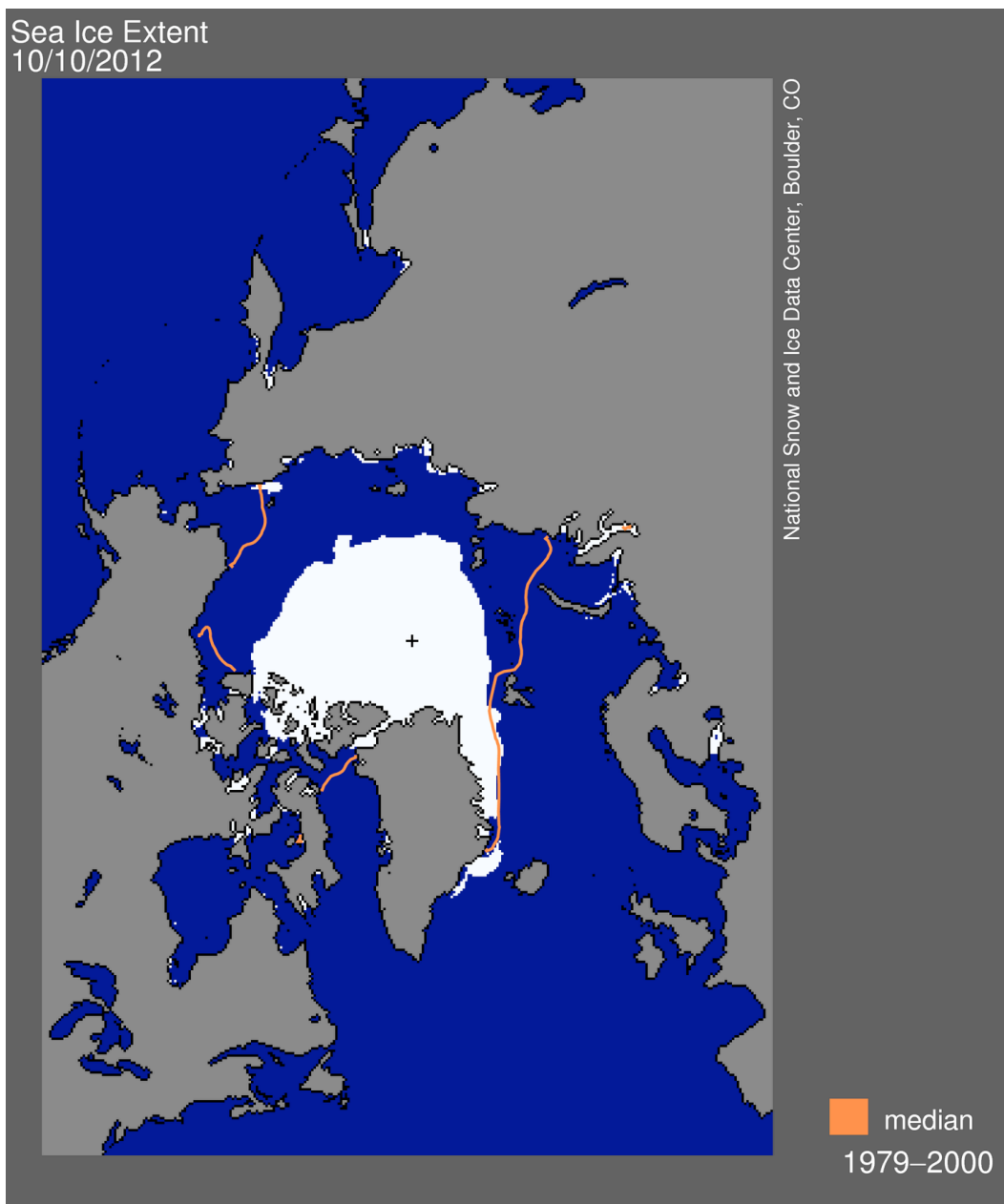


Figure 2. Average sea ice extent (ice shown in white; blue is ocean and light grey is land mass) just after the September 2012 minimum (image downloaded 10/10/2012 from the NSIDC website), showing the vast reduction in sea ice extent that was witnessed in 2012.

Arctic Sea Ice Age

September 2007

September 2012

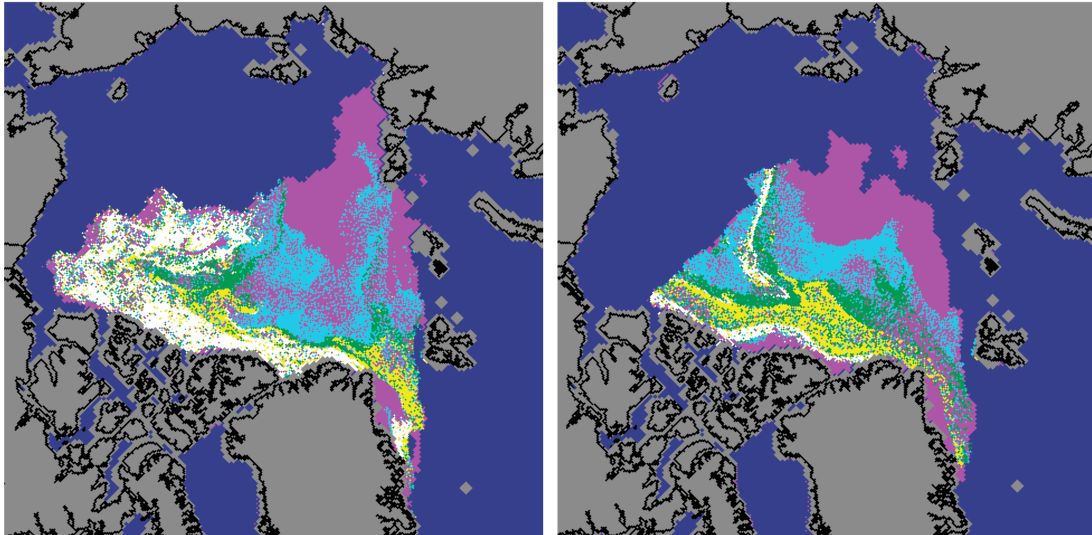
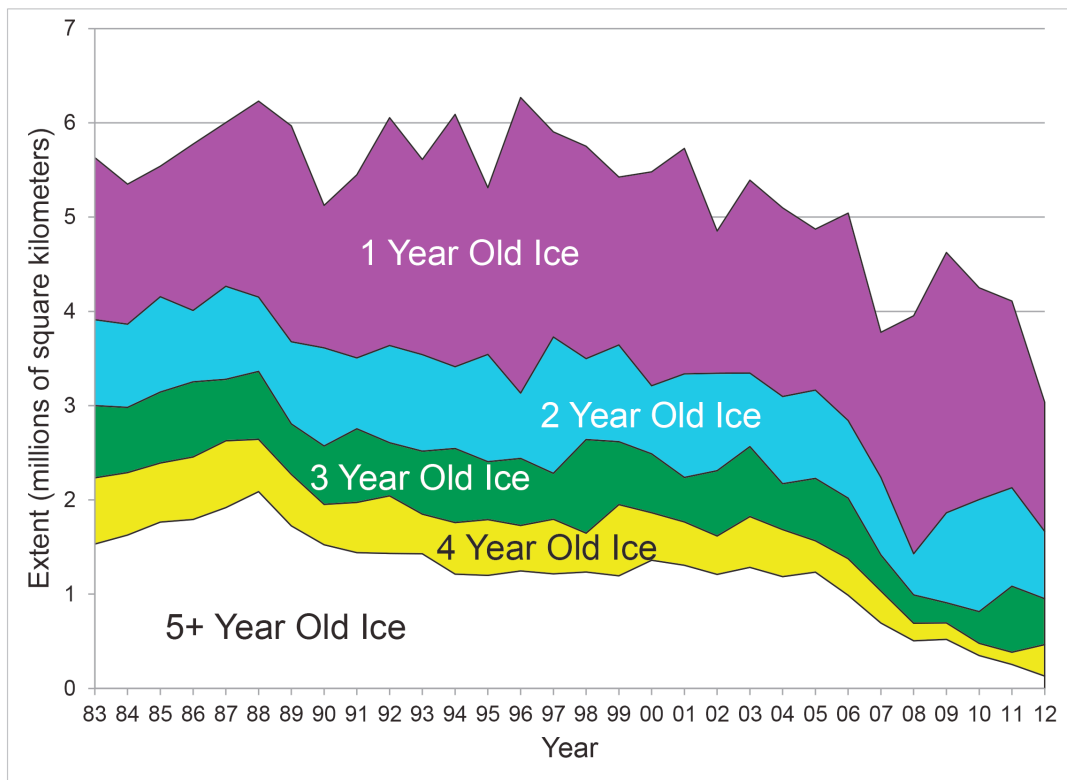


Figure 3. Arctic sea ice age from September 2007 (left) and September 2012 (right) (dark blue is ocean, light grey is land mass; Greenland is the bottom center island for reference). Ice colors: purple – first year ice; blue – 2-yr old ice; green – 3-yr old ice; yellow – 5-yr old ice; white – 5+ yr old ice. Multiyear ice (purple) has greatly declined since the previous record ice minimum was achieved in 2007. Source: NSIDC 2012.



NSIDC courtesy M. Tschudi and J. Maslanik, University of Colorado Boulder

Figure 4. Estimated ice in various age classes from 1983-2012, showing that ice of all ages has declined, with the sharpest declines in the 5+ year old ice (NSIDC 2012). First year ice (purple) now dominates much of the Arctic sea ice cover. Note the previous ice minimum in 2007, when large quantities of first year ice were melted. In the 2012-2013 winter, only 20% of the old (5+ year) ice remains compared to the 1980s (image courtesy of NSIDC 2012 and M. Tschudi and J. Maslanik, University of Colorado Boulder.).



Figure 5. The main currents and hydrography of the Arctic Ocean; blue represents relatively cool, fresh surface currents, whereas red represents the relatively warmer, saltier Atlantic water that sits at 100-200 m depth all throughout the Arctic region. Note on the left side where the Bering Strait acts as one of the two main inflows to the Arctic Ocean (the other is the North Atlantic current, which enters at depth in the eastern Arctic). Illustration by Jack Cook, Woods Hole Oceanographic Institution (www.whoi.edu).

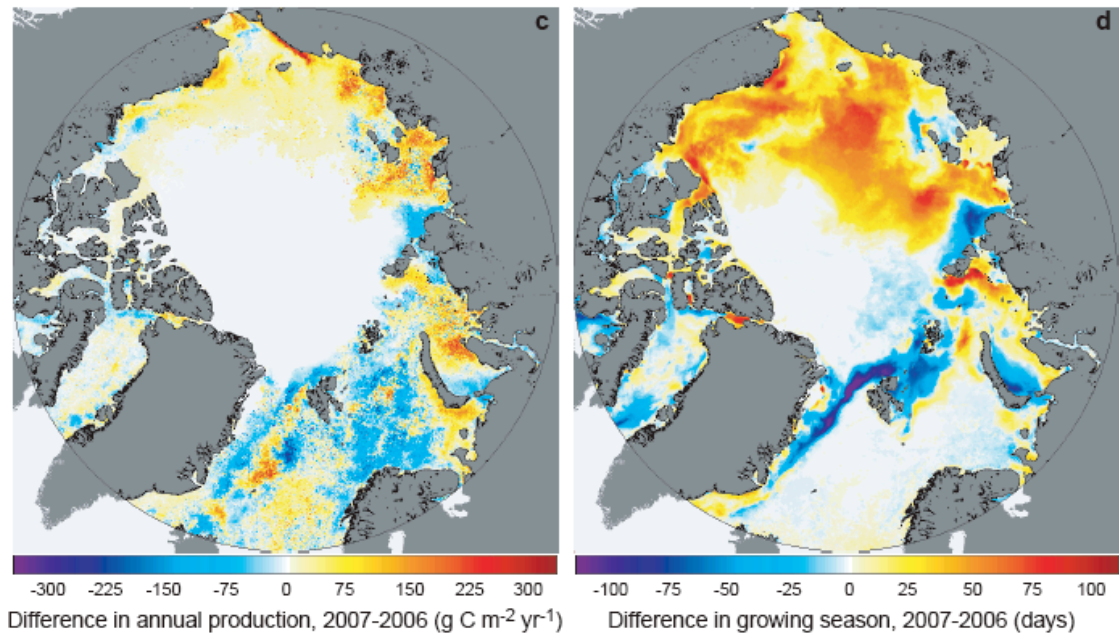


Figure 6. Difference in annual primary production between 2007 and 2006 (left), compared to the difference in the length of the growing season (right), based on satellite remote sensing data (source: Arrigo and van Dijken 2011). Much of the increase in primary production in 2007, when substantial sea ice melt occurred, was attributed to the increase in the length of the growing season (ice-free season) rather than due to the increase in area of open water.

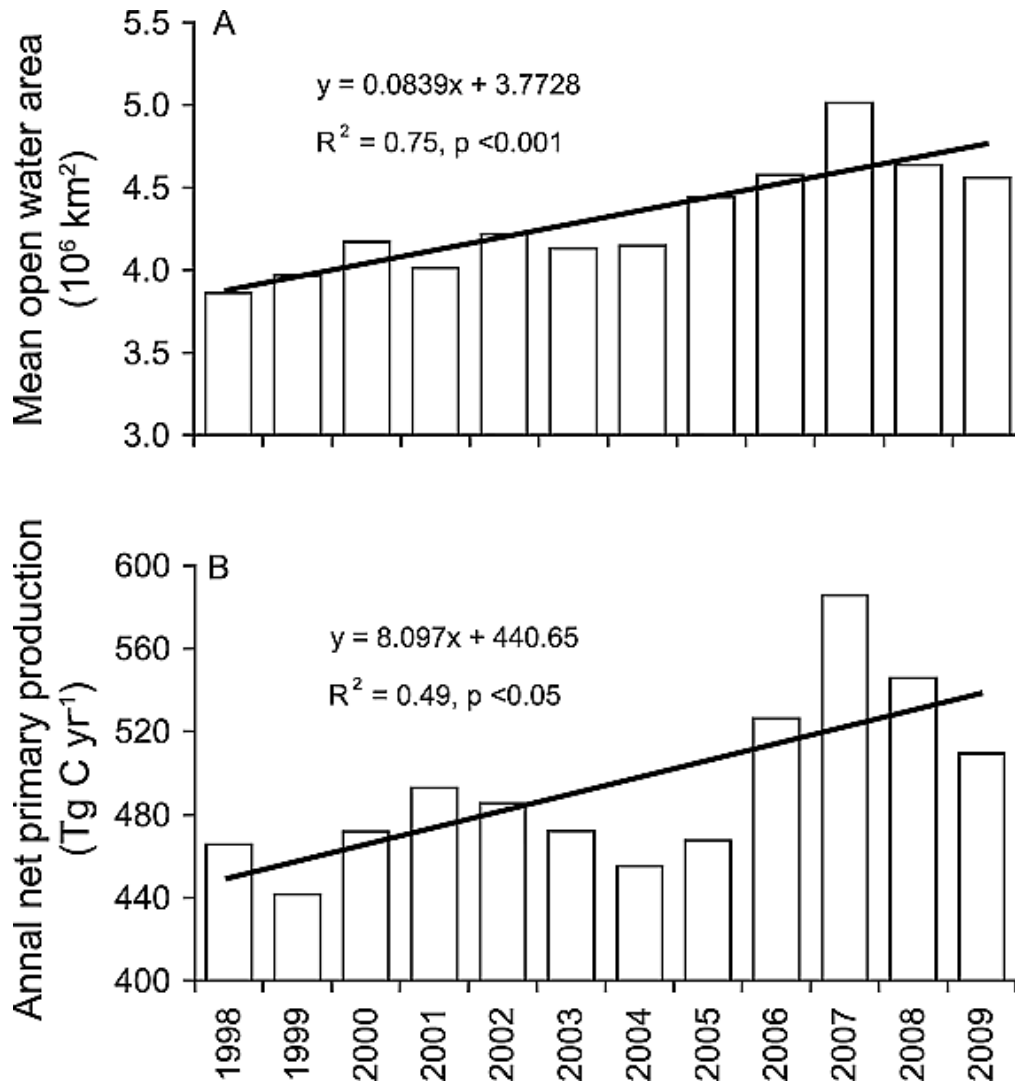


Figure 7. Graphs from Arrigo and van Dijken (2011) showing the increase in open water area (top) and increase in annual primary production between 1998 and 2009 based on satellite remote sensing data. Open water area increased by 27%, whereas the length of the growing season increased by 45 days, resulting in a 20% increase in total primary production in the Arctic Ocean (Arrigo and van Dijken 2011).

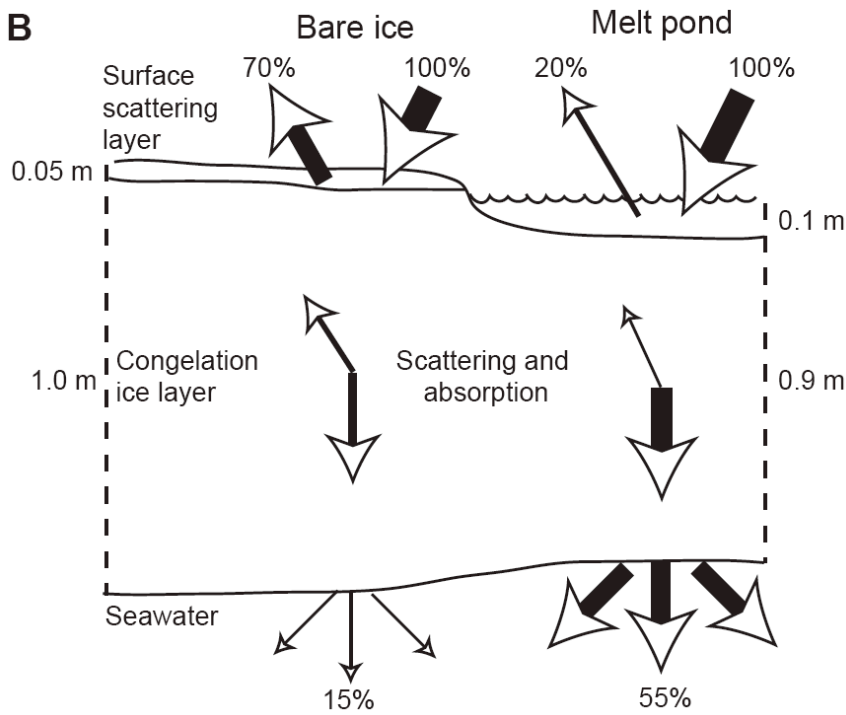


Figure 8. Impact of ice loss on the underwater light field, from Arrigo et al. *submitted*. **A:** image showing melt ponds (dark blue) covering first year sea ice (white) in the Chukchi Sea in the summer of 2011. Photograph 13 July 2011 courtesy of Christie Wood. **B:** Diagram depicting how melt ponds enhance light transmission through sea ice as compared to bare ice. Melt ponds do not scatter as much light as bare ice, plus ice is thinner below ponded ice, and thus more substantially more light gets through to the ocean below.

CHAPTER 2:
SPATIAL AND TEMPORAL VARIATION OF PHOTOSYNTHETIC
PARAMETERS IN NATURAL PHYTOPLANKTON ASSEMBLAGES IN THE
BEAUFORT SEA, CANADIAN ARCTIC

Spatial and temporal variation of photosynthetic parameters in natural phytoplankton assemblages in the Beaufort Sea, Canadian Arctic

Molly A. Palmer¹, Kevin R. Arrigo¹, C.J. Mundy², Jens K. Ehn³, Michel Gosselin², David G. Barber⁴, Johannine Martin⁵, Eva Alou², Suzanne Roy², Jean-Éric Tremblay⁵

¹ Department of Environmental Earth System Science, Stanford University, Stanford, California 94305, USA

² Institut des sciences de la mer, Université du Québec à Rimouski, Rimouski, Québec G5L 2A1, Canada

³ Marine Physical Laboratory, Scripps Institution of Oceanography, University of California at San Diego, La Jolla, California, USA

⁴ Centre for Earth Observation Science, Faculty of Environment, Earth and Resources, University of Manitoba, Winnipeg, Manitoba R3T 2N2, Canada

⁵ Québec-Océan, Département de biologie, Université Laval, Québec, Québec G1V OA6, Canada

Chapter 2, including figures, has been reproduced with permission from Springer and Polar Biology from the published article: Palmer, MA, KR Arrigo, CJ Mundy, JK Ehn, M Gosselin, DG Barber, J Martin, E Alou, S Roy, and J-E Tremblay. 2011. Polar Biology 34(12): 1915-1928, doi:10.1007/s00300-011-1050-x. With kind permission from Springer Science and Business Media.

From: Molly A. Palmer
Environmental Earth System Science
Stanford University
Stanford, CA 94305

4 Oct. 2012

To: Springer Science and Business Media
Copyright Clearance Center

Dear Springer Permissions Manager,

I am completing a doctoral dissertation at Stanford University entitled “Primary productivity and biogeochemical carbon cycling in the Beaufort and Chukchi Seas, Arctic Ocean”. I would like your permission to reprint in my dissertation excerpts from the following article, of which I am the primary author of the original material:

The article text, figures, and tables will be reproduced in my dissertation with no modifications in any form, including abbreviations, additions, deletions, or any other alterations without prior written authorization, and would include a citation within the introductory remarks and complete article citation on the chapter title page.

The material will be formatted in accordance with Stanford University dissertation guidelines. This material will only be used for the purpose of defending my thesis.

My dissertation will be produced electronically and made available through the Stanford University Library and its publication partners. These rights will in no way limit republication of the material in any other form by you or others authorized by you. Your agreement will verify that your company owns the copyright to the above material.

If this meets with your approval, please return a License Agreement form, which I will include with my dissertation. Thank you very much for your attention to this matter.

Sincerely,
Molly A. Palmer

PERMISSION GRANTED FOR THE USE REQUESTED ABOVE:

By: Springer Science + Business Media
License Number: 3002130919192
Date: 4 October 2012

**SPRINGER LICENSE
TERMS AND CONDITIONS**

Oct 04, 2012

This is a License Agreement between Molly A Palmer ("You") and Springer ("Springer") provided by Copyright Clearance Center ("CCC"). The license consists of your order details, the terms and conditions provided by Springer, and the payment terms and conditions.

All payments must be made in full to CCC. For payment instructions, please see information listed at the bottom of this form.

License Number	3002130919192
License date	Oct 04, 2012
Licensed content publisher	Springer
Licensed content publication	Polar Biology
Licensed content title	Spatial and temporal variation of photosynthetic parameters in natural phytoplankton assemblages in the Beaufort Sea, Canadian Arctic
Licensed content author	Molly A. Palmer
Licensed content date	Jan 1, 2011
Volume number	34
Issue number	12
Type of Use	Thesis/Dissertation
Portion	Full text
Number of copies	1
Author of this Springer article	Yes and you are a contributor of the new work
Order reference number	
Title of your thesis / dissertation	Primary productivity and biogeochemical carbon cycling in the Beaufort and Chukchi Seas, Arctic Ocean
Expected completion date	Dec 2012
Estimated size(pages)	100
Total	0.00 USD
Terms and Conditions	

Introduction

The publisher for this copyrighted material is Springer Science + Business Media. By clicking "accept" in connection with completing this licensing transaction, you agree that the following terms and conditions apply to this transaction (along with the Billing and Payment terms and conditions established by Copyright Clearance Center, Inc. ("CCC"), at the time that you opened your Rightslink account and that are available at any time.

Limited License

With reference to your request to reprint in your thesis material on which Springer Science and Business Media control the copyright, permission is granted, free of charge, for the use indicated in your enquiry.

Licenses are for one-time use only with a maximum distribution equal to the number that you identified in the licensing process.

This License includes use in an electronic form, provided its password protected or on the university's intranet or repository, including UMI (according to the definition at the Sherpa website: <http://www.sherpa.ac.uk/romeo/>). For any other electronic use, please contact Springer at (permissions.dordrecht@springer.com or permissions.heidelberg@springer.com).

The material can only be used for the purpose of defending your thesis, and with a maximum of 100 extra copies in paper 

Although Springer controls copyright to the material and is entitled to negotiate on rights, this license is only valid, provided permission is also obtained from the (co) author (address is given with the article/chapter) and provided it concerns original material which does not carry references to other sources (if material in question appears with credit to another source, authorization from that source is required as well).

Permission free of charge on this occasion does not prejudice any rights we might have to charge for reproduction of our copyrighted material in the future.

Altering/Modifying Material: Not Permitted

You may not alter or modify the material in any manner. Abbreviations, additions, deletions and/or any other alterations shall be made only with prior written authorization of the author(s) and/or Springer Science + Business Media. (Please contact Springer at (permissions.dordrecht@springer.com or permissions.heidelberg@springer.com)

Reservation of Rights

Springer Science + Business Media reserves all rights not specifically granted in the combination of (i) the license details provided by you and accepted in the course of this licensing transaction, (ii) these terms and conditions and (iii) CCC's Billing and Payment terms and conditions.

Copyright Notice:Disclaimer

You must include the following copyright and permission notice in connection with any reproduction of the licensed material: "Springer and the original publisher /journal title, volume, year of publication, page, chapter/article title, name(s) of author(s), figure number(s), original copyright notice) is given to the publication in which the material was originally published, by adding: with kind permission from Springer Science and Business Media"

Warranties: None

Example 1: Springer Science + Business Media makes no representations or warranties with respect to the licensed material.

Example 2: Springer Science + Business Media makes no representations or warranties with respect to the licensed material and adopts on its own behalf the limitations and disclaimers established by CCC on its behalf in its Billing and Payment terms and conditions for this licensing transaction.

Indemnity

You hereby indemnify and agree to hold harmless Springer Science + Business Media and CCC, and their respective officers, directors, employees and agents, from and against any and all claims arising out of your use of the licensed material other than as specifically authorized pursuant to this license.

No Transfer of License

This license is personal to you and may not be sublicensed, assigned, or transferred by you to any other person without Springer Science + Business Media's written permission.

No Amendment Except in Writing

This license may not be amended except in a writing signed by both parties (or, in the case of Springer Science + Business Media, by CCC on Springer Science + Business Media's behalf).

Objection to Contrary Terms

Springer Science + Business Media hereby objects to any terms contained in any purchase order, acknowledgment, check endorsement or other writing prepared by you, which terms are inconsistent with these terms and conditions or CCC's Billing and Payment terms and conditions. These terms and conditions, together with CCC's Billing and Payment terms and conditions (which are incorporated herein), comprise the entire agreement between you and Springer Science + Business Media (and CCC) concerning this licensing transaction. In the event of any conflict between your obligations established by these terms and conditions and those established by CCC's Billing and Payment terms and conditions, these terms and conditions shall control.

Jurisdiction

All disputes that may arise in connection with this present License, or the breach thereof, shall be settled exclusively by arbitration, to be held in The Netherlands, in accordance with Dutch law, and to be conducted under the Rules of the 'Netherlands Arbitrage Instituut' (Netherlands Institute of Arbitration). OR: All disputes that may arise in connection with this present License, or the breach thereof, shall be settled exclusively by arbitration, to be held in the Federal Republic of Germany, in accordance with German law. Other terms and conditions:v1.3

ABSTRACT

During summer 2008, as part of the Circumpolar Flaw Lead system study, we measured phytoplankton photosynthetic parameters to understand regional patterns in primary productivity, including the degree and timescale of photoacclimation and how variability in environmental conditions influences this response. Photosynthesis-irradiance measurements were performed at 15 sites primarily from the depth of the subsurface chlorophyll *a* (Chl *a*) maximum (SCM) within the Beaufort Sea flaw-lead polynya. The physiological response of phytoplankton to a range of light levels was used to assess maximum rates of carbon (C) fixation (P_m^*), photosynthetic efficiency (α^*), photoacclimation (E_k), and photoinhibition (β^*). SCM samples taken along a transect from under ice into open water exhibited a >3-fold increase in α^* and P_m^* , showing these parameters can vary substantially over relatively small spatial scales, primarily in response to changes in the ambient light field. Algae were able to maintain relatively high rates of C-fixation despite low light at the SCM, particularly in the large (>5 μm) size fraction at open water sites. This may substantially impact biogenic C drawdown if species composition shifts in response to future climate change. Our results suggest that phytoplankton in this region are well acclimated to existing environmental conditions, including sea ice cover, low light, and nutrient pulses. Furthermore, this photoacclimatory response can be rapid and keep pace with a developing SCM, as phytoplankton maintain photosynthetic rates and efficiencies in a narrow “shade-acclimated” range.

Keywords: *phytoplankton; photosynthesis-irradiance measurements; subsurface chlorophyll maximum; Beaufort Sea; polynya*

1. Introduction

The Arctic sea ice cover will be subject to large reductions in future years due to climate warming and the associated complex feedbacks (Stroeve et al. 2008; Wang and Overland 2009). It has been suggested that the reduction in ice cover, through the increase in nutrient supply from wind-induced upwelling and greater number of open water days, may increase primary productivity (PP) in the Arctic by as much as 3-fold (Arrigo et al. 2008; Pabi et al. 2009; Zhang et al. 2010). In contrast, a freshening of polar surface waters in the Canada Basin due to increases in meltwater and river runoff has been suggested to limit the winter renewal of nutrients, providing a more favorable environment for a smaller celled phytoplankton community (Li et al. 2009; McLaughlin and Carmack 2010). These contrasting scenarios demonstrate the need for a better understanding of PP dynamics in the polar marine ecosystem.

Polar marine environments are characterized by extreme variability in light, temperature, and nutrient availability. Phytoplankton form the base of the marine food web and play an important role in Earth's carbon (C) and climate cycles through the photosynthetic fixation of atmospheric CO₂. In a typical Arctic marine ecosystem, PP follows a seasonal progression from ice-associated algae in spring prior to ice break-up, followed by ice-edge and open water blooms of phytoplankton in early summer, with subsurface chlorophyll *a* (Chl *a*) maxima (SCM) commonly forming at depth after nutrient exhaustion in surface waters (e.g., Arrigo and van Dijken 2004; Martin et al. 2010). The recent determination by Martin et al. (2010) of the prevalence of the SCM testifies to their potential importance to the Arctic marine ecosystem, yet these areas pose a particular challenge to remote-sensing estimates of PP (Pabi et al. 2008).

The seasonal PP cycle in the Arctic Ocean is further influenced by a series of interconnected flaw lead polynyas that form where the central ice pack pulls away from landfast ice (Carmack and Macdonald 2002; Barber and Massom 2006; Barber et al. 2010). These persistent open water areas are thought to critically influence PP patterns and regional biogeochemical cycles, yet little is known about the role they play in seeding the spring bloom and driving SCM development (Cavalieri and Martin 1994; Hill and Cota 2005; Tremblay et al. 2008). Nonetheless, in order to survive and

be photosynthetically competent in these dynamic areas, phytoplankton must be able to acclimate to the constantly changing conditions.

Phytoplankton can vary their photosynthetic machinery to acclimate to changing combinations of light, temperature, and nutrient conditions. Two basic photoacclimation responses in algae include changes in the number of photosynthetic units (PSU) and changes in the functional size of light-harvesting antennae serving the photosystem reaction centers (Sukenic et al. 1987). Alteration of the photosynthetic apparatus in response to changes in light (intensity and/or spectral distribution) is usually measured as a change in either total pigment concentration per cell, the ratio of different pigments, or both (Falkowski and La Roche 1991). These biochemical changes in turn affect the rate of photochemical reactions and the efficiency of light utilization, both of which ultimately affect CO₂ uptake. For example, cells acclimated to high irradiance typically have less pigment per cell, fewer PSU, and higher maximum rates of photosynthesis per unit chlorophyll than low-light acclimated cells (Falkowski 1980). In contrast, the heavy investment in light-harvesting and photosynthetic pigments required by low-light acclimated cells can lead to excess excitation and photodamage under high irradiances.

These photoacclimatory responses can help explain the presence and/or dominance of one phytoplankton group over others in polar marine environments (e.g., Hill et al. 2005; Kropuenske et al. 2009; Arrigo et al. 2010). It has been observed for the Arctic shelf regions that when under ice phytoplankton or sloughed ice algae are exposed to high irradiance (e.g., associated with ice break-up), they exhibit severe photoinhibition and may take two to six weeks to fully acclimate (Gallegos et al. 1983; Kirst and Wiencke 1995). The timescale of an acclimation response impacts net C drawdown since photoinhibited or photodamaged cells do not fix as much C per quanta absorbed as do healthy growing cells (Kirk 1994). Furthermore, this has profound implications for the entire food web due to the different biogeochemical and ecological roles played by different taxa.

As part of the International Polar Year (IPY) - Circumpolar Flaw Lead (CFL) system study (Barber et al. 2010), we examined spatial and temporal variability in

phytoplankton photosynthetic parameters in the Cape Bathurst polynya (CBP) during the summer of 2008. The project provided a unique opportunity to investigate how polynyas influence PP patterns, and how phytoplankton cope in sea-ice affected areas (including at the SCM). Using data collected primarily from the SCM both in open waters of the CBP and below adjacent sea ice, we explored how environmental conditions affect the photosynthetic performance of phytoplankton. Photosynthesis-irradiance (P-E) analyses were used to assess photoacclimation, photosynthetic efficiency, and maximum Chl *a*-normalized rates of CO₂ fixation. Our main objective was to explore how the data from P-E analyses could inform our understanding of PP dynamics in this region. Within the context of the IPY-CFL project, we were interested in understanding (1) the extent to which Arctic phytoplankton are shade-acclimated and (2) how photosynthetic parameters vary spatially and temporally in both open water and under ice regions of the flaw polynya.

2. Materials and Methods

2.1. Study area

The CBP forms semi-annually in the southern Beaufort Sea and Amundsen Gulf as the mobile central Arctic ice pack rotates westward (anticyclonic) away from landfast ice lying over the Mackenzie Shelf (Barber and Hanesiak 2004) (Fig. 1). The continental shelf here is broad and shallow (50 – 100 m), with heavy seasonal inputs of freshwater from the Mackenzie River, one of the largest Arctic rivers (average output of 330 km³ yr⁻¹) (Carmack et al. 2004). Field observations were conducted onboard the CCGS *Amundsen* between 6 June and 6 July 2008. Prior to 22 June, all oceanographic data were collected beneath landfast first-year ice in Darnley Bay (DB; 69° 49.6' N, 123° 37.9' W, depth ~80 m) and Franklin Bay (FB; 69° 59.4' N, 125° 52.5' W, depth ~100 m); after this (and at one station on 10 June), data were gathered in open waters of the CBP. We divide our results based on location (under ice [UI] or open water [OW]), as well as by type (mostly we sampled the SCM, although we show data from two UI surface water [UISW] samples taken at stations DB7 and FB5).

Hydrography and nutrient dynamics in this region of the Beaufort Sea have been described elsewhere (Tremblay et al. 2008). Briefly, the upper 200-300 m is dominated by waters of Pacific origin that are heavily influenced by river input and the freeze-melt cycle, resulting in a relatively cold, fresh layer ($T \approx -1.5^\circ\text{C}$, $S < 33$ psu) (Carmack and Macdonald 2002; Melling and Moore 1995). Surface mixed layer depths (MLD) range from 10-50 m with depth heavily dependent on seasonality of winds and ice cover (Carmack and Macdonald 2002). Melt ponds form on the surface of the sea ice by early summer, greatly increasing the penetration of photosynthetically active radiation (PAR; 400 to 700 nm) to the water column. We witnessed a short-lived ice-edge upwelling event during the course of our field season (Mundy et al. 2009). At the time, sustained easterly winds of $>10 \text{ m s}^{-1}$ blew parallel to the ice edge in Darnley Bay over a 72 h period (4 to 7 June), inducing upwelling of nutrient-rich Pacific intermediate water ($S > 32.5$ psu, $T < -1^\circ\text{C}$, $\text{NO}_3 > 5 \text{ mM}$) from a depth of >40 m to the upper 10 m. This resulted in a very productive under ice phytoplankton bloom lasting until ice break-up on 22 June (Chl *a* peak values: $\sim 25 \text{ mg m}^{-3}$; 345 mg m^{-2} integrated over upper 50 m). The bloom accumulated above the 32.5 halocline as it gradually descended (see Fig. 2, Mundy et al. 2009).

2.2. Sampling protocols

Vertical profiles of water temperature, salinity, *in vivo* Chl *a* fluorescence, and PAR were measured using a SBE-911+ CTD sensor (Sea-Bird Electronics, Inc.) mounted on a rosette equipped with 24 12-L Niskin-type bottles (OceanTest Equipment), a fluorometer (Seapoint Sensors, Inc.), and a QCP-2300 PAR/Irradiance sensor (Biospherical Instruments, Inc.). Post-cruise calibration and processing of CTD data were performed as in Mundy et al. (2009). Fluorometer data were calibrated against extracted Chl *a* and used to convert fluorescence to Chl *a* concentration (mg m^{-3} , $r^2=0.94$; see Tremblay et al. 2008, Mundy et al. 2009). MLD at each station was estimated from CTD data by locating the maximum value of the Brunt-Väisälä frequency (N^2) as calculated from the density gradient of individual profiles (Martin et al. 2010).

Water samples were taken from the depth of the SCM as determined using the CTD fluorometer. For UI sites, the CTD rosette was deployed through the ship's moon pool; for OW sites, the rosette was deployed from a winch mounted on the ship's deck. Samples gathered from the rosette were transferred from Niskin bottles into previously acid-washed and triple-rinsed opaque 7 L polyethylene insulated coolers (Coleman Company, Inc.) using clean silicon rubber tubing. Two UISW samples were collected directly under the ice at a man-made hole using a Kemmerer water sampler. All sample coolers were kept in the dark at ambient outside air temperatures prior to analysis.

At some sites, spectral downwelling irradiance $E_d(\lambda)$ through the upper water column and surface incident spectral downwelling irradiance $E_s(\lambda)$ were measured using a free-falling optical radiometer system with surface reference (Satlantic HyperOCR). In open water conditions, the instrument was deployed from the zodiac at least 500 m from the ship. Under sea ice, it was deployed by SCUBA divers ~20-25 m from the entrance hole (drop sites were selected under areas where white ice mounds covered >50% of surface area). Irradiance was corrected for the immersion effect in water and any measurements with tilt $>5^\circ$ were removed. *In situ* PAR ($\mu\text{mol quanta m}^{-2} \text{s}^{-1}$) for these sites was defined as the spectral integral of $E_d(\lambda)$ from 400 to 700 nm measured at each depth. The euphotic depth, Z_{eu} , was defined as the depth where light was reduced to 0.2% of surface PAR (Tremblay et al. 2009).

2.3. Nutrients, DIC, and extracted Chl *a*

Nutrient concentrations (ammonium $[\text{NH}_4]$, nitrate+nitrite $[\text{NO}_3+\text{NO}_2]$, phosphate $[\text{PO}_4]$, and silicic acid $[\text{Si}(\text{OH})_4]$; mM, uncertainty ≤ 0.05 mM) and extracted Chl *a* (uncertainty $\leq 0.05 \text{ mg m}^{-3}$) were determined onboard as in Martin et al. (2010). Extracted Chl *a* samples were used to estimate Chl *a* from *in vivo* fluorescence data where discrete measurements were not available (Mundy et al. 2009). Dissolved inorganic C (DIC; μM) was measured onboard by the coulometric titration method using a VINDTA (Versatile Instrument for the Determination of Titration Alkalinity, Marianda; uncertainty $\leq 0.5\%$) as described in Johnson et al. (1993).

2.4. Pigment analysis

Under dim light, 0.25 to 2 L water was filtered through Whatman GF/F for pigment analysis, immediately frozen in liquid N₂, and then stored at -80°C. Separation and identification of chlorophyll, chlorophyll derivatives, and carotenoids was done using the reverse-phase (RP)-HPLC. Gradient elution was controlled by a Thermo Separation (TSP) P4000 pump with solvents as indicated in the HPLC method developed by Zapata et al. (2000). Pigments were detected with a TSP UV 6000 LP diode-array absorbance detector (400 to 700 nm) and a TSP FL3000 fluorescence detector to confirm the presence of chlorophyll-related compounds. Calibration was done with external pigment standards obtained commercially from DHI Water & Environment (Hørsholm, Denmark) and extinction coefficients from Jeffrey (1997).

2.5. Calculation of spectral absorption coefficients

Spectral absorption of particulates was measured following standard ocean optics protocol (Mitchell et al. 2003) and analyzed using the transmittance-reflectance method of Tassan and Ferrari (1995, 1998, 2002). Briefly, under dim light, 0.5 to 2 L of seawater (depending on particle concentration) was filtered using low vacuum pressure (<125 mm Hg) through hydrated Whatman GF/F filters, which were then frozen in liquid nitrogen and stored until analysis post-cruise. The optical density (*OD*; dimensionless) of these filters before, $OD_{fp}(\lambda)$, and after, $OD_{fd}(\lambda)$, methanol extraction (Kishino et al. 1985) was measured using a dual-beam spectrophotometer (300 to 850 nm; Perkin-Elmer Lambda 2) equipped with a 50 mm integrating sphere (Labsphere RSA-PE-20). Particulate (a_p) and detrital (a_d) absorption coefficients (m⁻¹) were calculated as:

$$a_{p,d}(\lambda) = \frac{2.303}{X} \{ [OD_{fp,fd}(\lambda) - OD_{bf}(\lambda)] - OD_{fp,fd}(800) \}$$

where $OD_{bf}(\lambda)$ is the optical density of a fully hydrated blank filter, $OD_{fp,fd}(800)$ is the optical density averaged between 750 and 800 nm where particulate absorption is assumed to be minimal, and X is the ratio of the filtered volume (m³) to the filter

clearance area (m^2) times the pathlength amplification factor (estimated empirically following Tassan and Ferrari 1998).

The Chl *a*-specific spectral absorption coefficient of phytoplankton, $a_{ph}^*(\lambda)$ ($\text{m}^2 \text{ mg Chl } a^{-1}$), was then calculated by normalizing this value to fluorometrically determined Chl *a*. The spectrally weighted Chl *a*-specific absorption coefficient for phytoplankton (\bar{a}^* , $\text{m}^2 \text{ mg Chl } a^{-1}$) was calculated as:

$$\bar{a}^* = \frac{\sum_{400}^{700} a_{ph}^*(\lambda) E(\lambda)}{\sum_{400}^{700} E(\lambda)}$$

where $E(\lambda)$ is the spectral irradiance of the P-E incubator.

2.6. Photosynthesis-irradiance (P-E) measurements

P-E measurements were conducted using the method of Robinson et al. (2003) with the following modifications. To obtain a final activity of ca. $1 \mu\text{Ci mL}^{-1}$ per sample, 12 mL of $20 \mu\text{Ci mL}^{-1} \text{NaH}^{14}\text{CO}_3$ (Amersham Biosciences) was added to 235 mL of algal sampled, and 10 mL aliquots of this sample were placed in pre-chilled plastic scintillation vials (Wheaton). Samples were incubated at -1.5°C for 2 h under a cool white fluorescent bulb (Mini Cool by Cool-lux) at 17 light levels ranging from 6 to $900 \mu\text{mol quanta m}^{-2} \text{s}^{-1}$. Immediately after incubation, samples were split into 5 mL subsamples and filtered through $5 \mu\text{m}$ polycarbonate membrane filters and Whatman GF/F filters (nominal pore size $\sim 0.7 \mu\text{m}$) for size-fractionated results. The filters were placed in individual scintillation vials, and $100 \mu\text{L}$ of 6N HCl and 1 mL of milli-Q water was added to each. The vials were then placed in a fume hood to shake overnight. The following day, $100 \mu\text{L}$ of 6N NaOH and 5 mL of Ecolume scintillation cocktail (ICNTM) were added to each vial, which was then shaken and left to sit for at least 3 h before being counted in a Packard Tri-Carb 2900 TR liquid scintillation counter onboard the ship. In total, 15 P-E curves were completed from 8 June to 4 July. All P-E analyses were adjusted for DIC concentration.

P-E curves were fit by least squares nonlinear regression to the model of Platt et al. (1980) as modified by Arrigo et al. (2010):

$$P^* = P_s^* \left(1 - e^{-\frac{\alpha^* E}{P_s^*}} \right) e^{-\frac{\beta^* E}{P_s^*}} - P_o^*$$

where P^* is the C fixation rate (mg C mg Chl a^{-1} h $^{-1}$) at irradiance E , P_s^* is the light-saturated maximum C fixation rate in the absence of photoinhibition (mg C mg Chl a^{-1} h $^{-1}$), P_o^* is C fixation at zero irradiance (mg C mg Chl a^{-1} h $^{-1}$), α^* is the initial slope of the P-E curve [photosynthetic efficiency; mg C mg Chl a^{-1} h $^{-1}$ ($\mu\text{mol quanta m}^{-2} \text{s}^{-1}$) $^{-1}$], and β^* is a measure of photoinhibition [mg C mg Chl a^{-1} h $^{-1}$ ($\mu\text{mol quanta m}^{-2} \text{s}^{-1}$) $^{-1}$]. The asterisk indicates Chl a normalization. The maximum Chl a -specific C fixation rate is then calculated as:

$$P_m^* = P_s^* \left(\frac{\alpha^*}{\alpha^* + \beta^*} \right) \left(\frac{\beta^*}{\alpha^* + \beta^*} \right)^{\frac{\beta^*}{\alpha^*}}$$

The photoacclimation parameter, E_k , was calculated as P_m^*/α^* .

The maximum quantum yield of photosynthesis, Φ_m [mol C (mol absorbed) $^{-1}$], was then determined by relating \bar{a}^* to the initial slope of the P-E curve, α^* , using the equation:

$$\Phi_m = \frac{\alpha^*}{43.2\bar{a}^*}$$

where the value of 43.2 represents a unit conversion to mol C (mol quanta absorbed) $^{-1}$. Unfortunately, a few of our OW samples were lost/damaged during transit following the cruise. For these stations, Φ_m was estimated from the mean \bar{a}^* of nearby stations with similar environmental conditions as assessed by CTD data.

2.7. Statistical analysis

The association between environmental variables and P-E parameters was analyzed using Statistica software (v7, StatSoft, Inc.). We used a two-way ANOVA to analyze the independent and interaction effects between size-fraction and location on P-E parameters. Multiple linear regression analysis was then used to analyze the effect of three key independent environmental variables (percent fraction of surface PAR at sample depth, water temperature, and dissolved inorganic N concentration) on the P-E parameters separated by size fraction and location. Detailed information about

each analysis is given in the results section and table headings.

3. Results

3.1. General OW and UI physical, chemical, and biological conditions

We sampled a variety of OW sites in the CBP, including nearshore, mid-shelf, and mid-slope areas (Fig. 1). MLD in OW sites ranged from 7 to 36 m (Table 1), with the degree of stratification increasing throughout the sampling time period (the maximum value of N^2 increased from 0.001 s^{-2} at sta. 405B on 10 June, to 0.005 s^{-2} at sta. 6006 on 4 July). The SCM depths in OW sites ranged from 22 to 62 m and were below the MLD except for station FB1 (open water in Franklin Bay). Water temperatures and salinities at OW SCM were confined to a narrow range as is typical of the upper water column in this region (Carmack et al. 2004).

Nitrogen was generally depleted ($\text{NO}_3+\text{NO}_2 < 5 \text{ }\mu\text{M}$) from surface layers in OW down to the SCM, suggesting that phytoplankton had bloomed prior to our sampling at some or all locations. NO_3+NO_2 was below $5 \text{ }\mu\text{M}$ at all OW SCM depths and below $1 \text{ }\mu\text{M}$ at three sites. Si(OH)_4 and PO_4 were similarly depleted but neither were exhausted; both were much higher below the SCM. NH_4 concentrations were also very low ($< 0.2 \text{ }\mu\text{M}$ except at one site, FB1, in a shallow bay near ice cover). Chl *a* in OW SCM ranged from 0.64 to 4.83 mg m^{-3} . PAR levels at the OW SCM ranged from 0.2 to 3.1% of surface values, with less light reaching SCM located at greater depths, but generally all SCM were at or above Z_{eu} .

We also sampled at five sites under ice cover in two neighboring bays (Franklin Bay and Darnley Bay; Fig. 1) adjacent to the CBP, both at the SCM and in surface waters directly beneath the ice cover (UISW). MLD at these sites ranged from 15 to 38 m, although sites were only weakly stratified ($N^2 \leq 0.00075 \text{ s}^{-2}$). Under ice MLDs were not statistically different from OW stations. However, UI SCM depths were significantly shallower than OW SCM (t-test, $p < 0.01$), ranging from 8.6 to 34 m. Moreover, three out of the five UI SCM we sampled were within the mixed layer. Temperatures and salinities within the UI SCM exhibited a similarly narrow range as in the OW SCM (no statistical difference between OW and UI sites).

NO_3+NO_2 , NH_4 , and $\text{Si}(\text{OH})_4$ were significantly higher in the UI SCM compared to the OW SCM (t-test, $p<0.05$; no difference in PO_4). Chl *a* was also significantly higher (t-test, $p<0.05$) in the UI SCM than in the OW SCM (range: 0.49 – 24.20 mg m^{-3}). The two UISW samples had Chl *a* concentrations in the middle of the range we observed, although nutrients in the two UISW sites were very low, which was likely a function of ice melt, the presence of nutrient-poor surface waters, and uptake by phytoplankton prior to sampling (Mundy et al. *this issue*).

PAR levels at the UI SCM were strongly depth-dependent, with 0.04 to 2.6% of above-ice surface PAR reaching these depths. These PAR levels were not significantly different from the amount reaching OW SCM. Approximately 10% of above-ice surface PAR was transmitted through the ice cover to reach both the UISW sites. Z_{eu} in UI sites was shallower than in OW sites ($p<0.001$; t-test), yet the depths of all UI SCM were above Z_{eu} except at station DB7 (18 June) where the SCM was at 34 m. Under ice downwelling irradiance spectra at selected depths (Fig. 2) reflect the severe attenuation imposed by the high concentrations of phytoplankton and particulate matter associated with the under ice bloom in Darnley Bay, shifting the light towards green-yellow wavelengths (520-580 nm) that are not readily absorbed by algal pigments.

3.2. Phytoplankton pigment analysis

HPLC pigment analysis was performed on eight OW SCM samples, four UI SCM samples, and one UISW sample (sta. DB7) (Table 2). After Chl *a*, the most abundant pigment found in all samples was fucoxanthin (Fuco), followed by Chl *b*, Chl *c*₂, and the photoprotective pigments diadinoxanthin (DD) and diatoxanthin (DT) (DD+DT). Most stations had trace amounts of prasinoxanthin (Pras) and Mg-2,4-divinyl pheoporphyrin a5 monomethyl ester (Mg-DVP; common in many algal groups and often high in the prasinophytes order *Mamiellales*), but only some had zeaxanthin (Zea), 19'-hexanoyloxyfucoxanthin (Hex-fuco), or Chl *c*₃. When normalized to Chl *a*, UI SCM samples had significantly more DD+DT than OW sites; Chl *a*-normalized Mg-DVP, Pras, and Zea were significantly higher in OW sites (Table 2). The UISW

sample had a lower Chl *a* concentration compared to most UI SCM samples; Fuco and Chl *b* accounted for almost half the accessory pigments, with Chl *c*₂ and DD+DT the next most abundant.

We combined these pigment analyses with onboard microscopy and observational data from previous studies in the region (e.g., Vidussi et al. 2004; Lovejoy et al. 2007; Brugel 2009) to estimate the composition of algal groups present in this study. Using these observations, we assumed that Fuco was indicative of the presence of diatoms, Pras of certain prasinophytes, Chl *b* of “green algae” (most likely chlorophytes and/or prasinophytes) and Hex-fuco of various haptophytes. Other pigments are present in several algal classes; allocation to these various classes will require more sophisticated analysis such as Chemtax (Alou et al. *in prep*). Pigment results suggest that UI communities were dominated by diatoms (Chl *a*-normalized Fuco was 0.48, more than 3 times higher than any other Chl *a*-normalized accessory pigment). Conversely, OW stations were likely composed of a more mixed community, with higher amounts of Pras and Mg-DVP indicating a greater abundance of prasinophytes such as *Micromonas*, which has been previously observed to continuously occupy the region (Lovejoy et al. 1997).

3.3. Phytoplankton spectral absorption characteristics

The Chl *a*-normalized mean absorption coefficient, \bar{a}^* , for OW SCM samples averaged $0.035 \pm 0.01 \text{ m}^2 (\text{mg Chl } a)^{-1}$ (Table 3). Absorption coefficients for UI SCM and UISW samples were much less than OW values ($p < 0.05$), although we note that this is based on some simplifying approximations (more than half our OW samples were lost in transit or analysis; we estimated \bar{a}^* for these samples from stations with similar environmental characteristics as determined by the CTD). In all UI SCM samples, \bar{a}^* ranged from 0.005 to $0.010 \text{ m}^2 (\text{mg Chl } a)^{-1}$ with a mean value of $0.0076 \pm 0.0021 \text{ m}^2 (\text{mg Chl } a)^{-1}$ (Table 3; Fig. 3). We used \bar{a}^* to estimate the degree of pigment packaging and shade acclimation in our UI SCM samples. The degree of pigment packaging can be estimated by observing a flattening of the absorption spectra between 400-500 nm, as well as by the value of $a_{ph}^*(676)$; values for $a_{ph}^*(676)$

in the range 0.023 to 0.029 m² (mg Chl *a*)⁻¹ indicate relatively unpackaged pigments for Arctic species (Wang et al. 2005; Matsuoka et al. 2009). Using this range for reference, and observing some flattening of our absorption spectra, our UI SCM samples indicate a modest degree of pigment packaging (average a_{ph}^* (676) for all samples is 0.011 m² (mg Chl *a*)⁻¹) (Fig. 3).

3.4. Summary of P-E parameters for OW and UI sites

P-E parameters for OW SCM samples showed some variation between size fractions (Table 3). P_m^* and E_k were higher ($p < 0.05$) in large cells (>5 μm) than in the total community fraction (all cells >0.7 μm). However, no statistical difference in α^* and β^* was observed between size fractions. The UI SCM showed less variation in photosynthetic parameters between size fractions than the OW SCM (no statistical differences) (Table 3). P_m^* , α^* , E_k , and β^* were similar in value to the OW SCM samples. However, Φ_m in UI SCM samples was significantly higher than those of the OW SCM.

We observed the largest differences in photosynthetic parameters between the size fractions of UISW samples. For example, P_m^* was 4 times higher in the >5 μm fraction than for all cells >0.7 μm, while both α^* and E_k were more than twice as high (Table 3). The UISW values for E_k were significantly higher than samples taken from the SCM both under the ice and in OW. Φ_m in UISW samples fell in the middle of the observed range and were similar in value to UI SCM samples. Interestingly, no photoinhibition was apparent in the P-E curves of UISW samples.

3.5. Effect of Environmental Factors on P-E Parameters

We used multiple linear regression analysis (not shown) on data separated by location and size fraction (large or all cells) to assess the effect of three key environmental variables, percent of surface incident PAR transmitted to sample depth, water temperature, and total dissolved inorganic nitrogen concentration (NO₃+NO₂+NH₄), on the P-E parameters P_m^* , α^* , E_k , β^* , and Φ_m . The magnitude of the standard regression coefficient (beta) can be used to compare the relative

contribution of each independent environmental variable in the prediction of the dependent P-E parameter. Each regression model was fit using all three environmental variables. Despite our low sample size, we were able to detect a significant relationship between both the %PAR (beta = 0.78 ± 0.05) and Temp at sample depth (beta = 0.54 ± 0.03) on E_k in the $>0.7 \mu\text{m}$ UI SCM data set ($p < 0.05$ for both; $n=6$, $r^2 = 0.99$). Not surprisingly, %PAR was the best predictor of E_k . No other environmental variable had a significant effect on any P-E parameter at the 0.05 confidence level.

3.6. Spatial Variability in P-E Parameters: Franklin Bay

The horizontal spatial variability in P-E parameters at the SCM was explored using a north-south transect (~ 4 km) from open water to under sea ice in Franklin Bay. Station FB1 was in open water ~ 2 km north of the ice edge, station FB3 was located under sea ice at the ice edge, and station FB5 was located under the landfast ice cover ~ 2 km south of the ice-edge. These samples are compared to a UISW sample from station FB5 (see Table 1 for station data).

P-E parameters showed substantial variability along the transect (Fig. 4), with the large size fraction at the OW SCM exhibiting the highest values for all P-E parameters. P^*_m decreased 7-fold over the relatively small spatial scale of the transect, from the highest value recorded among all samples in the $>5 \mu\text{m}$ fraction at the OW SCM to one of the lowest values recorded in the $>0.7 \mu\text{m}$ UISW sample (Fig. 4a). P^*_m in the UI SCM fell in the range between these two extremes and did not vary as much between size fractions (Fig. 4a). Similar to P^*_m , α^* showed a >3 -fold change over the distance of the transect, with the highest value recorded at the OW station; both the UISW and UI SCM sites were substantially lower (Fig. 4b). E_k followed the trend in P^*_m and α^* , with the large size fraction in the OW SCM exhibiting E_k values that were almost double all the other values measured (Fig. 4c). As expected, the ice edge station (FB3) exhibited P-E values that fell in the range between the open water and under ice samples for all parameters. Unfortunately, the \bar{a}^* sample from the OW SCM was lost during analysis so we could not compare between sites.

3.7. Temporal Variability in P-E Parameters: Darnley Bay

To analyze the temporal variability of P-E parameters and \bar{a}^* and to aid in our understanding of timescales of photoacclimation in this region, we repeatedly sampled station DB7 during the course of a 10-day (8 June to 18 June) upwelling-enhanced phytoplankton bloom (Table 4; Fig. 5). Over this time period, the SCM gradually deepened from 8.6 m to 34 m. Initially, the SCM was formed at a depth well above (>20 m) both the MLD and Z_{eu} . After 3 days, the SCM remained at nearly the same depth, but the dense bloom resulted in substantially reduced light penetration, such that Z_{eu} had risen nearly 20 m, and the percent PAR reaching the SCM had decreased by half. By the end of our sampling on 18 June, barely any surface PAR reached the SCM at 34 m, which was well below both the MLD and Z_{eu} . Chl *a* concentrations at the SCM increased from 6.36 to 24.2 mg m⁻³ over the first 3 days, and remained high throughout the 10 day period despite the increasing depth of the SCM and reduced PAR transmitted to the SCM. Nutrients were rapidly depleted from the upper water column above the SCM during this time, falling below 5 μ M by 18 June in the upper 20 m. Nutrient concentrations at the SCM itself did not vary much and were generally low (see Table 1 for nutrient comparisons).

P-E parameters tracked the bloom progression and physical dynamics over this time period (Table 4). At the beginning of the sampling period (8-9 June), P-E parameters from UISW and the UI SCM both showed large variation between size fractions in P^*_m , α^* , E_k , and Φ_m . The large size fraction of the UISW sample in particular had the highest values of P^*_m and α^* measured during the time series. As the bloom progressed, the two size fractions became increasingly similar in all P-E parameters. Interestingly, the samples taken at the beginning of the bloom on 9 June showed no tendency towards photoinhibition and had relatively high values for E_k . However, within three days (on 12 June), these samples developed the tendency to become inhibited at super-saturating irradiances ($\beta^* = 0.001$ for both size fractions) and maintained this tendency over the sampling period. At the end of the sampling period on 18 June, P^*_m was half that of the UISW large size fraction measured at the beginning. The deepening of the SCM by >20 m over 6 days, from 10.5 m on 12 June

to 34 m on 18 June, resulted in a ~25% reduction in P^*_m (measured in the large size fraction) although phytoplankton remained relatively photosynthetically competent, exhibiting values for α^* and Φ_m that were similar to the initial sample. \bar{a}^* also changed rapidly over the course of the bloom, from an upper limit of $0.0109 \text{ m}^2 (\text{mg Chl } a)^{-1}$ on 9 June decreasing to $0.0060 \text{ m}^2 (\text{mg Chl } a)^{-1}$ on 12 June. Six days later at the same site (18 June), \bar{a}^* was similar even though the SCM had dropped to 34 m (Table 4).

4. Discussion

Phytoplankton growing in the SCM associated with the CBP are relatively well acclimated to take advantage of the low-light conditions that characterize this environment. We found that ice-edge phytoplankton blooms could reach very high biomass ($\text{Chl } a \sim 24 \text{ mg m}^{-3}$) while maintaining typical “shade-acclimated” maximum rates of CO_2 fixation ($\sim 1 \text{ mg C mg Chl } a^{-1} \text{ h}^{-1}$) (Kirst and Wiencke 1995). Furthermore, the physiological adjustment of photosynthetic parameters was relatively rapid, keeping pace with the development and deepening of the SCM over the course of the bloom. Phytoplankton populations in Darnley Bay acclimated to an ice-edge upwelling event and steady deepening of the SCM by over 20 m (with its associated reduction in PAR) by reducing both P^*_m and E_k over a 10 day period, but with little or no change in α^* and Φ_m .

It has been hypothesized that high latitude phytoplankton are photosynthetically equipped to take advantage of the short growing season and reduced light levels in partially ice-covered areas (Platt et al. 1982). The physiological adjustments required to grow under these light conditions include an increase in the size of the photosynthetic unit and/or an increase in the effectiveness of each at producing a photochemical reaction (Falkowski 1980). This typically results in a decrease in \bar{a}^* , increase in α^* , and/or an increase in Φ_m in “shade-acclimated” communities. Phytoplankton acclimated to low light also tend to have lower P^*_m and E_k than those grown at high light. Our values for P^*_m (0.21 to $2.59 \text{ mg C mg Chl } a^{-1} \text{ h}^{-1}$) fit well within the range of 0.29 to $2.60 \text{ mg C mg Chl } a^{-1} \text{ h}^{-1}$ reported in the literature for this

region (Platt et al. 1982; Gallegos et al. 1983; Cota 1985; Harrison and Platt 1986; Kirst and Wiencke 1995; Brugel et al. 2009). We also observed a strong dependence of E_k on both the %PAR and temperature at sample depth in the UI SCM. Furthermore, our measured values for E_k fit within the range for “shade-acclimated” algae in the Arctic (2.5 to 120 $\mu\text{mol quanta m}^{-2} \text{s}^{-1}$; same references as P^*_m).

Typically, α^* is higher at lower growth irradiances as phytoplankton increase their photosynthetic accessory pigments (Kirk 1994). The values for α^* measured in this study fall within the literature range of 0.003 to 0.039 $\text{mg C mg Chl } a^{-1} \text{ h}^{-1}$ ($\mu\text{mol quanta m}^{-2} \text{s}^{-1}$)⁻¹ for polar phytoplankton (same references as P^*_m), although we did not observe significant variations in α^* by location, time, or between size fractions. However, we did observe that the UI SCM had higher Φ_m compared to OW SCM samples. In general, Φ_m tends to increase at low light levels due to an increase in the proportion of pigments that are capable of transferring excitation energy to reaction centers (and thus algae become more efficient per photon absorbed at producing a photochemical reaction) (MacIntyre et al. 2002). Similarly, \bar{a}^* varies with the ratio of accessory pigments to Chl a . \bar{a}^* may decrease in response to low growth irradiance because of the so called “package effect”, whereby cells accumulate so much Chl a that each additional molecule becomes less effective at light absorption due to self-shading of the chromophores (Morel and Bricaud 1981), and indeed our UI SCM samples did show evidence of a modest degree of pigment packaging. Nonetheless, the differences in Φ_m observed here are more likely related to changes in α^* , which represents the efficiency of light utilization and thus plays a large part in controlling the maximum quantum yield of photosynthesis.

Overall, our P-E results demonstrate substantial photoacclimation potential of phytoplankton to lower irradiance levels, which has been commonly observed in high latitude algae (e.g., Kirst and Wiencke 1995). This ability for shade acclimation allows algae to maximize their growth rate within the SCM, particularly late in the season when the SCM is commonly observed below the MLD (Martin et al. 2010). However, all other things being equal, OW SCM will experience a higher mean light level than UI SCM when they are both above the MLD, resulting in higher maximum

rates of CO₂ fixation. We see evidence of this on the Franklin Bay transect data, where the OW SCM, despite being deeper in the water column than the UI SCM, had higher values for P_m^* , E_k , and α^* than the UI site in the >5 mm size fraction (Fig. 4; all SCM on the transect were above the MLD). In fact, the OW SCM had higher rates of P_m^* than even the UISW, reflecting the impact that sea ice has on underwater light conditions compared to open water sites (e.g., Fig. 2). However, once below the MLD, phytoplankton in both the OW and UI SCM exhibited similar photosynthetic characteristics. We suggest this is mostly related to light conditions: both UI and OW SCM trapped below the MLD experience similarly stable but very low light regimes (<2% surface PAR transmitted) that they can acclimate to (Table 1). We saw evidence of this in Darnley Bay, for example, where over the course of 10 days the SCM gradually deepened until it was below the MLD (Table 4) and %PAR decreased from 2.6 to 0.04%. This resulted in a reduction in P_m^* and E_k as compared to the SCM located above the MLD earlier in the bloom.

Some of this response is likely related to changes in phytoplankton community structure in addition to the photoacclimatory changes described above, as many species have been observed to exhibit little or no change in photosynthetic response with changes in growth irradiance (MacIntyre et al. 2002). The photosynthetic parameters in different size fractions of UI sites were almost identical, while OW sites showed more variation (Table 3). For example, in Franklin Bay, P_m^* was >7 fold higher in the large size fraction at the OW SCM than the UI SCM. Based on HPLC pigment data, these OW communities were more mixed than the UI sites, with a significantly greater proportion of prasinophytes. The greater contribution these and other of smaller sized cells may reflect different light and depth characteristics of OW sites, more varied mixing regimes, or longer time since the bloom developed (as compared to the UI sites we sampled). The fact that the large size fraction at OW SCM exhibited such high P_m^* shows they have the potential to be active even though they aren't dominating biomass, and suggests they may be the remnants of an older bloom. Further research is needed to better elucidate the way phytoplankton communities change over time to acclimate to different environmental conditions.

Although limited in scope and size, one of the goals of this study was to assess how P-E analyses can help us to better understand some of the many complex and interconnected controls on PP in an Arctic shelf ecosystem. In this dynamic area, open water and sea ice-covered areas are influenced by river input of freshwater and shelf-break upwelling to create a unique set of conditions that may provide insight into future patterns of C exchange. In this region of the Arctic, and likely the coastal Arctic as a whole, previous studies have shown that pelagic productivity is parsed between two fundamentally different regimes: (i) a high light, rapid onset phytoplankton bloom in the spring, when surface nutrients are sufficient to sustain phytoplankton growth (e.g., Arrigo and Van Dijken 2004; Wang et al. 2005; Tremblay et al. 2008); and (ii) a low light, extended-timescale bloom where an SCM follows the depth of the descending nitracline (e.g., Tremblay et al. 2009; Martin et al. 2010).

Photosynthetic parameters in these two different regimes are governed by their respective nutrient and light climates, and thus, P-E analyses can yield some insight into how small-scale environmental variability affects PP patterns. In case (i), river runoff and ice melt quickly stratify the upper water column, providing a relatively stable high light environment that enables phytoplankton to quickly utilize available nutrients. As nutrients in the surface layer are diminished, production moves towards the nutricline and the system transforms into case (ii), eventually forming a SCM. Over time, the SCM descends as the growing phytoplankton balance their need for nutrients and light. In general, the SCM descends well below the pycnocline (>80% of the time, Martin et al. 2010), meaning that these SCM communities experience stable low light conditions. Deeper mixing or upwelling events can transform this case (ii) regime into case (i), thereby resetting the system (although this transformation may be short-lived due to rapid nutrient utilization combined with a settling water column following the event).

In the current study, the OW SCM we sampled were mostly well below the MLD and relatively depleted in nutrients, consistent with the case (ii) regime. In contrast, the UI SCM we sampled were more representative of the case (i) productivity regime positioned well above the MLD with high nutrients. Once the SCM is trapped below

the MLD, Φ_m and \bar{a}^* increase, and E_k decreases with no significant change in P_m^* or α^* . Thus, the results of our P-E analyses highlight the importance of considering the length of time an SCM has been developing as well as the cause of its formation, especially the mixing regime (e.g., case (i) vs. case (ii) and the associated light and nutrient histories), when interpreting PP patterns and photosynthetic response.

The timescale over which these type of photoacclimatory changes take place has been explored in several studies seeking to understand how physical and biological processes in the Arctic covary in their rate of change (Platt et al. 1982; Gallegos et al. 1983; Cota 1985; Harrison and Platt 1986; Hill et al. 2005; Matsuoka et al. 2009). Of particular interest in our study was the formation of the SCM, which has been undersampled both in the field and by satellite remote sensing techniques (Pabi et al. 2008). The appropriate timescale to consider for photoacclimation at the SCM is not the time it takes a cell to transit the mixed layer, but the time it takes for the establishment of the pycnocline (e.g., a barrier to vertical mixing).

Using the time series of data collected in Darnley Bay (Table 4), we can make a few limited inferences on the timescale of photoacclimation in this region. Consistent with other observations in the region, phytoplankton in Darnley Bay became photoinhibited at super-saturating irradiances relatively soon (only three days) after the SCM formed (e.g., Platt et al. 1982; Gallegos et al. 1983). Furthermore, within this same time frame, maximum rates of CO₂ fixation dropped by 25% whereas Chl *a* concentrations stayed the same. We also observed an increase in Φ_m with SCM depth. The implications of this are that phytoplankton can maintain high levels of Φ_m at low light levels, thereby being relatively efficient within the SCM (even though their maximal rates of CO₂ fixation decreased over time). Although more rigorous field testing is needed to corroborate this hypothesis, the results from this transect, based on the analysis of variations in P-E parameters, suggest that phytoplankton continuously acclimated to the changing environmental conditions over a period of roughly 4-10 days.

The data from this phytoplankton bloom are particularly interesting given that they document a wind-induced upwelling event just prior to a large increase in algal

biomass. In the future, upwelling events like this may become more common if the ice-edge retreats past the shelf break and wind-induced shelf-break upwelling intensifies (Carmack and Chapman 2003; Yang et al. 2004). This may result in increasing depths of the nitracline and SCM over the continental shelves (McLaughlin and Carmack 2010), which should favor species that can acclimate quickly to take advantage of a pulse of nutrients, especially in areas adjacent to sea ice cover where light is limited. Our results suggest that phytoplankton can acclimate quickly to take advantage of a pulse of nutrients by maintaining maximum rates of C fixation, photosynthetic efficiency, and quantum yields within a relatively narrow “shade-acclimated” range constrained by the environmental conditions associated with these regions, even during the course of a bloom and a deepening of the SCM. Future research that focuses on the way phytoplankton communities adjust to the dynamic light and nutrient conditions of the flaw polynya will be key to predicting PP patterns in the changing Arctic.

Acknowledgements

This work is a contribution to the International Polar Year-Circumpolar Flaw Lead system study (IPY-CFL), supported through grants from the Canadian IPY Federal program office, the Natural Sciences and Engineering Research Council in Canada, and many international collaborators. Support was also provided by the National Science Foundation (grant ANT07325535 to K.R. Arrigo) and NASA (grant NNX09AO48H to K.R. Arrigo and M.A. Palmer). We would like to thank all our international collaborators as well as SCUBA divers J. Stewart and H. Hop; E. Shadwick and H. Thomas for dissolved inorganic carbon data; C. Bourgault-Brunelle for helping process the absorption spectra; Y. Gratton and his team for processing and distributing the CTD data; A. Rossnagel, B. Philippe, A. Sallon, and M. Ardyna for laboratory and field assistance; D. Leitch and the officers and crew of the CCGS *Amundsen* for logistical support; and the Arrigo lab and three anonymous reviewers for comments.

References

1. Arrigo KR, van Dijken GL (2004) Annual cycles of sea ice and phytoplankton in Cape Bathurst polynya, southeastern Beaufort Sea, Canadian Arctic. *Geophys Res Lett* 31:L08304. doi:10.1029/2003GL018978
2. Arrigo KR, van Dijken G, Pabi S (2008) Impact of a shrinking ice cover on marine primary production. *Geophys Res Lett* 35:L19603. doi:10.1029/2008GL035028
3. Arrigo KR, Mills MM, Kropuenske LR, van Dijken GL, Alderkamp AC, Robinson DH (2010) Photophysiology in two major Southern Ocean phytoplankton taxa: Photosynthesis and growth of *Phaeocystis antarctica* and *Fragilariopsis cylindrus* under different irradiance levels. *Integr Comp Biol* 50:950-966. doi:10.1093/icb/icq021
4. Barber DG, Hanesiak JM (2004) Meteorological forcing of sea ice concentrations in the southern Beaufort Sea over the period 1979 to 2000. *J Geophys Res* 109:C06014. doi: 10.1029/2003JC002027
5. Barber DG, Massom R (2007) The Role of Sea Ice in Arctic and Antarctic Polynyas. In: Smith WO, Barber DG (eds) *Polynyas: Windows To The World*. Elsevier Oceanogr Ser 74. Elsevier, Amsterdam, pp 1-43
6. Barber DG, Asplin M, Gratton Y, Lukovich J, Galley R, Raddatz R, Leitch D (2010) The International Polar Year (IPY) Circumpolar Flaw Lead (CFL) system study: Introduction and physical system. *Atmosphere Ocean* 48:225–243
7. Brugel S (2009) Étude des variations spatiales et temporelles du phytoplancton en mer de Beaufort : biomasse, production et structure de taille des communautés. Dissertation, Université du Québec à Rimouski
8. Brugel S, Nozais C, Poulin M, Tremblay J-É, Miller LA, Simpson KG, Gratton Y, Demers S (2009) Phytoplankton biomass and production in the southeastern Beaufort Sea in autumn 2002 and 2003. *Mar Ecol Prog Ser* 377:63-77. doi:10.3354/meps07808
9. Carmack E, Chapman DC (2003) Wind-driven shelf/basin exchange on an Arctic shelf: The joint roles of ice cover extent and shelf-break bathymetry. *Geophys Res Lett* 30:1778. doi:10.1029/2003GL017526

10. Carmack EC, Macdonald RW (2002) Oceanography of the Canadian Shelf of the Beaufort Sea: A Setting for Marine Life. *Arctic* 55:29-45
11. Carmack EC, Macdonald RW, Jasper S (2004) Phytoplankton productivity on the Canadian Shelf of the Beaufort Sea. *Mar Ecol Prog Ser* 277:37-50.
doi:10.3354/meps277037
12. Cavalieri DJ, Martin S (1994) The contribution of Alaskan, Siberian, and Canadian coastal polynyas to the cold halocline layer of the Arctic Ocean. *J Geophys Res* 99:18343-18362. doi:10.1029/94JC01169
13. Cota GF (1985) Photoadaptation of high Arctic ice algae. *Nature* 315:219-222.
doi:10.1038/315219a0
14. Falkowski PG (1980) Light-shade adaptation in marine phytoplankton. In: Falkowski PG (ed) *Primary productivity in the sea*. Plenum, New York, pp 99-117
15. Falkowski PG, LaRoche J (1991) Acclimation to spectral irradiance in algae. *J Phycol* 27:8-14. doi:10.1111/j.0022-3646.1991.00008.x
16. Gallegos CL, Platt T, Harrison WG, Irwin B (1983) Photosynthetic parameters of arctic marine phytoplankton: vertical variations and time scales of adaptation. *Limnol Oceanogr* 28:698-708
17. Harrison WG, Platt T (1986) Photosynthesis-irradiance relationships in polar and temperate phytoplankton populations. *Polar Biol* 5:153-164.
doi:10.1007/BF00441695
18. Hill V, Cota G (2005) Spatial patterns of primary production on the shelf, slope and basin of the Western Arctic in 2002. *Deep Sea Res Part II* 52:3344-3354.
doi:10.1016/j.dsr2.2005.10.001
19. Jeffery SW (1997) Chlorophyll and carotenoid extinction coefficients. In: Jeffrey SW, Mantoura RFC, Wright SW (eds) *Phytoplankton pigments in oceanography*. UNESCO Publishing, Paris, pp 595-596
20. Johnson KM, Wills KD, Butler DB, Johnson WK, Wong CS (1993) Coulometric total carbon dioxide analysis for marine studies: Maximizing the performance of an automated gas extraction system and coulometric detector. *Mar Chem* 44:167-187. doi:10.1016/0304-4203(93)90201-X

21. Kirk JTO (1994) Light and photosynthesis in aquatic ecosystems, 2nd edn. Cambridge University Press, Cambridge
22. Kirst GO, Wiencke C (1995) Ecophysiology of polar algae. *J Phycol* 31:181-199. doi:10.1111/j.0022-3646.1995.00181.x
23. Kishino M, Takahashi N, Okami N, Ichimura S (1985) Estimation of the spectral absorption coefficients of phytoplankton in the sea. *Bull Mar Sci* 37:634-642
24. Kropuenske LR, Mills MM, van Dijken GL, Bailey S, Robinson DH, Welschmeyer NA, Arrigo KR (2009) Photophysiology in two major Southern Ocean phytoplankton taxa: photoprotection in *Phaeocystis antarctica* and *Fragilariopsis cylindrus*. *Limnol Oceanogr* 54:1176-1196. doi:10.4319/lo.2009.54.4.1176
25. Li WKW, McLaughlin FA, Lovejoy C, Carmack EC (2009) Smallest algae thrive as the Arctic Ocean freshens. *Science* 326:539. doi:10.1126/science.1179798
26. Lovejoy C, Vincent WF, Bonilla S, Roy S, Martineau M-J, Terrado R, Potvin M, Massana R, Pedrós-Alió C (2007) Distribution, phylogeny, and growth of cold-adapted picoprasinophytes in Arctic seas. *J Phycol* 43:78-89. doi:10.1111/j.1529-8817.2006.00310.x
27. MacIntyre HL, Kana TM, Anning T, Geider RJ (2002) Photoacclimation of photosynthesis irradiance response curves and photosynthetic pigments in microalgae and cyanobacteria. *J Phycol* 38:17-38. doi: 10.1046/j.1529-8817.2002.00094.x
28. Martin J, Tremblay J-È, Gagnon J, Tremblay G, Lapoussière A, Jose C, Poulin M, Gosselin M, Gratton Y, Michel C (2010) Prevalence, structure and properties of subsurface chlorophyll maxima in Canadian Arctic waters. *Mar Ecol Prog Ser* 412:69-84. doi:10.3354/meps08666
29. Matsuoka A, Larouche P, Poulin M, Vincent W, Hattori H (2009) Phytoplankton community adaptation to changing light levels in the southern Beaufort Sea, Canadian Arctic. *Estuar Coast Shelf Sci* 82:537-546. doi:10.1016/j.ecss.2009.02.024

30. McLaughlin FA, Carmack EC (2010) Deepening of the nutricline and chlorophyll maximum in the Canada Basin interior, 2003-2009. *Geophys Res Lett* 37:L24602. doi:10.1029/2010GL045459
31. Melling H, Moore RM (1995) Modification of halocline source waters during freezing on the Beaufort Sea shelf: evidence from oxygen isotopes and dissolved nutrients. *Cont Shelf Res* 15:89-113. doi:10.1016/0278-4343(94)P1814-R
32. Mitchell BG, Kahru M, Wieland J, Stramska M (2003) Determination of spectral absorption coefficients of particles, dissolved material and phytoplankton for discrete water samples. In: Mueller JL, Fargion GS, McClain CR (eds) *Ocean optics protocols for satellite ocean color sensor validation, rev 4, vol IV*, NASA Technical Memo 2003-211621. NASA Goddard Space Flight Center, Greenbelt, Maryland, pp 39-64
33. Morel A, Bricaud A (1981) Theoretical results concerning light absorption in a discrete medium, and application to specific absorption of phytoplankton. *Deep-Sea Res* 28:1375-1393. doi:10.1016/0198-0149(81)90039-X
34. Mundy CJ, Gosselin M, Ehn JK, Gratton Y, Rossnagel AL, Barber DG, Martin J, Tremblay J-È, Palmer M, Arrigo K, Darnis G, Fortier L, Else B, Papakyriakou TN (2009) Contribution of under-ice primary production to an ice-edge upwelling phytoplankton bloom in the Canadian Beaufort Sea. *Geophys Res Lett* 36:L17601. doi:10.1029/2009GL038837
35. Mundy CJ, Gosselin M, Ehn JK, Belzile C, Poulin M, Alou E, Roy S, Hop H, Lessard S, Papakyriakou TN, Barber DG, Stewart J (this issue) Characteristics of two distinct high-light acclimated algal communities during advanced stages of sea ice melt. *Polar Biol* submitted.
36. Pabi S, van Dijken GL, Arrigo KR (2008) Primary production in the Arctic Ocean, 1998-2006. *J Geophys Res* 113:C08005. doi:10.1029/2007JC004578.
37. Platt T, Gallegos CL, Harrison WG (1980) Photoinhibition of photosynthesis in natural assemblages of marine phytoplankton. *J Mar Res* 38:687-701

38. Platt T, Harrison WG, Irwin B, Horne EP, Gallegos CL (1982) Photosynthesis and photoadaptation of marine phytoplankton in the Arctic. *Deep-Sea Res* 29:1159-1170. doi:10.1016/0198-0149(82)90087-5
39. Robinson DH, Arrigo KR, DiTullio GR, Lizotte MP (2003) Evaluating photosynthetic carbon fixation during *Phaeocystis antarctica* blooms, In: DiTullio GR, Dunbar RB (eds) *Biogeochemistry of the Ross Sea*. Antarctic Research Series 78, pp 77-91
40. Stroeve J, Serreze M, Drobot S, Gearheard S, Holland M, Maslanik J, Meier W, Scambos T (2008) Arctic sea ice extent plummets in 2007. *Eos Trans AGU* 89:13-14. doi:10.1029/2008EO020001
41. Sukenic A, Bennett J, Falkowski P (1987) Light-saturated photosynthesis – limitation by electron transport or carbon fixation? *Biochimica et Biophysica Acta* 891:205–215. doi:10.1016/0005-2728(87)90216-7
42. Tassan S, Ferrari GM (1995) An alternative approach to absorption measurements of aquatic particles retained on filters. *Limnol Oceanogr* 40:1358-1368. doi:10.4319/lo.1995.40.8.1358
43. Tassan S, Ferrari GM (1998) Measurement of light absorption by aquatic particulates retained on filters: determination of the optical pathlength amplification by the ‘transmittance-reflectance’ method. *J Plankton Res* 20:1699-1709. doi:10.1093/plankt/20.9.1699
44. Tassan S, Ferrari GM (2002) A sensitivity analysis of the ‘Transmittance-Reflectance’ method for measuring light absorption by aquatic particles. *J Plankton Res* 24:757-774. doi:10.1093/plankt/24.8.757
45. Tremblay G, Belzile C, Gosselin M, Poulin M, Roy S, Tremblay J-É (2009) Late summer phytoplankton distribution along a 3500 km transect in Canadian Arctic waters: strong numerical dominance by picoeukaryotes. *Aquat Microb Ecol* 54:55-70. doi:10.3354/ame01257
46. Tremblay J-É, Simpson K, Martin J, Miller L, Gratton Y, Barber D, Price NM (2008) Vertical stability and the annual dynamics of nutrients and chlorophyll

- fluorescence in the coastal, southeast Beaufort Sea. *J Geophys Res* 113:C07S90.
doi:10.1029/2007JC004547
47. Vidussi F, Roy S, Lovejoy C, Gammelgaard M, Thomsen HA, Booth B, Tremblay J-E, Mostajir B (2004) Spatial and temporal variability of the phytoplankton community structure in the North Water Polynya, investigated using pigment biomarkers. *Can J Fish Aquat Sci* 61:2038-2052. doi:10.1139/f04-152
 48. Wang J, Cota GF, Comiso JC (2005) Phytoplankton in the Beaufort and Chukchi Seas: distribution, dynamics, and environmental forcing. *Deep-Sea Res Part II* 52:3355-3368. doi:10.1016/j.dsr2.2005.10.014
 49. Wang M, Overland JE (2009) A sea ice free summer Arctic within 30 years? *Geophys Res Lett* 36:L07502. doi:10.1029/2009GL037820
 50. Yang J, Comiso JC, Walsh D, Krishfield R, Honjo S (2004) Storm-driven mixing and potential impact on the Arctic Ocean. *J Geophys Res* 109:C04008.
doi:10.1029/2001JC001248
 51. Zapata M, Rodriguez F, Garrido JL (2000) Separation of chlorophylls and carotenoids from marine phytoplankton: a new HPLC method using a reversed phase C8 column and pyridine-containing mobile phases. *Mar Ecol Prog Ser* 195:29-45. doi:10.3354/meps195029

Table 1. Physical and hydrological information in chronological order for 2008 CFL P-E curve data: Station information (name, depth, mixed layer depth) and variables at sample depth (water temperature; salinity; nutrients NO₂+NO₃, NH₄, Si(OH)₄, PO₄; Chl *a*), *Z_{eu}*, and percent surface PAR transmitted to sample depth (units table heading). Shaded rows indicate under ice (UI) sites.

Date 2008	Sta. Name	Sta. depth (m)	MLD (m)	Samp depth ^c (m)	Water Temp. (°C)	Sal. (psu)	NO ₂ + NO ₃ (μM)	NH ₄ (μM)	Si(OH) ₄ (μM)	PO ₄ (μM)	Chl <i>a</i> (mg m ⁻³)	<i>Z_{eu}</i> (m)	% PAR
6/8	DB7	80	32 ^a	2	n.d.	n.d.	0.17	0.09	7.55	0.83	2.12	35 ^a	10.2 ^a
6/9	DB7	80	32	8.6	-1.06	32.50	2.05	0.25	18.14	1.17	6.36	35	2.6
6/10	405B	562	36	36	-1.27	31.67	2.51	0.10	8.33	0.79	0.69	60 ^b	3.1
6/12	DB7	80	38	10.5	-0.91	32.24	6.11	0.37	17.61	0.65	24.20	16	1.2
6/14	FB1	98	27	22	-1.46	32.18	4.15	0.69	11.21	1.01	0.64	37	0.5
6/14	FB3	105	25	20	-1.45	32.09	6.24	0.71	14.69	1.10	0.49	27	0.3
6/15	FB5	107	15	17.2	-1.06	31.80	5.82	0.90	13.84	1.09	2.36	33	0.8
6/16	FB5	107	15 ^a	2	n.d.	n.d.	0.11	0.04	3.21	0.74	2.11	33 ^a	10.0 ^b
6/18	DB7	80	22	34	-0.72	32.28	5.16	0.35	12.09	0.99	24.00	26	0.04
6/23	1216	158	10	33.4	-1.31	31.90	3.56	0.18	8.32	0.95	2.67	64	2.1
6/27	1200	199	13	37	-1.25	31.72	0.96	0.09	8.22	0.85	0.80	61	1.7
7/1	421	1142	13	62	-1.22	32.04	0.87	0.08	2.83	1.43	4.83	65	0.3
7/2	435	292	7	50	-1.00	31.38	0.94	0.23	6.86	0.66	1.58	51	0.2
7/4	6006	222	14	51	-1.23	31.95	4.75	0.06	3.29	1.01	3.26	62	1.0

Notes: percent surface transmitted PAR calculated as fraction incident surface PAR remaining at sample depth, $E_d(\text{PAR})/E_s(\text{PAR})$; n.d.: no data. ^a surface values estimated from nearest day HyperOCR cast; ^b estimated from CTD logs; ^c depths for samples taken under ice cover are measured relative to open water sea surface height.

Table 2. Chl *a* (mg m⁻³) and Chl *a*-normalized HPLC-derived pigment concentrations (mg m⁻³ pigment per mg m⁻³ Chl *a*) for P-E curve samples (mean ± standard deviation). The number of samples for each calculation is indicated in the left column unless otherwise noted. For accessory pigment abbreviations see text. Asterisks indicate a significant difference between OW and UI SCM samples (t-test; * $p \leq 0.05$;

Location	Chl <i>a</i> **	Chl <i>b</i>	Chl <i>c</i> ₂	Chl <i>c</i> ₃	Mg-DVP *	Fuco	Hex-fuco	Pras *	Zea **	DD+ DT **
OW SCM (<i>n</i> =8)	1.33 (1.07)	0.31 (0.29)	0.11 (0.05)	0.04 (0.04)	0.05 (0.03) (<i>n</i> =6)	0.34 (0.20)	0.01 (0.00) (<i>n</i> =3)	0.07 (0.05) (<i>n</i> =7)	0.01 (0.01) (<i>n</i> =6)	0.02 (0.01)
UI SCM (<i>n</i> =4)	7.00 (4.76)	0.10 (0.14)	0.13 (0.03)	0.01 (0.01)	0.02 (0.01)	0.48 (0.10)	0.01 (0.01) (<i>n</i> =2)	0.02 (0.03)	0.00 (0.00)	0.03 (0.01)
UIS W (<i>n</i> =1)	0.45	0.15	0.09	n.d.	0.04	0.32	n.d.	0.03	0.03	0.07

** $p \leq 0.01$). n.d.: not detected.

Table 3. Photosynthetic parameters in OW SCM, UI SCM (shaded), and UISW samples for large size cells (>5 μm) and total communities (>0.7 μm) (except \bar{a}^* and Φ_m , which are not size fractionated). Number of samples indicated in second column (except for β^* , which are shown in column 5). Significant differences between size classes (S) or locations (L) (two-way ANOVA) are indicated in the top row (* $p \leq 0.05$; ** $p \leq 0.01$). Units: P_m^* , $\text{mg C mg Chl } a^{-1} \text{ h}^{-1}$; α^* and β^* , $\text{mg C mg Chl } a^{-1} \text{ h}^{-1} (\mu\text{mol quanta } \text{m}^{-2} \text{ s}^{-1})^{-1}$; E_k , $\mu\text{mol quanta } \text{m}^{-2} \text{ s}^{-1}$; \bar{a}^* , $\text{m}^2 \text{ mg}^{-1} \text{ Chl } a$; Φ_m , $\text{mol C mol quanta}^{-1}$.

		P_m^* (S*)	α^*	E_k (S*, L*)	β^*	\bar{a}^* (L**)	Φ_m (L**)
OW SCM	Large Cells $n=5$	1.29 \pm 0.93	0.015 \pm 0.009	61 \pm 32	0.002 \pm 0.002 ($n=5$)	0.035 \pm 0.01	0.011 \pm 0.005
	All Cells $n=6$	0.71 \pm 0.38	0.019 \pm 0.009	41 \pm 22	0.001 \pm 0.001 ($n=5$)		
UI SCM	Large Cells $n=5$	1.00 \pm 0.41	0.014 \pm 0.004	73 \pm 45	0.001 \pm 0.001 ($n=3$)	0.0076 \pm 0.0021	0.044 \pm 0.015
	All Cells $n=5$	0.93 \pm 0.54	0.014 \pm 0.006	67 \pm 14	0.001 \pm 0.001 ($n=3$)		
UISW	Large Cells $n=2$	1.61 \pm 0.77	0.017 \pm 0.015	146 \pm 31	0.000 \pm 0.000 ($n=2$)	0.005 ($n=1$)	0.032 \pm 0.030
	All Cells $n=2$	0.42 \pm 0.30	0.007 \pm 0.006	66 \pm 14	0.000 \pm 0.000 ($n=2$)		

Table 4. Time series data from Darnley Bay taken at the same station (DB7) under ice cover over the course of a large phytoplankton bloom. Shown are MLD, Z_{eu} , percent transmitted PAR, Chl a , water temperature, nitrate, the spectral absorption coefficient, and photosynthetic parameters (units as in Table 3). Note: each is split into large size cells ($>5 \mu\text{m}$; top) and total community ($>0.7 \mu\text{m}$; bottom) samples except \bar{a}^* and Φ_m , which are not size-fractionated.

Date	Samp Dept h (m)	MLD (m)	Ze _u (m)	% PA R	Chl <i>a</i> (mg m ⁻³)	Temp (°C)	NO ₃ (μM)	P*m	α^*	Ek	β^*	\bar{a}^*	Φ_m
6/8	2 (UIS W)	32	35	10. 2a	2.12	- 1.06a	0.05 9	2.15	0.028	77.2	0.000	0.0	0.0
								0.63	0.011	55.8	0.000	050	51
6/9	8.6 (SCM)	32	35	2.6	6.36	-1.06	1.87	1.24	0.010	139.5	0.000	0.0	0.0
								1.74	0.020	85.3	0.000	109	43
6/12	10.5 (SCM)	38	16	1.2	24.2	-0.91	5.94	1.15	0.020	56.7	0.001	0.0	0.0
								1.08	0.015	72.4	0.001	060	58
6/18	34 (SCM)	22	26	0.0 4	24.0	-0.72	5.00	0.84	0.012	67.6	0.002	0.0	0.0
								0.94	0.014	65.2	0.001	057	57

Notes: ^a estimated from next day since no measurement was taken

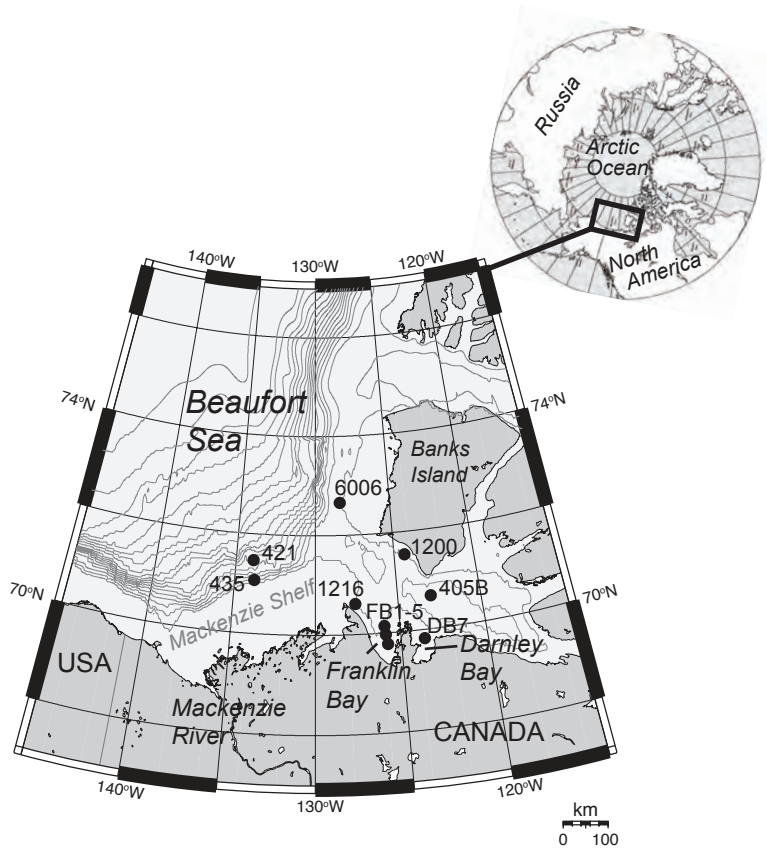


Figure 1. Map of Beaufort Sea sampling area with larger global-scale map highlighting study region; dots show sample locations and station names for photosynthesis-irradiance curves; the contour lines represent bathymetry along the continental shelf region.

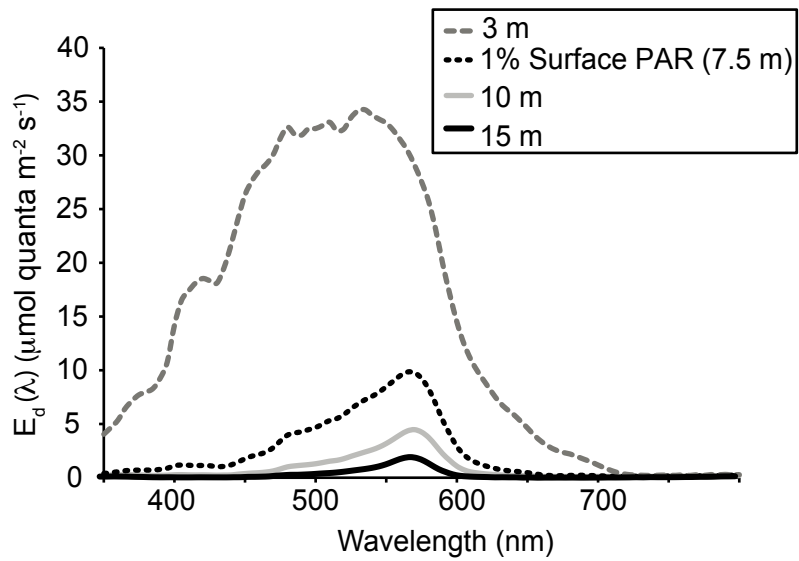


Figure 2. Spectral downwelling irradiance ($E_d(\lambda)$, mol quanta $m^{-2} s^{-1}$) at various depths under white ice cover at Darnley Bay, 11 June 2008 as measured by a free-falling optical radiometer. There was a large bloom of diatoms with a chlorophyll maximum of $\sim 24 \text{ mg } m^{-3}$ near 10-12 m depth.

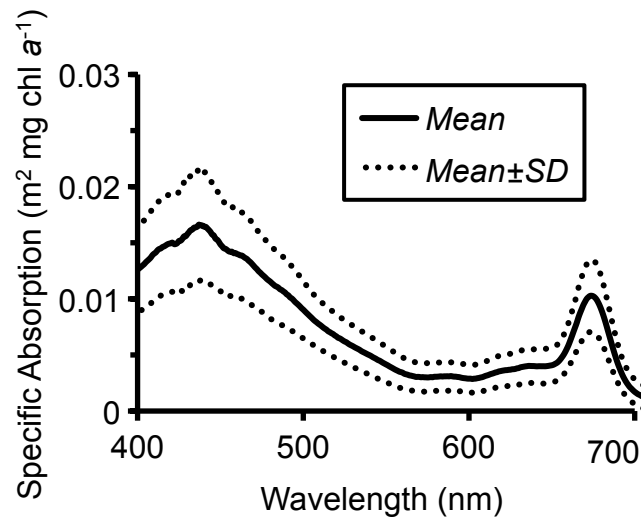


Figure 3. Phytoplankton specific absorption spectra normalized to Chl *a* (a^*_{ph} , in $\text{m}^2 \text{mg Chl-a}^{-1}$) for under ice (UI) communities. Shown are mean (solid line) \pm one standard deviation (dotted line)

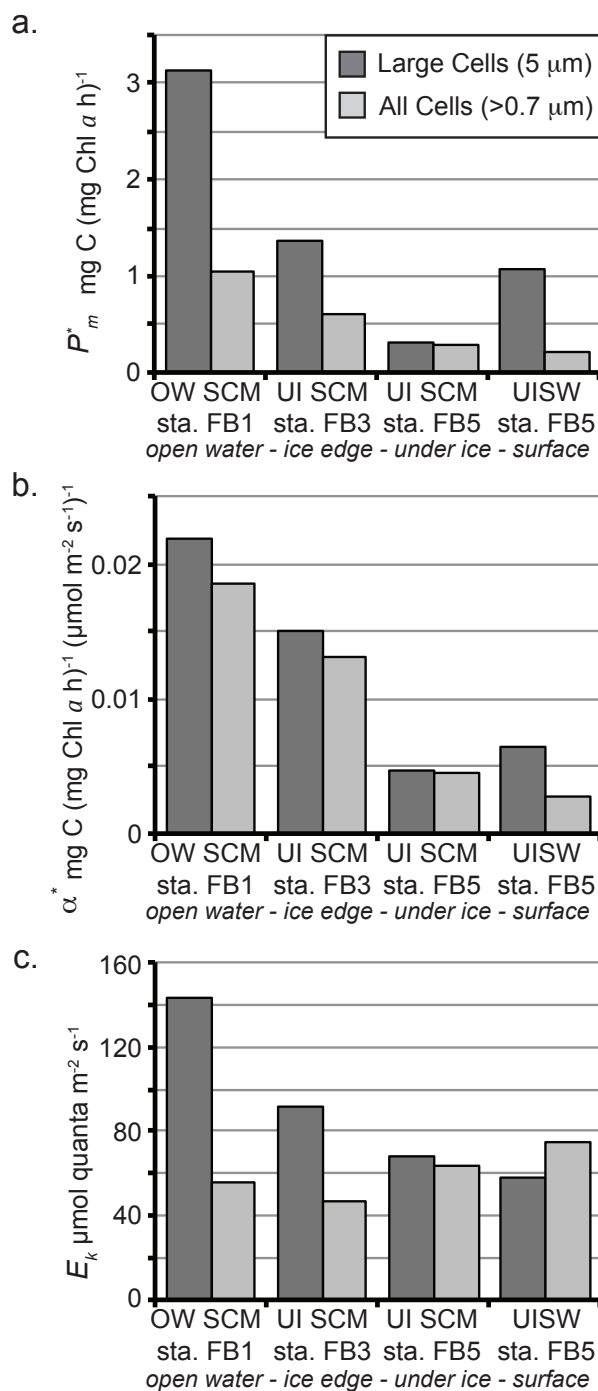


Figure 4. a) Maximum rate of carbon fixation (P_m^*), b) photosynthetic efficiency (α^*), and c) the photoacclimation parameter (E_k) from P-E curves along a transect in Franklin Bay from OW (station FB1, SCM 23 m) to ice edge (FB3, SCM 20 m) to UI (station FB5, SCM 18 m), and a UISW sample (station FB5, depth 2 m). Dark shades are large (>5 μm) cells only; lighter shades are the total community size (>0.7 μm).

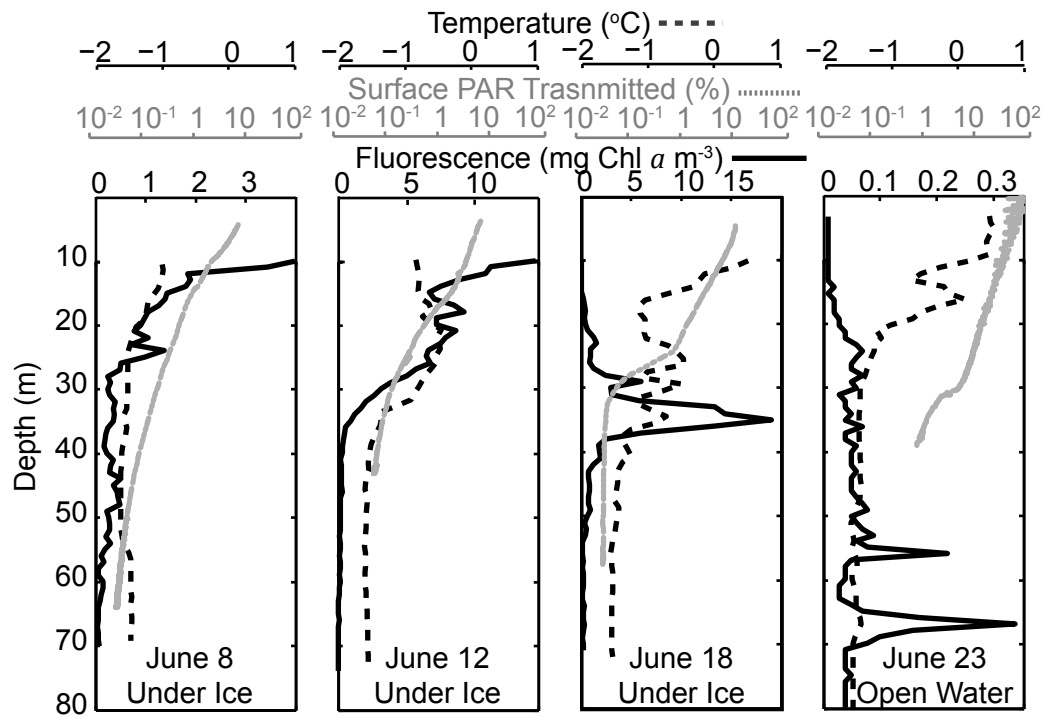


Figure 5. Vertical profiles of temperature (dashed line; from CTD), fluorescence (black line; from *in vivo* fluorescence sensor), and % PAR transmitted (grey line; measured by the Satlantic HyperOCR) under sea ice during a phytoplankton bloom (left; Darnley Bay sta. DB), June 8, 11, and 18, 2008), and in open water (far right; Cape Bathurst sta. 1216, 23 June 2008). Note: fluorescence scales differ.

CHAPTER 3:
LIGHT AND NUTRIENT CONTROL OF PHOTOSYNTHESIS IN NATURAL
PHYTOPLANKTON POPULATIONS FROM THE CHUKCHI AND BEAUFORT
SEAS, ARCTIC OCEAN

Light and nutrient control of photosynthesis in natural phytoplankton populations from the Chukchi and Beaufort Seas, Arctic Ocean

Molly A. Palmer¹, Gert L. van Dijken¹, B. Greg Mitchell², Brian J. Seegers^{2,*}, Kate E. Lowry¹, Matthew M. Mills¹, and Kevin R. Arrigo¹

¹ Department of Environmental Earth System Science, Stanford University, Stanford, California, USA

² Scripps Institution of Oceanography, University of California, San Diego, La Jolla, California USA

* *Now at* University of Southern California, Los Angeles, California USA

ABSTRACT

During ICESCAPE 2010-2011, we measured photosynthetic parameters in natural phytoplankton assemblages from the Chukchi and Beaufort Seas. Water column samples were taken from the surface (~3 m) and subsurface (~28 m) at ~85 stations each year representing a wide range of ecological conditions, including under sea ice (UI) and in open water (OW). The physiological response of phytoplankton to light was used to assess photoacclimation, photosynthetic efficiency, and maximum chlorophyll *a* (Chl *a*) normalized rates of carbon fixation. We found that photosynthetic parameters were tightly coupled to light and nutrient dynamics. Phytoplankton from the subsurface were acclimated to lower irradiance, as evidenced by higher photosynthetic efficiencies, reduced mean absorption spectra (\bar{a}^*) associated with heavy pigment packaging, higher maximum quantum yields of photosynthesis (Φ_m), increased Chl *a* content, and higher potential growth (μ_m) rates than surface samples. We found that phytoplankton growing in the UI subsurface had higher μ_m , increased Φ_m , and higher Chl *a* content, as well as reduced \bar{a}^* compared to those found in OW. The differences in photosynthetic parameters are related to a significant increase in light-harvesting pigments found in both UI and subsurface samples, resulting from a combination of relatively low light and high nutrient availability. We suggest that these photoacclimation patterns are relatively consistent over the range of Arctic environments, allowing for efficient phytoplankton photosynthesis and growth in low light conditions. A key difference between the environment measured in ICESCAPE and that of past studies is the presence of thinner ice that allows for UI phytoplankton blooms earlier in the season, where abundant winter-replenished nutrients can sustain growth.

Keywords: photosynthesis-irradiance measurements; phytoplankton; subsurface chlorophyll maximum; Chukchi Sea; Arctic Ocean

1. Introduction

The Arctic Ocean exhibits extreme seasonality between the dark winter months and the 24-hour sunlit summer, resulting in drastically varying light, temperature, and sea ice regimes throughout the year (Loeng et al. 2006). Marine primary production - the photosynthetic fixation of carbon dioxide (CO₂) by phytoplankton - in the Arctic is controlled by physical processes which modulate seasonal changes in light, nutrient, and temperature dynamics in the surface ocean (Sakshaug 2004; Carmack et al. 2006; Codispoti et al. 2009). To survive in areas of rapidly changing environmental conditions, phytoplankton must acclimate through physiological adjustments that balance photosynthesis with photoprotection, repair, and biosynthesis (Kirk 1994; MacIntyre et al. 2002; Falkowski and Raven 2007). Here, we investigate how these processes interact to control primary productivity in the Chukchi and Beaufort Seas.

In a typical seasonal cycle, Arctic phytoplankton begin to bloom in surface waters adjacent to the ice edge (marginal ice zone, MIZ) in late spring when sea ice starts to thin and retreat (Sakshaug 2004; Wang et al. 2005; Perrette et al. 2011). During this period, warming, runoff, and melt-water rapidly stratify the upper 20-50 m of the water column, creating a shallow stable mixed layer that is conducive for algal growth (Hill and Cota 2005; Loeng et al. 2006). This rapidly-developing MIZ bloom quickly exhausts surface nutrients, particularly nitrate (NO₃), the primary limiting nutrient in the Arctic (Cota et al. 1996; Carmack et al. 2004; Codispoti et al. 2005). Following this, a subsurface chlorophyll *a* (Chl *a*) maximum (SCM) often forms at the nitracline, where NO₃ is still available and light is sufficient for growth, although it is unclear exactly how these SCM develop (e.g., whether they form in situ or are a relict feature of the previous MIZ bloom; Martin et al. 2010). In addition, phytoplankton may also bloom under sea ice (Legendre et al. 1981; Fortier et al. 2002; Mundy et al. 2009), an under-sampled habitat thought to be too inhospitable for growth, but where one of the most intense blooms ever recorded was observed in the Chukchi Sea in 2011 (Arrigo et al. 2012).

Several key processes precede bloom initiation and control bloom magnitude in the Arctic Ocean (Sakshaug 2004; Loeng et al. 2006). First, insolation slowly

increases with solar elevation throughout the spring season into summer, and a minimum light availability threshold must be surpassed before phytoplankton photosynthesis results in increased phytoplankton biomass (Sakshaug [2004] suggests a day length >11-12 h for bloom initiation). Second, thick sea ice and snow strongly attenuate and reflect incoming solar radiation, causing severe light limitation in the underlying water column that remains in effect until both snow and ice melt (Perovich 1998; Perovich and Polashenski 2012). Third, nutrient availability is vital to bloom initiation; in the Chukchi Sea, local remineralization and winter mixing, plus the input of nutrient-rich Anadyr waters through the Bering Strait, pre-condition the region for high rates of phytoplankton productivity (Harrison and Cota 1991; Codispoti et al. 2005; Pickart 2004).

In recent decades, observed changes in the Arctic physical environment have had profound impacts on marine primary productivity (Arrigo et al. 2008; Arrigo and Van Dijken 2011). Such changes include a >30% reduction in the extent of the Arctic ice pack (Stroeve et al. 2005; Comiso et al. 2008), as well as sizeable reductions (>40%) in average ice thickness (Rothrock et al. 1999; Lindsay and Zhang 2005) and the large-scale replacement of multi-year ice with thinner first-year ice (Nghiem et al. 2007; Maslanik et al. 2011). This has both lengthened the growing season and increased the area of open water suitable for phytoplankton growth (Arrigo et al. 2008; Pabi et al. 2008; Arrigo and Van Dijken 2011). Environmental changes have been particularly large in the Beaufort and Chukchi Seas, especially in regards to sea ice thinning and retreat (Comiso et al. 2008; Shirasawa et al. 2009). In this region, the timing and intensity of the summer bloom are strongly affected by the dynamics of sea ice and water column stabilization (Arrigo and Van Dijken 2004; Wang et al. 2005; Carmack et al. 2006).

In response to the changing physical environment (temperature, light), phytoplankton can vary molecular, morphological, and physiological traits that ultimately impact photosynthesis and growth rates (e.g., through photoacclimation and photoadaptation; see reviews in Falkowski 1992; Kirk 1994; Falkowski and Raven 2007). Phytoplankton balance light-harvesting needs with the ability to use the energy

generated for growth (e.g., the quantum efficiency of photosynthesis), and thus energetically-expensive tradeoffs within the cell are made (Kirk 1994; MacIntyre et al. 2002; Falkowski and Raven 2007). For example, in response to low irradiance, phytoplankton maximize photosynthetic rates by altering either the number of photosynthetic units (typically, by increasing photosynthetic pigment content) or the rate of electron turnover in the photosynthetic transport chain (Sukenik et al. 1987; Falkowski and LaRoche 1991; Falkowski and Raven 2007). However, nutrient limitation can affect the synthesis of pigment protein complexes (Falkowski 1992). For example, NO_3 limitation reduces growth rates and photosynthetic rates, both of which are linked to the reduction in protein synthesis through a reduction in functional reaction centers (Falkowski 1992). Temperature is thought to be a key factor limiting primary production in the Arctic, because photosynthetic rates are influenced by the activity of specific enzymes, whose activity is reduced at low temperatures (Li et al. 1984; Falkowski 1992).

In response to varying irradiance, the need to increase light-harvesting capability at low light is typically met with an increase in the synthesis of photosynthetic pigments, particularly Chl *a* (Falkowski and Owens 1980; Falkowski and LaRoche 1991). This increases photosynthetic efficiency (α^*) and the maximum quantum yield of photosynthesis (Φ_m), but decreases the maximum Chl *a*-normalized rate of photosynthesis, P_m^* (Kirk 1994; Falkowski and Raven 2007). It can also lead to a decrease in the mean Chl *a*-specific absorption coefficient (\bar{a}^*), because of the package effect, whereby adding pigment molecules reduces absorption efficiency per unit Chl *a* due to self-shading (Morel and Bricaud 1981). At higher irradiance, photosynthetic rates increase as cells synthesize more photosynthetic units to process the increased delivery of photons, and photosynthesis is controlled by the rate of electron transport (the concentration of photosynthetic pigment decreases as well; Falkowski and Raven 2007). However, exposure to supersaturating irradiances can damage photosynthetic reaction centers and lead to an increase in photoprotective pigments, both of which decrease the quantum efficiency of photosynthesis, α^* , and P_m^* (Falkowski and Raven 2007). Thus, within the limits of species-specific genetic

potential (adaptation), photoacclimation may result from changes in pigment concentrations and ensembles, and/or the structure of the photosynthetic apparatus (Falkowski 1980; Falkowski and Owens 1980; Falkowski and LaRoche 1991).

It is important to distinguish between genotypic changes that occur over longer timescales in response to low light, which is referred to as shade-adaptation, and phenotypic changes that occur over shorter timescales within a range constrained by genetic potential that are called shade-acclimation (Falkowski and Raven 2007). This is because species-specific variations in photoacclimation and adaptation can determine the presence or dominance of one phytoplankton group over others in polar marine waters, as phytoplankton groups can respond (acclimate) differently to variations in nutrient supply and irradiance on a timescale of hours to days and eventually years (Hill and Cota 2005; Kropuenske et al. 2009; Arrigo et al. 2010). The chronic exposure to low light in Arctic regions has given rise to the notion that most Arctic phytoplankton are shade-adapted and thus well suited to exploit the extreme environmental conditions present in the MIZ (Platt et al. 1982; Subba Rao and Platt 1984; Kirst and Wiencke 1995). However, it is unknown if there are differences in acclimation between phytoplankton groups from different environments. Moreover, it is unknown how future changes in sea ice and climate may affect the physical marine environment and thus phytoplankton distributions, although it has been suggested that a surface freshening would favor communities dominated by smaller algal species (Li et al. 2009). This has important implications for the entire food web as different taxa play different ecological and biogeochemical roles and link primary production to marine mammals, birds, fish, and benthic communities (Stirling 1997; Grebmeier et al. 2006; Wassmann 2006).

We explored the physiological response of phytoplankton to different environmental conditions as part of the 2010-2011 ICESCAPE (“Impacts of Climate Change on the EcoSystems and Chemistry of the Arctic Pacific Environment”) project. We report here the results of short-term photosynthesis vs. irradiance (P-E) measurements, and focus our analysis on the photophysiological differences between surface and subsurface populations, and between samples gathered in open water

(OW; <25% ice) and under the sea ice (UI, >25% ice). Finally, we use transects extending in the direction of ice retreat from OW to ~100 km into the ice pack as a proxy for the temporal evolution of an under ice bloom, to explore changes in P-E parameters over time. Using the largest P-E dataset published for this region, our goal is to characterize the patterns and processes controlling phytoplankton-based CO₂ uptake. It is critical, in this time of rapid ice melt and transformation, to provide a frame of reference for which to compare and predict future changes in biogeochemical carbon cycling for this region.

2. Materials and Methods

2.1 Study area

Hydrographic measurements and observations of the Chukchi and western Beaufort Seas, Arctic Ocean, were performed onboard the USCGC *Healy* from 18 June to 16 July 2010 and 28 June to 24 July 2011 (Fig. 1). Stations were primarily located over the continental shelf in waters <50 m deep (although several >1000 m deep stations were sampled in 2011), and were selected to represent the typical ecological and environmental conditions present in the region. In both years, we experienced spring-like conditions transitioning into summer, and encountered the southern margin of the sea ice zone (SIZ) between 67-72°N that retreated northwestwards during the course of sampling (Fig. 1). A variety of ice types were encountered in both years, including land-fast ice near the coast of Alaska, broken drifting ice floes, large sheets of first-year ice dotted with melt-ponds, and thick multi-year ice from the central Arctic ice pack. In total, 253 P-E analyses were completed during ICESCAPE. These include 113 surface (3.1 ± 0.9 m depth) and 140 subsurface (28.0 ± 0.3 m depth) samples (Table 1), which were subsequently separated into two classes based on the concentration of sea ice (Table 2): 141 OW sites (<25% ice; 63 surface, 78 subsurface), and 112 UI sites ($\geq 25\%$ ice; 50 surface, 62 subsurface) (Table 2).

2.2 General sampling

Water column casts were performed using a rosette with twelve 30-L Niskin bottles and equipped with a Sea-Bird Electronics SBE9plus CTD with sensors for temperature, conductivity, and photosynthetically active radiation (PAR, 400-700 nm; QSP2300). Typically, CTD and PAR data were noisy in the first several meters of each cast and were removed. Water from Niskin bottles was poured immediately into triple-rinsed insulated plastic sample coolers and stored in the dark until analysis (<1 h). Analyses of Chl *a*, POC, and nutrient concentrations were performed as described in Arrigo et al. (unpubl.). Dissolved inorganic carbon (DIC) concentrations were measured as in Bates et al. (2005). At a few select stations (Table 3), more detailed light profiles were measured as in Frey et al. (2011) (for the under ice stations) and Arrigo et al. (unpubl.) (for the open water stations).

2.3 %PAR, MLD, and sea ice concentration

Because the upper few meters of PAR data from each vertical profile were unavailable after CTD post-processing, PAR just beneath the seawater surface (E_o) was determined by linearly extrapolating log transformed PAR data from greater depths to the surface. PAR at each depth (E_z) was adjusted for variation in incident solar radiation (E_s) during the CTD deployment by normalizing E_z to E_s . The percent of surface PAR transmitted to each depth (%PAR) was calculated as $E_z:E_s$ divided by $E_o:E_s$ multiplied by 100. The euphotic depth (Z_{eu}) was defined as the depth where E_z was reduced to $\leq 0.1\%$ of E_o . In Table 3, we show the percent of incident downwelling irradiance transmitted to sample depth, calculated as $E_{d,z,PAR}/E_{d0,PAR}$, using data from the UI and OW profiles (as opposed to the CTD; see Frey et al. 2011 for details).

Potential density (σ_θ) was calculated for each depth from temperature, salinity, and pressure using R code generated in the OCE toolbox (Kelley 2012). Upper mixed layer depth (MLD, m) was calculated as the depth where σ_θ exceeded the surface value by 0.05 kg m^{-3} . In some cases, the water column was well-mixed and MLD could not be determined.

The concentration of sea ice at each station was estimated by a combination of: (1) standardized visual observations made while at sea (over a three hour period from the bridge), (2) analysis of photographs taken from the USCGC *Healy* camera mounted over the bridge at the time of CTD deployment, and (3) analysis of daily composites of satellite imagery from MODIS-Aqua (National Aeronautics and Space Administration) and SSM/I (National Snow and Ice Data Center) compiled during the cruise. Stations were placed into one of the predefined sea ice categories (OW or UI); the limit of 25% ice threshold was chosen as this best represented the two habitat types as encountered during the cruise and later defined by satellite imagery.

2.4 P-E measurements

P-E measurements were conducted using a short-term (one hour) ¹⁴C-bicarbonate technique (Lewis and Smith 1983, as modified by Arrigo et al. 2010) at two depths per station (typically ~2 m and ~25 m) using 20 light intensities ranging from 0-1500 ($\mu\text{mol quanta m}^{-2} \text{s}^{-1}$). P-E curves were fit using least squares nonlinear regression to the model of Platt et al. (1980) as modified by Arrigo et al. (2010). For the P-E calculations, the measured seawater DIC concentrations were used prior to curve fitting. Briefly, the CO₂-fixation rate (P^*), at irradiance E was determined as

$$P^* = P_s^* \left(1 - e^{-\frac{\alpha^* E}{P_s^*}} \right) e^{-\frac{\beta^* E}{P_s^*}} - P_o^*$$

where P_s^* and P_o^* ($\text{mg C mg}^{-1} \text{ Chl } a \text{ h}^{-1}$) are the light-saturated maximum CO₂-fixation rates in the absence of photoinhibition and at zero E , respectively; α^* is the photosynthetic efficiency, defined as the initial slope of the P-E curve ($\text{mg C mg}^{-1} \text{ Chl } a \text{ h}^{-1} (\mu\text{mol quanta m}^{-2} \text{s}^{-1})^{-1}$); and β^* is a measure of photoinhibition ($\text{mg C mg}^{-1} \text{ Chl } a \text{ h}^{-1} (\mu\text{mol quanta m}^{-2} \text{s}^{-1})^{-1}$). Asterisks indicate Chl a -normalization. The maximum Chl a -specific CO₂-fixation rate, P_m^* , was then calculated as

$$P_m^* = P_s^* \left(\frac{\alpha^*}{\alpha^* + \beta^*} \right) \left(\frac{\beta^*}{\alpha^* + \beta^*} \right) \frac{\beta^*}{\alpha^*}$$

P-E curve fits were accepted only if the coefficient of multiple determination, $R^2_{yy(x)}$, of the fit was >60% (correlation of multiple correlation, $R_{yy(x)}$, $\geq 75\%$), and/or the

significance of the fit for each individual statistic had a p value of ≤ 0.05 . The photoacclimation parameter, E_k , was then calculated from P-E data as P_m^*/α^* . The maximum biomass-specific growth rate (μ_m , d^{-1}) for a given sample was calculated as P_m^* divided by the POC:Chl a ratio for that sample.

2.5 Absorption coefficients and quantum yields

Spectral light absorption by particulates (phytoplankton and detritus) was determined onboard at 1-nm resolution (300 to 800 nm) using a dual-beam spectrophotometer (Perkin-Elmer-Lambda-19) equipped with an integrating sphere following standard ocean optics protocols as described in Mitchell et al. (2003). Absorption by phytoplankton (a_{ph}) was calculated as the difference between the particulate (a_p) and detrital (a_d) absorption coefficients (m^{-1}). The Chl a -specific spectral absorption coefficient for phytoplankton (a_{ph}^* , $m^2 mg^{-1}$ Chl a) is a_{ph} normalized to fluorometrically-determined Chl a . The spectrally-averaged Chl a -specific absorption coefficient for phytoplankton (\bar{a}^* , $m^2 mg^{-1}$ Chl a) was then calculated as

$$\bar{a}^* = \frac{\sum_{700}^{400} a_{ph}(\lambda)E(\lambda)}{\sum_{700}^{400} E(\lambda)}$$

where $E(\lambda)$ is the spectral output of the photosynthetron light source.

The maximum quantum yield of photosynthesis, Φ_m , was calculated from α^* and \bar{a}^* as

$$\Phi_m = \frac{\alpha^*}{43.2\bar{a}^*}$$

where 43.2 represents a unit conversion to mol C (mol quanta absorbed) $^{-1}$.

2.6 Statistics

Data from 2010 and 2011 were pooled into a single dataset after first using the Pearson Chi-square test to ascertain that P-E parameters determined for either ice category or depth sampled were not significantly different between years (all statistics were conducted using Statistica Software v10, StatSoft, Inc.). To investigate how P-E

parameters varied between the two depth classes (surface vs. subsurface) and the two ice classes (OW vs. UI), as well as between each ice class for a given depth (OW surface vs. UI surface, OW subsurface vs. UI subsurface), we used the nonparametric Kruskal-Wallis ANOVA test (α level: 0.05) because the data were not normally distributed (based on the Kolmogorov-Smirnov test, Shapiro-Wilks' W test, and a visual inspection of the histograms for each variable; we also attempted the Box-Cox and log data transformations but these did not correct the skew or make the data normal). One big advantage of this data set is that the large sample size allows for a very robust statistical analysis regardless of the specific test performed, such that we are able to distinguish between small differences in the data.

The association between explanatory environmental variables and P-E response variables was analyzed using multiple regression analysis. We first used pairwise comparisons of all environmental variables to eliminate redundancy in the dataset. From this, we selected three key environmental factors for the regression: temperature, dissolved inorganic nitrogen (DIN, NO_3+NO_2), and the amount of PAR transmitted to sample depth (%PAR). Multiple forward-stepwise regression was then used to analyze the effect of these independent explanatory variables on P-E parameters using a significance cutoff of $p \leq 0.05$. The standardized multiple regression coefficient (denoted b^* here) was used to compare the relative contribution of each independent variable in the prediction of the dependent P-E parameter. Finally, we used the nonparametric Spearman rank test to analyze the correlation between specific P-E parameters.

2.7 Summary of analyses conducted

We sampled a variety of ice types, depths, and bloom conditions in the nearshore, shelf, and mid-slope areas of the Chukchi Sea during both 2010 and 2011 (Fig. 1), allowing for a robust examination of how photosynthetic variables change with different environmental conditions. Our analysis here focuses on the photosynthetic parameters P_m^* , α^* , E_k , and β^* and the related variables \bar{a}^* and Φ_m . In addition, we include maximal potential growth rates, μ_m , and Chl a :POC ratios in our

analysis, which help elucidate how phytoplankton vary their photosynthetic machinery and physiological characteristics. We first focus on bulk differences between the two sampling depths (Table 1; Figs. 2 and 3), then explore variations with depth within the two ice categories (Table 2; Figs. 4 and 5). Two >300 km transects extending from open water deep into the ice pack parallel to the direction of sea ice retreat are used to explore the temporal evolution of the phytoplankton bloom, assuming that the horizontal distance along the transect represents different stages of the bloom (Figs. 4 and 5). Finally, we use stepwise multiple regression (Table 4) and correlation analysis (Table 5) to explore some of the important links between environmental conditions and selected P-E parameters.

3. Results

3.1 Site description

Our cruise track progressed northwards through the Bering Strait, along the Alaskan shelf, up through the Chukchi Sea, and eventually off the continental slope in the western Beaufort Sea (Fig. 1). Sea ice was encountered as far south as 68°N in 2010 and 71°N in 2011, including both pack ice and some land-fast ice along most of the Alaskan coast (Fig. 1 shows the location and shape of the ice edge at the beginning of sampling). In 2010, a large arm of pack ice from the central Arctic ice pack extended as far south as 68°N at the beginning of the cruise (18 June), but there were many large areas of open water open along the Alaskan coastline. This line of pack ice at 68°N formed the main ice edge, which retreated in a northwesterly direction to 71°N by the end of the 2010 cruise (16 July), a distance of ~300 km in nearly one month.

In 2011, pack ice extended southwards to 68°N a month prior (28 May) to sampling, forming the main ice edge. This ice edge retreated in a northwesterly direction to 71°N (see 2011 ice line, Fig. 1) by the beginning of the cruise (28 June), and to 74°N by the end of the cruise (24 July), a distance of ~300 km. Thus, ice conditions and rates of ice retreat were similar in both years, with the main difference being that we sampled at a later date in 2011, and hence the ice edge was roughly 300

km further north at the beginning of sampling in 2011 than in 2010.

The majority of sea ice we observed in both years was first-year ice approximately 0.5-1.8 m thick, although we encountered several patches of very thick, ridged multi-year ice (2-4 m) near the Chukchi shelf-break ($\sim 74^\circ\text{N}$) in both years. Melt ponds were common in first-year ice, covering from 25-50% of the sea ice surface. The ice edge was generally very well defined, although strong northerly winds occasionally advected ice southwards, loosening the pack and reducing sea ice concentrations near the southern margin of the MIZ. In both years, a large under-ice phytoplankton bloom was observed in the region known as “Chukchi North”, indicated by boxes A and B in Fig. 1 (the west side of box A was under sea ice, the east side was in open water; box B was completely under ice).

3.2 Differences between the surface and subsurface at all stations

3.2.1 Environmental conditions, Chl a, nutrients, and DIC

Environmental conditions at the surface (3.1 ± 0.9 m depth; mean \pm standard deviation) and subsurface (28 ± 0.3 m depth) differed significantly (Table 1A; Fig. 2). Temperatures were significantly higher in the surface than in the subsurface ($1.90 \pm 2.62^\circ\text{C}$ and $-0.38 \pm 1.71^\circ\text{C}$, respectively; $p < 0.001$; Fig. 2A-D) and salinity was significantly lower (30.71 ± 1.98 and 32.11 ± 0.71 , respectively; $p < 0.001$) (Table 1A). MLD averaged 11 ± 6 m for all stations sampled. Euphotic depth (Z_{eu}) averaged 34 m for stations where surface samples were obtained ($n=40$), and 37 m for stations where subsurface samples were obtained ($n=50$), thus most samples were collected from within the euphotic zone. Mean Z_{eu} for surface and subsurface samples differed slightly because valid data were not always available for both the surface and subsurface at every station. Surface samples were exposed to, on average, 20 times more downwelling irradiance than subsurface samples ($p < 0.001$), with PAR averaging 57.7% and 2.9% of E_o , respectively (Table 1A).

Chl *a* concentrations were significantly lower in surface (5.02 ± 10.35 mg m^{-3}) than in subsurface samples (7.28 ± 8.78 mg m^{-3} , $p < 0.01$), although there was substantial variability at both depths since we sampled phytoplankton in many different phases of

bloom development (Table 1A; Fig. 2I-L). Similarly, there was considerable variability in POC concentration such that surface and subsurface concentrations were not significantly different, averaging $27.6 \pm 36.1 \mu\text{mol L}^{-1}$ and $31.1 \pm 29.2 \mu\text{mol L}^{-1}$, respectively (Table 1A; Fig. 2M-P).

Inorganic nutrients were significantly lower in the surface than in subsurface waters ($p < 0.001$). In particular, $\text{NO}_3 + \text{NO}_2$ (Fig. 2E-H) and NH_4 concentrations were near zero in surface waters ($0.30 \pm 1.03 \mu\text{mol kg}^{-1}$ and $0.13 \pm 0.26 \mu\text{mol kg}^{-1}$, respectively) and substantially less than in the subsurface ($4.21 \pm 4.60 \mu\text{mol kg}^{-1}$ and $0.52 \pm 0.73 \mu\text{mol kg}^{-1}$, respectively) (Table 1B). PO_4 was also low in surface waters but not quite as depleted as $\text{NO}_3 + \text{NO}_2$, averaging $0.59 \pm 0.17 \mu\text{mol kg}^{-1}$, and was nearly twice as high at depth ($1.09 \pm 0.40 \mu\text{mol kg}^{-1}$) (Table 1B). The most abundant nutrient was $\text{Si}(\text{OH})_4$, averaging $5.94 \pm 6.09 \mu\text{mol kg}^{-1}$ in surface waters and $14.01 \pm 13.04 \mu\text{mol kg}^{-1}$ in the subsurface (Table 1B). Similarly, DIC was significantly lower in the surface than in the subsurface ($p < 0.001$), averaging $1942.9 \pm 94.0 \mu\text{mol kg}^{-1}$ and $2079.8 \pm 76.9 \mu\text{mol kg}^{-1}$, respectively (Table 1B).

3.2.2. Photosynthetic parameters

There were significant differences between pooled surface and subsurface samples for almost all photosynthetic parameters studied (Table 1C; Fig. 3). Only two parameters were significantly higher in surface than subsurface populations: E_k was 39% greater in the surface than the subsurface ($p < 0.001$), averaging 69.6 ± 45.9 and $50.1 \pm 36.1 \mu\text{mol quanta m}^{-2} \text{s}^{-1}$, respectively (Fig. 3I-L), and \bar{a}^* was 11% higher in the surface than the subsurface ($p < 0.05$), averaging 0.0099 ± 0.0047 and $0.0086 \pm 0.0051 \text{ m}^2 \text{ mg}^{-1} \text{ Chl } a$, respectively (Fig. 3Q-T) (Table 1C). In contrast, α^* was 47% higher in subsurface than surface samples (0.025 ± 0.022 and $0.017 \pm 0.011 \text{ mg C mg}^{-1} \text{ Chl } a \text{ h}^{-1} (\mu\text{mol quanta m}^{-2} \text{ s}^{-1})^{-1}$, respectively; $p < 0.05$; Fig. 3E-H), and Φ_m was 46% greater (0.076 ± 0.047 and $0.052 \pm 0.042 \text{ mol C (mol quanta absorbed)}^{-1}$, respectively; $p < 0.001$; Fig. 3U-X) (Table 1C). Similarly, subsurface maximum growth rates (μ_m) were more than double surface values, averaging 0.47 ± 0.87 and $0.22 \pm 0.36 \text{ d}^{-1}$, respectively ($p < 0.001$) (Fig. 2Q-T) and Chl *a*:POC ratios were 2.4 times higher (0.019 ± 0.032 and

0.008±0.010 w:w, respectively; $p<0.001$; Fig. 2U-X) (Table 1C).

There was no significant difference in P_m^* between surface and subsurface samples (Table 1C; Fig. 3A-D), averaging 0.95±0.48 and 1.04±0.78 mg C mg⁻¹ Chl *a* h⁻¹, respectively. Some of the highest P_m^* values observed were in the nutrient-rich Anadyr water in the Bering Strait (Fig. 3A-D), and in regions under the ice and near the ice edge where NO₃ concentrations (Fig. 2E-H) were high. Significant photoinhibition, β^* , was observed in over 75% of the subsurface samples, averaging 0.0005±0.0003 mg C mg⁻¹ Chl *a* h⁻¹ (μmol quanta m⁻² s⁻¹)⁻¹ (Fig. 3O,P). In contrast, only 17.7% of surface samples exhibited signs of photoinhibition, with β^* averaging 0.0007± 0.0008 mg C mg⁻¹ Chl *a* h⁻¹ (μmol quanta m⁻² s⁻¹)⁻¹ (Fig. 3M,N) (Table 1C).

3.3 Differences between surface and subsurface in open water and under ice areas

We explored variability within and between the open water (OW) and under ice (UI) samples in our study region using two separate analysis of variance (ANOVA) tests: (1) for different depths within the same ice class and (2) for similar depths between the two ice classes (Table 2).

3.3.1 Open water areas: surface vs. subsurface

3.3.1.1 Environmental conditions, Chl *a*, nutrients, and DIC

OW areas displayed extensive variability between depths, with almost all environmental parameters exhibiting significant differences between the surface and subsurface (Table 2A-B). OW surface temperatures were the highest of all areas measured, averaging 3.41±2.18°C, and were significantly higher ($p<0.001$) than in the OW subsurface, which averaged 0.28±1.94°C (Table 2A). Salinity was significantly lower at the OW surface than in the subsurface ($p<0.001$), averaging 31.35±1.12 and 32.17±0.71, respectively (Table 2A). PAR was 16 times higher in the OW surface than subsurface (60.1±22.3% and 3.7±9.6% of E_0 , respectively; $p<0.001$) (Table 2A). The MLD at stations from which OW surface and subsurface samples were collected did not significantly differ, both averaging 12±7 m. Similarly, Z_{eu} was not significantly different between stations where OW surface and subsurface samples

were obtained, averaging 32 ± 14 m and 35 ± 18 m, respectively (Table 2A).

Although there was substantial spatial variability in OW samples, Chl *a* concentrations were >3-fold lower in the OW surface than at the subsurface ($p<0.001$), averaging 2.75 ± 5.40 mg m⁻³ and 7.74 ± 10.48 mg m⁻³, respectively (Table 2A). Similarly, POC was significantly lower at the surface than in the subsurface ($p<0.05$) in OW, averaging 20.5 ± 21.3 and 33.7 ± 35.3 $\mu\text{mol L}^{-1}$, respectively (Table 2A).

NO₃+NO₂ and NH₄ averaged 0.40 ± 1.25 and 0.17 ± 0.32 $\mu\text{mol kg}^{-1}$ in OW surface samples, respectively, both significantly lower ($p<0.001$) than OW subsurface values (3.58 ± 4.18 $\mu\text{mol kg}^{-1}$ and 0.58 ± 0.85 $\mu\text{mol kg}^{-1}$, respectively) (Table 2B). PO₄ and Si(OH)₄ concentrations at the surface (0.56 ± 0.18 and 5.29 ± 5.51 $\mu\text{mol kg}^{-1}$, respectively) were approximately half the values ($p<0.001$) in the subsurface (1.00 ± 0.38 and 10.14 ± 9.76 $\mu\text{mol kg}^{-1}$, respectively) (Table 2B). Similarly, DIC was lower at the OW surface than in the subsurface ($p<0.001$), averaging 1955.4 ± 57.3 and 2070.0 ± 80.1 $\mu\text{mol kg}^{-1}$, respectively (Table 2B).

3.3.1.2 Photosynthetic parameters

Significant differences with depth were observed in most OW P-E parameters (Table 2C). One exception was P_m^* , which did not differ significantly between the OW surface and subsurface, averaging 0.95 ± 0.50 and 0.96 ± 0.45 mg C mg⁻¹ Chl *a* h⁻¹, respectively (Table 2C). Another exception was β^* , which averaged 0.0006 ± 0.0004 mg C mg⁻¹ Chl *a* h⁻¹ ($\mu\text{mol quanta m}^{-2} \text{ s}^{-1}$)⁻¹ at both depths (Table 2C), but it is important to note that this includes only 17.5% of OW surface samples vs. 79.5% of OW subsurface samples (e.g., these were the only samples where photoinhibition was observed). α^* was 41% greater ($p<0.001$) in the OW subsurface (0.024 ± 0.014 mg C mg⁻¹ Chl *a* h⁻¹ ($\mu\text{mol quanta m}^{-2} \text{ s}^{-1}$)⁻¹) than at the surface (0.017 ± 0.011 mg C mg⁻¹ Chl *a* h⁻¹ ($\mu\text{mol quanta m}^{-2} \text{ s}^{-1}$)⁻¹) (Table 2C). Similarly, Φ_m and μ_m were both >65% higher ($p<0.001$) at the OW subsurface (0.070 ± 0.044 mol C (mol quanta absorbed)⁻¹ and 0.36 ± 0.44 d⁻¹, respectively) than in the surface (0.042 ± 0.038 mol C (mol quanta absorbed)⁻¹ and 0.20 ± 0.36 d⁻¹, respectively) (Table 2C). Chl *a*:POC was twice as high ($p<0.001$) in the OW subsurface than in the OW surface, averaging 0.015 ± 0.012 and

0.007±0.008 w:w, respectively (Table 2C). Conversely, E_k was 43% greater ($p<0.001$) at the OW surface than in the subsurface, averaging 67±37 and 47±24 $\mu\text{mol quanta m}^{-2} \text{s}^{-1}$, respectively (Table 2C). Similarly, \bar{a}^* was 22% higher ($p<0.01$) at the OW surface than in the subsurface, averaging 0.0115±0.0050 and 0.0093±0.0047 $\text{m}^2 \text{mg}^{-1} \text{Chl } a$, respectively (Table 2C).

3.3.2 Under ice areas: surface vs. subsurface

3.3.2.1 Environmental conditions, Chl *a*, nutrients, and DIC

UI areas also differed significantly between depths for most environmental conditions sampled (Table 2A-B), although not as much as in OW. Temperatures under the sea ice were $<0^\circ\text{C}$ for both UI surface and subsurface samples, but UI subsurface areas were nearly a full degree colder than in the UI surface (-1.20 ± 0.83 and $-0.25\pm 1.52^\circ\text{C}$, respectively) (Table 2A). Salinity was lower in the UI surface than in the subsurface ($p<0.001$), averaging 29.94±2.48 and 32.04±0.72, respectively; the UI surface salinity was the lowest of all the habitats measured (Table 2A). The UI subsurface had a significantly lower %PAR than the UI surface (2.0±2.0 and 55.0±16.7%, respectively; $p<0.001$) (Table 2A). MLD did not differ significantly in UI surface stations and UI subsurface stations, averaging 10±4 and 9±4 m, respectively (Table 2A). Similarly, Z_{eu} did not differ between stations where UI surface (36±20 m) and subsurface (39±18 m) samples were collected (Table 2A).

Chl *a* and POC varied substantially between depths in UI areas. Although displaying a wide range, Chl *a* was significantly higher ($p<0.001$) in the UI surface than in the subsurface, averaging 7.88±13.9 and 6.69±6.05 mg m^{-3} , respectively (Table 2A). POC also exhibited a very large range between the UI surface and subsurface (38.8±47.6 and 28.5±18.6 $\mu\text{mol L}^{-1}$, respectively) and no significant difference between depths could be ascertained (Table 2A).

Nutrients were significantly different between depths in the UI sites sampled, showing a general pattern of depletion in the surface and significantly higher concentrations ($p<0.001$) at depth (Table 2B). NO_3+NO_2 and NH_4 exhibited the lowest concentrations, with surface values of 0.16±0.59 and 0.08±0.12 $\mu\text{mol kg}^{-1}$,

respectively, and subsurface values of 5.16 ± 5.10 and $0.45 \pm 0.55 \mu\text{mol kg}^{-1}$, respectively (Table 2B). Similarly, PO_4 was very low in the UI surface, averaging $0.65 \pm 0.16 \mu\text{mol kg}^{-1}$, which was approximately half the UI subsurface concentration ($1.20 \pm 0.41 \mu\text{mol kg}^{-1}$; $p < 0.001$) (Table 2B). Although $\text{Si}(\text{OH})_4$ was much more plentiful than the other inorganic nutrients, concentrations were still more than twice as high in the subsurface than the surface (18.95 ± 14.99 and $7.33 \pm 7.15 \mu\text{mol kg}^{-1}$, respectively; $p < 0.001$) (Table 2B). DIC in the UI surface was the lowest of all areas sampled, and was much lower ($p < 0.001$) than in the UI subsurface (1925.8 ± 127.2 and $2091.1 \pm 71.8 \mu\text{mol kg}^{-1}$, respectively) (Table 2B).

3.3.2.2 *Photosynthetic parameters*

In contrast to the OW areas, only the physiological variables E_k , μ_m , and Chl a :POC varied significantly between the UI surface and subsurface (Table 2C). E_k was significantly higher in the UI surface than the subsurface (72.3 ± 55.5 and $53.6 \pm 46.9 \mu\text{mol quanta m}^{-2} \text{ s}^{-1}$, respectively) while μ_m and Chl a :POC were both significantly lower in the surface ($0.25 \pm 0.26 \text{ d}^{-1}$ and $0.011 \pm 0.012 \text{ w:w}$, respectively) than subsurface ($0.48 \pm 0.38 \text{ d}^{-1}$ and $0.020 \pm 0.012 \text{ w:w}$).

In contrast, there was no significant difference between the UI surface and subsurface for the variables P_m^* (0.95 ± 0.47 and $1.15 \pm 1.05 \text{ mg C mg}^{-1} \text{ Chl } a \text{ h}^{-1}$, respectively), α^* (0.018 ± 0.011 and $0.027 \pm 0.030 \text{ mg C mg}^{-1} \text{ Chl } a \text{ h}^{-1} (\mu\text{mol quanta m}^{-2} \text{ s}^{-1})^{-1}$, respectively), β^* (0.0005 ± 0.0002 and $0.0008 \pm 0.0012 \text{ mg C mg}^{-1} \text{ Chl } a \text{ h}^{-1} (\mu\text{mol quanta m}^{-2} \text{ s}^{-1})^{-1}$, respectively), \bar{a}^* (0.0082 ± 0.0042 and $0.0082 \pm 0.0059 \text{ m}^2 \text{ mg}^{-1} \text{ Chl } a$, respectively), and Φ_m (0.066 ± 0.048 and $0.081 \pm 0.050 \text{ mol C (mol quanta absorbed)}^{-1}$, respectively) (Table 2C). However, a statistically significant β^* was observed only in 18% of UI surface samples, compared to 73% of UI subsurface samples.

3.3.3 *Open water and under-ice areas at the same depth*

3.3.3.1 *Environmental conditions, Chl a, nutrients, and DIC*

Not surprisingly, conditions at OW sites differed in many respects from those at the UI sites (“S” for differences between OW and UI surface samples, or “Sb” for

differences between OW and UI subsurface samples, indicated in top row of Tables 2A-C). In OW, mean seawater temperature was $>3^{\circ}\text{C}$ higher at the surface ($p<0.001$) and $\sim 1.5^{\circ}\text{C}$ warmer in the subsurface ($p<0.001$; Table 2A) than in the UI. Salinity in the UI surface was the lowest of all habitats (Table 2A), and was significantly lower than in the OW surface ($p<0.001$; Table 2A). Salinity did not differ significantly between the OW subsurface and the UI subsurface (Table 2A).

Because of greater light attenuation by sea ice, UI sites received far less surface light than OW sites (Table 3), regardless of Chl *a* concentration. Unfortunately, we do not have light profiles for every station, and thus only present data from a few example stations in Table 3. We also note that in Tables 1 and 2, the light data are presented as %PAR calculated relative to the topmost values obtained by the PAR sensor on the CTD rosette, and thus no significant differences were observed between the %PAR reaching surface or subsurface zones in the two habitats (%PAR is calculated relative to the light just under the ocean surface in both habitats, and thus already includes attenuation by sea ice). Similarly, the calculated Z_{eu} did not differ significantly between OW and UI sites while the UI exhibited a slightly (but significantly, $p<0.05$) shallower MLD than at the OW sites (Table 2A). Surface Chl *a* and POC were both significantly higher at the UI sites ($p<0.05$), but did not differ between habitats in the subsurface waters (Table 2A).

NO_3+NO_2 and $\text{Si}(\text{OH})_4$ were both significantly higher in the subsurface in UI habitats than in OW ($p<0.05$ and 0.001 , respectively, see Table 2B), but did not differ significantly between the two habitats in the surface. PO_4 was significantly higher in the UI than in OW both in the surface ($p<0.01$) and the subsurface ($p<0.01$) (Table 2B). NH_4 did not differ significantly between depths in the two habitats sampled, being very low everywhere (Table 2B). DIC was significantly higher in the OW surface than UI surface and lower in the OW subsurface than UI subsurface ($p<0.05$; Table 2B).

3.3.3.2 *Photosynthetic parameters*

For P-E parameters and related variables, \bar{a}^* and Chl *a*:POC were significantly

different between the OW and UI sites at both the surface and subsurface (Table 2C). Surface values of \bar{a}^* were ~38% higher in the OW than the UI ($p < 0.001$) and subsurface values were ~13% higher ($p < 0.05$) (Table 2C). Chl *a*:POC was significantly lower in the OW than in the UI, by approximately 35% in the surface ($p < 0.001$) and 25% in the subsurface ($p < 0.05$) (Table 2C). In contrast, Φ_m only differed in the surface between the two habitats, and was 36% lower in the OW than in the UI (Table 2C). Finally, μ_m only differed significantly between the two habitats in the subsurface, being ~33% higher in the UI than in OW ($p < 0.01$) (Table 2C). However, since UI sites receive far less light than the OW habitats (Table 3), the actual growth rate (μ) may seldom, if ever, be as high as μ_m calculated for many of the areas we sampled.

3.4 Temporal variability of P-E parameters: Chukchi North Transect

In both 2010 (Fig. 4) and 2011 (Fig. 5), we sampled a transect (Chukchi North) that extended from the open water off the coast of Alaska in a northwesterly direction for over 300 km into the SIZ in the direction of ice retreat, allowing us to observe how P-E parameters varied during different stages of a phytoplankton bloom (Fig. 1, Box A and B, with the assumption that the bloom had developed under the sea ice and was thus progressively more advanced at further distances south of the ice edge; see below for more detail). In order to focus on the key patterns in P-E parameters revealed from this analysis, we combine both years together in the description of results below, as both years were similar in pattern with the exception that the bloom in 2010 was more developed than in 2011 (e.g., as evidenced by deeper and more severe nutrient depletion, greater and deeper concentrations of Chl *a* and POC, etc.). Although the years are lumped together below, we do highlight several key differences between years; please refer to Fig. 4 and Fig. 5 for more detailed descriptions of P-E and environmental parameters along each transect.

3.4.1 Open water (oldest bloom type sampled)

3.4.1.1 Physical and chemical environment

In both years, we encountered a strong SCM in the OW portion (0-100 km of Fig. 4 and 5) of the transect (open water was on the east side of box A in Fig. 1). In this area, temperatures were relatively constant ($\sim 3-4^{\circ}\text{C}$) in the well-mixed upper layer, and declined sharply to -2°C below the pycnocline at ~ 28 m (Fig. 4A; Fig. 5A). A well-developed nitracline was present around 28 m as well, with virtually no NO_3 in the surface, increasing to $5-12 \mu\text{mol kg}^{-1}$ below the nitracline (Fig. 4B; Fig. 5B). Surface Chl *a* in the OW was near zero, but averaged $10-15 \text{ mg m}^{-3}$ in 2010 and exceeded 30 mg m^{-3} in 2011 in the SCM at ~ 30 m depth (Fig. 4C; Fig. 5C). POC in OW was also higher in the SCM than in the OW surface, averaging $40-60 \mu\text{mol L}^{-1}$ (Fig. 4D; Fig. 5D). Based on the vertical patterns of Chl *a*, POC, oxygen (not shown), nutrients, and DIC along these transects, the OW SCM in the southwest portion of both transects appeared to be in a relatively late stage of bloom development compared to the other areas sampled, most likely a remnant of an earlier bloom that had previously depleted surface nutrients and was migrating deeper with the nutricline (Fig. 4A-D; Fig. 5A-D).

3.4.1.2 Photosynthetic parameters

In the OW surface, P_m^* was $\sim 0.5 \text{ mg C mg}^{-1} \text{ Chl } a \text{ h}^{-1}$ in both years (Fig. 4E; Fig. 5E), and exhibited similar values ($0.5-1.0 \text{ mg C mg}^{-1} \text{ Chl } a \text{ h}^{-1}$) in the OW SCM (Fig. 4E), except in one case in the 2011 transect where P_m^* was relatively high, near $1.5 \text{ mg C mg}^{-1} \text{ Chl } a \text{ h}^{-1}$, where the SCM was associated with the depth of the nitracline (Fig. 5E). Similarly, α^* and E_k in the OW SCM were comparable to OW surface values, although we note that values were slightly lower in 2010 than 2011 (α^* range: $0.01-0.03 \text{ mg C mg}^{-1} \text{ Chl } a \text{ h}^{-1} (\mu\text{mol quanta m}^{-2} \text{ s}^{-1})^{-1}$; E_k range: $\sim 30 \mu\text{mol quanta m}^{-2} \text{ s}^{-1}$ in 2010, $40-60 \mu\text{mol quanta m}^{-2} \text{ s}^{-1}$ in 2011) (Fig. 4F, G and Fig. 5F, G). Photoinhibition (β^*) was apparent only in the OW SCM (Fig. 4H), and \bar{a}^* was slightly higher at the OW surface than in the SCM in both years (Fig. 4I; Fig. 5I). Conversely, Φ_m was higher in the OW SCM than the OW surface in both years (Fig. 4J; Fig. 5J).

3.4.2 Ice edge (mid-to-late bloom)

3.4.2.1 Physical and chemical environment

Continuing along the transect (in a northwesterly direction in box A, Fig. 1), in both years we first encountered sea ice in small pockets of mostly broken floes near the 100 km mark (ice concentration: top left box, Figs. 4 and 5). Here (~100 km into transect) the pycnocline and associated nitracline had shoaled and surface temperatures were reduced (Figs. 4A,B and Fig. A,B at 100 km). The true ice edge was encountered in both 2010 and 2011 at ~200 km from the start of the transect; sea ice concentration was ~100% and ice thickness was >0.8 m. Close to the ice edge, the depth of the nitracline shoaled and surface temperatures were slightly warmer, abruptly transitioning to much colder waters under the sea ice (Fig. 4A,B; Fig. 5A,B). Similar to the OW sections of the transect, Chl *a* in the surface at the ice edge (~200 km) was very low (<1 mg m⁻³), but the SCM at the ice edge was shallower (near 15-20 m) than in the OW (Fig. 4C; Fig. 5C). Chl *a* in the ice edge SCM exceeded 30 mg m⁻³ in 2010, and the high concentrations of Chl *a* extended over >60 km along the transect (Fig. 4C). POC in the SCM at the ice edge in 2010 was similarly very high, averaging >100 μmol L⁻¹ (Fig. 4D). The pattern observed in 2011 was similar to that in 2010 except that the 2010 bloom had had more time to develop by the time we sampled, and thus Chl *a* and POC were slightly lower in 2011 than in 2010 (Chl *a* in the 2011 SCM averaged only 10-15 mg m⁻³, and POC averaged ~50 μmol L⁻¹) (Fig. 5C and 5D). Based on our chemical and biological data, this transition zone between OW and UI likely represents an earlier bloom stage than that observed in open water, as nutrients were higher, less particulate material had accumulated, and Chl *a* was lower.

3.4.2.2 Photosynthetic parameters

At the ice edge, we saw more variability in P-E parameters than in the OW (Figs. 4E-J and 5E-J). P_m^* was slightly higher than in OW, near 1.5 mg C mg⁻¹ Chl *a* h⁻¹ (i.e., at 200 km along the transect in 2010 and 250 km in 2011; Fig. 5E), and both P_m^* and α^* showed a slight increase with depth (Fig. 4E,F; Fig. 5E,F). Similarly, \bar{a}^*

was low and Φ_m was higher at depth in both years (Fig. 4I,J and 5I,J). There was little to no photoinhibition in either year near the ice edge, except for in 2011 where β^* in one surface sample was high ($0.0015 \text{ mg C mg}^{-1} \text{ Chl } a \text{ h}^{-1} (\mu\text{mol quanta m}^{-2} \text{ s}^{-1})^{-1}$) relative to the other samples (Fig. 4H; Fig. 5H).

One interesting difference between years in P-E parameters was observed near a patch of high NO_3 water (Fig. 4B) at the first ice floe at 100 km in 2010 (Sta. 83 and 84). At this site, P_m^* and α^* were both very high, the highest measured along both transects ($>3 \text{ mg C mg}^{-1} \text{ Chl } a \text{ h}^{-1}$ and $>0.08 \text{ mg C mg}^{-1} \text{ Chl } a \text{ h}^{-1} (\mu\text{mol quanta m}^{-2} \text{ s}^{-1})^{-1}$ for P_m^* and α^* , respectively) (Fig. 4E, F), and E_k was low ($\sim 30 \mu\text{mol quanta m}^{-2} \text{ s}^{-1}$) (Fig. 4G). Mean specific absorption spectra were also very high in this zone, as was Φ_m (Fig. 4I, J).

3.4.3 Under ice (earliest bloom type sampled)

3.4.3.1 Physical and chemical environment

Under $>50\%$ ice cover, phytoplankton were in the earliest stages of bloom development, as shown by the highest observed concentrations of Chl *a*, POC, and NO_3 in the UI compared to the OW portions of the transects (Figs. 4A-D; Fig. 5A-D). In the most advanced bloom areas, NO_3 was severely depleted at the UI surface, but this did not extend vertically as deep as in the OW (i.e., the nitracline was shallowest here) (Fig. 4B; Fig. 5B). In the UI, temperatures were cold ($<0^\circ\text{C}$) except for a few patches of recent ice break-up that showed some surface warming (Fig. 4A; Fig. 5A). UI Chl *a* was higher than in OW stations, reaching values $>30 \text{ mg m}^{-3}$ for a large portion of the UI transect (Fig. 4C; Fig. 5C), with maximum concentrations near the ice/water interface. UI POC was similarly high, averaging $60\text{-}80 \mu\text{mol L}^{-1}$ and reaching values $>100 \mu\text{mol L}^{-1}$ over a large area (Fig. 4D; Fig. 5D). However, as described above for the case in OW, we note that the bloom sampled beneath the ice in 2010 was also at a slightly later stage of development than in 2011, as evidenced by the deeper Chl *a* penetration ($>30 \text{ m}$), greater and deeper accumulation of POC, and more severe NO_3 depletion in 2010 than in 2011 (Fig. 4A-D; Fig. 5A-D).

3.4.3.2 Photosynthetic parameters

In the under ice bloom, P_m^* (Fig. 4E and 5E) averaged 1.0-1.5 mg C mg⁻¹ Chl *a* h⁻¹ (including the maximum value of >2 mg C mg⁻¹ Chl *a* h⁻¹ measured where NO₃ was >10 μmol kg⁻¹; Sta. 56, Fig. 5E). The initial slope of the P-E curve, α^* , was variable, but generally very low in the UI surface and slightly higher in the subsurface (near 0.02-0.04 mg C mg⁻¹ Chl *a* h⁻¹ (μmol quanta m⁻² s⁻¹)⁻¹) (Fig. 4F; Fig. 5F). E_k was higher in the surface than subsurface, averaging ~70 μmol quanta m⁻² s⁻¹ compared to ~40 μmol quanta m⁻² s⁻¹ at depth) (Fig. 4G; Fig. 5G). Values for mean specific absorption spectra (\bar{a}^*) were much lower under the ice, suggesting intense pigment packaging associated with the very high Chl *a* in the bloom (Fig. 4I; Fig. 5I). Little to no photoinhibition was observed in the under ice samples (Fig. 4H; Fig. 5H). Finally, Φ_m showed a noticeable increase under the ice and at depth (Fig. 4J; Fig. 5J).

3.5 Regression analysis

To explore the environmental factors controlling variability in P-E parameters throughout our study region, we performed multiple stepwise regression analysis using the variables NO₃+NO₂, water temperature, and %PAR at the depth where samples were taken (Table 4), as well as correlation analyses between all P-E parameters (Table 5). Results indicate that the strongest predictor of P_m^* is the concentration of NO₃+NO₂ ($b^*=0.19$; $p<0.01$). Similarly, NO₃+NO₂ was the best predictor of α^* ($b^*=0.19$, $p<0.01$), and although the overall regression fit was improved by adding %PAR into the equation ($p<0.001$), the coefficient itself was not significant ($b^*=-0.12$, *ns*) (Table 4). Not surprisingly, %PAR was the best predictor of E_k ($b^*=0.20$, $p<0.01$) (Table 4). Similar to α^* , the regression for E_k was improved by adding NO₃+NO₂ into the model ($b^*=-0.08$, *ns*), but the individual predictor was not significant even though the overall regression was ($p<0.001$, Table 4). Photoinhibition, β^* , was most closely predicted by temperature, with a negative relationship between the two ($b^*=-0.20$, $p<0.05$) (Table 4). Adding the parameter NO₃+NO₂ also improved the overall fit of the regression for β^* ($b^*=-0.17$), but we note that neither this nor the overall fit of the regression were significant (Table 4). The best predictor of \bar{a}^* was temperature, with

a strong positive relationship of $b^*=0.37$ ($p<0.001$) (Table 4).

Φ_m was significantly correlated with two variables: temperature had a strong negative relationship with Φ_m ($b^*=-0.33$, $p<0.001$) while NO_3+NO_2 had a positive relationship ($b^*=0.19$, $p<0.01$) (Table 4). One of the strongest relationships revealed in the regression analysis was the strong positive association between μ_m and NO_3+NO_2 ($b^*=0.43$, $p<0.001$) (Table 4). The regression also identified temperature as being a key negative predictor of μ_m ($b^*=-0.18$, $p<0.001$). Interestingly, the only P-E parameter influenced by all three environmental variables was Chl *a*:POC (Table 4). Similar to μ_m , the strongest predictor of Chl *a*:POC was NO_3+NO_2 ($b^*=0.38$, $p<0.001$). The other two regression variables both negatively influenced Chl *a*:POC, with temperature ($b^*=-0.23$, $p<0.001$) having a slightly stronger impact than %PAR ($b^*=-0.15$, $p<0.05$).

4. Discussion

During ICESCAPE 2010-2011, we measured photosynthetic parameters over a range of environmental conditions, including under 0.5-1.8 m thick fully consolidated (~100% concentration) sea ice and in open water. Our values agree well with literature values for Arctic phytoplankton, particularly for “shade-adapted” species growing at or near the ice edge, or in the OW at the SCM. In an early study of the Chukchi Sea, Hameedi (1978) measured assimilation numbers of $\sim 1.5 \text{ mg C mg}^{-1} \text{ Chl } a \text{ h}^{-1}$ in an actively blooming SCM ($10\text{-}40 \text{ mg m}^{-3} \text{ Chl } a$) near the ice edge in July-August. Similarly, Brugel (2009) reported a mean summertime P^*_m of $2.77 \text{ mg C mg}^{-1} \text{ Chl } a \text{ h}^{-1}$ from the nearby Canadian Beaufort Sea, and Kirst and Wiencke (1996) give a range for the whole Arctic of $0.03\text{-}2.41 \text{ mg C mg}^{-1} \text{ Chl } a \text{ h}^{-1}$. Comparable to what we measured during ICESCAPE, Hill and Cota (2005) measured a summertime range for P^*_m of $0.60\text{-}1.10 \text{ mg C mg}^{-1} \text{ Chl } a \text{ h}^{-1}$ for phytoplankton in the continental shelf and slope of the Chukchi and Beaufort Seas in summer, and Palmer et al. (2011) report results from the same region of 0.93 and $0.71 \text{ mg C mg}^{-1} \text{ Chl } a \text{ h}^{-1}$ from the UI and OW subsurface, respectively.

Interestingly, P^*_m in our study showed relatively little spatial variability and exhibited values near the lower end of the range typically attributed to Arctic phytoplankton ($\sim 1 \text{ mg C mg}^{-1} \text{ Chl } a \text{ h}^{-1}$). This includes surface and subsurface populations (Table 1C) both UI and in OW (Table 2C). In comparison, Harrison and Platt (1986) report an average P^*_m from 276 P-E experiments conducted in the eastern Canadian Arctic of $1.64 \text{ mg C mg}^{-1} \text{ Chl } a \text{ h}^{-1}$ in samples taken from the 50% light level and $1.31 \text{ mg C mg}^{-1} \text{ Chl } a \text{ h}^{-1}$ for samples from the 1% light depth (typically associated with the SCM), both of which are substantially higher than the mean values presented here.

Our results for α^* and E_k (Table 1C and 2C) fit well into the overall range for Arctic phytoplankton reported by Kirst and Wiencke (1995) (E_k : $19\text{-}432 \text{ } \mu\text{mol quanta m}^{-2} \text{ s}^{-1}$; α^* : $0.003\text{-}0.14 \text{ mg C mg}^{-1} \text{ Chl } a \text{ h}^{-1} (\mu\text{mol quanta m}^{-2} \text{ s}^{-1})^{-1}$). We cannot compare our values for α^* and E_k to those presented in Harrison and Platt (1986) because they measured light in W m^{-2} rather than $\mu\text{mol quanta m}^{-2} \text{ s}^{-1}$, and conversion would require knowledge of the spectral quality of their light source. Hill and Cota (2005) do not present values for α^* and E_k . In comparison to studies specific to the Chukchi and Beaufort Sea region, our results for α^* and E_k agree well with those of Brugel (2009), who reported a mean summertime α^* of 0.054 (range 0.003-0.113) $\text{mg C mg}^{-1} \text{ Chl } a \text{ h}^{-1} (\mu\text{mol quanta m}^{-2} \text{ s}^{-1})^{-1}$ and an average E_k of $69 \mu\text{mol quanta m}^{-2} \text{ s}^{-1}$. Similarly, Palmer et al. (2011) report an average α^* of 0.019 and $0.014 \text{ mg C mg}^{-1} \text{ Chl } a \text{ h}^{-1} (\mu\text{mol quanta m}^{-2} \text{ s}^{-1})^{-1}$ and E_k of 41 and $67 \mu\text{mol quanta m}^{-2} \text{ s}^{-1}$ for SCM samples from OW and UI, respectively. In addition, the tendency in our data towards much more frequent photoinhibition in subsurface than surface samples (Table 1C; Fig. 3M-P) was also observed by Harrison and Platt (1986) and Palmer et al. (2011).

Finally, our values of Chl *a*:POC (0.007-0.020 w:w; Table 1C and 2C) are similar to those of Platt et al. (1982), who measured Chl *a*:C ratios of 0.015 w:w and 0.026 w:w for samples from the 50% and 1% light levels, respectively. Similarly, our results for \bar{a}^* and Φ_m from the SCM compare well with those reported in Palmer et al. (2011) from the nearby Canadian Beaufort Sea, which averaged $0.008 \text{ m}^2 \text{ mg}^{-1} \text{ Chl } a$

and $0.044 \text{ mol C (mol quanta absorbed)}^{-1}$, respectively, in the UI habitat (data for OW SCM are estimates and not comparable).

Light and nutrient control of P-E parameters during ICESCAPE

In the Chukchi and Beaufort Seas, light, nutrients, and temperature have been cited as important factors controlling photosynthetic rates of phytoplankton (e.g., Harrison and Platt 1986; Carmack et al. 2004; Tremblay et al. 2008). Particularly, the exposure to chronically low light levels (because of heavy cloud and ice cover, short summers, and low sun angles), and the high α^* and Φ_m and low P_m^* and E_k measured in most Arctic phytoplankton, are often cited as key evidence that Arctic algae are shade-adapted (or “shade-acclimated”, depending on the timescale considered; e.g., Platt et al. 1982; Harrison and Platt 1986; Kirst and Wiencke 1995). For example, Platt et al. (1982) showed that in Baffin Bay, as in the Chukchi (Hameedi 1978; Lee et al. 2010) and Beaufort Seas (Palmer et al. 2011), phytoplankton from the 1% light level had higher P_m^* and were more productive than phytoplankton from the 50% light level, indicating that shade-acclimated phytoplankton can perform well even at very low ambient light conditions if nutrients are in sufficient supply (Carmack et al. 2006; Tremblay et al. 2008; Lee et al. 2011). Another example of this is in the North Water polynya, where complete consumption of NO_3 in the euphotic zone limited the photoacclimation ability of phytoplankton (Tremblay et al. 2006). In addition, temperature may play a role in controlling P-E parameters, since at low temperatures ($<0^\circ\text{C}$), the large investment in enzymes required to increase photosynthetic rates is too energetically expensive for most species (Li et al. 1984; Harrison and Platt 1986; Harrison and Cota 1991).

While it is clear that light, nutrients, and temperature may all play a role in controlling the magnitude and range of P-E parameters in the dynamic ice-edge and open water region of the summer phytoplankton bloom in the Chukchi Sea, it is of interest to determine which of these factors most influenced P-E parameters during ICESCAPE. The four main habitats we sampled during ICESCAPE (surface and subsurface communities both under the sea ice and in open water) differed with

respect to temperature, light levels, and nutrient concentrations, and thus provide a model system in which to investigate the factors controlling phytoplankton photosynthesis and the range in P-E parameters.

(A) Under the sea ice

Low values for P^*_m and E_k , and elevated β^* suggest that the low light conditions in the UI habitat imposed by the sea ice cover (Table 3) results in a shade-acclimated phytoplankton population, particularly in the subsurface. However, these populations also appear to respond to vertical variations in nutrients that develop over the course of the actively-growing UI phytoplankton bloom. In the UI surface, severe nutrient depletion by the preceding UI bloom constrained P^*_m to relatively modest rates ($\sim 1 \text{ mg C mg}^{-1} \text{ Chl } a \text{ h}^{-1}$), despite higher light availability than in the UI subsurface at the SCM. In contrast, in the UI subsurface, light was greatly reduced but nutrients were in the greatest concentration of any of the four habitats sampled. Consequently, shade-acclimated phytoplankton in the UI subsurface were still able to maintain P^*_m rates of $\sim 1 \text{ mg C mg}^{-1} \text{ Chl } a \text{ h}^{-1}$ despite these low light levels. The higher nutrient concentrations at the SCM likely allowed phytoplankton to synthesize more antenna pigments and photosynthetic units (increase Chl a :POC) for enhanced light absorption and produce more enzymes to facilitate faster rates of CO_2 fixation and growth (as evidenced by higher values for μ_m). The balance between low light and variable nutrient conditions under sea ice was used by Hill et al. (2005) to explain similar patterns of spring P-E parameters and total primary productivity and are consistent with the photoacclimatory models presented in MacIntyre et al. (2002) and Falkowski (1980, 1992).

Supporting our conclusion that P-E parameters are controlled by both light and nutrients are the more rare cases where nutrients remained elevated within the euphotic zone. In these locations, we observed as much as 5-fold higher than average rates of P^*_m (see Sta. 56, Fig. 5E, for under 100% ice cover; or the marginal ice of Sta. 83-84 in Fig. 4E). In addition, the highest P^*_m values of both years ($5\text{-}6 \text{ mg C mg}^{-1} \text{ Chl } a \text{ h}^{-1}$) were measured in nutrient-rich Anadyr water where NO_3^- greatly exceeded

10 $\mu\text{mol kg}^{-1}$ and phytoplankton were growing well within the euphotic zone. Thus, our data demonstrate that while phytoplankton maintain modest rates of photosynthesis due to low light availability under the sea ice, high nutrients can support higher maximal rates so long as sufficient light is available.

We suggest that the balance between higher light and lower nutrients at the surface and lower light and higher nutrients at the subsurface at the time of our cruises minimized the depth-related differences in P-E parameters. Essentially, the physiological benefits from having higher nutrient availability in the UI subsurface were counteracted by the very low light availability, such that the photoacclimatory differences observed between surface and subsurface phytoplankton were little to no net change in P_m^* , and very little change in other P-E parameters. The primary difference we observed was an increase in light-harvesting pigments in low light subsurface waters where nutrients were still available (Table 2C). The results from our regression analysis corroborate these findings, as NO_3+NO_2 exerted the strongest control on most P-E parameters (Table 4). It should also be noted that waters under the sea ice were not strongly stratified, allowing for the possibility that there was some exchange between the UI surface and subsurface, which may explain some of the similarity in many P-E parameters.

(B) Open water

In contrast to the UI habitats, nearly all environmental and P-E variables differed significantly between the OW surface and subsurface (Table 2). This difference is likely related, at least in part, to differences in stratification between the UI and OW environments. Because the OW region was more heavily stratified than UI, it is likely that there was little to no vertical exchange of phytoplankton or nutrients between the OW surface and subsurface. In addition, light availability in OW was much greater than in the UI habitats (Table 3), but surface nutrients were virtually exhausted in almost all OW surface sites sampled because of the earlier UI bloom, resulting in relatively strong vertical gradients. As such, our data indicate that in the OW, low surface nutrient availability results in P-E parameters that are

controlled by the slow diffusion of NO_3 across the pycnocline. Because nearly all the nutrients in OW are located at or below the SCM, phytoplankton growth is similarly restricted to this depth, and thus subsurface OW phytoplankton must also be shade-acclimated, as light is much lower at the SCM than at the surface (Tables 2A, 3). Shade acclimation in the SCM was evidenced by higher values for α^* , Chl α :POC, and β^* and a lower E_k and \bar{a}^* (due to pigment packaging) than in surface samples (Table 2C).

However, the light levels at the SCM were higher in the OW than the UI habitat (Table 3), so that phytoplankton at the SCM in OW had to devote fewer resources to acquiring light than in the UI habitat. This is seen particularly clearly by the lower Chl α :POC in OW at both the surface and subsurface. Hence, OW phytoplankton likely synthesized fewer photosynthetic pigments and were less shade-acclimated than those growing in the UI.

As in the UI habitat, the pattern in P-E parameters in OW was also clearly related to nutrient concentrations, which were higher at the SCM than at the surface. As a result, Φ_m and μ_m were both higher in the OW subsurface, despite the lower light availability (Table 2C). In addition, nutrient availability was generally lower in OW habitats than UI habitats and μ_m was lower as well (Table 2C). Thus, the OW data suggests that the counteracting effects of lower nutrients but higher light availability in OW habitat results in a range of values for P-E parameters (especially P_m^*) similar to that measured in the UI environment.

(C) Temperature

Finally, in contrast to other authors (e.g., Platt et al. 1982; Li et al. 1984; Harrison and Platt 1986), we note that the influence of temperature on P-E parameters seemed to be small, as the highest rates were associated with the coldest temperatures (Table 2C). This is contrary to what would be expected if temperatures controlled primary productivity through the regulation of enzymatic activity (e.g., Li et al. 1984). Although the regression analysis does show that temperature was a key factor in the prediction of five of the eight parameters analyzed, we suggest that the importance of

the temperature term was exaggerated because of its high degree of covariation with both light (positively correlated) and nutrient concentration (inversely correlated). Because variations in temperature in our study region were generally small, the magnitude of thermodynamic and/or kinetic control of physiological rate processes was likely small as well.

Ecological Implications of Variability in P-E Parameters

An important implication of our results is that the observed spatial patterns in P-E parameters may be a unique feature of the thinning ice cover now present in the region. With thinner, first-year ice largely dominating the ice types surveyed here, plus the vast proliferation of melt ponds, light penetration to the surface waters under the ice cover has increased 4-fold (Perovich and Polashenski 2012), and algae now bloom under the sea ice (Arrigo et al. 2012; Arrigo et al. unpubl.). However, light under the ice is lower than in the near-surface waters of the ice edge and in ice-free waters (Table 3), and thus shade-adapted phytoplankton growing under sea ice must be able to increase their ability to harvest light in order to achieve the large levels of biomass we observed. Ultimately, this cannot be done without sufficient nutrients, which explains why P-E parameters are so tightly coupled to NO_3 availability, and why P^*_m is limited to such a narrow range.

Additionally, since phytoplankton that grow within the UI bloom are physiologically adapted to low-light conditions, they are likely well suited to exploit the similar low-light/high-nutrient conditions in the OW SCM once the sea ice retreats. In fact, our data suggest that because under-ice phytoplankton are already acclimated to grow at low-light conditions, these phytoplankton may grow faster and perform better photosynthetically at the OW SCM than surface phytoplankton originating in a well-lit MIZ. Furthermore, the ability of shade-acclimated phytoplankton to grow beneath the sea ice and consume most of the surface nutrients while the region is still ice-covered means that phytoplankton growth in the normally productive surface waters of the MIZ will be reduced (Cota et al. 1996; Hill and Cota 2005; Perrette et al. 2011). Eventually, regions of the Arctic with diminishing ice

cover, like the Chukchi Sea, may shift away from a primarily MIZ-type bloom cycle (e.g., Perrette et al. 2011) to one that is dominated by under-ice phytoplankton blooms.

The observed shade-acclimation of phytoplankton in our study region and high potential growth rates under the ice illustrates how nutrient availability can regulate the ability of phytoplankton to cope with low-light conditions. This is consistent with studies by Carmack et al. (2006), Tremblay et al. (2008), and Lee et al. (2010) which suggested that P-E parameters in the ice-associated region of the Chukchi Sea vary mostly based on nutrients, because shade-adapted phytoplankton can utilize light at much lower levels than their high-light adapted counterparts. However, our results do not as closely support the temperature- and light-control theory of some earlier studies of the region (Li et al. 1984; Harrison and Platt 1986; Harrison and Cota 1991), hinting at the possibility that recent changes in sea ice and environmental conditions may be altering phytoplankton growth and photosynthesis in several fundamental and important ways, and/or that the data sets are not as comparable as we are assuming in this study (e.g., possibly because of biases in sampling location, timing, methodology, etc.). More work is needed to fully understand the impacts of changing environmental conditions on P-E parameters of natural phytoplankton populations from this dynamic region.

Finally, it is also interesting to consider whether our sporadic observations of high P_m^* associated with high NO_3 and sufficient light have important consequences for the annual bloom cycle. Early in the Arctic spring, light will always be low, and thus P_m^* will always be controlled by light availability, especially under ice cover, regardless of temperature or nutrient concentrations. However, incident irradiance increases rapidly in spring, and light transmission through the sea ice becomes sufficient to support net phytoplankton growth when surface NO_3 concentrations are still high. Indeed, model results indicate that most of the Chukchi shelf contains $>10 \mu\text{mol kg}^{-1} \text{NO}_3$ (e.g., Zhang et al. 2010) under the ice prior to the spring bloom due to wintertime mixing, transport, and remineralization (the main exception being the waters associated with the Alaska Coastal Current). Thus, it is likely that phytoplankton communities over much of the Chukchi Sea had substantially higher

P_m^* prior to our ICESCAPE cruises than we present here. By under-sampling the SIZ in spring, we are missing a key component of the seasonal cycle of primary productivity and may be underestimating annual production (e.g., Pabi et al. 2008; Arrigo and Van Dijken 2011; Perrette et al. 2011). Although rapid nutrient drawdown under the ice means that these potentially high rates of early-season P_m^* are likely to be short-lived, the very high values for P_m^* observed in ICESCAPE during this period suggests we may need to more seriously consider under ice primary production as the Arctic sea ice cover continues to recede and thin.

A New Paradigm of Primary Productivity in the Chukchi Sea

Based on our data, we see a new pattern emerging in the seasonal cycle of phytoplankton growth in the Chukchi Sea. The different phases can be summarized as follows:

(1) Early in the season, wintertime nutrient replenishment and regeneration increases nutrient concentrations throughout the water column, with low light preventing net photosynthesis. As solar elevation increases throughout the spring, extensive sea ice blocks light penetration to the surface ocean, and phytoplankton do not grow.

(2) Once the snow has melted and light beneath the 100% sea ice cover exceeds the compensation irradiance for phytoplankton net growth, the spring bloom develops *under the sea ice*. Melt pond formation enhances light penetration through the ice, accelerating the time to reach the light threshold necessary for photosynthesis. This is aided by shade-adaptation by phytoplankton. Low light availability initially limits P_m^* , but nutrients are high so phytoplankton can synthesize additional Chl *a*, allowing them to absorb more of the available light. This large investment in light-harvesting machinery increases the photosynthetic efficiency, growth rate, and accumulation of phytoplankton biomass under the ice. Nutrients begin to be depleted from the surface waters under the ice pack.

(3) As solar intensity increases, sea ice continues to thin and melt, and the UI phytoplankton utilize the enhanced light to extend deeper in the water column,

depleting nutrients at increasingly greater depths. Phytoplankton may grow to depths of up to 30 m under the ice as they move deeper to exploit nutrients; a SCM may also begin to develop once nutrients are exhausted in the surface layers. The highest rates of P_m^* are associated with depths where NO_3 is still available and light is sufficient for photosynthesis. The phytoplankton blooming under the ice are photoacclimated to the low-light conditions and maintain comparable levels of P_m^* , α^* , \bar{a}^* , and Φ_m between the surface and the SCM. Importantly, the phytoplankton community growing near the surface has high light availability, whereas the community growing in the subsurface has high nutrient availability; it is this distinction that creates the key differences in many of the P-E parameters

(4) Finally, the ice melts and retreats, stratifying the water column and isolating the nutrient-poor surface waters from nutrient rich waters below. Algae that were growing in the low-light UI environment are already acclimated to the low light conditions of the OW SCM. In areas where there was significant phytoplankton production under the ice, no bloom develops in surface waters of the MIZ because of depleted nutrients. In this MIZ and OW zone, the SCM is a remnant under-ice bloom. The OW subsurface communities have higher growth rates, Chl a :POC ratios, Φ_m , and α^* , and lower \bar{a}^* than those in the OW surface (Table 2C). The OW SCM becomes progressively deeper as shade-acclimated phytoplankton continue to grow well at depths where both light and nutrients are available. Later in the season, wind mixing or storm events may enhance surface nutrients, allowing for a secondary bloom in the OW surface, but otherwise, most primary productivity is concentrated in the OW SCM for the remainder of the season.

Conclusions

Phytoplankton from the UI and OW SCM in the Chukchi and Beaufort Seas were more shade-adapted, more efficient per light absorbed at producing a photochemical reaction, and were growing at a faster rate than phytoplankton in surface waters (Fig. 3, Table 1-2). We infer that these adjustments are related to the significant increase in light-harvesting pigments found in subsurface samples, as well

as the more stable low-light (e.g., below MLD) and high nutrient (all inorganic nutrients were more than double surface values) environment found under the ice and at the SCM (Table 2). Based on historical data, we suggest that these properties are relatively consistent over the range of Arctic environments. It seems that the main difference between the environment sampled in ICESCAPE and that of past studies is the presence of thinner ice with more melt ponds than ever before. The increased light penetration through the sea ice created a near ideal environment for an under-ice phytoplankton bloom that set the pattern for the rest of the seasonal bloom cycle (Arrigo et al. 2012). One of the key concepts suggested by our data in this new seasonal bloom cycle is the possibility that SCM found in MIZ or post-ice-retreat areas may be a direct result of a previous under ice bloom.

The pattern of primary productivity in this region of the Arctic is one in which low light availability due to ice cover gradually gives way to nutrient-control of P-E parameters. Sea ice thinning has dramatically changed the underwater light field to allow for enhanced under ice productivity, and importantly shifting the growing season to much earlier in the year. Furthermore, in this new paradigm, SCM-based production in the open water is a direct consequence of early season productivity under the ice, essentially meaning that the OW SCM is a remnant UI bloom. As temperatures continue to warm and the ice continues to thin, we can no longer consider the Pacific sector of the Arctic solely as a MIZ- and open-water-based productivity environment (e.g., Perrette et al. 2011). We will need new tools to understand the significance and importance of under ice and SCM-based primary production, as well as the consequences these shifting patterns of production have on the rest of the food web. Our data indicate that we may need to change our characterization of the seasonal Arctic bloom cycle, including placing more emphasis on under ice productivity and modifying our understanding of SCM development. More research is needed to fully elucidate this process and the potential links between nutrients, light, and/or temperature in the under-ice environment.

Acknowledgements

This research is a contribution to the ICESCAPE project, which was sponsored by the Ocean Biology and Biogeochemistry and Cryospheric Sciences programs at NASA (NASA grant NNX10AF42G to K. R. Arrigo), and is also supported by NASA grant NNX09AO48H to M.A. Palmer. We thank the officers and crew of the USCGC *Healy* for their assistance and support; N. Bates for providing the DIC data; K. Frey for providing under ice light measurements; J. Swift and his team for providing nutrient data; and the entire ICESCAPE team, especially K.E. Lowry, Z.W. Brown, A. Santiago, S. Martin, B.D. Schieber, and E. Weiss, for field and laboratory support.

References

- Arrigo, K. R. and G. L. van Dijken. 2004. Annual cycles of sea ice and phytoplankton near Cape Bathurst, southeastern Beaufort Sea, Canadian Arctic. *Geophys. Res. Lett.* **31**: L08304, [doi:10.1029/2003GL018978](https://doi.org/10.1029/2003GL018978)
- Arrigo, K. R., G. L. van Dijken and S. Pabi. 2008. Impact of a shrinking Arctic ice cover on marine primary production. *Geophys. Res. Lett.* **35**: L19606, [doi:10.1029/2008GL035028](https://doi.org/10.1029/2008GL035028).
- Arrigo, K. R., M. M. Mills, L. R. Kropuenske, G. L. van Dijken, A. C. Alderkamp, D. H. Robinson. 2010. Photophysiology in two major Southern Ocean phytoplankton taxa: Productivity and growth of *Phaeocystis antarctica* and *Fragilariopsis cylindrus* under constant irradiance. *Integr. Comp. Biol.* **50**(6): 950-966, [doi:10.1093/icb/icq021](https://doi.org/10.1093/icb/icq021)
- Arrigo, K. R. and G. L. van Dijken. 2011. Secular trends in Arctic Ocean net primary production. *J. Geophys. Res.* **116**: C09011, [doi:10.1029/2011JC007151](https://doi.org/10.1029/2011JC007151)
- Arrigo, K. R., D. K. Perovich, R. S. Pickart, Z. W. Brown, G. L. van Dijken, K. E. Lowry, M. M. Mills, M. A. Palmer, W. M. Balch, F. Bahr, N. R. Bates, C. Benitez-Nelson, B. Bowler, E. Brownlee, J. K. Ehn, K. E. Frey, R. Garley, S. R. Laney, L. Lubelczyk, J. Mathis, A. Matsuoka, B. G. Mitchell, G. W. K. Moore, E. Ortega-Retuerta, S. Pal, C. M. Polashenski, R. A. Reynolds, B. Scheiber, H. M. Sosik, M. Stephens, and J. H. Swift. 2012. Massive phytoplankton blooms under Arctic sea ice. *Science* **336**(6087): 1408, [doi:10.1126/science.1215065](https://doi.org/10.1126/science.1215065)
- Bates, N. R., M. H. P. Best, and D. A. Hansell. 2005. Spatiotemporal distribution of dissolved inorganic carbon and net community production in the Chukchi and Beaufort Seas. *Deep-Sea Res. II*: **52**: 3303-3323, [doi:10.1016/j.dsr2.2005.10.005](https://doi.org/10.1016/j.dsr2.2005.10.005).
- Brugel, S. 2009. Étude des variations spatiales et temporelles du phytoplancton en mer de Beaufort : biomasse, production et structure de taille des communautés (Study on the spatial and temporal variability of phytoplankton in the Beaufort Sea: biomass, production, and community structure). Ph.D. thesis. Université du Québec à Rimouski.

- Carmack E. C., R. W. Macdonald, and S. Jasper. 2004. Phytoplankton productivity on the Canadian Shelf of the Beaufort Sea. *Mar. Ecol. Prog. Ser.* **277**: 37-50, doi:10.3354/meps277037
- Carmack, E. C., D. G. Barber, J. Christensen, R. Macdonald, B. Rudels, E. Sakshaug. 2006. Climate variability and physical forcing of the food webs and the carbon budget on panarctic shelves. *Progr. Oceanogr.* **71**(2-4): 145-181.
- Codispoti, L. A., C. N. Flagg, V. Kelly, and J. H. Swift. 2005. Hydrographic conditions during the 2002 SBI process experiments. *Deep Sea Res. II* **52**: 3199-3226.
- Codispoti, L. A., C. N. Flagg, and J. H. Swift. 2009. Hydrographic conditions during the 2004 SBI process experiments. *Deep Sea Res. II* **56**: 1144-1163.
- Comiso, J. C., C. L. Parkinson, R. Gersten, and L. Stock. 2008. Accelerated decline in the Arctic sea ice cover. *Geophys. Res. Lett.* **35**: L01703.
- Cota, G. F., L. R. Pomeroy, W. G. Harrison, E. P. Jones, F. Peters, W. M. Sheldon Jr., and T. R. Weingartner. 1996. Nutrients, primary production and microbial heterotrophy in the southeastern Chukchi Sea: Arctic summer nutrient depletion and heterotrophy. *Mar. Ecol. Prog. Ser.* **135**: 247-258, doi:10.3354/meps135247
- Falkowski, P. G. 1980. Light-shade adaptation in marine phytoplankton, p. 99-177. *In*: P. G. Falkowski (ed) *Primary productivity in the sea*. Plenum.
- Falkowski, P. G. 1992. Molecular ecology of phytoplankton photosynthesis, p. 47-67. *In*: P. G. Falkowski and A. Woodhead (eds) *Primary productivity and biogeochemical cycles in the sea*. Plenum.
- Falkowski, P. G., and T. G. Owens. 1980. Light-shade adaptation: two strategies in marine phytoplankton. *Plant. physiol.* **66**(4):592-595, doi:10.1104/pp.66.4.592.
- Falkowski, P. G., and J. LaRoche. 1991. Acclimation to Spectral Irradiance in Algae. *J. Phycol.* **27**: 8-14, doi:10.1111/j.0022-3646.1991.00008.x
- Falkowski, P. G. and J. A. Raven. 2007. *Aquatic photosynthesis*, 2nd ed. Princeton Univ. Press.

- Fortier, M., L. Fortier, C. Michel, and L. Legendre. 2002. Climatic and biological forcing of the vertical flux of biogenic particles under seasonal Arctic sea ice. *Mar. Ecol. Prog. Ser.* **225**: 1-16.
- Grebmeier, J. M., L. W. Cooper, H. M. Feder, B. I. Sirenko. 2006. Ecosystem dynamics of the Pacific-influenced Northern Bering and Chukchi Seas in the Amerasian Arctic. *Progr. Oceanogr.* **71**(2-4): 331-361.
- Hameedi, M. J. 1978. Aspects of water column primary productivity in the Chukchi Sea during summer. *Mar. Biol.* **48**: 37-48.
- Harrison, W. G., and G. F. Cota. 1991. Primary production in polar waters: relation to nutrient availability. *Polar Res.* **10**: 87-104.
- Harrison W. G., and T. Platt. 1986. Photosynthesis-irradiance relationships in polar and temperate phytoplankton populations. *Polar Biol.* **5**: 153-164, doi:10.1007/BF00441695
- Hill V., and G. Cota. 2005. Spatial patterns of primary production on the shelf, slope and basin of the Western Arctic in 2002. *Deep-Sea Res. II* **52**: 3344-3354, doi:10.1016/j.dsr2.2005.10.001
- Hill, V., G. Cota, and D. Stockwell. 2005. Spring and summer phytoplankton communities in the Chukchi and Eastern Beaufort Seas. *Deep Sea Res. II* **52**(24-26): 3369-3385, doi:10.1016/j.dsr2.2005.10.010.
- Kirk, J. T. O. 1994. *Light and photosynthesis in aquatic ecosystems*. Cambridge Univ. Press.
- Kirst, G. O., and C. Wiencke. 1995. Ecophysiology of Polar Algae. *J. Phycol.* **31**: 181-199, doi:10.1111/j.0022-3646.1995.00181.x
- Kropuenske, L. R., M. M. Mills, G. L. van Dijken, S. Bailey, D. H. Robinson, N. A. Welschmeyer, and K. R. Arrigo. 2009. Photophysiology in two major Southern Ocean phytoplankton taxa: photoprotection in *Phaeocystis antarctica* and *Fragilariopsis cylindrus*. *Limnol. Oceanogr.* **54**(4): 1176-1196, doi:10.4319/lo.2009.54.4.1176

- Lee, S. H., D. Stockwell, and T. E. Whitledge. 2010. Uptake rates of dissolved inorganic carbon and nitrogen by under-ice phytoplankton in the Canada Basin in summer 2005. *Polar Biol* **33**: 1027-1036.
- Legendre, L., R. G. Ingram, and M. Poulin. 1981. Physical control of phytoplankton production under sea ice (Manitounuk Sound, Hudson Bay). *Can. J. Fish. Aquat. Sci.* **38**: 1385-1392.
- Lewis, M.R., J. C. Smith. 1983. A small volume, short-incubation-time method for measurement of photosynthesis as a function of incident irradiance. *Mar. Ecol. Prog. Ser.* **13**: 99-102.
- Li, W. K. W., J. C. Smith, and T. Platt. 1984. Temperature response of photosynthetic capacity and carboxylase activity in Arctic marine phytoplankton. *Mar. Ecol. Prog. Ser.* **17**: 237-243.
- Li, W. K. W., F. A. McLaughlin, C. Lovejoy, E. C. Carmack. 2009. Smallest algae thrive as the Arctic Ocean freshens. *Science* **326**(5952): 539, doi:10.1126/science.1179798.
- Lindsay, R. W. and J. Zhang. 2005. The thinning of Arctic sea ice, 1988-2003: have we passed a tipping point? *J. Climate* **18**: 4879-4894.
- Loeng, H., K. Brander, E. Carmack, S. Denisenko, K. Drinkwater, B. Hansen, K. Kovacs, P. Livingston, F. McLaughlin, and E. Sakshaug. 2006. Marine Systems, p. 453-538 In: *Arctic Climate Impact Assessment: An Assessment of Consequences of Climate Variability and Change and the Effects of Increased UV in the Arctic Region*, Cambridge Univ. Press.
- MacIntyre, H. L., T. M. Kana, T. Anning, and R. J. Geider. 2002. Photoacclimation of photosynthesis irradiance response curves and photosynthetic pigments in microalgae and cyanobacteria. *J. Phycol.* **38**(1): 17-38.
- Maslanik, J., J. Stroeve, C. Fowler, W. Emery. 2011. Distribution and trends in Arctic sea ice age through spring 2011. *Geophys. Res. Lett.* **38**: L13502.
- Martin J., J.-È. Tremblay, J. Gagnon, G. Tremblay, A. Lapoussiere, C. Jose, M. Poulin, M. Gosselin, Y. Gratton, and C. Michel. 2010. Prevalence, structure and

- properties of subsurface chlorophyll maxima in Canadian Arctic waters. *Mar. Ecol. Prog. Ser.* **412**: 69-84, doi:10.3354/meps08666
- Morel, A. and A. Bricaud (1981) Theoretical results concerning light absorption in a discrete medium, and application to specific absorption of phytoplankton. *Deep-Sea Res* **28**: 1375-1393.
- Mundy, C.J., M. Gosselin, J. Ehn, Y. Gratton, A. Rossnagel, D. G. Barber, J. Martin, J.-È. Tremblay, M. A. Palmer, K. R. Arrigo, G. Darnis, L. Fortier, B. Else, and T. Papakyriakou. 2009. Contribution of under-ice primary production to an ice-edge upwelling phytoplankton bloom in the Canadian Beaufort Sea. *Geophys. Res. Lett.* **36**: L17601, doi:10.1029/2009GL038837
- Nghiem, S. V., I. G. Rigor, D. K. Perovich, P. Clemente-Colon, J. W. Weatherly, G. Neumann. 2007. Rapid reduction of Arctic perennial sea ice. *Geophys. Res. Lett.* **34**: L19504.
- Pabi, S., G. L. van Dijken and K. R. Arrigo. 2008. Primary Production in the Arctic Ocean, 1998-2006. *J. Geophys. Res.* **113**: C08005, doi:10.1029/2007JC004578
- Palmer, M. A., K. R. Arrigo, C. J. Mundy, J. K. Ehn, M. Gosselin, D. G. Barber, J. Martin, E. Alou, S. Roy, and J.-È. Tremblay. 2011. Spatial and temporal variation of photosynthetic parameters in natural phytoplankton assemblages in the Beaufort Sea, Canadian Arctic. *Polar Biol.* **34**: 1915-1928, doi:10.1007/s00300-011-1050-x
- Pickart, R. S. 2004. Shelf break circulation in the Alaskan Beaufort Sea: Mean structure and variability. *J. Geophys. Res.* **109**: C04024.
- Perovich, D. K. 1998. *Physics of ice covered seas, Volume 1*, pp. 446. Univ. of Helsinki Press.
- Perovich, D. K., and C. Polashenski. 2012. Albedo evolution of seasonal Arctic sea ice. *Geophys. Res. Lett.* **39**: L08501, doi:10.1029/2012GL051432
- Perrette M., A. Yool, G. D. Quartly, and E. E. Popova. 2011. Near-ubiquity of ice-edge blooms in the Arctic. *Biogeosciences* **8**: 515-524.
- Platt, T., C. L. Gallegos, W. G. Harrison. 1980. Photoinhibition of photosynthesis in natural assemblages of marine phytoplankton. *J. Mar. Res.* **38**(4): 687-701.

- Platt, T., W. G. Harrison, B. Irwin, E. P. Horne, and C. L. Gallegos. 1982. Photosynthesis and photoadaptation of marine phytoplankton in the Arctic. *Deep-Sea Res.* **29**(10):1159-1170, doi:10.1016/0198-0149(82)90087-5
- Sakshaug, E. 2004. Primary and secondary production in Arctic Seas, p. 57-81. *In*: R. Stein and R. W. Macdonald (eds.) *The organic carbon cycle in the Arctic Ocean*, Springer-Verlag.
- Shirasawa, K., H. Eicken, K. Tateyama, T. Takatsuka, and T. Kawamura. 2009. Sea ice thickness variability in the Chukchi Sea, spring and summer 2002-2004. *Deep-Sea Res. II* **56**(17): 1182-1200.
- Stroeve, J. S., M. C. Sereze, F. Fetterer, T. Arbetter, W. Meier, J. Maslanik, K. Knowles. 2005. Tracking the Arctic's shrinking ice cover: another extreme September minimum in 2004. *Geophys. Res. Lett.* **32**(4): L04501.1-L04501.4.
- Stirling, I. 1997. The importance of polynyas, ice edges, and leads to marine mammals and birds. *J. Mar. Sys.* **10**: 9-21.
- Subba Rao, D.V., and T. Platt. 1984. Primary production of Arctic waters. *Polar Biol.* **3**: 191-201.
- Sukenik, A., J. Bennett, and P. G. Falkowski. 1987. Light-saturated photosynthesis – limitation by electron transport or carbon fixation. *Biochimica et Biophysica Acta* **891**:205–215. doi:10.1016/0005-2728(87)90216-7
- Tremblay, J.-É., C. Michel, K. A. Hobson, M. Gosselin, and N. M. Price. 2006. Bloom dynamics in early opening waters of the Arctic Ocean. *Limnol Oceanogr* **51**(2): 900-012.
- Tremblay, J.-É., K. Simpson, J. Martin, L. A. Miller, Y. Gratton, D. G. Barber, and N. M. Price. 2008. Vertical stability and the annual dynamics of nutrients and chlorophyll fluorescence in the coastal, southeast Beaufort Sea. *J. Geophys. Res.* **113**: C07S90, doi:10.1029/2007JC004547
- Wang, J., G. F. Cota, and J. Comiso. 2005. Phytoplankton in the Beaufort and Chukchi Seas: distribution, dynamics, and environmental forcing. *Deep-Sea Res. II* **52**: 3355-3368, doi:10.1016/j.dsr2.2005.10.014

Wassmann, P. 2006. Structure and function of contemporary food webs on Arctic shelves: an introduction. *Progr. Oceanogr.* **71**(2-4): 123-128.

Zhang, J., Y. H. Spitz, M. Steele, C. Ashjian, R. Campbell, L. Berline, M. Matrai. 2010. Modeling the impact of declining sea ice on the Arctic marine planktonic ecosystem. *J. Geophys. Res.* **115**: C10015, doi:[10.1029/2009JC005387](https://doi.org/10.1029/2009JC005387)

Table 1. Environmental data (**A:** physical and biological data; **B:** chemical data) and P-E parameters (**C**) from 2010-2011 ICESCAPE cruise, divided by depth class (shaded: surface; unshaded: subsurface). Shown in top row are significant differences between depth classes (Kruskal-Wallis ANOVA, * = $p < 0.05$, ** = $p < 0.01$, *** = $p < 0.001$). Units for P-E parameters: P_m^* : mg C mg Chl $a^{-1} h^{-1}$; α^* and β^* : mg C mg Chl $a^{-1} h^{-1}$ ($\mu\text{mol quanta m}^{-2} \text{s}^{-1}$) $^{-1}$; E_k : $\mu\text{mol quanta m}^{-2} \text{s}^{-1}$; \bar{a}^* : m^2 (mg Chl a) $^{-1}$; Φ_m : mol C (mol quanta absorbed) $^{-1}$; μ_m : d^{-1} ; Chl:C: w:w.

1A.	Temp (°C) ***	Sal (psu) ***	%PAR ***	MLD (m)	Z_{eu} 0.1% (m)	Chl a (mg m^{-3}) *	POC (μmol kg^{-1}) *
Surface (3.1 ± 0.9 m)	1.90 ± 2.62 (n=109)	30.71 ± 1.98 (n=109)	57.7 ± 20.4 (n=104)	11 ± 6 (n=108)	34 ± 17 (n=80)	5.02 ± 10.35 (n=113)	27.6 ± 36.1 (n=103)
Subsurface (28.0 ± 10.3 m)	-0.38 ± 1.71 (n=140)	32.11 ± 0.71 (n=140)	2.9 ± 7.2 (n=135)	11 ± 6 (n=136)	37 ± 18 (n=96)	7.28 ± 8.78 (n=140)	31.1 ± 29.2 (n=133)

1B.	NO ₃ + NO ₂ (μmol kg^{-1}) ***	PO ₄ (μmol kg^{-1}) ***	Si(OH) ₄ (μmol kg^{-1}) ***	NH ₄ (μmol kg^{-1}) ***	DIC (μmol kg^{-1}) ***
Surface (3.1 ± 0.9 m)	0.30 ± 1.03 (n=109)	0.59 ± 0.17 (n=109)	5.94 ± 6.09 (n=109)	0.13 ± 0.26 (n=109)	1942.9 ± 94.0 (n=109)
Subsurface (28.0 ± 10.3 m)	4.21 ± 4.60 (n=139)	1.09 ± 0.40 (n=139)	14.01 ± 13.04 (n=139)	0.52 ± 0.73 (n=139)	2079.8 ± 76.9 (n=140)

1C.	P_m^*	α^* ***	E_k ***	β^*	\bar{a}^* *	Φ_m ***	μ_m ***	Chl a :POC ***
Surface (3.1 ± 0.9 m)	0.95 ± 0.48 (n=113)	0.017 ± 0.011 (n=113)	69.6 ± 45.9 (n=113)	0.0005 ± 0.0003 (n=20)	0.0099 ± 0.0047 (n=105)	0.052 ± 0.044 (n=105)	0.22 ± 0.36 (n=103)	0.008 ± 0.010 (n=103)
Subsurface (28.0 ± 10.3 m)	1.04 ± 0.78 (n=140)	0.025 ± 0.022 (n=140)	50.1 ± 36.1 (n=140)	0.0007 ± 0.0008 (n=107)	0.0086 ± 0.0051 (n=134)	0.075 ± 0.047 (n=134)	0.47 ± 0.87 (n=133)	0.019 ± 0.032 (n=133)

Table 2. P-E and related data from 2010-2011 ICESCAPE cruise, divided by ice class (top rows: open water; bottom rows: under sea ice) and depth class (shaded rows: surface; unshaded rows: subsurface). Results from ANOVA between ice classes are shown in column headings for surface (S) or subsurface (Sb) samples (Kruskal-Wallis: * = $p < 0.05$; ** = $p < 0.01$; *** = $p < 0.001$). Below each ice class, the results from ANOVA between depth class within each ice class are shown, with significance as above. Shown are: (A) physical and biological data for P-E samples. (B and C on subsequent pages).

2A.		Temp (°C) (S***, Sb***)	Sal (psu) (S***)	%PAR	MLD (m) (Sb*)	Z_{eu} 0.1% (m)	Chl <i>a</i> (mg m ⁻³) (S*)	POC (µmol kg ⁻¹) (S*)
Open Water	Surface (3 ± 1 m)	3.41 ± 2.18 (n=63)	31.35 ± 1.12 (n=63)	60.1 ± 22.3 (n=61)	12 ± 7 (n=58)	32 ± 14 (n=40)	2.75 ± 5.40 (n=63)	20.5 ± 21.3 (n=58)
	Subsurface (28 ± 10 m)	0.28 ± 1.94 (n=78)	32.17 ± 0.71 (n=78)	3.7 ± 9.6 (n=73)	12 ± 7 (n=74)	35 ± 18 (n=50)	7.74 ± 10.48 (n=78)	33.7 ± 35.3 (n=75)
		***	***	***			***	*
Under Ice	Surface (3 ± 1 m)	-0.25 ± 1.52 (n=49)	29.94 ± 2.48 (n=49)	55.0 ± 16.7 (n=46)	10 ± 4 (n=50)	36 ± 20 (n=40)	7.88 ± 13.89 (n=50)	38.8 ± 47.6 (n=47)
	Subsurface (28 ± 10 m)	-1.20 ± 0.83 (n=62)	32.04 ± 0.72 (n=62)	2.0 ± 2.0 (n=62)	9 ± 4 (n=62)	39 ± 18 (n=46)	6.69 ± 6.05 (n=62)	28.5 ± 18.6 (n=59)
		***	***	***			***	

Table 2 (cont.). P-E and related data from 2010-2011 ICESCAPE cruise, divided by ice class (top rows: open water; bottom rows: under sea ice) and depth class (shaded rows: surface; unshaded rows: subsurface). Results from ANOVA between ice classes are shown in column headings for surface (S) or subsurface (Sb) samples (Kruskal-Wallis: * = $p < 0.05$; ** = $p < 0.01$; *** = $p < 0.001$). Below each ice class, the results from ANOVA between depth class within each ice class are shown, with significance as above. Shown are: **(B)** chemical data for P-E parameters.

2B.		NO₃+NO₂ ($\mu\text{mol kg}^{-1}$) (Sb**)	PO₄ ($\mu\text{mol kg}^{-1}$) (S**, Sb**)	Si(OH)₄ ($\mu\text{mol kg}^{-1}$) (Sb***)	NH₄ ($\mu\text{mol kg}^{-1}$)	DIC ($\mu\text{mol kg}^{-1}$) (S*, Sb*)
Open Water	Surface (3 ± 1 m)	0.40 ± 1.25 (n=63)	0.56 ± 0.18 (n=63)	5.29 ± 5.51 (n=63)	0.17 ± 0.32 (n=63)	1955.4 ± 57.3 (n=63)
	Subsurface (28 ± 10 m)	3.58 ± 4.18 (n=78)	1.00 ± 0.38 (n=78)	10.14 ± 9.76 (n=78)	0.58 ± 0.85 (n=78)	2070.0 ± 80.1 (n=78)
		***	**	**	***	***
Under Ice	Surface (3 ± 1 m)	0.16 ± 0.59 (n=49)	0.65 ± 0.15 (n=49)	7.33 ± 7.15 (n=49)	0.08 ± 0.12 (n=49)	1925.8 ± 127.2 (n=46)
	Subsurface (28 ± 10 m)	5.16 ± 5.10 (n=61)	1.20 ± 0.41 (n=61)	18.95 ± 14.99 (n=61)	0.45 ± 0.55 (n=61)	2091.1 ± 71.8 (n=62)
		***	**	***	***	***

Table 2 (cont.). P-E and related data from 2010-2011 ICESCAPE cruise, divided by ice class (top rows: open water; bottom rows: under sea ice) and depth class (shaded rows: surface; unshaded rows: subsurface). Results from ANOVA between ice classes are shown in column headings for surface (S) or subsurface (Sb) samples (Kruskal-Wallis: * = $p < 0.05$; ** = $p < 0.01$; *** = $p < 0.001$). Below each ice class, the results from ANOVA between depth class within each ice class are shown, with significance as above. Shown are: (C) P-E parameters. Units for P-E parameters: P_m^* : mg C mg Chl $a^{-1} h^{-1}$; α^* and β^* : mg C mg Chl $a^{-1} h^{-1} (\mu\text{mol quanta m}^{-2} \text{s}^{-1})^{-1}$; E_k : $\mu\text{mol quanta m}^{-2} \text{s}^{-1}$; \bar{a}^* : $\text{m}^2 (\text{mg Chl } a)^{-1}$; Φ_m : mol C (mol quanta absorbed) $^{-1}$; μ_m : d^{-1} ; Chl:C: w:w.

2C.		P_m^*	α^*	E_k	β^*	\bar{a}^* (S^{***} , Sb^*)	Φ_m (S^{**})	μ_m (Sb^{**})	Chl a:POC (S^{***} , Sb^*)
Open Water	Surface (3 ± 1 m)	0.95 ± 0.50 (n=63)	0.017 ± 0.011 (n=63)	67.4 ± 37.0 (n=63)	0.0006 ± 0.0004 (n=11)	0.0115 ± 0.0050 (n=60)	0.042 ± 0.038 (n=60)	0.20 ± 0.36 (n=58)	0.007 ± 0.008 (n=58)
	Subsurface (28 ± 10 m)	0.96 ± 0.45 (n=78)	0.024 ± 0.014 (n=78)	47.3 ± 24.3 (n=78)	0.0006 ± 0.0004 (n=62)	0.0093 ± 0.0047 (n=73)	0.070 ± 0.044 (n=73)	0.36 ± 0.44 (n=75)	0.015 ± 0.012 (n=75)
			***	***		**	***	***	***
Under Ice	Surface (3 ± 1 m)	0.95 ± 0.47 (n=50)	0.018 ± 0.011 (n=50)	72.3 ± 55.5 (n=50)	0.0005 ± 0.0002 (n=9)	0.0082 ± 0.0042 (n=45)	0.066 ± 0.048 (n=45)	0.25 ± 0.36 (n=44)	0.011 ± 0.012 (n=47)
	Subsurface (28 ± 10 m)	1.15 ± 1.05 (n=62)	0.027 ± 0.030 (n=62)	53.6 ± 46.9 (n=62)	0.0008 ± 0.0012 (n=45)	0.0082 ± 0.0059 (n=61)	0.081 ± 0.050 (n=61)	0.48 ± 0.38 (n=59)	0.020 ± 0.012 (n=59)
				*			***	***	

Table 3. Amount of irradiance ($E_{d,z,PAR}$) at two depths (3 m and 28 m) in different ICESCAPE habitats and environments: under bare ice and under ponded ice (top) and in open water (bottom), with differing incident surface irradiance ($E_{d,0,PAR}$), percent of incident above-surface irradiance transmitted to depth (calculated as $E_{d,z,PAR}/E_{d,0,PAR}$), and bloom conditions (Chl *a*) (units given in table heading).

		Surface (3 m)					Subsurface (28 m)				
		Date & Time (GMT)	Chl <i>a</i> (mg m ⁻³)	$E_{d,0,PAR}$ (μmol quanta m ⁻² s ⁻¹)	$E_{d,z,PAR}$ (μmol quanta m ⁻² s ⁻¹)	Trans. $E_{d,0,PAR}$ (%)	Date & Time (GMT)	Chl <i>a</i> (mg m ⁻³)	$E_{d,0,PAR}$ (μmol quanta m ⁻² s ⁻¹)	$E_{d,z,PAR}$ (μmol quanta m ⁻² s ⁻¹)	Trans. $E_{d,0,PAR}$ (%)
Under Sea Ice	UI – Bare (Sta. 55)	7/4/11 22:22	17.4	644	56.3	8.71%	7/4/11 22:24	3.12	643	0.127	0.020%
	UI – Ponded (Sta. 55)	7/4/11 23:00	17.4	599	129	21.6%	7/4/11 23:01	3.12	532	0.074	0.014%
	UI – Bare (Sta. 56)	7/5/11 21:52	38.9	693	25.1	3.62%	7/5/11 21:54	10.5	744	0.006	0.0008%
	UI – Ponded (Sta. 56)	7/5/11 22:34	38.9	683	99.6	14.6%	7/5/11 22:36	10.5	707	0.005	0.002%
	UI – Bare (Sta. 57)	7/6/11 22:11	0.91	847	89.2	10.5%	7/6/11 22:13	6.72	854	1.39	0.163%
	UI – Ponded (Sta. 57)	7/6/11 23:00	0.91	1142	445	38.9%	7/6/11 23:01	6.72	1091	2.17	0.199%
Open Water	OW (Sta. 25)	7/1/11 22:52	0.48	832	394	47.3%	7/1/11 22:53	0.58	884	12.5	1.42%
	OW (Sta. 81)	7/9/11 21:25	5.01	1119	738	65.9%	7/9/11 21:26	9.10	1101	5.95	0.405%
	OW (Sta. 113)	7/15/11 21:55	0.12	882	513	58.1%	7/15/11 21:56	15.1	875	37.2	4.25%

Table 4. Results from multiple stepwise regression analysis. Shown are standardized regression coefficients (beta), plus their individual significance (* = $p < 0.05$, ** = $p < 0.01$, *** = $p < 0.001$) as well as the details of the overall regression fit: significance (p), degrees of freedom (df), number of samples (n), correlation coefficient (r), and coefficient of multiple determination (r^2).

	Temp	NO ₃ +NO ₂	%PAR	p	df, n	r	r^2
P_m^*		0.19 **		**	1,235	0.19	0.04
α^*		0.19 **	-0.12	***	2,234	0.27	0.07
E_k		-0.08	0.20 **	***	2,234	0.24	0.06
β^*	-0.20 *	-0.17		0.09	2,116	0.20	0.04
\bar{a}^*	0.37 ***			***	1,225	0.37	0.13
Φ_m	-0.33 ***	0.19 **		***	2,224	0.45	0.20
μ_m	-0.18 **	0.43 ***		***	2,221	0.54	0.29
Chl a :POC	-0.23 ***	0.38 ***	-0.15*	***	3,220	0.61	0.38

Table 5. Correlation matrix using the nonparametric Spearman rank test for P-E parameters and associated variables. Bold indicates significance at the $p < 0.05$ level. Units for P-E parameters: P_m^* : mg C mg Chl $a^{-1} h^{-1}$; α^* and β^* : mg C mg Chl $a^{-1} h^{-1}$ ($\mu\text{mol quanta m}^{-2} \text{s}^{-1}$) $^{-1}$; E_k : $\mu\text{mol quanta m}^{-2} \text{s}^{-1}$; \bar{a}^* : $\text{m}^2 (\text{mg Chl } a)^{-1}$; Φ_m : mol C (mol quanta absorbed) $^{-1}$; μ_m : d^{-1} ; Chl:C: w:w.

	P_m^*	α^*	E_k	β^*	\bar{a}^*	Φ_m	μ_m	Chl a :POC
P_m^*	1.00							
α^*	0.55	1.00						
E_k	0.23	-0.62	1.00					
β^*	0.55	0.18	0.35	1.00				
\bar{a}^*	-0.09	-0.08	0.04	0.12	1.00			
Φ_m	0.48	0.79	-0.48	0.07	-0.64	1.00		
μ_m	0.49	0.38	-0.04	0.19	-0.61	0.66	1.00	
Chl a :POC	0.14	0.18	-0.13	-0.09	-0.69	0.54	0.91	1.00

Figure Legends

Figure 1. Map showing the location of all 2010 and 2011 ICESCAPE stations (circles); filled-in circles indicate stations where P-E experiments were performed. Box A encompasses the main stations for the 2010 and 2011 Chukchi North transect (stations 71-89 for 2010, Fig. 3; stations 36-54 for 2011, Fig. 4); box B shows the extension into the sea ice for 2011 only (stations 55-57, Fig. 4). Dark grey is landmass; shading white to light grey is ocean bottom depth (scale at right). Dotted lines show ice edge at the beginning of sampling in 2010 (June 18) and 2011 (June 28).

Figure 2. Spatial plots of ICESCAPE environmental and associated variables in the surface (left two columns, any sample depths <6 m; average surface sample depth: 3.1 ± 0.9 m) and subsurface (right two columns, any sample depth >6 m; average subsurface sample depth: 28.0 ± 10.3 m), separated by year (2010 and 2011) (note: colorbars at right same for each row variable). Dark grey is Alaska landmass, white is Chukchi Sea and Arctic Ocean; see Fig. 1 for location info. Environmental variables and units: (A-D) temperature (Temp., °C); (E-H) nitrate (NO_3 , $\mu\text{mol kg}^{-1}$); (I-J) chlorophyll *a* (Chl *a*, mg m^{-3}); and (M-N) particulate organic carbon (POC, $\mu\text{mol L}^{-1}$) (colorbars below). Also shown are: (Q-T) maximum growth rates (μ_m : d^{-1}); and (U-X) Chl *a*:POC ratios (w:w).

Figure 3. Spatial plots of ICESCAPE photosynthetic variables in the surface (left two columns, any sample depths <6 m; average surface sample depth: 3.1 ± 0.9 m) and subsurface (right two columns, any sample depth >6 m; average subsurface sample depth: 28.0 ± 10.3 m), separated by year (2010 and 2011) (note: colorbars at right same for each row variable). Dark grey is Alaska landmass, white is Chukchi Sea and Arctic Ocean; see Fig. 1 for location info. Photosynthetic variables and units: (A-D) P_m^* ($\text{mg C mg Chl } a^{-1} \text{ h}^{-1}$); (E-H) α^* ($\text{mg C mg Chl } a^{-1} \text{ h}^{-1} (\mu\text{mol quanta m}^{-2} \text{ s}^{-1})^{-1}$); (I-L) E_k ($\mu\text{mol quanta m}^{-2} \text{ s}^{-1}$); (M-P) β^* ($\text{mg C mg Chl } a^{-1} \text{ h}^{-1} (\mu\text{mol quanta m}^{-2} \text{ s}^{-1})^{-1}$);

(Q-T) $\bar{\alpha}^*$ ($\text{m}^2 (\text{mg Chl } a)^{-1}$); and (U-X) Φ_m ($\text{mol C} (\text{mol quanta absorbed})^{-1}$) (colorscapes bottom left).

Figure 4. Environmental (left; A-D) and photosynthetic (right; E-J) variables along the 2010 Chukchi North transect (stations 71-89; box A only in Fig. 1 with the section starting from the leftmost side of box A) vs. depth, sampled July 6-7, 2010. Dark grey is ocean bottom; light grey contours show potential density (units: kg m^{-3}); black dots show sample locations. Top left box shows sea ice concentration (0-100%) along transect, top right box shows light penetration to sample depth for depths shown in column below. Environmental variables and units: (A) temperature (Temp., $^{\circ}\text{C}$); (B) nitrate (NO_3 , $\mu\text{mol kg}^{-1}$); (C) chlorophyll *a* (Chl *a*, mg m^{-3}); and (D) particulate organic carbon (POC, $\mu\text{mol L}^{-1}$) (colorscapes below). Photosynthetic variables and units: (E) P_m^* ($\text{mg C mg Chl } a^{-1} \text{ h}^{-1}$); (F) α^* ($\text{mg C mg Chl } a^{-1} \text{ h}^{-1} (\mu\text{mol quanta m}^{-2} \text{ s}^{-1})^{-1}$); (G) E_k ($\mu\text{mol quanta m}^{-2} \text{ s}^{-1}$); (H) β^* ($\text{mg C mg Chl } a^{-1} \text{ h}^{-1} (\mu\text{mol quanta m}^{-2} \text{ s}^{-1})^{-1}$); (I) $\bar{\alpha}^*$ ($\text{m}^2 (\text{mg Chl } a)^{-1}$); and (J) Φ_m ($\text{mol C} (\text{mol quanta absorbed})^{-1}$) (colorscapes bottom left).

Figure 5. Environmental (left; A-D) and photosynthetic (right; E-J) variables along the 2011 Chukchi North transect (stations 36-57; boxes A and B in Fig. 1) vs. depth, sampled July 3-7, 2011. Dark grey is ocean bottom; light grey contours show potential density (units: kg m^{-3}); black dots show sample locations. Top left box shows sea ice concentration (0-100%) along transect, top right box shows light penetration to sample depth for depths shown in column below. Environmental variables and units: (A) temperature (Temp., $^{\circ}\text{C}$); (B) nitrate (NO_3 , $\mu\text{mol kg}^{-1}$); (C) chlorophyll *a* (Chl *a*, mg m^{-3}); and (D) particulate organic carbon (POC, $\mu\text{mol L}^{-1}$) (colorscapes below). Photosynthetic variables and units: (E) P_m^* ($\text{mg C mg Chl } a^{-1} \text{ h}^{-1}$); (F) α^* and (H) β^* ($\text{mg C mg Chl } a^{-1} \text{ h}^{-1} (\mu\text{mol quanta m}^{-2} \text{ s}^{-1})^{-1}$); (G) E_k ($\mu\text{mol quanta m}^{-2} \text{ s}^{-1}$); (I) $\bar{\alpha}^*$ ($\text{m}^2 (\text{mg Chl } a)^{-1}$); and (J) Φ_m ($\text{mol C} (\text{mol quanta absorbed})^{-1}$) (colorscapes bottom left).

Fig. 1

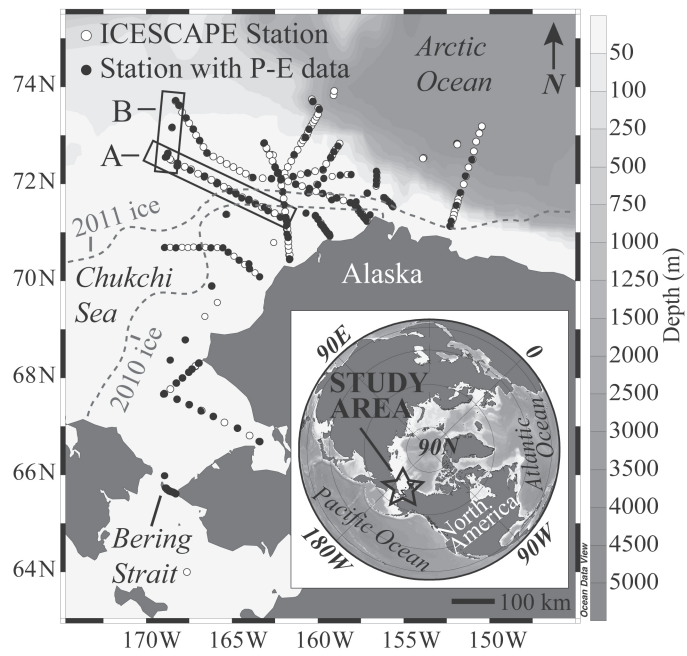


Fig. 2

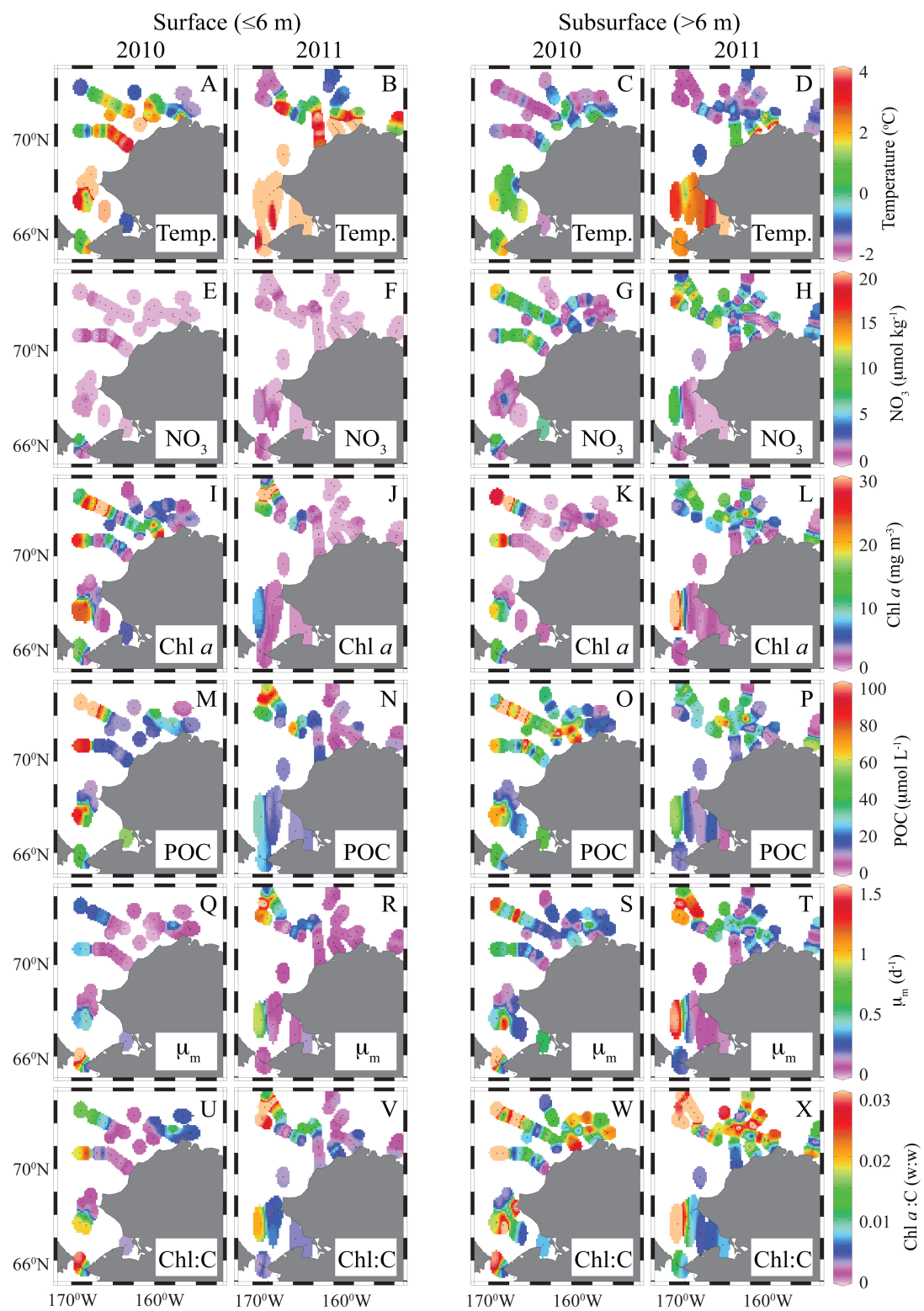


Fig. 3

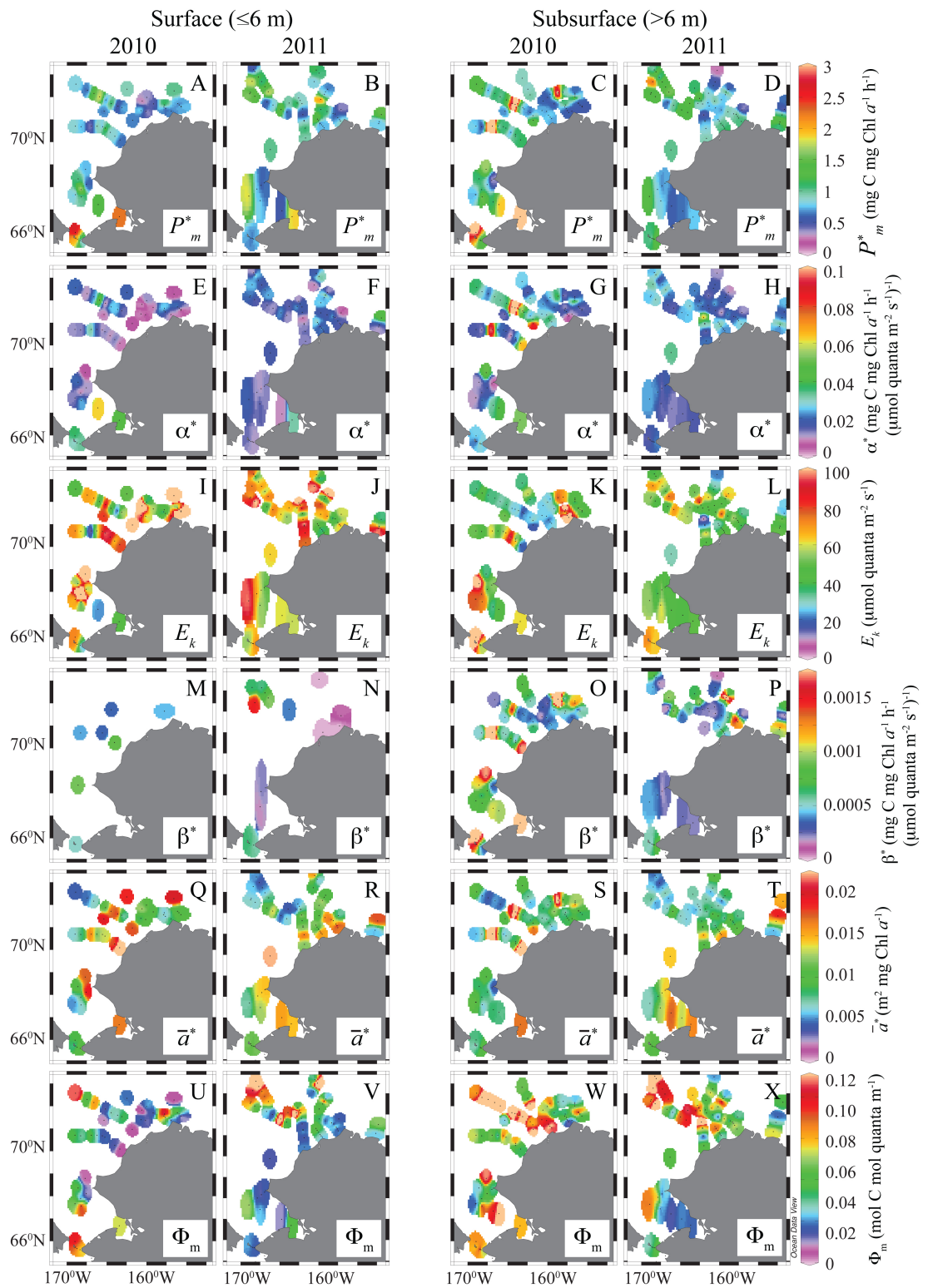


Fig. 4

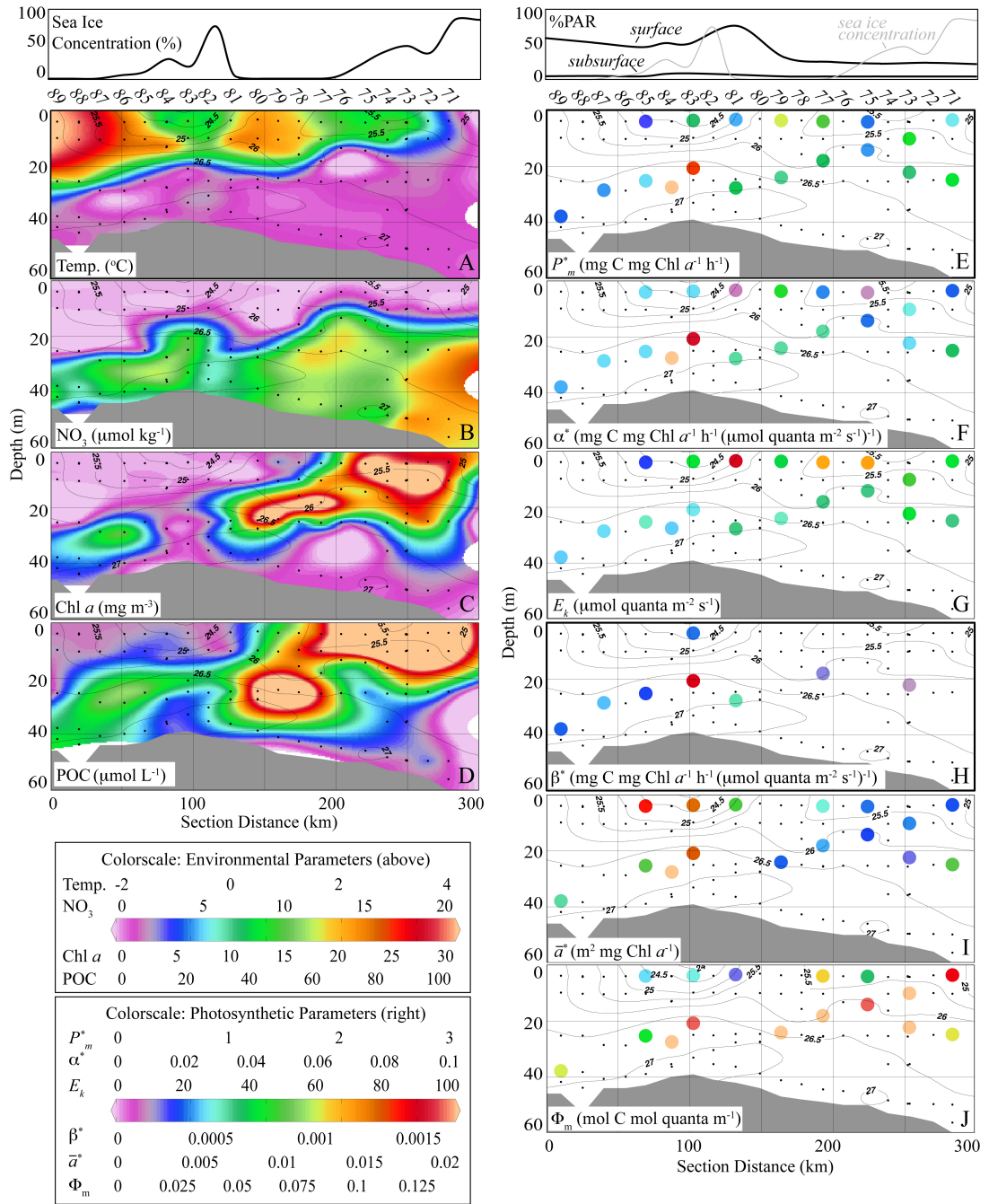
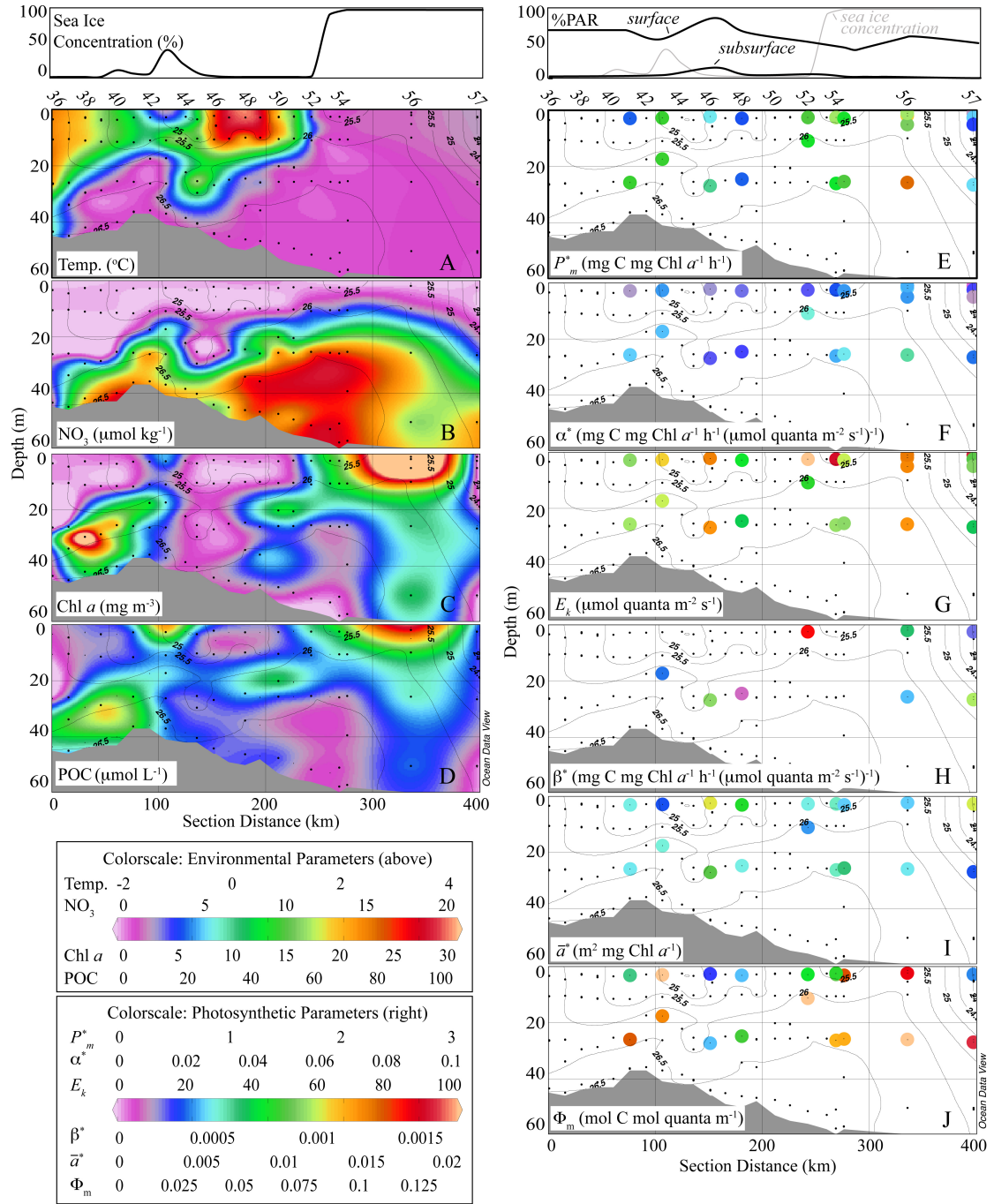


Fig. 5



CHAPTER 4:
MODELING PRIMARY PRODUCTIVITY AND BIOGEOCHEMICAL CARBON
CYCLING IN THE CHUKCHI SEA, ARCTIC OCEAN:
IMPACTS OF SEA ICE RETREAT, THINNING, AND MELT POND
PROLIFERATION ON THE SUMMER PHYTOPLANKTON BLOOM

Modeling primary productivity and biogeochemical carbon cycling in the Chukchi Sea, Arctic Ocean: Impacts of sea ice retreat, thinning, and melt-pond proliferation on the summer phytoplankton bloom

By Molly A. Palmer and Kevin R. Arrigo

Dept. of Environmental Earth System Science, Stanford University

1. Introduction

The Arctic Ocean has undergone unprecedented changes in sea ice extent and thickness in recent decades, including a 30% reduction in the overall extent of the Arctic ice pack (Stroeve et al. 2005; Comiso et al. 2008) and a considerable reduction (>40%) in average ice thickness (Lindsay and Zhang 2005; Kwok and Rothrock 2009). These changes are predicted to affect Arctic marine primary productivity (PP; the photosynthetic fixation of carbon dioxide by tiny algae called phytoplankton) because the timing and intensity of the summer phytoplankton bloom are strongly controlled by the dynamics of sea ice and water column stabilization (Arrigo and van Dijken 2004; Wang et al. 2005; Carmack et al. 2006). Satellite-based estimates indicate that PP in ice-free waters has increased dramatically over the last few decades as a result of the increases in open water area and length of the growing season associated with the thinning ice cover (Pabi et al. 2008; Arrigo et al. 2008; Arrigo and van Dijken 2011).

Furthermore, climate models predict that the Arctic will experience greater and more rapid warming than other areas of the planet over the next century, suggesting that these changes may become even more prevalent in the future, possibly due to complex feedbacks that may accelerate ice loss over time (Loeng et al. 2006; Douglas 2010). Indeed, sea ice loss has accelerated in recent years, culminating in a new record minimum extent reached in September 2012 (the previous record was 2007, which was 42% below the 30-year average), despite average surface air temperatures (NSIDC 2012). In addition, the overall thickness of sea ice has decreased significantly in recent years, with old, stable multiyear ice (MYI) largely replaced by young, brittle

first-year ice (FYI) (Nghiem et al. 2007; Maslanik et al. 2011). Within this pattern of overall Arctic sea ice loss, regional differences have been observed. The Beaufort and Chukchi Seas in particular have exhibited some of the most pronounced losses of sea ice extent and thickness (Meier et al. 2007; Comiso et al. 2008).

In the Pacific sector of the Arctic, which includes the Beaufort and Chukchi Seas, the summer bloom typically begins in surface waters adjacent to the ice edge where melting and retreating sea ice creates a shallow (10-20 m over the continental shelf), stable mixed layer that is conducive for phytoplankton growth (Hill and Cota 2005; Loeng et al. 2006; Perrette et al. 2011). This bloom grows rapidly, fueled by sufficient light and abundant nutrients that have been remineralized either in place or carried in from outside the region during the long winter months (Cota et al. 1996; Codispoti et al. 2005, 2009). As nitrate (NO_3), the primary limiting nutrient, is quickly drawn down to below detection levels in the surface mixed layer during the initial bloom period, phytoplankton eventually congregate in deeper waters adjacent to the nitracline, forming subsurface chlorophyll *a* (Chl *a*) maximum (SCM) layers that may reach high biomass and typically are photosynthetically active (Martin et al. 2010; Palmer et al. 2011; Palmer et al. in prep).

It is traditionally thought that phytoplankton growth in waters beneath the ice is minimal (Grebmeier et al. 1995; Sakshaug 2004) because sea ice and snow strongly reflect and attenuate incoming solar radiation (Perovich 1998; Perovich and Polashenski 2012). However, recent evidence suggests that this pattern of the seasonal cycle of marine PP may be changing as a result of the thinning sea ice cover. In 2011, one of the most intense phytoplankton blooms ever recorded was observed under the sea ice in the Chukchi Sea, over the Chukchi shelf region where bottom depths average 50 m (Arrigo et al. 2012; Arrigo et al. submitted). This bloom, composed primarily of pelagic diatoms of the genera *Thalassiosira*, *Chaetoceros*, and *Fragilariopsis* spp., reached biomass levels of 1291 mg m^{-2} Chl *a* as far as 100 km into the main ice pack under 100% sea ice cover that was 0.8-1.2 m thick (Arrigo et al. 2012). Data indicate that the areas surveyed in open water south of the main ice edge likely had previously experienced an under ice bloom as well (Arrigo et al. submitted;

Palmer et al. in prep). These open water areas were largely characterized by completely depleted NO_3 in the surface layers to 20-30 m, and the presence of an SCM near the nitracline at depths ranging from 20-40 m (Arrigo et al. submitted).

Preliminary efforts towards understanding how and why phytoplankton were able to grow so rapidly and reach such high biomass levels under the ice in 2011 indicate that the thinning sea ice cover may play a role (Frey et al. 2011; Arrigo et al. submitted). The hypothesis is that thinner sea ice, in combination with the increasing abundance of melt ponds on the ice surface, resulted in enhanced light penetration to the underlying water column, exceeding the threshold in light availability needed for shade-adapted Arctic phytoplankton communities to successfully photosynthesize and grow (Arrigo et al. 2012; Arrigo et al. submitted; Palmer et al. in prep). Indeed, it was shown that the ice covered by melt ponds during this study exhibited four-fold more light penetration than the nearby unponded bare ice (Arrigo et al. submitted; Frey et al. 2011; Arrigo et al. 2012). In this scenario, shade-adapted under-ice Arctic phytoplankton are able to achieve high biomass because they maintain relatively modest rates of photosynthesis with ample under-ice nutrients (Palmer et al. in prep). Whether these under-ice blooms developed in this region when they were historically covered by much thicker multi-year ice in the summer (~3-6 m thick), which lets through much less light (e.g., insufficient to surpass the threshold needed for photosynthesis; Frey et al. 2011), is not known.

This phenomenon may not just be restricted to the Chukchi Sea: a recent report that used a remotely operated vehicle to explore light transmission through various sea ice covers all over the Arctic in 2011 confirms that on average, (non-deformed) FYI transmits three-fold more light compared to MYI (0.11 vs. 0.04) largely because of the much higher fraction of melt-ponds (42% vs. 23%) (Nicolaus et al. 2012). The amount of light transmittance through the ice was highly variable depending on ice type (ponded vs. white ice) as well as age, with average transmittances of 0.22 for ponded FYI, 0.04 for white FYI, 0.14 for ponded MYI, and 0.01 for white MYI (Nicolaus et al. 2012). Part of the reason for this increase in transmittance through ponded ice is the lack of the surface scattering layer present on bare ice (which is

highly reflective), and that under melt-ponds, ice is thinner than in adjacent unponded ice (Nicolaus et al. 2012).

Variability in snow depth on sea ice is considered an important factor limiting the initiation of the summer bloom in the Chukchi Sea, as snow itself strongly reflects incoming solar radiation. Grebmeier et al. (1995) describe how early studies of the region showed that variable snow depths accounted for 70-85% of the variance in under ice biomass, and that the loss of snow may increase light penetration by >10-fold. Perovich (1996) confirms this finding, showing that especially in May and June, the distribution of snow types and coverage is critically important in determining light penetration and controlling spatial variability in the under-ice light field. In recent years, late spring snow cover has continued to decline, with a new record low set in 2012 (NSIDC 2012). This decline in snow thickness may also be an important factor contributing to the development of massive under-ice blooms, as the location where these new blooms were observed was in areas where snow historically was much thicker (average of ~0.4 m in the summer, down to little to no snow cover at the time of the bloom in 2011; Frey et al. 2011).

In addition to the enhanced light penetration caused by the thinning/changing snow and ice cover, there are other possible reasons why phytoplankton can now bloom under the ice. First, reduced grazing by zooplankton, which do not grow as rapidly in the cold, under ice waters, may allow the bloom to reach higher biomass levels than when grazing is heavy (e.g., Smith et al. 1988; Grebmeier et al. 1995; Hunt et al. 2011). Second, sea ice strongly attenuates harmful ultraviolet radiation (UVR), which may allow the community to survive better than when blooming in open water (Holm-Hansen et al. 1993; Holm-Hansen 1997; Helbling et al. 2002; Helbling and Villafañe 2002; Leu et al. 2007). Third, reduced competition for nutrients with other members of the microbial loop in cold waters (Anderson 1988; Grebmeier et al. 1995) may allow phytoplankton access to more nutrients and attain greater biomass beneath the ice.

It has been traditionally thought that consumption of PP by microbes and zooplankton in the highly productive Chukchi Sea is a small fraction of that produced

by phytoplankton, resulting in a very rich food source for the benthos and a high rate of export to the deeper Canada Basin (Grebmeier et al. 1995). However, a recent study in the nearby Beaufort Sea showed that microbial activity was not only much higher than predicted based on temperature alone, but also much more complicated than traditionally thought (Kellogg et al. 2011). It appears that the magnitude of marine-produced particulate organic carbon production governs the rate of microbial activity, thus indicating a tightly-linked remineralization loop, as well as suggesting that the microbial community may consume a greater proportion of organic carbon and nitrogen (N) than zooplankton (Kellogg et al. 2011).

Clearly, the complex interactions between thinning sea ice cover, reduced snow levels, greatly enhanced melt-pond coverage, and accelerating rates of ice loss and retreat have resulted in dramatically different light and nutrient dynamics in the under-ice marine habitat. Our goal with this study is to investigate how rapidly changing environmental variables, including sea ice and snow thickness; melt pond formation, persistence, and areal coverage; and changing dates of ice retreat/break-up; interact to initiate and control the magnitude of the spring and summer phytoplankton blooms beneath the sea ice in the Chukchi Sea, Arctic Ocean. To accomplish this, we will utilize a one-dimensional biological model that we have developed to simulate the continental shelf ecosystem of the Chukchi Sea.

2. Background

2.1. Seasonal sea ice, snow, and pond cycle

In the Chukchi Sea, first-year sea ice (FYI) covers most of the region between fall and spring, typically growing from a minimum thickness of 0.5-1.0 m in September to a maximum thickness of 1.5-2.0 m by March-April prior to melt onset (Figs. 1a,b; 2a-e; Perovich et al. 2003). During the melt period, the sea ice field transitions from thick, snow-covered ice to a variable fraction of pond-covered and bare ice, until the ice breaks up (Perovich et al. 2003). Over the summer, the ice edge retreats in a northerly direction over the Chukchi continental shelf, eventually forming a well-defined continuous ice edge that defines the southerly extent of the permanent

central Arctic ice pack (reaching its maximum northerly extent typically by mid to late September) (Maslanik et al. 2011). Sea ice begins to refreeze and grow by October once decreasing solar radiation allows for air and water temperatures to cool, expanding once again in a southerly direction through late winter (Maslanik et al. 2011). Wintertime ice conditions are relatively homogenous, being composed of regular solid floes with some ridging, although leads and cracks often form between land-fast ice adjacent to the Alaskan coastline and the main central Arctic ice pack (Perovich et al. 2003). Historically, multi-year ice (MYI) >4 m thick covered the Chukchi shelf during the entire year, although this has not been the case for at least the last 30 years, as sea ice has begun to retreat and thin at much faster rates (Maslanik et al. 2011).

2.2. Data details for ice and snow inputs

For the model specifications of ice, snow, and ponds, we rely on several data sources as well as general observations from the region (Figs. 1a,b; 2a-e). Below, we detail some of the important aspects needed to model light transmission through the sea ice to the underlying water column, which are needed to accurately simulate the initiation and development of the under-ice phytoplankton bloom.

2.2.1. Ice advance and retreat

The average date and rate of sea ice advance and retreat varies from year to year. In typical seasonal cycle, the ice edge retreats to just past the shelf-break in the Chukchi Sea, at around the 500-m isobath. Ice typically breaks up between 18 June - 18 July, but smaller floes of ridged ice may be present through late July and even into August in the area (Druckenmiller et al. 2009). Models predict that by the end of this century (2090-2099), February-April will remain ice covered while August-October will be ice-free (Douglas 2010). The rate of ice retreat and advance varies in the Beaufort and Chukchi region and does not always follow the same trend as the rest of the Arctic Ocean. For example, the National Snow and Ice Data Center (NSIDC) reports that in October 2012, the rate of ice advance during the re-freeze in the Arctic

as a whole was near record, nearly doubling overall ice extent in the Arctic at an average rate of 121,000 km² per day, but the Chukchi and Beaufort Seas experienced much less growth, at a rate of 8,500 km² per day, with large areas of open water still present (NSIDC 2012).

2.2.2. Temperature and salinity profiles in the ice and snow

Much of the ice surface during winter is covered by snow, and temperatures in both snow and the top of the sea ice surface are very cold and near air temperatures (Perovich et al. 2003). For example, temperatures in dry snow are typically -12°C to -8°C prior to melt, and waters and sea ice under the cover of dry snow are similarly consistently cold, near -2°C in the ocean and -8 to -2°C in the ice. Within the sea ice, temperature changes linearly from roughly near the air temperature at the ice surface to near the ocean temperature (-2°C) at the ice-water interface (Fig. 2e). Salinity in the sea ice is more variable, but typically more saline near the top of the ice and more fresh at the bottom (range: 4-10 psu), depending on whether the ice has drained or not. These properties are important for accurately simulating light transmission through the sea ice and snow, which varies depending on temperature and salinity (Perovich 1990).

2.2.3. Transition periods: dry to wet snow and pond formation

Snow depths in the Chukchi vary considerably also, but data from a decade of observations in Barrow, AK (Druckenmiller et al. 2009; seaice.alaska.edu) indicates that maximum snow depths in April, when we begin our model runs, range from 9-22 inches (22-56 cm). In a typical season, this surface cover of dry snow may transition to wet snow when air temperatures rise above -1°C, although we note that snowfall and drifting/blowing snow make the prediction of this transition difficult. The more significant timing is when substantial amounts of wet snow begin to melt, which typically happens once temperatures are above 0°C. The date of when the melt season officially begins in the Chukchi region (as marked by the transition of dry snow to wet snow) can vary considerably (>1 month), but usually ranges from 11 May to 11 June.

The first stage of the melt season is the transition from sea ice covered in “dry snow” into sea ice covered by “wet snow”. Dry snow is highly reflective (high albedo, >0.7) and thus most incoming solar radiation is reflected at the dry snow-air interface. In contrast, wet snow (as well as bare ice) has a much lower albedo (0.2-0.7) and thus both warms considerably in the days following its transition from dry snow and lets significantly more shortwave radiation through to reach the snow-ice interface (Perovich 1990).

Following at least partial melting of this snow, the second stage of the melt season is the transition from snow-covered ice to sea ice dotted with melt ponds, which typically comprise about 10-50% of the areal coverage of first year ice by early summer (average date for pond formation near Barrow: June 5) (Perovich et al. 2003; Druckenmiller et al. 2009). Melt ponds lack a surface scattering layer and appear dark on the surface of the sea ice, and thus absorb a significant fraction of the incoming solar radiation, promoting warming and melt of ponded sea ice as well as the ocean below (Perovich et al. 2003, Frey et al. 2011).

2.3. Impacts of ultraviolet radiation

The light model employed for this study (described in Methods below) was modified to include scattering and absorption in the UV spectrum using the measured UVR data obtained from Barrow, AK. The impact of ultraviolet radiation (UVR, 280 – 400 nm) on phytoplankton photosynthesis and marine PP has been widely investigated, as UVR has been shown to inhibit the rate of photosynthesis and can severely damage genetic material (de Mora et al. 2000). It has been predicted that UVR, especially the shorter, higher-energy and more damaging UVB (280-320 nm) end of the spectrum, may rise over the next century due to changes in atmospheric ozone concentrations, as ozone typically prevents much of the incoming UVB from reaching the Earth’s surface (Madronich et al. 1998). In recent years, the development of the stratospheric ozone (O₃) hole in the Antarctic, where springtime O₃ depletion resulted in an observed increase in UVR reaching the Earth’s surface, allowed for many in situ and theoretical approaches for estimating the impact of UVR on polar

phytoplankton in the natural marine environment (e.g., Smith et al. 1992, Holm-Hansen et al. 1993; Neale et al. 1998a,b; Arrigo et al. 2003). However, the impacts of this increase in UVR on net marine PP were less profound than predicted, with most studies concluding that the O₃ hole resulted in <2% reduction in marine PP (e.g., Smith et al. 1992; Arrigo 1994; Neale et al. 1998a; Arrigo et al. 2003).

To cope with UVR in the marine environment, phytoplankton can employ various photoprotection strategies, such as by synthesizing compounds that absorb and effectively “screen” algae from the deleterious effects of UVR (for example, microsporine-like amino acids, MAA, which absorb 310-360 nm radiation), and/or actively repair photodamage caused by UVR stress (de Mora et al. 2000). However, phytoplankton community structure may also change in response to enhanced UVR (due to different species-specific coping mechanisms), which may have profound effects on marine biogeochemical cycles, including modifying nutrient pathways and carbon export flux to the benthos (Helbling et al. 1992; Neale et al. 1998a,b; Arrigo et al. 1999; Helbling and Villafañe 2002; Arrigo et al. 2003).

In the Arctic, the largest ozone depletions have occurred in the late winter and early spring, when photosynthesis and phytoplankton growth is minimal (Madronich et al. 1998). Although historically these ozone depletion events in the Arctic have been nowhere near as dramatic as those in the Antarctic, in 2011 for the first time ever an ozone hole on par with the size of the Antarctic minimum in 1985 was observed over the Arctic (Rex 2012). Furthermore, sea ice, particularly when covered with snow, results in a large decrease in the transmission of UVR to the underlying water column (Perovich 1993). As the seasonal pattern in Arctic sea ice continues to change, however, including beginning the melt season much earlier in the year, we may begin to see large-scale changes in both the magnitude and composition of marine PP due to the increase in UVR associated with decreased shielding from sea ice.

Additionally, it has been hypothesized that polar phytoplankton may lack many of the mechanisms needed to cope with enhanced UVR, due to the persistent sea ice cover, low sun-angles, and species-specific differences in UVR response (Helbling et al. 1992; Helbling and Villafañe 2002). For example, some studies suggest that

natural assemblages of Arctic phytoplankton may be more sensitive than those of Antarctic phytoplankton to UVR because Arctic phytoplankton predominantly reside in deeper mixed layers (Helbling and Villafañe 2002). In a comparative study, it was shown that Arctic phytoplankton responded to enhanced UVR over time by shifting species composition to a more resistant, smaller-sized nanoplankton diatom community, whereas Antarctic phytoplankton shifted to microplankton-sized diatoms which are more effective in synthesizing UV-absorbing compounds (Villafañe et al. 1995; Helbling and Villafañe 2002).

For these reasons, we chose to include UVR in the light model, so that we could assess the impact that UVR may have in controlling the development, magnitude, or timing of the under-ice and spring phytoplankton bloom in the Chukchi Sea. Both UVA (320-400 nm) and UVB (280-320 nm) affect phytoplankton photosynthesis, with wavelength-dependent effects being observed, and thus UVR inhibition is often modeled as a function of biologically effective irradiance (e.g., a measure of the weighted impact of wavelength-specific UVR on phytoplankton using a specified action spectrum; Holm-Hansen 1997; Neale et al. 1998b; Neale and Keiber 2000). Although UVB has been shown to be much more damaging to phytoplankton and have a much greater inhibitory effect on growth due to increased sensitivity of phytoplankton, it is attenuated much more quickly in the water column and thus UVA tends to have the greater net effect on photosynthesis when measured in situ (Neale and Kieber 2000). Furthermore, some studies have shown that cells use incident UVA levels to assess and internally regulate their response to UVB, the more damaging form of UVR, which suggests that it is not just the absolute level of UVR that governs the biological response, but the relative amounts of UVA, UVB, and PAR received by each cell (Smith et al. 1992).

In the case where phytoplankton have significant potential for repair to counteract UV damage, instantaneous models are the best choice to use for modeling the impacts of UVR on phytoplankton growth, whereas cumulative exposure models are better suited for phytoplankton with weak repair mechanisms (such that photosynthesis is effectively inhibited throughout the entire daily cycle upon reaching

a specified threshold in UVR dosage) (Neale et al. 1998b; Neale and Kieber 2000; Neale et al. 2001). Leu et al. (2007) showed that cultures of three common diatoms found in the Arctic (*Thalassiosira borealis*, *Chaetoceros socialis*, and *Bacterosira bathyomphala*) decreased in biomass and photosynthetic efficiency under UV exposures similar in magnitude to the amount of UVR experienced in the spring bloom (compared to those where UV was shielded), but algal nutritional quality (stoichiometry of carbon, C, N, and phosphorous, P) did not change significantly. In fact, they observed a 90% reduction in the quantum yield of photosynthesis after 8 h of daily exposure to UV, but all species showed substantial recovery between periods of UV exposure (Leu et al. 2007).

Thus, to model this response to UVR exposure in the Arctic spring bloom, we chose a method for representing UVR inhibition of phytoplankton growth that uses a biological weighting function (BWF) for instantaneous UVR exposure at each time step, with no change in C:N:P stoichiometry. The BWF formulation can have a large impact on the predicted biological effects, as overall sensitivity to UV inhibition varies between and among populations from diverse environments (Neale et al. 1998b; Neale and Kieber 2000). UVR inhibition of photosynthesis can also be achieved by relating the cumulative effect of UV dose to the weighted exposure, such that inhibition is greatest in the early parts of the day and stabilizes to a new, lower steady state later in the day (as is consistent with complete lack of repair processes) (as in Neale et al. 1998b).

2.4. Phytoplankton in the Chukchi and Beaufort Seas

In this region, the large phytoplankton functional group, comprised of primarily of large microplankton (mostly centric diatoms such as *Thalassiosira* and *Chaetoceros* spp.), have been shown to dominate over the shelf region, especially in the under-ice bloom and at the ice-edge subsurface chlorophyll *a* maximum (SCM) (Gosselin et al. 1997; Sakshaug 2004; Hill et al. 2005; Arrigo et al. 2012). The large size (>5 μm) has been shown to contribute >50% to total primary production, and accounts for most of the biomass and contributes substantially to carbon export during

the spring bloom (Hill et al. 2005; Hill and Cota 2005). Under-ice pre-bloom and open water post-bloom and SCM areas tend to be dominated by smaller (0.7-5 μm) algal cells, mainly dinoflagellates and flagellates (Gosselin et al. 1997), consistent with post-bloom community structure and indicative of regenerated production (Hill and Cota 2005). These smaller producers increase in abundance as the season wears on (Cota et al. 1996), and thus can contribute substantially and play an important role in the seasonal cycle of primary production. Other phytoplankton functional types, including nitrogen fixers and *Phaeocystis*, are not typically found in the Chukchi region, and are not included in the model. In the Chukchi Sea, N is the predominant limiting nutrient and controls algal growth, which is why we focus on it in this model (e.g., Sakshaug 2004; Hill and Cota 2005; Arrigo et al. 2012).

2.5. *Bacteria in the Chukchi and Beaufort Seas*

In the Arctic Ocean, bacterial abundance tends to be highest near the sediment-ocean interface and at the mouth of rivers, where high DOC can fuel production, but bacteria have also been found to be associated with autotrophic production (Parsons et al. 1988). Furthermore, bacterial communities appear to be very active in the Arctic Ocean, utilizing *in situ* primary productivity nearly as rapidly as at low latitudes (Cota et al. 1996; Kellogg et al. 2011). However, as very little published data currently exists for bacterial production or abundance in the Chukchi Sea, we keep the bacterial pool simple as one main group that represents all of the major players in the microbial loop.

3. Methods

Sea ice, snow, and pond development are all explicitly specified based on data measured during the Surface Heat Budget of the Arctic Ocean (SHEBA) campaign (Perovich et al. 2003), with inputs from other large databases (including long term measurements from 1972-1992 made in the Beaufort Sea by Environment Canada; Lindsay 2010) and modifications from the 2010-2011 ICESCAPE cruise (Frey et al. 2011; Arrigo et al. submitted). A spectral atmospheric radiative transfer model (Gregg

and Carder 1990, as modified by Arrigo et al. 1998a) is used to calculate surface fluxes of both UVR and PAR (400-700 nm). This light is then propagated through the ice, snow, or water based on the two-stream multiple-scattering radiative transfer Delta-Eddington model as modified by Saenz (2011). The biological model used here is loosely based on the ecosystem model for the Ross Sea, Antarctica described in Arrigo et al. (2003) and modified for N-based currency as in Fasham et al. (1990). It includes explicit representations of zooplankton grazing, and bacterial-mediated remineralization. We do not consider ice-algal-based PP, as our primary goal here is to model the under-ice bloom and also because sea ice algae likely account for a very small (<3%) amount of total primary production in the Chukchi Sea (Gosselin et al. 1997).

3.1. Model Domain

The 1-D model is designed to simulate a 50 m deep water column (1 m vertical resolution) at 72°N, 169°W in the Chukchi Sea. Sea ice, snow, and melt pond coverage overlying the water column are represented by a maximum of 10 vertical layers of varying thicknesses (described below), with the minimum thickness of any layer set at 0.02 m.

3.2. Model inputs

Sea ice, snow, and pond development are all explicitly specified based on the data collected in several large databases of measurements for the Chukchi and Beaufort Seas. For the main model runs (Table 1), sea ice and snow thicknesses and seasonal evolution are based on both measurements from the 1972-1992 dataset published for the nearby Beaufort Sea (Fig. 1a, 1b; Lindsay 2010; online at http://psc.apl.washington.edu/sea_ice_cdr/data_tables.html) and data collected during the SHEBA campaign (Perovich et al. 2003; data online at http://data.eol.ucar.edu/codiac_data/sheba/data/perovich/ICEWEB/).

Pond data and sea ice evolution was approximated following the patterns presented in Perovich 1990 (Fig. 1c) and Perovich et al. 2003 (Fig. 1d).

Supplementary data showing how the transition periods of air temperature, snow cover, and ice thicknesses were determined is shown in Figs. 2a-2b (from the recently measured data from Barrow, AK; Druckenmiller et al. 2009). Specific details for the multi-year ice (MYI) run and an example of the snow-pond-ice seasonal evolution in first-year ice (FYI) are shown in Figs. 2c-2d (Pervoich et al. 2003), and Fig. 2e shows the evolution of air temperatures compared to ice temperatures used for model input.

The full seasonal cycle for snow, ponds, and ice for the all model runs is shown in Fig. 3. The seasonal evolution of snow, ponds, and sea ice does not impact model water column physics or volume (i.e., the model does not conserve water and salt mass balance), but seawater temperature and salinity in the 1-D water column do change throughout the season in a pattern and at rates consistent with ice/snow/pond melt and observations of the region. The magnitude and timescale for changes in modeled water column temperature and salinity were prescribed based on data from the Chukchi Sea (collected during the ICESCAPE program, data online at <http://ocean.stanford.edu/icescape>).

The timing of sea ice retreat was specified based on satellite and in situ observations. We assumed that sea ice was at its peak thickness by the time of model initiation (April 15). Starting from this initial thickness, sea ice is modeled to decrease at a linear rate using an approximation of the rates given in Perovich et al. (2003) from the SHEBA study. Detailed data for the main model runs for ice thickness, snow thickness, and pond development are given in Table 1 and shown in Figure 3.

Nutrients were initialized based on the annual climatology presented in Codispoti et al. (2005) and (2009) from the Shelf-Basin Interactions (SBI) program. Biological parameters were initialized based on observations from the SBI program, the ICESCAPE program (Arrigo et al. 2012, Arrigo et al. submitted, Palmer et al. in prep), and from the literature (e.g., Fasham et al. 1990, etc.).

Temperature is specified to remain at a constant -1.9°C when ice cover is present, and gradually warms to 5°C in the top 10 m and 3°C in the 10-20 m depth interval through August and September as is observed in the region.

3.3. Solar irradiance and radiative transfer model

3.3.1. Solar irradiance: ultraviolet radiation data

Spectral UV data were obtained from the National Science Foundation (NSF) Polar Programs UV Monitoring Network in Barrow, AK (71°19'N, 156°41'W) for the year 2003 (online at <http://uv.biospherical.com/Version2/data.asp>; reference: Bernhard et al. 2007). The year 2003 was chosen to be representative of the solar cycle for a typical year in the Arctic. The NSF monitoring program collects continuous (quarterly-hour) spectral irradiance data from 280-600 nm using a Biospherical Instruments SUV-100 spectroradiometer at a resolution of 1 nm (reported average uncertainty: 0.7% at 330 nm). Calibrations and data pre-processing were done as described in Bernhard et al. (2007). These data were binned into 16 separate wavelengths to match to the spectral absorption coefficients obtained for water by Segelstein (1981) and Lu (2006) and for ice by Perovich and Govoni (1991). UV spectra were then integrated from 280-400 nm (Fig. 4a) and converted from units of mW cm^{-2} to $\text{mEin m}^{-2} \text{s}^{-1}$ using Planck's equation for energy in each wavelength.

3.3.2. Solar irradiance: atmospheric radiative transfer model

The atmospheric radiative transfer model used here is based on the clear-sky model of Gregg and Carder (1990), which uses atmospheric inputs (including extraterrestrial irradiance; atmospheric path length; Rayleigh scattering; ozone, oxygen, and water vapor absorption; aerosol scattering and absorption, etc.) obtained from the daily mean products provided by the National Centers for Environmental Prediction/National Center for Atmospheric Research (NCEP/NCAR) Reanalysis Project 2 and TOMS ozone concentration as described in Arrigo et al. (2003). This provides direct and diffuse spectral downwelling solar irradiance to the sea ice, snow, or water column surface, and is assumed to be uniform across the top of the layer. The model is corrected for scattering by clouds as in McClain et al. (1996) and spectral irradiance is binned into 31 wavelengths at 10 nm increments between 400 and 700 nm (modeled daily PAR for the year 2003 is shown in Fig. 4a). The annual cycle of daily surface PAR (integrated from 400-700nm) is shown in Fig. 4b. One additional

band represents the solar energy outside the PAR band (700-2000 nm), and UVR data were similarly binned into the 16 wavelengths described in section 3.4.1.

3.3.3. Solar irradiance: sea ice, snow, and water radiative transfer model

The sea ice radiative transfer model employed in this study is based on the two-stream spectral (upwelling and downwelling) radiative transfer model of Briegleb and Light (2007) as modified by Saenz (2011), which uses the Delta-Eddington approximation for scattering to account for multiple scattering effects on direct and diffuse radiation. This model takes in the diffuse and direct surface atmospheric irradiance calculated in the atmospheric radiative transfer model described in section 3.3.2.

To represent the sea ice and snow layers in our model, five categories were chosen: wet (old) snow, dry (new) snow, drained surface ice, regular sea ice, and water (Table 2). Five was found in a previous study to be the minimum number of categories required to accurately simulate radiative transfer through the sea ice (Saenz 2011). The spectrally-dependent inherent optical properties for the five snow and sea ice categories were prescribed based on published absorption and scattering coefficients, and they vary in each model layer of snow or ice depending on the temperature, salinity, density, and algal or detrital content of the ice (Briegleb and Light 2007; the development of this method, testing, and validation are described in Saenz 2011). In the main model runs, multiyear ice and ice with ponds above contain no drained ice layer; this layer is only present in first-year ice. Typically, the drained ice layer has a very high scattering coefficient, and comprises 4-10% of the total ice thickness (Perovich 1990). For the simplicity of this model, the thickness of the scattering layer is constrained within this range and decreases with total ice thickness.

To account for the heterogeneity in snow cover, modeled snow thickness was assumed to be log-normally distributed (Arrigo et al. 1998b), with the mean specified snow depth divided into nine different snow depth categories (representing 1/9 of a hypothetical grid cell, which is then averaged for the 1-D grid cell). Furthermore, dry snow is considered pure, and contains no brine, salt, algae, or detritus.

Finally, to account for variable melt-pond coverage on ice, we model the light transmission as the weighted average of the amount of light that would pass through the specified percentage of pond-covered ice times the amount of light that would pass through 100% bare ice cover. No ice or brine thermodynamics or physics are including in the model. Sea ice algae were arbitrarily assumed to be negligible for the purposes of radiative transfer through the ice. However, we included a detrital layer of ~2 cm thick in the bottom-most ice layer to represent accumulation of particulate material in the sea ice (either from algae or elsewhere).

Light that passes through the snow and ice layers is then propagated through the underlying ocean using the same method, with the category type set to water for the entire profile, i.e., using the same Delta-Eddington approach and absorption and scattering coefficients for seawater, plus the absorption by phytoplankton and detritus based on the amount of chlorophyll, detritus, and CDOM present in the water column.

3.4. Computation and time stepping

All components of the model were written in the FORTRAN 95 programming language, except parts of the Delta-Eddington radiative transfer model that were coded in C, and run on the server at Stanford University (icy.stanford.edu). The model time step is 15 min. The radiative transfer model is calculated at each time step and light is assumed to be constant over the 15-min period.

3.5. Biological response to UVR

Since it has been observed that Arctic phytoplankton may be able to repair UV damage either during the lower period of UV exposure during the daily cycle, and/or during deep mixing (e.g., because of a deep mixed layer; Helbling and Villafaña 2002; Leu et al. 2007), we chose to employ the instantaneous method here, as described in Cullen et al. (1992), Cullen and Neale (1997), and Neale and Kieber (2000).

In this method, spectral UV(λ) at each time step is weighted by the wavelength-specific sensitivity to UVR exposure (Table 2; BWF, ϵ in units reciprocal ($\mu\text{Ein m}^{-2} \text{s}^{-1}$)⁻¹) as:

$$E_{inh}^* = \bar{\epsilon}_{PAR} E_{PAR} + \sum_{\lambda=280\text{ nm}}^{400\text{ nm}} \epsilon(\lambda) E(\lambda) \Delta\lambda$$

where $\bar{\epsilon}_{PAR}$ (in units $(\mu\text{Ein m}^{-2} \text{s}^{-1})^{-1}$) is the BWF for inhibition of growth (and/or damage to photosynthesis) by PAR (E_{PAR}) and $\epsilon(\lambda)$ is the wavelength-dependent biological efficiency for damage to photosynthesis by UVR. As in Cullen et al. (1992), Neale et al. 2001, and Neale and Kieber (2000), however, we set $\bar{\epsilon}_{PAR}$ equal to zero, as this is otherwise included in the photoinhibition term E_k (see below).

Photosynthesis at each time step is modified using the weighting function, E_{inh}^* , as in Cullen et al. (1992):

$$P_{tot} = P_{pot} \left(\frac{1}{1 + E_{inh}^*} \right)$$

where P_{tot} is the actual realized rate of photosynthesis, and P_{pot} is the potential rate after calculating the other limitation terms. In this sense, the instantaneous UV dose essentially scales the nutrient- and light-limited growth rate of phytoplankton that would otherwise be realized at each time step as described below. Thus, below we scale photosynthesis by $[1/(1+E_{inh}^*)]$ as:

$$UVR_{lim} = \left(\frac{1}{1 + E_{inh}^*} \right)$$

to simulate the impact of UVR on phytoplankton photosynthesis.

3.6. Biological Model

The N-based biological model includes two phytoplankton groups, two zooplankton groups, bacteria, inorganic N, and dissolved organic N (DON) and particulate N (in detritus) pools. The model is modified for the Chukchi Sea from previous models of the Ross Sea, Antarctic (Arrigo et al. 2003) and the widely-used N model of Fasham et al. (1990). Phytoplankton and zooplankton have been modeled to represent the major functional types (producers and consumers) for this region as determined from field studies (discussed below), and are divided into large and small size-based functional groups.

We use minimum thresholds for all uptake terms so that no state variable can drop below $\sim 0.001 \text{ mmol N m}^{-3}$. Limitation of growth in the model is calculated such that one functional group can be favored over others (such as being able to consume nutrients at a slightly lower threshold, or assimilating more food into growth per feeding session). In this sense, adaptation and acclimation are taken into account in the model (e.g., Fasham et al. 1990). The main state variables and fluxes and flows are shown in Fig. 7, and described in detail below.

All state variables diffuse slowly at each time step, which is not shown in each equation below for simplicity. Diffusion in the model is calculated based on Fick's law as:

$$\frac{dC_i}{dt} = D \left(\frac{C_{i+1} - 2C_i + C_{i-1}}{\Delta x^2} \right)$$

where C_i is the concentration of each state variable in vertical grid cell i , x is the length scale of each grid cell (specified as 1 m here), and D is a constant vertical water column diffusivity, D , of $0.11 \times 10^{-4} \text{ m}^2 \text{ s}^{-1}$ (note: we use no-flux boundaries at the top and bottom) (Law et al. 2003). This chosen value for K_z represents the cumulative effect of all turbulent mixing processes in the surface ocean mixed layer over each model time step, and has been shown to be a robust parameterization for representing upper ocean exchange and biogeochemical cycling (although we do note that in reality, K_z can vary substantially with depth; Law et al. 2003). This simple representation of diffusion was chosen because it has been shown to successfully reflect the impact of vertical diffusion on nutrient supply and carbon transport in the surface mixed layer, which can be a significant pathway for nutrient supply and support a significant amount of new production in polar regions (Law et al. 2003).

Sinking is modeled based on Arrigo et al. (2003), where the vertical sinking flux of particulate matter (in this case, only the two phytoplankton groups and detritus, as zooplankton are assumed to be sufficiently motile to escape sinking processes) is calculated at the bottom of each grid cell based on the vertical sinking flux into the top of that grid cell and the concentration gradient of the tracer within that grid cell. The chosen sinking velocities, w_P and w_D , are based on measurements for particles in polar

regions, which were tested within the model to verify that they realistically captured the observations made during recent field programs (e.g., SHEBA and ICESCAPE).

3.6.1. Phytoplankton

Phytoplankton growth (G , d^{-1}) at time t and depth z is determined by the amount of available light and nutrients and possible inhibition by UVR such that

$$G_i(z, t) = G_{max}(z, t) R_{lim}(z, t) UVR_{lim}(z, t)$$

where i is the phytoplankton group (small or large), R_{lim} is the resource (light or nutrients) limitation term, $UVR_{lim}(z, t)$ is the UVR inhibition term, and

$$G_{max}(z, t) = G_o \exp[r_o T(z)]$$

where G_o is the phytoplankton specific growth rate at 0°C (varies for each phytoplankton group, see Table 3) and r_o is a rate constant that determines the sensitivity of G_{max} to the temperature (T) at that depth (Eppley 1972 as described in Arrigo et al. 1998).

R_{lim} for each phytoplankton size class and bacteria were calculated as the minimum of $N_{lim}(z, t)$ and $L_{lim}(z, t)$:

$$R_{lim}(z, t) = \min[N_{lim}(z, t), L_{lim}(z, t)].$$

N_{lim} for each group depends on the nutrient concentration and the half saturation constant for growth on that nutrient. Two forms of N are available (NO_3 and NH_4) and both are considered when calculating N_{lim} (modified from McClain et al. 1996 to be additive):

$$N_{lim} = \text{NH}_{4lim} + \text{NO}_{3lim}$$

$$\text{NH}_{4lim} = \frac{\text{NH}_4}{K_{\text{NH}_4} + \text{NH}_4}$$

$$\text{NO}_{3lim} = \frac{\text{NO}_3}{K_{\text{NO}_3} + \text{NO}_3} \frac{1}{1 + \text{NH}_4/K_{\text{NH}_4}}$$

The NH_4 limitation term is in the Monod form (Monod 1942), where K_{NH_4} is the half saturation constant, representing the concentration of NH_4 where growth rate is half maximal (values for K in Table 3). The NO_3 limitation term is similar to the NH_4 term, with K_{NO_3} (Table 3) representing the half-saturation constant for algal growth on NO_3 , except the right includes a term to represent the inhibition of NO_3 uptake by the

more easily assimilated NH_4 (scaled this way to make the nutrient limitation term dimensionless, varying between 0 and 1, as described in Fennel et al. 2006). Values for the half-saturation constants for each group, as well as growth constants, were chosen so that smaller phytoplankton are better at taking up nutrients of either type at low concentrations (due to lower surface area-to-volume ratios), whereas large phytoplankton can grow faster when nutrients are high (as has been observed in the Arctic; Sakshaug 2004).

$L_{lim}(z, t)$ is modeled as in Arrigo et al. (1998) such that

$$L_{lim}(z, t) = 1 - \exp\left(-\frac{PUR(z, t)}{E'_k(z, t)}\right)$$

where $PUR(z, t)$ is the photosynthetically usable radiation at each depth and time step calculated from the radiative transfer model, and E'_k is the photoacclimation parameter (see Table 3 for values for small and large phytoplankton functional groups). E'_k is allowed to vary as a function of light history as described by Arrigo et al. (1998). E'_k is calculated as the maximum rate of photosynthesis (P_m^*) divided by the initial slope of the photosynthesis-irradiance curve (α^*) (Platt et al. 1980) (see Table 3 for values for small and large phytoplankton functional groups). We use published values for P_m^* , α^* , and E'_k from Arrigo et al. submitted and Palmer et al. in prep).

PUR is calculated from the downwelling spectral irradiance and the absorption characteristics of the phytoplankton (Arrigo et al. 1998):

$$PUR(z, t) = \int_{\lambda=400}^{700} E_d(\lambda, z, t) \frac{a_{ph}^*(\lambda)}{a_{max}^*} d\lambda$$

where a_{max}^* is the maximum value of the phytoplankton absorption spectrum (a_{ph}^*) between 400 and 700 nm (Fig. 6) and $E_d(\lambda, z, t)$ is the downwelling spectral irradiance at depth z and time t .

Partitioning growth between large and small phytoplankton is important because food webs dominated by smaller phytoplankton recycle nutrients more efficiently, retaining a high level of inorganic nitrogen in the euphotic zone, whereas large phytoplankton tend to sink more rapidly, thus removing N from the system. Furthermore, different rate- and abundance-controlled loss processes affect the

different size classes in different ways. Phytoplankton loss terms include death (*mort*), whereby a constant fraction of the phytoplankton population enters the detrital pool as particulate organic N (PON) at each time step. Phytoplankton can also sink at each time step at the rate w_P ; here we use a standard rate of 0.1 m d^{-1} .

Phytoplankton abundance is also controlled by zooplankton grazing, with small phytoplankton serving as the primary food source for small zooplankton and large phytoplankton being consumed by large zooplankton.

With these processes included, the full equations for small (*Sphy*) and large (*Lphy*) phytoplankton are:

$$\frac{dSphy}{dt} = (G_{sphy} - mort_{sphy})Sphy - (g_{szoo-sphy})SZOO - w_P\left(\frac{\partial Sphy}{\partial z}\right)$$

$$\frac{dLphy}{dt} = (G_{lphy} - mort_{lphy})Lphy - (g_{lzoo-lphy})LZOO - w_P\left(\frac{\partial Lphy}{\partial z}\right)$$

3.6.2. Bacteria

The main role of bacteria in the model is to remineralize N; in the ocean, this is typically accomplished through attachment on particles (see Kellogg et al. 2011 for a description of this in the nearby Beaufort Sea), which are broken down through extracellular enzymatic activity into dissolved organic N (DON) that can be readily regenerated into NH_4 . Bacteria often must supplement the carbon-rich organic matter source with NH_4 in order to balance metabolic needs (see Fasham et al. 1990). For the sake of simplicity, as well as to account for the fraction of DON that is labile (i.e., that which bacteria can consume), a constant fraction of the PON pool (r_{det}) enters the DON pool each time step and becomes available for bacteria to consume (Fasham et al. 1990).

The rate of change in bacteria is then calculated as described in Fasham et al. (1990):

$$\frac{dBact}{dt} = (G_{Bact} - ex_{Bact} - mort_{Bact})Bact - (g_{szoo-bact})SZOO$$

where G_{Bact} is the bacterial growth rate, ex_{Bact} and $mort_{Bact}$ are the excretion rate and death rate (d^{-1}), respectively, both of which are constant fractions of the bacterial population at each time step, and $g_{szoo-bact}$ represents consumption of bacteria by small zooplankton (*Szoo*).

3.6.3. Zooplankton

In the Chukchi Sea, smaller proto-zooplankton (5-200 μm) such as heterotrophic ciliates and flagellates graze preferentially on small phytoplankton and bacteria, and their ingestion rates are closely tied to growth rates of their prey (Sakshaug 2004). Numerically, these smaller zooplankton, which also includes smaller omnivorous calanoid species, typically dominate the zooplankton community (Parsons et al. 1988). However, large carnivorous meso-zooplankton (>2 mm), primarily of the calanoid spp., play an important role in the ecosystem (Gosselin et al. 1997) as they graze large phytoplankton and smaller zooplankton, and are consumed by larger organisms like fish. They also contribute significantly to export flux, as they produce large and fast-sinking fecal pellets, although in this model that component is part of the detrital pool (Kellogg et al. 2011).

Based on these observations, two zooplankton functional types are included in the model, representing small (*Szoo*) and large zooplankton (*Lzoo*). Their rates of change are calculated as in Fasham et al. (1990):

$$\frac{dSzoo}{dt} = \gamma(g_{szoo-bact} + g_{szoo-sphy})Szoo - (mort_{szoo} + ex_{szoo} + mt_{szoo})Szoo - (g_{lzoo-szoo})Lzoo$$

$$\frac{dLzoo}{dt} = \gamma(g_{lzoo-lphy} + g_{lzoo-szoo})Lzoo - (mort_{lzoo} + ex_{lzoo} + mt_{lzoo})Lzoo$$

where g is the grazing rate (on bacteria, small phytoplankton, or large phytoplankton), $mort$ is the mortality rate, ex is the excretion rate, and mt is the rate of N loss during basal metabolism. Zooplankton are assumed to be sufficiently motile to escape the basic slow sinking processes included in the model, and losses to higher trophic levels

or out of the model (such as by swimming) are implicitly included as part of the mortality and loss terms.

3.6.4. Particulate and dissolved organic pools

The detrital pool includes all forms of non-living PON in the ecosystem. In reality, this pool would consist of particles of many sizes, ranging from fecal pellets to dead plankton. Although some fraction of recalcitrant PON would be present, for the sake of simplicity, we ignore this pool, assuming it to be inaccessible by bacteria. Instead, we model detritus as single pool and assume a constant fraction, r_{det} , is converted (via remineralization) to DON each time step. Detrital PON can also sink between layers at a rate of w_D , 1 m d^{-1} . The rate of change of the detrital pool at each time step is:

$$\begin{aligned} \frac{dDetr}{dt} = & (mort_{szoo})Szoo + (mort_{lzoo})Lzoo + (mort_{sphy})Sphy \\ & + (mort_{lphy})Lphy + (mort_{Bact})Bact + (1 - \gamma)(g_{szoo-bact} + g_{szoo-sphy})Szoo \\ & + (1 - \gamma)(g_{lzoo-lphy} + g_{lzoo-szoo})Lzoo - r_{det}Detr - w_D\left(\frac{\partial Detr}{\partial z}\right) \end{aligned}$$

Inputs to the DON pool include the fraction of excreted N by zooplankton not converted to NH_4 and the fraction of detritus remineralized to DON at each time step. Losses of DON include remineralization to NH_4 , and uptake by bacteria. The rate of change in DON is:

$$\begin{aligned} \frac{dDON}{dt} = & (1 - z_{\text{NH}_4\text{ex}})(ex_{szoo}Szoo + ex_{lzoo}Lzoo) + r_{det}Detr - r_{DON}DON \\ & - G_{Bact}DON_{limB}Bact \end{aligned}$$

3.6.5. Inorganic N pools

The model includes both NO_3 and NH_4 , which are the most abundant components of the DIN pool (Codispoti et al. 2005). Nutrient regeneration *in situ* was once thought to be insignificant in the region, and although N (particularly NO_3) is

still largely believed to be the most important limiting nutrient in the region, regeneration of NH_4 has been observed in the upper mixed layer in late summer (Cota et al. 1996; Kellogg et al. 2011). Both NO_3 and NH_4 are thus included in the model. We do not include other inorganic nutrients, as phosphate and silicate were not shown to be limiting in field studies from the Chukchi Sea (Arrigo et al. 2012). We assume that production of NO_3 via nitrification is negligible. Losses to the NO_3 pool include the amount taken up by both phytoplankton groups during growth. The rate of change in NO_3 is:

$$\frac{d\text{NO}_3}{dt} = -G_{\text{SPhy}}\text{Sphy} - G_{\text{Lphy}}\text{Lphy}$$

NH_4 is produced through both remineralization and excretion, and is removed by growth of both phytoplankton groups and bacteria. We also note that this pool represents all forms of regenerated N, included urea, that are not explicitly represented in the model (as in Fasham et al. 1990). The rate of change in NH_4 is:

$$\begin{aligned} \frac{d\text{NH}_4}{dt} = & (ex_{\text{Bact}})\text{Bact} + z_{\text{NH}_4\text{ex}}(ex_{\text{szoo}}\text{Szoo} + ex_{\text{lzoo}}\text{Lzoo}) + eg_{\text{szoo}}\text{Szoo} \\ & + eg_{\text{lzoo}}\text{Lzoo} + r_{\text{DON}}\text{DON} - G_{\text{Bact}}\text{NH}_{4\text{limB}}\text{Bact} - G_{\text{SPhy}}\text{Sphy} - G_{\text{Lphy}}\text{Lphy} \end{aligned}$$

4. Results and discussion

4.1. Standard model run

4.1.1. Ice, snow, and melt pond cycle

In mid-April, sea ice is 1.6 m thick and covered by cold, dry snow that is 0.32 m thick (Table 1, Fig. 3). Snow begins to melt on May 19, when the air temperature rises above the critical -1°C threshold, transforming the dry snow to wet snow. Snow thickness declines at an approximately linear rate from 0.32 m on May 19 to 0.11 m by June 13, and eventually disappears by June 28. The sea ice melt period begins once the snow cover has melted. Sea ice thickness decreases at an approximately linear rate from 1.6 m on June 13 to 1.1 m on July 18 when the ice breaks up. Melt ponds begin to form on the ice surface once the snow cover has disappeared and the ice has begun to melt. Pond depth increases from 0 m on June 28 to 0.3 m by July 18,

the day of ice break-up. The standard run for which all other runs will be compared consists of this seasonal ice, snow, and pond cycle with 30% pond coverage.

4.1.2. Light transmittance

Light transmission through the sea ice (Fig. 8) compares well to measurements made under similar ice conditions (e.g., comparable ice, snow and pond thicknesses and ice types, as well as similar incident surface irradiances) during the 2011 ICESCAPE project (Table 5). In the bare ice runs (light blue: modeled, compared to measured values shown in dark green and dark blue), PAR under the ice cover decreases exponentially from near $100 \mu\text{Ein m}^{-2} \text{ s}^{-1}$ in the first few meters under the ice to near zero by 10 m. Thinner bare ice (dark blue, 1.0 m) lets through slightly more light than thicker bare ice (light blue, 1.2 m), and the transmission through bare ice is similar to that in thicker ice, as both ice thicknesses are the same (1.2 m). The transmittance through bare ice on June 27, just before pond formation begins, is 6.83% (Table 5). This compares well with the results measured in Nicolaus et al. (2012) for first-year ice in the region, which show that on average non-deformed bare FYI transmits 4% of the incident surface irradiance, as well as the transmittances measured in ICESCAPE, in which 12.7-17.5% of incident surface light was transmitted to the water column below bare ice (Arrigo et al. submitted). Furthermore, Ehn et al. (2011) report transmittances of 5-16% beneath white bare ice in the nearby Canadian Arctic, similar to the range simulated by our model.

For these ponded ice runs, downwelling PAR in the first few meters under the sea ice is $\sim 300 \mu\text{Ein m}^{-2} \text{ s}^{-1}$ (Fig. 8), which is within 25% of values measured during ICESCAPE, which was closer to $400 \mu\text{Ein m}^{-2} \text{ s}^{-1}$ (dark red, ice 1.0 m thick; dark purple, ice 1.2 m thick; both have roughly 25% pond coverage, with ponds varying from 10-30 cm thick). This agreement is encouraging, considering the spatial variability in sea ice cover, including varying thicknesses of ice and ponds and heterogeneity in ice properties. This has been suggested by Frey et al. (2011) as an important aspect controlling light distribution under spatially variable ice cover (e.g., ponded and bare ice), since although light transmission through the different ice

covers to the top 1-2 m of the water column under the ice may vary 4-fold, as simulated in our model (Fig. 8) and observed in field studies, the transmission through ponded and bare ice cover converges to roughly the same pattern and magnitude of light by ~10 m under the ice cover. Indeed, we see this same pattern in both the modeled and measured PAR transmittances (Fig. 8) in which little to no light penetrates past 10 m depth no matter what the surface ice cover. This hypothesis is further confirmed by Ehn et al. (2011), who suggest that transmittance through sea ice varies due to not only the surface type (ponds or white ice) but also the heterogeneity of the ice surface and distribution and proximity of other surface ice types, which influences the horizontal spreading of light in the water column and creates a similar convergence as observed in the model (Fig. 8) and previous studies (Frey et al. 2011).

Nicolaus et al. (2012) report average transmittances of 22% for ponded FYI, and transmittances of 46.7-58.6% were measured through ponded ice in ICESCAPE (where the massive under ice bloom was observed; Arrigo et al. submitted). Similarly, in the Canadian Arctic, Ehn et al. (2011) measured transmittances of 38-67% for ponded first year ice. In the model, the amount of light transmitted through the ponded ice ranges from 24.9% when the ponds initially form on June 29 (and the surface scattering layer on the sea ice disappears), to 38.8% through 1.1 m thick ice on July 11 when ponds were 0.18 m thick (Table 5). Interestingly, in the ponded ice runs, nearly the same amount of light was transmitted through the sea ice from July 7 to July 18, despite the pond thickness increasing from 0.12-0.30 m. This suggests that the surface scattering layer impacts light transmittance more than the pond thickness, and/or that it may depend on the relative amount of pond to ice thickness more so than the absolute pond thickness. In addition, the surface area of pond coverage may be important, as described by Nicolaus et al. (2012), who note that ponds on first year ice are much thinner than ponds on multi-year ice (a few cm on FYI and >0.3 m on MYI), and spread out over larger distances (rather than being constrained by the more variable ice surface features common to MYI), allowing for enhanced “windows to the ocean”.

By 10 m in the water column under the ice, all the light transmittances converge to similar values, and very little light penetrates to greater depths. This is comparable to the light transmission profiles measured during ICESCAPE (Frey et al. 2011), SHEBA (Perovich et al. 2003 and the associated online database), and other studies of sea ice (Perovich 1990; Ehn et al. 2011). We conclude that the light in our standard run is a good representation of the light conditions during the 2011 ICESCAPE cruise, when the massive under ice phytoplankton bloom was observed.

4.1.3. NO₃

Before the under-ice bloom begins, NO₃ is uniform throughout the water column at the initial concentration set in the model run of 16 mmol m⁻³ (June 15-30) (as measured in the region during the SBI program; Codispoti et al. 2005, 2009). An under ice bloom begins following snow melt and pond formation; ponds begin to form on June 28, and there is a lag of a few days before the phytoplankton begin to bloom and NO₃ begins to be drawn down. By July 7, NO₃ has been depleted to ~12 mmol m⁻³ at the surface (turquoise), which extends to roughly 10 m depth, where the nitracline has developed. Below 15 m, NO₃ concentrations remain at initial values (~16 mmol m⁻³) (Fig. 9). By July 11, as the under ice bloom accelerates, concentrations near the surface decrease to 8 mmol m⁻³ (orange), although the nitracline remains at a similar depth (10-15 m) as on July 7 (Fig. 9). By July 18, when the ice breaks up and ponds are nearly 30 cm deep, <2 mmol m⁻³ (medium blue) is observed at the ocean surface, and the nitracline has deepened to 20 m, below which NO₃ values remain at initial values (Fig. 9). In the open water period, shown for August (medium purple), September (medium red), and October (medium green), NO₃ has been depleted to near zero in the top 10-15 m, and the nitracline progressively deepens from 30 m to 45 m (Fig. 9).

The model captures the overall vertical distribution in NO₃ measured during ICESCAPE, shown for Stations 48, 60, 63, and 66 (Fig. 9), with the main difference being in the deep water NO₃, which was slightly higher in ICESCAPE (16-20 mmol m⁻³ at 35-45 m depth) than the value used to initialize the model (this is because in

ICESCAPE, we occasionally hit pockets of very nutrient-rich Anadyr current “winter water”, which is currently the subject of several studies to determine its impact on regional productivity). (Note: We use the ICESCAPE data for comparison here since the measurements were made in the spring and early summer, e.g., just prior to and after ice break up) in the exact region of the Chukchi shelf modeled here. Of course, vertical mixing and transport of different water masses can impact the nutrient patterns in any one station, but we present these stations as representative of the basic patterns and characteristics of nutrient dynamics observed in the region and simulated in the model.) The depletion of NO_3 is lower in the model than was observed during ICESCAPE (e.g. Station 45), although the modeled NO_3 depletion extends to this same depth (Fig. 9). Because the under ice bloom in the standard run (described below) was not quite as massive as the one measured in ICESCAPE, NO_3 drawdown was not as extreme (Arrigo et al. 2012; Arrigo et al. submitted).

Open water NO_3 profiles in the standard run compare very well to SBI data, (Fig. 9) (Hill and Cota 2005, and Codispoti et al. 2005, 2009). Over the 50-m deep shelf stations during SBI, NO_3 concentrations were 0-2 $\mu\text{mol L}^{-1}$ in the top 10 m, 2-10 $\mu\text{mol L}^{-1}$ at 10-30 m, and 10-14 $\mu\text{mol L}^{-1}$ at 30-50 m (Hill and Cota 2005). This compares very well to the profiles we simulate in the model, with NO_3 depletion to 10-15 m, followed by a gradual increase towards 20-30 m, below which NO_3 remains relatively constant near wintertime values (Fig. 9). From these comparisons, we conclude that the model simulates NO_3 dynamics relatively well over the Chukchi Shelf during the seasonal cycle.

4.1.4. *Phytoplankton and Chlorophyll a*

From June 15-29 (i.e., prior to snow melt and pond formation), Chl *a* in the water column under the sea ice is near zero (Fig. 10). Following the beginning of pond formation on June 28, Chl *a* on June 30 under the sea ice slowly begins increasing to $\sim 3 \text{ mg m}^{-3}$ in the top 5 m (Fig. 10). By July, as light availability begins to increase as ponds grow in thickness (Table 5), a substantial phytoplankton bloom has begun under the ice. Chl *a* reaches $>20 \text{ mg m}^{-3}$ in a layer $\sim 10 \text{ m}$ thick between 5

and 15 m. The bloom continues to develop over the next four days, and Chl *a* values reach $>20 \text{ mg m}^{-3}$ in a $\sim 20 \text{ m}$ thick band from 5 m to 25 m depth by July 11 (Fig. 10). By the day of ice break up, on July 18 (medium blue), the under ice bloom has already peaked and begun to sink, and Chl *a* ranged from $5\text{-}15 \text{ mg m}^{-3}$ in a nearly 40 m thick layer just under the ice (Fig. 10). In the open water for the duration of the season, a subsurface Chl *a* maximum of $5\text{-}15 \text{ mg m}^{-3}$ persists from 10 to 40 m depth, deepening as the season progresses (Fig. 10).

Large and small phytoplankton vary with NO_3 and light dynamics over the seasonal cycle (Fig. 12, top row, left corner, also shown in close-up in Fig. 13 in Chl *a* units for easier comparison to other studies). Large phytoplankton dominate the under-ice bloom, reaching peak values of $>20 \text{ mg Chl } a \text{ m}^{-3}$ in early July (July 7-11), with higher values near the surface (upper 10-20 m). Large phytoplankton extend to depths of 40 m by July 15 just before ice break up (Fig. 13). Abundance of small phytoplankton (Fig. 13, top) ranges from 3 to $5 \text{ mg Chl } a \text{ m}^{-3}$ during the under-ice bloom, mostly appearing near the end of July after the large phytoplankton have declined. During the under-ice bloom, large phytoplankton are $\sim 10\text{-}20$ times more abundant (as measured by Chl *a*) than small phytoplankton, and comprise more than 80% of the under-ice bloom biomass. This is a consequence of the higher growth rates of large phytoplankton when nutrients are abundant, as in the initial phase of under-ice bloom.

When the ice breaks up on July 18, a subsurface Chl *a* maximum comprised of both small and large phytoplankton persists throughout the season at 10-40 m depth (Fig. 13). The large phytoplankton die out more quickly than the small, which persists at concentrations of $2\text{-}4 \text{ mg Chl } a \text{ m}^{-3}$ at 10-30 m depth through August and September. However, large phytoplankton still dominate the SCM, ranging from $5\text{-}10 \text{ mg Chl } a \text{ m}^{-3}$ in a layer as thick as 30 m throughout August.

The overall pattern produced by the model is similar to the pattern observed during the massive phytoplankton bloom observed during the 2011 ICESCAPE cruise (Fig. 10). The main differences between modeled and measured Chl *a* are apparent in stations 60 and 63, where higher Chl *a* concentrations were observed (Fig. 10).

Although the model does not produce quite as high values for Chl *a* as was measured, the pattern in modeled Chl *a* is very robust (Fig. 10). In particular, Sta. 66 shows a peak in biomass between 5 m and 25 m, similar to what was modeled on July 11 during the peak of the under ice bloom, and Sta. 63 shows a SCM of similar magnitude and depth as the model (Fig. 10).

Hill and Cota (2005) observed biomass maximum of 10 mg Chl *a* m⁻³ in the SCM at 30 m over the shelf, averaging 1-6 mg Chl *a* m⁻³, similar to what was simulated by our model (Fig. 10). Furthermore, the pattern in Chl *a* presented in their Fig. 6B is very similar to what we simulate in the model, including a 10-30 m thick SCM with high Chl *a* (>8 mg m⁻³) and reduced Chl *a* above and below this feature. Spring values shown in Fig. 5B of Hill and Cota (2005) are much lower, and compare well with the Chl *a* simulated during our early-season runs shown in Fig. 10 (Chl *a* <0.3 mg m⁻³ throughout the water column). Thus, the model simulates observed conditions fairly well, with the caveat that the modeled under ice bloom does not achieve the extreme Chl *a* values as was observed during ICESCAPE (Arrigo et al. 2012; Arrigo et al. submitted).

At the peak of the under ice bloom, nearly 500 mg Chl *a* m⁻² was observed in the water column (Table 6). In the ICESCAPE data, the peak Chl *a* of the under ice bloom was nearly double this, 1016 mg Chl *a* m⁻², while Chl *a* at the ice edge was and 576 mg Chl *a* m⁻² (Arrigo et al. *submitted*). The early bloom stations measured in ICESCAPE had integrated values of 212 mg Chl *a* m⁻² and open water areas with no bloom south of the ice edge had values of 54 mg Chl *a* m⁻². Although the measured values were higher than the modeled values, the general spatial pattern is the same in both cases.

4.1.5. Zooplankton

Small zooplankton (Fig. 12) respond primarily to small phytoplankton with a lag of several days following the initial burst of phytoplankton growth after the ice breaks up. Later in the season, small zooplankton have a secondary small peak at 20-30 m depth in September, once the grazing pressure from large zooplankton is reduced

and bacteria provide a secondary food source for the small zooplankton (Fig. 12). However, we note that small zooplankton are not able to achieve high biomass until after the ice breaks up and the water column warms (Fig. 12).

Large zooplankton abundance is nearly double that of small zooplankton, but are mostly concentrated near the surface where the large phytoplankton bloom (Fig. 12). The large zooplankton respond to the large pulse of food during the under ice bloom, but also die out more quickly once this food source diminishes following ice break-up. This suggests that large zooplankton are not able to subsist sufficiently on the $<10 \text{ mg Chl } a \text{ m}^{-3}$ in the SCM layer in late August in open water. These general patterns fit well with those presented by Sakshaug (2004) and Loeng et al. (2005) for this region.

4.1.6. Detritus, DON, NH_4 , and Bacteria

Detritus gradually accumulates and sinks throughout the under-ice bloom period, followed by accumulation in deep layers in September before sinking to the bottom as the season progresses. This small late-season accumulation is driven by the slow sinking speed of small phytoplankton and detritus produced from small zooplankton fecal pellets. Fecal pellets generated by large phytoplankton sink much faster (e.g., Kellogg et al. 2011), as does detritus during the under-ice bloom period, and this is likely what accounts for the lack of early-season accumulation of detritus under the ice. During ICESCAPE, little to no accumulation of detritus was observed in the water column during the under-ice bloom, which was attributed to fast sinking rates and subsequent remineralization (rather than consumption by zooplankton, as shown in the model simulations as well) (Fig. 12; Arrigo et al. *submitted*).

NH_4 (Fig. 12) is near zero throughout the water column early in the season due to low remineralization rates. By late July into August, NH_4 follows the pattern of bacterial and detrital accumulation after the under ice bloom, reaching values of $\sim 1.5 \text{ mmol m}^{-3}$ at 30-40 m depth, similar to concentrations measured in the water column during ICESCAPE (Arrigo et al. *submitted*).

Bacteria do not begin to accumulate until much later in the season when the water temperature warms and enough DON and detritus have accumulated to serve as N sources for the microbial loop (Fig. 12). However, we note that DON begins to accumulate once substantial detritus has been remineralized after the bloom; this pool then is quickly consumed by the growing bacteria population as well as by phytoplankton.

4.1.7. Net primary productivity

Net primary productivity (NPP) in the standard run generally follows the patterns in phytoplankton growth and Chl *a* described above (Fig. 11; orange lines). Following snow melt in late June and the beginning of pond formation, the under ice phytoplankton bloom begins rapidly, with daily NPP increasing from 18.2 mg C m⁻² d⁻¹ on June 28 to 313 mg C m⁻² d⁻¹ on July 2. Daily NPP continued to increase rapidly between July 2 and July 7, more than doubling to 715 mg C m⁻² d⁻¹ on July 4, eventually peaking at 938 mg C m⁻² d⁻¹ on July 7. NPP remained above ~800 mg C m⁻² d⁻¹ for 5 days during the peak of the under ice bloom, from July 5-9, and exceeded ~500 mg C m⁻² d⁻¹ for 22 days (July 3-23). There was a slight decline in NPP in the under ice bloom near the time of ice break-up, from July 14-18, which then rapidly increased again once the ice broke up on July 18. Mean NPP for the 19 days of the under ice bloom was 603 mg C m⁻² d⁻¹, comparable to the mean rate of 546 mg C m⁻² d⁻¹ for the MIZ bloom that lasted for 7 days after ice break up. After the initial MIZ bloom, NPP averaged ~300 mg C m⁻² d⁻¹ in August and early September and decreased to 200 mg C m⁻² d⁻¹ by the end of September.

These results compare well to the other estimates of daily NPP in the Chukchi and Beaufort seas (Table 4). Lavoie et al. (2010) estimated daily rates in the range of 500-800 mg C m⁻² d⁻¹ in early July, when NPP peaks, which decline to 300-400 mg C m⁻² d⁻¹ by August and 100 mg C m⁻² d⁻¹ by September. Comparatively, Walsh et al. (2005) give peak NPP rates of 709 mg C m⁻² d⁻¹, in July-August, about a month later than what we simulate in our model. Walsh et al. (2005) do present daily NPP rates in April-May that are similar to our model (9.9 mg C m⁻² d⁻¹), as are the rates for June

(280 mg C m⁻² d⁻¹), although their rates for September-October (578 mg C m⁻² d⁻¹) is much higher than we simulate here since our bloom happened much earlier under the ice cover.

Our simulated NPP rates compare well to those measured in Chukchi Sea (Cota et al. 1996) of 300 mg C m⁻² d⁻¹ for the northwest region, and rates of 750 mg C m⁻² d⁻¹ in the northeast region. In the SBI program, spring NPP rates of <300 mg C m⁻² d⁻¹ were observed in the northeast Chukchi (near Barrow), and average summer NPP rates over the shelf were 783 mg C m⁻² d⁻¹. However, we do note that our rates are only about a third of those measured at the shelf break in the Chukchi Sea during SBI (2.90 g C m⁻² d⁻¹) and are at the lower end of the range reported in the July 4-8, 2011 ICESCAPE under-ice bloom (1200-4800 mg C m⁻² d⁻¹) (Arrigo et al. submitted). Part of this difference is due to the different environmental conditions at the time of the bloom. For example, the shelf-break bloom observed during SBI was sampled in late summer after thick multi-year ice broke up and resulted in a large MIZ bloom (Hill and Cota 2005). Vertical distributions of NPP produced by the model are similar to those observed during SBI and ICESCAPE, with maximum NPP observed at ~15 m over the shelf during the spring-summer bloom (Hill and Cota 2005, Arrigo et al. submitted).

Annual NPP in the standard run amounts to 34.4 g C m⁻² yr⁻¹. This compares well with the literature values that range of 15-50 g C m⁻² yr⁻¹ for the Chukchi-Beaufort region (Table 4). Similarly, the model by Lavoie et al. (2010) estimates an annual NPP value of 22.1 g C m⁻² yr⁻¹, slightly lower than our estimate that includes under ice production. However, our model produces only about a third of the annual NPP presented in Arrigo et al. (*submitted*), mostly due to lower NPP rates during the under ice bloom, and is lower than the estimate of 90 g C m⁻² yr⁻¹ by Hill and Cota (2005), which is mostly extrapolated from very high daily NPP rates measured in the initial MIZ bloom (Table 4).

4.2. Growth limitation terms

Growth limitation terms can be used to explain some of the key controlling factors that limit the under-ice and MIZ bloom. The magnitude of the light limitation term is similar for both the phytoplankton groups (Fig. 14), although the small phytoplankton group can grow to slightly greater depths than the large phytoplankton. The light limitation of phytoplankton in the under ice bloom period, from June 28 to July 18, is relatively consistent, with both groups able to grow to about 10 m depth. The light limitation term increases rapidly with the increase in light transmission at the end of June, which is when melt ponds begin to form on the sea ice surface. Following ice break up on July 18, the light limitation terms reveal that phytoplankton were able to grow progressively deeper in the water column, from 10 m to >30 m by the end of the model run. This is consistent with the pattern of light limitation at depth early in the bloom, followed by reduced light limitation once the sea ice breaks up.

Because sea ice and snow strongly attenuate UVR, phytoplankton are barely inhibited by UVR in the water column during the under ice bloom. In comparison, UVR inhibition of photosynthesis and phytoplankton growth plays a strong role in limiting primary production in the open water MIZ bloom and SCM. This inhibition extends to ~20 m depth throughout the open water period, and decreases NPP to ~60% of what it would be without UVR limitation (Fig. 14).

Small phytoplankton are able to reduce NH_4 concentrations to levels that do not as severely inhibit NO_3 uptake, and hence are less limited by NH_4 . Similarly, small phytoplankton are slightly less limited by low NO_3 , as they are better able to take up NO_3 at low concentrations (Fig. 14). Both phytoplankton groups are limited by the lack of NO_3 later in the season, and subsist on a combination of NH_4 and NO_3 in the SCM (Fig. 14).

The most interesting aspect from a biological standpoint is the intersection of the three limitation terms for both phytoplankton groups, where light limitation interacts with the nutrient limitation to constrain growth in the under ice bloom and in the SCM (Fig. 14). For example, at 20 m depth in August, substantial light penetrates

and phytoplankton growing at 60-80% of their maximum rate but NH_4 and NO_3 concentrations both limit growth to ~50% of their maximum rate.

Bacteria grow at 40-60% of their maximal rates based primarily on DON concentrations during July-Aug., and then grow at much higher rates based on the higher NH_4 concentrations at depths of 20-50 m in late August-September. This suggests that bacteria are substrate limited in the under ice bloom, and cannot achieve rapid growth until substantial NH_4 accumulates later in the season.

4.3. Model experiments

4.3.1. Effect of varying pond cover on under ice and annual NPP

One key question we wanted to answer with this model was how variability in melt pond coverage affects the magnitude and development of the under-ice bloom. To do so, we varied pond coverage by $\pm 20\%$ from the standard run, which had 30% areal pond coverage on the ice surface, as well as performed a run where the sea ice cover had no ponds, consisting instead of bare ice with a surface scattering layer.

4.3.1.1. 10% Pond coverage vs. standard run

Compared to the standard run, the 10% pond run (Fig. 11) shows a markedly diminished under-ice bloom due to the reduced light transmittance through the more highly scattering ice cover (not shown). The under-ice bloom in the 10% pond run peaked on the same day (July 7) as in the standard run, but its peak rate of NPP was 26% lower ($698 \text{ mg C m}^{-2} \text{ d}^{-1}$ vs. $938 \text{ mg C m}^{-2} \text{ d}^{-1}$) (Table 7). In total, the proportion of annual NPP contributed by the under ice bloom in the 10% pond run was 26.1%, with the remaining 73.9% of annual NPP contributed by phytoplankton in ice-free waters, including the MIZ. In the standard run, the proportion of annual NPP contributed by the under ice bloom increased to 30.1% (Table 7), due to reduced light limitation in waters beneath ice with a greater melt pond fraction (Fig. 14). Annual NPP for the 10% pond run was $33.8 \text{ g C m}^{-2} \text{ yr}^{-1}$, which was -1.84% lower than annual NPP in the standard run (Table 7).

Because the under-ice bloom was smaller in the 10% pond run, the MIZ bloom was larger than in the standard run (Table 7). The peak daily rate of NPP for the MIZ bloom in the 10% pond run (achieved on July 19 in the top 10 m of the water column) was $1160 \text{ mg C m}^{-2} \text{ d}^{-1}$, 18% higher than in the standard run (Table 7). Furthermore, this MIZ bloom lasted for several days longer than the MIZ bloom in the standard run (Fig. 11; Table 7).

Thus, a key feature of the 10% pond run is that the under-ice portion of the bloom was smaller than in the standard run (due to less light transmittance resulting from reduced pond coverage), resulting in higher nutrient concentrations in the open water once the ice broke up. These nutrients were then available to fuel and sustain a larger and longer open water bloom than in the standard run (Fig. 11). Extrapolating this concept to other ice types, this suggests that MIZ blooms adjacent to older ice with lower pond coverage (i.e., similar to the 10% pond coverage run) could reach higher daily rates of production and higher biomass immediately following ice break-up (e.g., once the intense light limitation imposed by ice cover is removed) than in ice with greater pond coverage, as long as sufficient nutrients remain in the water column. This has been observed, for example, in satellite based studies (Arrigo and van Dijken 2011; as well as previous field studies in the Chukchi Sea (Hill and Cota 2005).

However, it is important to note that a higher peak NPP and a higher percentage of NPP in the open water season does not necessarily lead to higher annual NPP, as shown in the 10% pond run where annual NPP was -1.84% lower than in the standard run. Rather, our results suggest that a higher pond coverage and a larger fraction of annual NPP under the ice may result in higher annual NPP even if the amount of NPP in open water is reduced. The key difference between the two runs seems to be in the intensity of nutrient limitation during the open water growing season, which lasts much longer than the under-ice growing season, as well as the fraction of annual NPP that is concentrated under the ice vs. in open water.

4.3.1.2. 50% Pond coverage vs. standard run

Compared to the standard run, increasing melt pond fraction to 50% (light green line, Fig. 11) increased the peak daily rate of NPP of the under ice bloom by only 7.8%, from $938 \text{ mg C m}^{-2} \text{ d}^{-1}$ to $1012 \text{ mg C m}^{-2} \text{ d}^{-1}$ (Table 7). The under-ice bloom peaked on the same day as in the standard run (July 7). This larger under-ice bloom removed a higher proportion of nutrients from the water column (as well as to a greater depth; not shown), and once the ice broke up on July 18, the peak rate of NPP measured in the MIZ bloom was reduced by 29% compared to the standard run ($695 \text{ mg C m}^{-2} \text{ d}^{-1}$ compared to $981.70 \text{ mg C m}^{-2} \text{ d}^{-1}$). Interestingly, the proportion of annual NPP taking place under the ice (31.2%) was almost identical to that of the standard run (Table 7), indicating that increasing pond fraction from 30% to 50% results in only a small increase in NPP by the under ice bloom. Furthermore, total annual NPP in the 50% pond run was $34.5 \text{ g C m}^{-2} \text{ yr}^{-1}$, only 0.2% greater than the standard model run.

4.3.1.3. No melt pond coverage vs. standard run

Continuing our exploration of the effect of varying melt pond fraction on sea ice cover, we also performed a model run having no melt ponds (Fig. 11, dark red line). Rather, the ice was covered by the surface scattering layer with a high albedo, typical of bare ice in many areas of the Arctic (e.g., Ehn et al. 2011; Nicolaus et al. 2012). In the 0% pond run, light transmission was insufficient to support NPP. Following the ice break-up on July 18, a large open water bloom eventually developed, peaking 11 days after the MIZ type bloom in the standard run (Fig. 11; Table 7). This open water bloom had a higher peak daily rate of NPP magnitude than the MIZ blooms observed in the 10%, 30%, or 50% pond runs, reaching a peak value of $1272 \text{ mg C m}^{-2} \text{ d}^{-1}$ on July 30, nearly 30% higher than the open water bloom in the standard run (Table 7).

Most importantly, the bloom length (days above $400 \text{ mg C m}^{-2} \text{ d}^{-1}$) was 27 days, or 9 days greater than for the standard run (Table 7). In the open water bloom, NO_3 was stripped rapidly from the surface, resulting in the bulk of NPP being

concentrated in the SCM (not shown), consistent with observations by Cota et al. (1996) and Codispoti et al. (2005, 2009). However, despite this much longer bloom length and higher peak value, the total annual NPP for the region was 4.66% less than for the standard run (Table 7). Thus, despite a seemingly much greater bloom in peak daily rates and duration, the lack of under-ice based production in the no-pond case results in reduced integrated annual production.

This is similar to what was observed in the 10% pond run (section 4.3.1.1.), where total annual NPP was reduced compared to the standard run, despite a larger fraction of NPP occurring in the open water as well as a very high peak daily rate of NPP measured in the MIZ bloom (Table 7). The fact that even lower annual NPP is observed in the 0% pond case than the 10% pond case suggests that under-ice based production is an important component of annual NPP in the region, no matter how small a contribution it makes, and that a greater fraction of NPP in the under-ice bloom consistently results in higher annual NPP. Nonetheless, model results suggest that at least 10% pond coverage is necessary to achieve significant under-ice production, but 30-50% pond coverage is needed to achieve the high of rates observed in ICESCAPE ($1.2-4.8 \text{ g C m}^{-2} \text{ d}^{-1}$, Table 4).

4.3.2 Effect of UVR inhibition of NPP

To investigate the effects of UVR inhibition on the seasonal cycle of primary production in the Chukchi Sea, we performed a model experiment in which UVR inhibition of phytoplankton photosynthesis was turned off in the standard run. Daily rates of NPP reached a peak on July 7 under the ice for the no-UVR run, the same day as in the standard run, and under-ice NPP was 2.3% greater than in the standard run ($959 \text{ mg C m}^{-2} \text{ d}^{-1}$ vs. $938 \text{ mg C m}^{-2} \text{ d}^{-1}$) (Table 7). In addition, 28.3% of annual NPP was associated with the under-ice bloom, compared to 30.1% in the standard run, a difference of only 1.8% (Table 7). Together, these data suggests that UVR inhibition of photosynthesis under sea ice cover, where little to no UVR penetrates, may result in only a ~2% reduction in NPP in the under ice bloom.

However, UVR has a more severe impact on NPP in open water following ice break up. Compared to the standard run, the no-UVR run shows a dramatic increase in peak daily rates of NPP in the open water bloom period, from 982 mg C m⁻² d⁻¹ to 1614 mg C m⁻² d⁻¹, or a 64% increase. The no-UVR open water bloom also lasted longer than the standard run bloom by 4 days, but reached its peak on the same day as the standard run (Table 7). 71.7% of annual NPP was attributable to production in open water.

Because of the lack of UVR inhibition of photosynthesis, the combined annual NPP both under ice and in open water in the no-UVR run (38.0 g C m⁻² yr⁻¹) was 10.3% higher than in the standard run. These results suggest that UVR inhibition of photosynthesis may indeed have an important impact on NPP in this region of the Arctic, reducing open-water based NPP by as much as 10% from what it would be without UVR-inhibition. Our results of a 10% impact of UVR on NPP is slightly higher than that reported for the effect of the ozone hole (and the resulting enhanced UVR dosage to the surface ocean) in Antarctic waters, where it was shown that UVR reduced PP by <2% (e.g., Smith et al. 1992; Arrigo 1994; Neale et al. 1998a; Arrigo et al. 2003).

The greater impact of UVR on photosynthesis and NPP in the Arctic as shown in our model may be related to the hypothesis that Arctic phytoplankton are particularly poor at employing successful strategies for photoprotection and/or repair of photodamage related to UVR stress (Helbling et al. 1992; Helbling and Villafañe 2002). This suggests that the under-ice habitat with 30% or greater melt pond coverage, where little to no UVR penetrates but sufficient light is transmitted to support high rates of NPP and net photosynthesis, represents a nearly ideal habitat for phytoplankton that are sensitive to UVR. This may help explain how massive under-ice blooms, like the one observed in 2011 ICESCAPE, are able to develop beneath >1 m of sea ice. Clearly, more research is needed to investigate the role the UVR plays in controlling photosynthesis, phytoplankton community composition, and the magnitude and seasonal cycle of NPP in the Arctic Ocean.

4.3.3. Effect of zooplankton grazing on NPP

To investigate the impact that zooplankton grazing has on controlling the under ice bloom, we ran a standard experiment (30% pond cover) with no grazing (Table 7). NPP was nearly identical to the standard run ($952 \text{ mg C m}^{-2} \text{ d}^{-1}$ and $938 \text{ mg C m}^{-2} \text{ d}^{-1}$, respectively) (Table 7), indicating that zooplankton grazing has very little impact on the under-ice bloom. However, zooplankton grazing appears to play a large role in reducing the MIZ-based bloom that follows ice break up. In the run with no zooplankton, peak NPP was the highest observed in any model runs, reaching a maximum rate of $1594 \text{ mg C m}^{-2} \text{ d}^{-1}$ on July 19 (the day immediately following ice break-up) (Fig. 11; Table 7). This was 62% higher than the peak reached in the standard run (Table 7). Furthermore, with no zooplankton grazing, the bloom persisted for 40 days, or 22 days longer than in the standard run, and reached an annual integrated rate of $41.8 \text{ g C m}^{-2} \text{ yr}^{-1}$, which was 21% higher than in the standard run (Table 7). Although it is difficult with limited data to validate this impact of zooplankton grazing on the seasonal NPP cycle, Hunt et al. (2013) report that 44%, or about double that measured here, of summer primary production is likely consumed by zooplankton in the Chukchi, the other half of which is exported to the benthos. Our results may be different from those presented in Hunt et al. (2013) for many reasons, including different composition of phytoplankton and/or zooplankton functional groups compared to those in the field; changing patterns in seasonal NPP cycles, which may have shifted the timing and/or magnitude of peak biomass; and the fact that we are integrated over the whole season rather than just presented summer values.

4.3.4. Variable timing of ice retreat and ice thickness

4.3.4.1. Early first-year ice break-up and pond formation

In this run, the ice starts thinner (1.07 m) than in the standard run, which decreases to 0.45 m prior to ice break up on July 4 (Fig. 3). Snow begins at 0.13 m and decreases starting May 21; it is completely gone by June 4, the start of the ice melt season. Pond growth begins on June 11, and grows from 0 to 30 cm depth by July 4, when the ice breaks-up (consistent with what was observed in SHEBA; Fig. 2d).

We also ran two additional simulations with pond coverage in the early ice run of 10% and 50% to see how this impacted seasonal and annual NPP (Fig. 15 and Table 8). As was observed in the standard run, the 30% and 50% pond runs in the early ice run were similar in magnitude, whereas the 10% pond run showed a decrease in peak production under the ice due to light limitation (Fig. 15). Also, in the 10% pond run, the MIZ bloom immediately following ice break-up had much higher peak rates in daily NPP than the under-ice bloom (Fig. 15).

However, the early pond run shows a reduced magnitude of peak NPP in the under-ice bloom period, reaching values of only $677 \text{ mg C m}^{-2} \text{ d}^{-1}$ for 50% pond cover and $619 \text{ mg C m}^{-2} \text{ d}^{-1}$ for 30% pond cover in the under ice bloom (Table 8), both of which were ~30% below the peak observed in the standard run under the ice with comparable melt pond fractions (Table 7). However, these represented a similar fraction of annual NPP as in the standard run, 30.8% and 32.9%, resulting in reduced annual NPP for the early ice runs (Table 8). The bloom length for the early ice runs was also shorter than in the standard run (Tables 7 and 8). The open water MIZ bloom following ice break-up observed in the 10% pond early ice case was also smaller in peak daily NPP values than in the standard run, although this represented a larger fraction of annual NPP than in the standard run (76.8% of annual NPP vs. 73.9% for the standard run) (Tables 7 and 8).

In total, these factors all resulted in the early ice breakup runs having reduced annual NPP compared to the standard runs, regardless of percent pond coverage (Tables 7 and 8). The results from the early ice and pond run ($29.9\text{-}30.6 \text{ g C m}^{-2} \text{ yr}^{-1}$; Table 8) fall well within the range of $15\text{-}50 \text{ g C m}^{-2} \text{ yr}^{-1}$ measured in the Chukchi Sea (Fig. 16), but are lower than values reported in satellite based studies (Arrigo and van Dijken 2011) or measured during either ICESCAPE (Arrigo et al. 2012) or SBI (Hill and Cota 2005). This is consistent with our hypothesis described in the standard runs above, wherein reduced magnitude of under-ice blooms results in lower annual NPP because of a larger percentage of NPP occurring during the open water portion of the season.

4.3.4.2. Multi-year ice

The results from the multi-year ice runs are shown in Fig. 15 (seasonal daily rates of NPP) and Fig. 16 (annual NPP) and described in Table 8. As expected due to the markedly reduced light transmittance through multi-year ice, regardless of whether ice was 2 or 5 m thick (see descriptions in Table 1 for ice and snow seasonal evolution), NPP was very low under the ice cover. Maximum NPP values for the MYI runs were achieved in August for both runs, with the 2 m run reaching values of $19.0 \text{ mg C m}^{-2} \text{ d}^{-1}$ and the 5 m run reaching rates of only $12.9 \text{ mg C m}^{-2} \text{ d}^{-1}$ (Table 8). Both of these rates are similar to the peak NPP of unponded ice in the standard run (prior to the later MIZ or open water blooms, for example in the 0% pond runs) (Table 8). However, annual NPP for the MYI runs was very low, $>1 \text{ g C m}^{-2} \text{ yr}^{-1}$ (Table 8). These results suggest that when this region was historically covered by thick MYI, NPP in the water column would have been very low.

4.3.4.3. No sea ice

In the no sea ice run, NPP peaked in early May, despite near freezing water temperatures, reaching $569 \text{ mg C m}^{-2} \text{ d}^{-1}$ (Fig. 16) much less than the peak values achieved in either the standard runs or the early ice run (Fig. 15; Table 8). The bloom lasted 22 days (Table 8). Most of the annual NPP was concentrated in an SCM layer 20-40 m deep that progressively deepened throughout the season, and regenerated N was the primary form of N utilized by phytoplankton (not shown).

However, because of the much longer growing season, annual NPP in the no-ice run was actually higher than that achieved in the standard run, although not as high as in the no-grazing run (Fig. 16). Annual NPP was $38.1 \text{ g C m}^{-2} \text{ yr}^{-1}$, which was 10.6% higher than the standard run and 25% higher than the early ice run (Table 8; Fig. 16). This suggests that if sea ice were to completely melt by the summer, as has been hypothesized by several prominent studies (e.g., Overpeck et al. 2005; Loeng et al. 2006), annual NPP will be as high or higher than when sea ice is present. This is in contrast to the cases described above, where under-ice blooms represent an important contribution to total annual NPP. In the case of no under-ice bloom, such as when no

sea ice is present, the much greater duration of a suitable growing season is apparently sufficient to increase annual NPP as compared to when ice limits productivity early in the year, in which case under-ice blooms represent an important contribution to annual NPP.

5. Conclusions

5.1. What can the model tell us about the controls on NPP?

Although our model is a simplified representation of the Chukchi Sea shelf, it allows us to make valuable inferences about the factors controlling the spring and summer phytoplankton bloom in the Chukchi Sea. Perhaps most importantly, our model simulations suggest that enhanced melt pond proliferation results in greater nutrient limitation and nutrient-based control of annual NPP. Conversely, fewer ponds result in enhanced light limitation and light-control of NPP. These factors can have a large impact on annual NPP, especially in years when the under ice bloom is light limited and the bulk of NPP occurs in the MIZ following ice break-up. When pond coverage was reduced in the standard run, we observed a higher peak MIZ bloom but lower overall seasonal production; this is important when considering the impacts of past sea ice cover changes on annual NPP.

Furthermore, we observed a higher under-ice bloom but lower MIZ bloom and very little difference in annual NPP when pond coverage increased from 30 to 50%. Hence, we suggest that in the future, if melt pond coverage on the ice surface increases, there may be little to no net impact on annual NPP in the region, but the timing and intensity of the different bloom peaks (under ice vs. MIZ) will likely change. This could potentially have a very large impact on the food web, as higher under-ice production goes largely ungrazed by zooplankton, which are the link to upper trophic levels such as fish and seabirds. Thus, our model suggests that in the future, although annual NPP may not change, there is the potential for large shifts in the food web. Of course, lateral transport by circulation, more complex sinking and vertical mixing processes, and differing water masses would all also impact this pattern, and future studies should focus on the more detailed water column physics in

order to better understand how these currently control and may control in the future the seasonal cycle of NPP in this region.

Another important insight from our model is in elucidating the role that under-ice blooms may play in controlling the magnitude of total annual NPP. When there were smaller under-ice blooms, as observed in model runs with fewer melt ponds (and thus reduced light transmission through the sea ice to the underlying water column), in every case annual NPP decreased as compared to the standard run with 30% pond cover, even if open water-based or MIZ-type blooms increased in peak magnitude, duration, and/or total percentage of annual NPP (Tables 7 and 8). The reason for reduced annual NPP in cases where a larger fraction of annual NPP occurs in open water may be for several reasons.

One reason for this may be the impact of UVR on seasonal and annual NPP: UVR inhibition of photosynthesis that occurs during the open water portion of the season was shown to reduce annual NPP by as much as 10%, including a 64% reduction in the rate of open-water peak daily NPP (Table 7). Total annual NPP was also reduced in the case where ice retreated earlier in the model run (Table 8, Fig. 16), resulting in nearly the same percentage of annual NPP occurring in the under-ice portion of the season despite the fact that this period was nearly a month shorter than in the standard run. Thus, when more annual NPP is concentrated in the open water period, our data suggests that UVR inhibition plays a larger role in controlling the annual NPP and peak rates of daily NPP. UVR may play an even bigger role in reducing total annual NPP the future if more NPP shifts to open-water based (rather than under-ice) production, such as the case when ice breaks up earlier. In addition, this would be exacerbated by any potential increases in the ozone hole over the Arctic, as was observed in 2011 (Rex 2012), which would enhance UVR transmission to the ocean surface and could result in further reduction in peak rates of NPP in open water and total annual NPP.

Total annual NPP may also be reduced in cases where little or no under-ice bloom forms because of the impact of zooplankton grazing. This is because zooplankton do not grow as fast in the cold waters under the ice, and have very little

impact on the magnitude of the under-ice bloom. In the model run with no zooplankton, the under ice bloom only increased by 1.49% in peak rate, and a similar fraction of annual NPP was produced during this period (Table 7). In contrast, zooplankton had a larger impact on the open water bloom, resulting in a 62% reduction in peak daily rate of NPP, and an overall 21.3% reduction in total annual NPP (nearly all of which was due to the reduced daily rates of NPP in open water when zooplankton were present) (Table 7). Thus, annual NPP may be lower for cases where a larger percentage of NPP occurs in open water because of the impact of zooplankton grazing. In the future, if more annual NPP occurs under the ice, and/or ice breaks up earlier so that a larger portion of NPP occurs during the open water period (such as in the early ice runs), we may see a greater reduction in annual NPP because of enhanced zooplankton grazing that occurs in open water. This may be exacerbated if water temperatures in the Chukchi warm in the future, as has been predicted by some models (Loeng et al. 2005).

Finally, total annual NPP may be reduced in years with lower under-ice based production because of the relative balance between nutrient and light limitation in controlling the magnitude, timing, and duration of the bloom. The debate about nutrient vs. light control of NPP in the Chukchi region is ongoing and complicated, and our model results offer only a few suggestions about this. First, we can clearly see that light limits the under-ice bloom in cases where pond fraction is 10% or less; this is evident by the large peaks achieved in the open water bloom following ice break-up, once light limitation is reduced. This agrees with many other observations from the region, such as Walsh et al. (2005), who conclude that in the spring, 98% of the region is light limited over the continental shelf, and Arrigo and van Dijken (2011), who suggest that this is a predominantly light-limited system based on the assessment that increases in total productivity over the last decade or so are driven largely by reductions in sea ice cover (and earlier retreat).

Our model also shows that light limitation can persist at depth even in open water, as shown in Fig. 14, where sufficient light for high growth only penetrates to ~30 m under ponds and in open water. This also agrees with Walsh et al. (2005)

which shows that in summer, 83% of NPP is controlled by light limitation, and 66% of NPP is light limited in September-October. However, Walsh et al. (2005) conclude that at all times of year phytoplankton are predominantly light-limited. In contrast, our results show that in years where a larger percentage of NPP is based on recycle N (associated with the SCM in longer open water seasons), total annual NPP decreases. These results agree more with the results presented by Carmack et al. (2004), which show that most Arctic shelves are nutrient rather than light limited. In summary, it is very difficult to tease out the total impact of light vs. nutrient limitation on controlling total annual NPP, except to say that both play important roles at various times in the season.

5.2. Importance of the SCM

A key topic for Arctic marine biologists is the role, importance, and magnitude of SCM-based production. Satellite-based studies by nature cannot simulate this type of NPP, and although most conclude that the SCM contributes little to the total annual primary production estimates for the region, the results from our model suggest that this may not be the case. For example, Arrigo and van Dijken (2011) include an analysis on the effect of including a subsurface productivity maximum (SPM) or SCM in their satellite-based estimates of annual NPP for the various Arctic regions, and conclude that omitting the SCM results in an underestimate in NPP of only 7.6% for the Chukchi and 11.7% for the Beaufort Sea.

In our model, we see not only a large amount of annual NPP concentrated at the SCM for 2-3 months of the year, but also enhanced SCM-based production in the reduced ice years (early ice; Fig. 15). In addition, nearly 70% of total annual NPP is concentrated in the open-water portion of the season, regardless of the timing of ice retreat (Table 8). Ignoring any part of this portion would result in a severe underestimate of NPP. Furthermore, in the run with no sea ice, nearly 100% of total annual NPP occurs in the SCM, following a small initial surface open water bloom very early in the season (Table 8; Fig. 15). Thus, the SCM may be a critical

component of current and future primary productivity patterns for the Chukchi Sea, especially if little to no sea ice is eventually present in the region.

5.3. Future changes

Lavoie et al. (2010) present model results showing a 6-9% increase in annual NPP in the Canadian Beaufort Sea between 1975-1992 and two future time periods (2042-2059 and 2082-2099), although they note a decrease in the contribution of the spring bloom as compared to subsurface summer production caused by reduced nutrient recycling in the mixed layer in winter. This is because reduced ice thickness in the future leads to a reduction in winter mixing, which in turn reduces surface nutrient loads for the spring bloom (and thus biomass in the spring bloom) and thus changes the timing of peak productivity from the spring to a more spread-out scenario in which phytoplankton persist in deeper, thicker SCM layers for much longer in the season (Lavoie et al. 2010). Additionally, Arrigo and van Dijken (2011) predict that NPP may increase 37% from current levels over the next half century, much higher than that predicted by Lavoie et al. (2010). This is very similar to the results observed here for no sea ice, when annual NPP increased 10.6% from the standard model run and 25% from the early ice run (Figs. 15 and 16).

5.4 Conclusions and future research directions

In conclusion, a key question surrounding the predictions that annual NPP will increase in the future as ice cover declines is whether this will require enhanced nutrient inputs to the region (especially in surface waters) or whether phytoplankton blooms can potentially persist for a longer period of time in open water by recycling the nutrient inventories currently available. If nutrients are insufficient to support enhanced NPP, even with ice retreat and increasing length of the growing season, new production associated with phytoplankton blooms will be unable to increase. It is also possible that the location of peak blooms will change in response to shifts in the relative magnitude of different nutrient sources (for example, a shift to shelf-break based NPP, fueled by high upwelling of nutrient-rich deep Atlantic water).

In the case where no sea ice existed in the model run, NPP was higher than even with 50% melt pond coverage (whether ice retreated early or late) (Tables 7 and 8). Furthermore, if NPP is higher under the ice in the future due to thinner ice and/or higher melt pond fraction, such as shown in the standard model run vs. 0% or 10% pond coverage, total annual NPP also increased (Table 7). These both suggest that nutrient recycling may in fact be sufficient to support higher future NPP. These results agree with Arrigo and van Dijken (2011), who suggested that the 20% increase in NPP over the last decade observed by satellites might not have required additional nutrient input from outside sources. Although annual NPP may increase, we also note that new vs. recycled (or regenerated) production is important to distinguish for the consideration of trophic transfer, as only new production will support higher trophic level production.

In the Chukchi Sea region, it has been suggested that nutrients may increase in the future through two main mechanisms: (1) enhanced storm activity, which may allow for enhanced shelf break upwelling and thus potentially tap into the wealth of nutrients trapped below the permanent halocline layer in the Arctic (Carmack and Chapman 2003), and (2) through increased inflow through the Bering Strait bringing nutrient-rich Anadyr water to the Chukchi shelf (Woodgate et al. 2006). Our model does not have any new sources of NO_3 and thus cannot tell much about how this would impact total annual NPP in the future, although the general pattern in results do seem to suggest that more NO_3 would increase annual NPP. However, enhanced freshwater input to the surface Arctic Ocean is expected to increase stratification and may reduce the future nutrient supply from wind-mixing and/or shelf-break upwelling (Miller and Russell 2000; Loeng et al. 2006). It is unclear whether either or both of these mechanisms will change in the future, and thus what role nutrients will continue to play in controlling annual NPP in the region. What our model does suggest is that recycled nutrients do play a crucial role in maintaining annual NPP and sustaining high season-long productivity. Nonetheless, this is a critically important question to answer, as it may have profound effects for the entire food web; more research is needed to address this essential biogeochemical topic.

Acknowledgements

The light transmission model was written by B. L. Saenz (as described in Saenz 2011), as modified from Light et al. 2008 and further modified by B. L. Saenz and M. A. Palmer in this study to work with melt ponds and light spectra in the UVR zone. Several very early modeling discussions were held with T. R. Reddy and D. M. Holland, and although that model was never realized, some of the initial progress on that model was used as a framework to begin this modeling project. That older model was adapted from the Arrigo et al. (1998a) model by M. A. Palmer and T. R. Reddy.

REFERENCES

- Anderson, P. 1988. The quantitative importance of the “microbial loop” in the marine pelagic: a case study for the North Bering/Chukchi Sea. *Arch. Hydrobiol. Beih.* 31: 243-251.
- Arrigo, K. R., (1994) Impact of ozone depletion on phytoplankton growth in the Southern Ocean: Large scale spatial and temporal variability, *Mar. Ecol. Prog. Ser.*, 114, 1–12.
- Arrigo, K. R., D. L. Worthen, A. Schnell, and M. P. Lizotte. (1998a) Primary production in Southern Ocean waters, *J. Geophys. Res.*, 103, 15,587–15,600.
- Arrigo, K. R., D. L. Worthen, P. Dixon, and M. P. Lizotte (1998b) Primary productivity of near surface communities within Antarctic pack ice, *Antarctic Research Series*, 73, 23-43.
- Arrigo, K. R., D. H. Robinson, D. L. Worthen, R. B. Dunbar, G. R. DiTullio, M. VanWoert, and M. P. Lizotte. (1999) Phytoplankton community structure and the drawdown of nutrients and CO₂ in the Southern Ocean. *Science*, 283, 365–367.
- Arrigo, K. R., G. L. van Dijken and S. Pabi. (2008) Impact of a shrinking Arctic ice cover on marine primary production. *Geophys. Res. Lett.* 35: L19606, [doi:10.1029/2008GL035028](https://doi.org/10.1029/2008GL035028).
- Arrigo, K. R. and G. L. van Dijken. (2011) Secular trends in Arctic Ocean net primary production. *J. Geophys. Res.* 116: C09011, [doi:10.1029/2011JC007151](https://doi.org/10.1029/2011JC007151)

- Arrigo, K. R., D. K. Perovich, R. S. Pickart, Z. W. Brown, G. L. van Dijken, K. E. Lowry, M. M. Mills, M. A. Palmer, W. M. Balch, F. Bahr, N. R. Bates, C. Benitez-Nelson, B. Bowler, E. Brownlee, J. K. Ehn, K. E. Frey, R. Garley, S. R. Laney, L. Lubelczyk, J. Mathis, A. Matsuoka, B. G. Mitchell, G. W. K. Moore, E. Ortega-Retuerta, S. Pal, C. M. Polashenski, R. A. Reynolds, B. Scheiber, H. M. Sosik, M. Stephens, and J. H. Swift. (2012) Massive phytoplankton blooms under Arctic sea ice. *Science* 336(6087): 1408, [doi:10.1126/science.1215065](https://doi.org/10.1126/science.1215065)
- Arrigo, K. R., D. K. Perovich, R. S. Pickart, Z. W. Brown, G. L. van Dijken, K. E. Lowry, M. M. Mills, M. A. Palmer, W. M. Balch, F. Bahr, N. R. Bates, C. Benitez-Nelson, E. Brownlee, K. E. Frey, S. R. Laney, J. Mathis, A. Matsuoka, B. G. Mitchell, G. W. K. Moore, R. A. Reynolds, H. M. Sosik, and J. H. Swift. (2012) Phytoplankton blooms beneath the sea ice in the Chukchi Sea. Submitted to *J. Geophys. Res. Oceans* 2 Nov. 2012.
- Barber, D., R. De Abreu, and E. LeDrew (1991) Optical Extinction And Microwave Scattering Within A Seasonally Varying Snow Covered Sea Ice Surface, *Geoscience and Remote Sensing Symposium*, 799-802.
- Bates, N.R., M.H.P. Best, D.A. Hansell. 2005. Spatio-temporal distribution of dissolved inorganic carbon and net community production in the Chukchi and Beaufort Seas. *Deep Sea Research II* 54:3303-3323.
- Bernhard, G., C. R. Booth, J. C. Ehamjian, R. Stone, and E. G. Dutton (2007) Ultraviolet and visible radiation at Barrow, Alaska: Climatology and influencing factors on the basis of version 2 National Science Foundation network data, *J. Geophys. Res.*, 112, D09101, [doi:10.1029/2006JD007865](https://doi.org/10.1029/2006JD007865).
- Briegleb, B. P., and B. Light (2007) A Delta-Eddington Multiple Scattering Parameterization for Solar Radiation in the Sea Ice Component of the Community Climate System Model, *NCAR Technical Note*, 1-108.
- Carmack, E.C. and D.C. Chapman. 2003. Wind-driven shelf/basin exchange on an Arctic shelf: The joint roles of ice cover extent and shelf-break bathymetry. *Geophys. Res. Lett.* 30(14): 9 (1-4).

- Carmack, E.C. and R.W. Macdonald. 2002. Oceanography of the Canadian Shelf of the Beaufort Sea: A Setting for Marine Life. *Arctic* 55:29-45.
- Carmack E. C., R. W. Macdonald, and S. Jasper. 2004. Phytoplankton productivity on the Canadian Shelf of the Beaufort Sea. *Mar. Ecol. Prog. Ser.* 277: 37-50, doi:10.3354/meps277037
- Carmack, E. C., D. G. Barber, J. Christensen, R. Macdonald, B. Rudels, E. Sakshaug. 2006. Climate variability and physical forcing of the food webs and the carbon budget on panarctic shelves. *Progr. Oceanogr.* 71(2-4): 145-181.
- Codispoti, L. A., C. N. Flagg, and J. H. Swift. 2009. Hydrographic conditions during the 2004 SBI process experiments. *Deep Sea Res. II* 56: 1144-1163.
- Codispoti, L. A., C. N. Flagg, V. Kelly, and J. H. Swift. 2005. Hydrographic conditions during the 2002 SBI process experiments. *Deep Sea Res. II* 52: 3199-3226.
- Comiso, J. C., C. L. Parkinson, R. Gersten, and L. Stock. 2008. Accelerated decline in the Arctic sea ice cover. *Geophys. Res. Lett.* 35: L01703.
- Cota, G. F., L. R. Pomeroy, W. G. Harrison, E. P. Jones, F. Peters, W. M. Sheldon Jr., and T. R. Weingartner. 1996. Nutrients, primary production and microbial heterotrophy in the southeastern Chukchi Sea: Arctic summer nutrient depletion and heterotrophy. *Mar. Ecol. Prog. Ser.* 135: 247-258, doi:10.3354/meps135247
- Cullen, J.J., P.J. Neale, and M.P. Lesser. (1992) Biological weighting function for the inhibition of phytoplankton photosynthesis by ultraviolet radiation, *Science*, 258, 646-650.
- de Mora, S.J., S. Demers and M. Vernet, 2000. The effects of UV radiation on marine ecosystems. *Environmental Chemistry Series*. 336 pp.
- Douglas, D. C. (2010) Arctic sea ice decline: Projected changes in timing and extent of sea ice in the Bering and Chukchi Seas: U.S. Geological Survey Open-File Report 2010-1176, 32 p.
- Druckenmiller, M.L.; H. Eicken; M. Johnson; D. Pringle; C. Williams (2009) Towards an integrated coastal sea-ice observatory: System components and a case study at Barrow, Alaska. *Cold Regions Science and Technology* 56 (1-2), 61-72.

- Eppley, R. (1972) Temperature and phytoplankton growth in the sea. *Fish. Bull.* 70: 1063-1085.
- Ehn, J., C. J. Mundy, D. Barber, H. Hop, A. Rossnagel, and J. Stewart. (2011) Impact of horizontal spreading on light propagation in melt pond covered seasonal sea ice in the Canadian Arctic. *J. Geophys. Res.* 116(C9), doi: 10.1029/2010JC006908.
- Fasham, M. J. R., H. W. Ducklow, and S. M. McKelvie (1990) A nitrogen-based model of plankton dynamics in the oceanic mixed layer. *J. Mar. Res.* 48: 591-639.
- Frey, K. E., D. K. Perovich, and B. Light (2011) The spatial distribution of solar radiation under a melting Arctic sea ice cover. *Geophys. Res. Lett.*, 38, L22501, doi:10.1029/2011GL049421
- Gosselin, M., M. Levasseur, P.A. Wheeler, R.A. Horner, and B.C. Booth. 1997. New measurements of phytoplankton and ice algal production in the Arctic Ocean. *Deep-Sea Research Part II* 44(8): 1623-1644.
- Grebmeier, J.M., J.E. Overland, S.E. Moore, E.V. Farley, E.C. Carmack, L.E. Cooper, K.E. Frey, J.H. Helle, F.A. McLaughlin, S.L. McNutt. 2006. A major ecosystem shift in the Northern Bering Sea. *Science* 311:1461-1464.
- Grebmeier, J., W. O. Smith Jr., and R. J. Conover (1995) Biological processes on Arctic Continental Shelves: Ice-Ocean-Biotic Interactions. In *Arctic Oceanography: Marginal Ice Zones and Continental Shelves*. Coastal and Estuarine Studies 49: pp. 231-261. AGU Press.
- Gregg, W., and K. Carder (1990) A simple spectral solar irradiance model for cloudless maritime atmospheres, *Limn. Oceanogr.*, 35(8), 1657-1675.
- Helbling, E. W., V. Villafane, M. Ferrario, and O. Holm-Hansen. (1992) Impact of natural ultraviolet radiation on rates of photosynthesis and on specific marine phytoplankton species, *Mar. Ecol. Prog. Ser.*, 92, 89–100.
- Helbling, E. W., and V. Villafañe (2002) UV radiation effects on phytoplankton primary production: a comparison between Arctic and Antarctic marine ecosystems. In: D. O. Hessen, ed., *UV Radiation and Arctic Ecosystems*. Ecological Studies vol. 153, Springer-Berlin.

- Hill V., and G. Cota. 2005. Spatial patterns of primary production on the shelf, slope and basin of the Western Arctic in 2002. *Deep-Sea Res. II* 52: 3344-3354, [doi:10.1016/j.dsr2.2005.10.001](https://doi.org/10.1016/j.dsr2.2005.10.001)
- Hill, V., G. Cota, and D. Stockwell. 2005. Spring and summer phytoplankton communities in the Chukchi and Eastern Beaufort Seas. *Deep Sea Research II* 52:3369-3385.
- Holm-Hansen, O. (1997) Short- and long-term effects of UVA and UVB on marine phytoplankton productivity, *Photochem. Photobiol.*, 65, 266–268.
- Holm-Hansen, O., E. W. Helbling, and D. Lubin. (1993) Ultraviolet-radiation in Antarctica: Inhibition of primary production, *Photochem. Photobiol.*, 58, 567–570.
- Hunt, G. L., K. O. Coyle, L. B. Eisner, E. V. Farley, R. A. Heintz, F. Mueter, J. M. Napp, J. E. Overland, P. H. Ressler, S. Salo, and P. J. Stabeno (2011) Climate impacts on eastern Bering Sea foodwebs: a synthesis of new data and an assessment of the Oscillating Control Hypothesis. *ICES J. Mar. Sci.* 68(6) 1230-1243. Doi: 10.1093/icesjms/fsr036
- Hunt, G. L., A. L. Blanchard, P. Boveng, P. Dalpadado, K. F. Drinkwater, L. Eisner, R. R. Hopcroft, K. M. Kovacs, B. L. Norcross, P. Renaud, M. Reigstad, M. Renner, H. R. Skjoldal, A. Whitehouse, and R. A. Woodgate. (2013) The Barents and Chukchi Seas: Comparison of two Arctic shelf ecosystems. *J. Mar. Sys.* 109-110, pp. 43-68.
- Jin, Z., K. Stamnes, W. F. Weeks, and S. Tsay (1994) The effect of sea ice on the solar energy budget in the atmosphere-sea ice-ocean system: A model study, *J. Geophys. Res.*, 99(C12), 25281-25294, doi:10.1029/94JC02426.
- Kellogg, C. T. E., S. D. Carpenter, A. A. Renfro, A. Sallon, C. Michel, J. K. Cochran, J. W. Deming (2011) Evidence for microbial attenuation of particle flux in the Amundsen Gulf and Beaufort Sea: elevated hydrolytic enzyme activity on sinking aggregates. *Polar Biol* 34: 2007-2023. doi:0.1007/s00300-011-1015-0.
- Kwok, R., and D. A. Rothrock (2009) Decline in Arctic sea ice thickness from submarine and ICESat records: 1958-2008, *Geophys. Res. Lett.*, 36.

- Lavoie, D., K. Denman, and C. Michel (2005), Modeling ice algal growth and decline in a seasonally ice-covered region of the Arctic (Resolute Passage, Canadian Archipelago), *J. Geophys. Res.*, 110, C11009, doi:[10.1029/2005JC002922](https://doi.org/10.1029/2005JC002922).
- Lavoie, D., K. L. Denman, and R. W. Macdonald. (2010) Effects of future climate change on primary productivity and export fluxes in the Beaufort Sea. *J. Geophys. Res.* 115: C4, doi:10.1029/2009JC005493.
- Law, C. S., E. R. Abraham, J. A. Watson, and M. I. Liddicoat. (2003) Vertical eddy diffusivity and nutrient supply to the surface mixed layer of the Antarctic Circumpolar Current. *J. Geophys. Res.* 108(C8) 3273.
- Laws, E. A., P. G. Falkowski, W. O. Smith Jr., H. Ducklow, J. J. McCarthy. (2000) Temperature effects on export production in the open ocean. *Global Biogeochemical Cycles* 14(4): 1231-1246.
- Leu, E., S. Falk-Peterson, and D. O. Hessen. (2007) Ultraviolet radiation negatively affects growth but not food quality of arctic diatoms. *Limnol. Oceanogr.* 52(2): 787-797.
- Litchman, E., P.J. Neale, and A.T. Banaszak. (2002) Increased sensitivity to ultraviolet radiation in nitrogen-limited dinoflagellates: photoprotection and repair, *Limnol. Oceanogr.*, 47, 86-94.
- Lindsay, R. W. and J. Zhang. (2005) The thinning of Arctic sea ice, 1988-2003: have we passed a tipping point? *J. Climate* **18**: 4879-4894.
- Lindsay, R. W. (2010) Unified Sea Ice Thickness Climate Data Record, Polar Science Center, Applied Physics Laboratory, University of Washington, psc.apl.washington.edu/sea_ice_cdr, digital media.
- Loeng, H., K. Brander, E. Carmack, S. Denisenko, K. Drinkwater, B. Hansen, K. Kovacs, P. Livingston, F. McLaughlin, and E. Sakshaug. (2006) Marine Systems, p. 453-538 In: *Arctic Climate Impact Assessment: An Assessment of Consequences of Climate Variability and Change and the Effects of Increased UV in the Arctic Region*, Cambridge Univ. Press.
- Lu, Zheng. (2006). Optical Absorption of Pure Water in the Blue and Ultraviolet. Ph.D. Thesis, Texas A&M University.

- Madronich, S., R. L. McKenzie, L. O. Bjorn, and M. M. Caldwell. (1998) Changes in biologically active ultraviolet radiation reaching the Earth's surface. *J. Photochemistry Photobiology B: Biology* 46(1-3): 5-19.
- Maslanik, J., J. Stroeve, C. Fowler, and W. Emery. (2011) Distribution and trends in Arctic sea ice age through spring 2011. *Geophys. Res. Lett.* 38(L13502), doi:10.1029/2011GL047735.
- Martin J., J.-È. Tremblay, J. Gagnon, G. Tremblay, A. Lapoussiere, C. Jose, M. Poulin, M. Gosselin, Y. Gratton, and C. Michel. (2010) Prevalence, structure and properties of subsurface chlorophyll maxima in Canadian Arctic waters. *Mar. Ecol. Prog. Ser.* 412: 69-84, doi:10.3354/meps08666.
- McClain, C. R., K. R. Arrigo, K. Tai, and D. Turk (1996) Observations and simulations of physical and biological processes at ocean weather station P, 1951-1980, *J. Geophys. Res.*, 101, 3697-3713, doi:10.1029/95JC03052.
- Meier, W. N., J. Stroeve, and F. Fetterer. (2007) Whither Arctic sea ice? A clear signal of decline regionally, seasonally and extending beyond the satellite record. *Annals of Glaciology* 46, 428-434.
- Miller, J. R., and G. L. Russell (2000), Projected impact of climate change on the freshwater and salt budgets of the Arctic Ocean by a global climate model, *Geophys. Res. Lett.*, 27(8), 1183–1186, doi:[10.1029/1999GL007001](https://doi.org/10.1029/1999GL007001).
- Monod, J. (1942) *Recherches sur la Croissance des Cultures Bacteriennes*. Hermann, Paris.
- National Snow and Ice Data Center (NSIDC) (2012). Accessed November 1, 2012 at <http://nsidc.org/arcticseaicenews>
- Nicolaus, M., C. Katlein, J. Maslanik, and S. Hendricks. (2012) Changes in Arctic sea ice result in increasing light transmittance and absorption. *Geophys. Res. Lett.*, in press, doi:10.1029/2012GL053738
- Neale P. J., R. F. Davis, and J. J. Cullen. (1998a) Interactive effects of ozone depletion and vertical mixing on photosynthesis of Antarctic phytoplankton. *Nature* 392:585–589.

- Neale, P.J., J.J. Cullen and R.F. Davis (1998b). Inhibition of marine photosynthesis by ultraviolet radiation: Variable sensitivity of phytoplankton in the Weddell-Scotia Sea during the austral spring. *Limnol. Oceanogr.* 43: 433–448.
- Neale, P. J., and D. J. Kieber. (2000) Assessing biological and chemical effects of UV in the marine environment: spectral weighting functions. In: Hester RE, Harrison RM (eds) *Causes and environmental implications of increased U.V.-B. radiation*. Royal Society of Chemistry, Cambridge.
- Neale, P. J., J. J. Fritz, and R. F. Davis. (2001) Effects of UV on photosynthesis of Antarctic phytoplankton: Models and application to coastal and pelagic assemblages, *Rev. Chil. Hist. Nat.*, 74, 283-292.
- Nghiem, S. V., I. G. Rigor, D. K. Perovich, P. Clemente-Colon, J. W. Weatherly, G. Neumann. (2007) Rapid reduction of Arctic perennial sea ice. *Geophys. Res. Lett.* 34: L19504.
- Pabi, S., G. L. van Dijken and K. R. Arrigo. (2008) Primary Production in the Arctic Ocean, 1998-2006. *J. Geophys. Res.* 113: C08005, doi:10.1029/2007JC004578
- Palmer, M. A., K. R. Arrigo, C. J. Mundy, J. K. Ehn, M. Gosselin, D. G. Barber, J. Martin, E. Alou, S. Roy, and J.-È. Tremblay. (2011) Spatial and temporal variation of photosynthetic parameters in natural phytoplankton assemblages in the Beaufort Sea, Canadian Arctic. *Polar Biol.* 34: 1915-1928, doi:10.1007/s00300-011-1050-x
- Pickart, R. S. (2004) Shelf break circulation in the Alaskan Beaufort Sea: Mean structure and variability. *J. Geophys. Res.* 109: C04024.
- Perovich, D. K. (1990) Theoretical estimates of light reflection and transmission by spatially complex and temporally varying sea ice covers. *J. Geophys. Res.* 95: 9557-9567.
- Perovich, D. K. (1993) A theoretical model of ultraviolet light transmission through Antarctic sea ice. *J. Geophys. Res.* 98: 22579-22587.
- Perovich, D. K. (1996) The Optical Properties of Sea Ice. *Cold Regions Research and Engineering Laboratory Monograph*, 96-1.
- Perovich, D. K. and J.W. Govoni. (1991) Absorption coefficients of ice from 250 to 400 nm. *Geophys. Res. Lett.* 18(7), 1233–1235.

- Perovich, D. K. (1998) Physics of ice covered seas, Volume 1, pp. 446. Univ. of Helsinki Press.
- Perovich, D. K., T. C. Grenfell, J. A. Richter-Menge, B. Light, W. B. Tucker III, and H. Eicken. (2003) Thin and thinner: sea ice mass balance measurements during SHEBA. *J. Geophys. Res.* 108, C3, 8050, doi:10.1029/2001JC001079.
- Perovich, D. K. (2005) On the aggregate-scale partitioning of solar radiation in Arctic sea ice during the Surface Heat Budget of the Arctic Ocean (SHEBA) field experiment. *J. Geophys. Res.* 110(C3), doi:10.1029/2004JC002512.
- Perovich, D. K., K. F. Jones, B. Light, H. Eicken, T. Markus, J. Stroeve, and R. Lindsay. (2011) Solar partitioning in a changing Arctic sea-ice cover, *Annals of Glaciology*, 52(57), 192-196.
- Perovich, D. K., and C. Polashenski. (2012) Albedo evolution of seasonal Arctic sea ice. *Geophys. Res. Lett.* 39: L08501, doi:10.1029/2012GL051432
- Perrette M., A. Yool, G. D. Quartly, and E. E. Popova. (2011) Near-ubiquity of ice-edge blooms in the Arctic. *Biogeosciences* 8: 515-524.
- Petrich, C., H. Eicken, J. Zhang, J. Krieger, Y. Fukamachi, and K. I. Ohshima. (2012) Coastal landfast sea ice decay and breakup in northern Alaska: key processes and seasonal prediction. *J. Geophys. Res.* 117(C02003), doi:10.1029/2011JC007339
- Rex, M. (2012) Arctic ozone loss and climate change. Presented at BSRN Workshop, Potsdam, 1-2 August 2012.
- Saenz, B. L. (2011) Spatial and temporal dynamics of primary production in Antarctic sea ice. Ph.D. thesis, Stanford University.
- Sakshaug, E. 2004. Primary and secondary production in the Arctic Seas, in *The Organic Carbon Cycle in the Arctic Ocean*, edited by R. Stein and R. W. Macdonald, pp. 57–81, Springer-Verlag, Berlin.
- Segelstein, D. J. (1981) The complex refractive index of water. Ph.D. thesis, University of Missouri-Kansas City.
- Shirasawa, K., H. Eicken, K. Tateyama, T. Takatsuka, and T. Kawamura. (2009) Sea ice thickness variability in the Chukchi Sea, spring and summer 2002-2004. *Deep-Sea Res.* II 56(17): 1182-1200.

- Smith, R. C. et al., (1992) Ozone depletion: ultraviolet radiation and phytoplankton biology in Antarctic waters. *Science* 255: 952-959.
- Tremblay, J.-É., C. Michel, K. A. Hobson, M. Gosselin, and N. M. Price. (2006) Bloom dynamics in early opening waters of the Arctic Ocean. *Limnol Oceanogr* 51(2): 900-012.
- Villafane, V. E., E. W. Helbling, O. Holm-Hansen, and B. E. Chalker. (1995) Acclimation of Antarctic natural phytoplankton assemblages when exposed to solar ultraviolet radiation. *J. Plankton Res.* 17: 2295-2306.
- Walsh, J.J., D.A. Dieterle, W. Maslowski, J.M. Grebmeier, T.E. Whitledge, M. Flint, I.N. Sukhanova, N. Bates, G.F. Cota, D. Stockwell, S.B. Moran, D.A. Hansell, and C.P. McRoy. 2005. A numerical model of seasonal primary production within the Chukchi/Beaufort Seas. *Deep Sea Research II* 52:3541-3576.
- Wang, J., G. F. Cota, and J. Comiso. (2005) Phytoplankton in the Beaufort and Chukchi Seas: distribution, dynamics, and environmental forcing. *Deep-Sea Res. II* 52: 3355-3368, [doi:10.1016/j.dsr2.2005.10.014](https://doi.org/10.1016/j.dsr2.2005.10.014)
- Woodgate, R. A., K. Aagaard, and T. J. Weingartner (2006), Interannual changes in the Bering Strait fluxes of volume, heat and freshwater between 1991 and 2004, *Geophys. Res. Lett.*, 33, L15609, doi:[10.1029/2006GL026931](https://doi.org/10.1029/2006GL026931).
- Wroblewski, J. S. (1977) A model of phytoplankton plume formation during variable Oregon upwelling. *J. Mar. Res.* (35): 357-394.
- Zhang, J., Y. H. Spitz, M. Steele, C. Ashjian, R. Campbell, L. Berline, M. Matrai. (2010) Modeling the impact of declining sea ice on the Arctic marine planktonic ecosystem. *J. Geophys. Res.* 115: C10015, doi:[10.1029/2009JC005387](https://doi.org/10.1029/2009JC005387)

TABLES

Table 1. Description model runs of snow, ice, and pond thickness and development.

References are given in relation to the SHEBA data that each run is based on if needed in the second column. The first row shows the data for the standard model run.

Ice Category	Description	Initial Ice Thickness (m)	Final Ice Thickness (m)	Date Final Ice Thickness	Initial Snow Thickness (m)	Date Final Snow	Notes on Transition Periods	Pond Thickness
FYI, with ponds *STANDARD RUN*	FYI, later ice year	1.6	1.1	July 18 (day 199)	0.32	Ice stays at 1.6 m until June 13 (day 164), then starts to decrease; Snow stays at 0.32 until May 19 (day 139), decreases to 0.11 by June 13 (day 164), 0 by June 28 (day 179)	Ponds form starting snow disappearance on June 28 (day 179), increases to 30 cm by ice break up on July 18 (day 199)	0-30 cm (See Fig. 1d)
MYI, no pond	Thicker MYI, modeled after gauge 26, The Ridge line (Fig. 2c), Perovich et al. 2003	5.4	3.22	-	0.76	0.76 m to 2-3 cm by July 7 (day 190); snow melts a month later than early snow melt year below	May 15-May 29 (day 135-149) transition from -1C to 0C	-
MYI, no pond	Thinner MYI, modeled after gauge 63, Baltimore line, Perovich et al. 2003; early snow melt	2.1 m	1.07 m	-	0.6	Continues through season, from 60 cm to 40 cm on June 12 (day 163), then 2 cm present through rest of season	Melt begins May 29 (day 149), Snow down to 40 cm by June 12 (day 163), then down to 2 cm by July 7 (day 188) and ice melts	-
FYI with ponds	FYI with ponds, early ice year; modeled after gauge 203 (Fig. 2d), Quebec line	1.07	0.45	July 4 (day 185)	0.13	Snow gone by June 4 (day 155)	Snow starts melting May 21 (day 141), melts away by June 4 (day 155); Ice starts melting June 4 (day 155) to 1.0 m by June 11 (day 162), melts from June 11 (day 162)-July 4 (day 185) 1.0 m to 0.45 m, then breaks up	0 – 30 cm, relatively linear growth between June 11 (day 162) and July 4 (day 185) (See Fig. 1d)

Table 2. Biological weighting functions and wavelengths used in UVR inhibition model. Reproduced from data presented in Neale and Kieber (2000).

Wavelength (nm)	BWF, ϵ ($\mu\text{Ein m}^{-2} \text{s}^{-1}$) ⁻¹
285	2.470
290	0.497
295	0.264
300	0.181
305	0.130
310	0.099
315	0.077
320	0.059
325	0.048
332	0.037
337	0.030
340	0.026
349	0.019
350	0.018
380	0.002
400	0.002

Table 3. Model parameters and variables for the biological model. If the variable value is based on literature, the reference is given in the right column.

Model Parameters and Variables	Description	Value	Units	Reference
Sphy	Small phytoplankton functional group	Varies; initial set at 0.01	mmol N m ⁻³	
Lphy	Large phytoplankton functional group	Varies; initial set at 0.01	mmol N m ⁻³	
Szoo	Small zooplankton functional group	Varies; initial set at 0.01	mmol N m ⁻³	
Lzoo	Large zooplankton functional group	Varies; initial set at 0.01	mmol N m ⁻³	
Detr	Detritus	Varies; initial set at 0.05	mmol N m ⁻³	ICESCAP E data
Chla	Chlorophyll <i>a</i>	Varies; initial set at 0.01	mg Chl <i>a</i> m ⁻³	
Sal	Salinity	33.0	psu	Codispoti et al. 2005
Temp	Temperature	Varies; -1.9°C initial in water column under ice	°C	Codispoti et al. 2005
K_z	Water column eddy diffusivity coefficient	0.11×10^{-4}	m ² s ⁻¹	Law et al. 2003
n_z	Number vertical layers in water column	50	m	
Δz	Thickness of each water column layer	1	m	
n_{ice}	Number of vertical ice and snow layers (thicknesses vary also)	varies	m	
Nitrate, NO ₃	Initial wintertime concentration throughout water column	16	mmol N m ⁻³	Codispoti et al. 2005
Ammonium, NH ₄	Initial wintertime concentration throughout water column	0.01	mmol N m ⁻³	Codispoti et al. 2005
Dissolved Organic Nitrogen, DON	Initial wintertime concentration throughout water column	0	mmol N m ⁻³	Codispoti et al. 2005
PAR	Photosynthetically active radiation, 400-700 nm	dynamic	μmol m ⁻² s ⁻¹	
PUR	Photosynthetically usable radiation (i.e., proportion of PAR that phytoplankton can utilize)	dynamic	μmol m ⁻² s ⁻¹	
E'_{kmax} Sphy	Maximum observed E_k (light saturation parameter) for small phytoplankton functional group	25	μEin m ⁻² s ⁻¹	Palmer et al. 2012 <i>submitted</i>
E'_{kmax} Lphy	Maximum observed E_k (light saturation parameter) for large phytoplankton functional group	45	μEin m ⁻² s ⁻¹	Palmer et al. 2012 <i>submitted</i>

K_{NO_3} Sphy	Half-saturation constant for NO_3 uptake by small phytoplankton functional group	0.5	mmol N m^{-3}	
K_{NO_3} Lphy	Half-saturation constant for NO_3 uptake by large phytoplankton functional group	0.9	mmol N m^{-3}	
K_{NH_4} Bact	Half-saturation constant for NO_3 uptake by bacteria functional group	0.5	mmol N m^{-3}	
K_{NH_4} Sphy	Half-saturation constant for NH_4 uptake by small phytoplankton functional group	0.5	mmol N m^{-3}	
K_{NH_4} Lphy	Half-saturation constant for NH_4 uptake by large phytoplankton functional group	0.9	mmol N m^{-3}	
K_{DON} Bact	Half-saturation constant for DON uptake by bacteria functional group	0.5	mmol N m^{-3}	
G_o Sphy	Specific growth rate of small phytoplankton functional group at 0°C	0.28	d^{-1}	Palmer et al. 2012 submitted
G_o Lphy	Specific growth rate of large phytoplankton functional group at 0°C	0.97	d^{-1}	Palmer et al. 2012 submitted
G_o Bact	Specific growth rate of bacteria functional group at 0°C	1.2	hr^{-1}	Laws et al. 2000
g_{ge}	Gross growth efficiency for bacteria, defined as the ratio of bacterial NH_4 to DON uptake	0.6	-	Fasham et al. 1990
r_o	Eppley growth constant for phytoplankton	0.0633		Arrigo et al. 1998
r_o	Growth constant for bacteria	0.092		Walsh et al. 2005
C/N Sphy	Carbon to nitrogen ratio of small phytoplankton functional group	106/16	mol:mol	
C/N Lphy	Carbon to nitrogen ratio of large phytoplankton functional group	106/12	mol:mol	
C/N Bact	Carbon to nitrogen ratio of bacteria functional group	100/20	mol:mol	
$mort$ Sphy	Death and loss rate of small phytoplankton functional group	0.045	d^{-1}	Fasham et al. 1990
$mort$ Lphy	Death and loss rate of large phytoplankton functional group	0.055	d^{-1}	Fasham et al. 1990
$mort$ Bact	Death and loss rate of bacteria functional group	0.2	d^{-1}	Fasham et al. 1990
$Sinking$	Sinking coefficient for detritus and phytoplankton	0.1-1	$m d^{-1}$	
ex_{Bact}	Remineralization and excretion rate of N to NH_4 pool by bacteria	0.1	d^{-1}	Maloney and Field 1991
$p_{lzoo-lphy}$	Food preference for grazer (large zooplankton functional group) on prey (large phytoplankton functional group)	0.3	mmol N m^{-3}	Maloney and Field 1991
$p_{lzoo-szoo}$	Food preference for grazer (large zooplankton functional group) on	0.7	mmol N m^{-3}	Maloney and Field

	prey (small zooplankton functional group)			1991
$p_{szoo-sphy}$	Food preference for grazer (small zooplankton functional group) on prey (small phytoplankton functional group)	0.7	mmol N m ⁻³	Maloney and Field 1991
$p_{szoo-bact}$	Food preference for grazer (small zooplankton functional group) on prey (bacteria functional group)	0.3	mmol N m ⁻³	Maloney and Field 1991
m	Degree of switching between prey sources	2.0		Fasham et al. 1990
g_{max}	Maximum food-acclimated grazing rate	1.0		Fasham et al. 1990
γ_{szoo}	Assimilation efficiency of prey for small zooplankton functional group	0.75	%	Fasham et al. 1990
γ_{Lzoo}	Assimilation efficiency of prey for large zooplankton functional group	0.75	%	Fasham et al. 1990
$mort\ Szoo$	Death and loss rate of small zooplankton functional group	0.01	d ⁻¹	Fasham et al. 1990
$mort\ Lzoo$	Death and loss rate of large zooplankton functional group	0.05	d ⁻¹	Fasham et al. 1990
ex_{szoo}	Excretion rate of N by small zooplankton functional group; fraction that goes to NH ₄ vs. DON pools given by Z_{NH_4ex}	0.03	d ⁻¹	Fasham et al. 1990
ex_{Lzoo}	Excretion rate of N by large zooplankton functional group; fraction that goes to NH ₄ vs. DON pools given by Z_{NH_4ex}	0.1	d ⁻¹	Fasham et al. 1990
Z_{NH_4ex}	Fraction excrete as NH ₄ vs. DON for all zooplankton	0.75	%	Fasham et al. 1990
mt_{szoo}	Basal metabolism of small zooplankton functional group to NH ₄	0.1	d ⁻¹	Fasham et al. 1990
mt_{Lzoo}	Basal metabolism of large zooplankton functional group to NH ₄	0.1	d ⁻¹	Fasham et al. 1990
$Remin\ detr$	Remineralization rate of detritus to DON pool	0.05	d ⁻¹	Fasham 1990
$Remin\ DON$	Remineralization rate of DON to NH ₄ pool	0.05	d ⁻¹	Fasham 1990
$C/Chl\ Sphy$	Carbon to Chlorophyll <i>a</i> ratio of small phytoplankton functional group	100	g:g	Sakshaug 2004
$C/Chl\ Lphy$	Carbon to Chlorophyll <i>a</i> ratio of large phytoplankton functional group	30	g:g	Sakshaug 2004
$a_{ph}^*(\lambda)$	Spectral phytoplankton absorption coefficient	Fig. 6		Arrigo et al. 1998
a_{max}^*	Maximum value of the spectral phytoplankton coefficient from 400-700 nm	Fig. 6		Arrigo et al. 1998 and recent

Table 4. References for comparison of model results for primary production. Shown in the left column are the referred literature, followed by the method for achieving the results, annual rates of net primary production (NPP) per area ($\text{g C m}^{-2} \text{yr}^{-1}$), average daily rates of NPP (g or $\text{mg C m}^{-2} \text{d}^{-1}$), and notes on bloom length/peak occurrence.

Reference	Method	Domain	Annual PP $\text{g C m}^{-2} \text{yr}^{-1}$	Daily Rates of NPP	Bloom Length and Peak
Arrigo and Van Dijken 2011	Satellite (SeaWiFS and MODIS Aqua), net PP algorithm ^a	Beaufort: 160°W to 100°W, Chukchi: 180° to 160°W	Chukchi: 96.9±7.4 $\text{g C m}^{-2} \text{yr}^{-1}$ Beaufort: 71.3±4.9 $\text{g C m}^{-2} \text{yr}^{-1}$	Peak for Arctic: 850 $\text{mg C m}^{-2} \text{d}^{-1}$ (range 786-1240 $\text{mg C m}^{-2} \text{d}^{-1}$) reached May 23±9.2 days; high through June and July (600-700 $\text{mg C m}^{-2} \text{d}^{-1}$), declines by Aug. (425 $\text{mg C m}^{-2} \text{d}^{-1}$) to 100 $\text{mg C m}^{-2} \text{d}^{-1}$ by end of Sept.	Chukchi: bloom length ^b 119±16.1 days, peaks June 10±24.7 days; Beaufort: bloom length 61.2 ±15.8 days, peaks July 5 ±15.3 days
Lavoie et al. 2010	Canadian Global Climate Model; 1D coupled to 3D	Canadian Beaufort Sea	22.1±1.8 $\text{g C m}^{-2} \text{yr}^{-1}$	Canadian Beaufort Sea only: peaks in early July, range 500-800 $\text{mg C m}^{-2} \text{d}^{-1}$; 300-400 $\text{mg C m}^{-2} \text{d}^{-1}$ by August and 100 $\text{mg C m}^{-2} \text{d}^{-1}$ by September	Bloom length estimated from Fig. 5: 40-50 days; Open water days: 95-128 days
Lavoie et al. 2010	Review of other sources ^c	Canadian Beaufort Sea and similar Arctic shelf-bay systems	15-50 $\text{g C m}^{-2} \text{yr}^{-1}$;		
Walsh et al. 2005	Model (3D fully coupled)	Western Arctic shelf/basin 170°W to 130°W	97.4 $\text{g C m}^{-2} \text{yr}^{-1}$	Peak in July-Aug. of 709 $\text{mg C m}^{-2} \text{d}^{-1}$; 9.9 $\text{mg C m}^{-2} \text{d}^{-1}$ in April-May, 279.7 $\text{mg C m}^{-2} \text{d}^{-1}$ in June, 578.3 $\text{mg C m}^{-2} \text{d}^{-1}$ in Sept.-Oct., 146.6 $\text{mg C m}^{-2} \text{d}^{-1}$ in Nov.-Dec.	
Hill and Cota 2005	Measured during SBI	Chukchi and Beaufort shelves	90 $\text{g C m}^{-2} \text{yr}^{-1}$	Pre-bloom: 0.3 $\text{g C m}^{-2} \text{d}^{-1}$; max. of 8 $\text{g C m}^{-2} \text{d}^{-1}$ during initial MIZ surface bloom; 0.08-2.90 $\text{g C m}^{-2} \text{d}^{-1}$ during bloom based on location (higher at shelf break, low in basin)	
Hill and Cota 2005	Measured in past studies	Chukchi Sea (shelf and basin)		Observed max 15 $\text{g C m}^{-2} \text{d}^{-1}$ in high nutrient water, average of 0.30-0.75 $\text{g C m}^{-2} \text{d}^{-1}$ over shelf, 0.12 $\text{g C m}^{-2} \text{d}^{-1}$ over the basin ^d	
Arrigo et al. <i>submitted</i>	Measured during ICESCAPE	Chukchi and Beaufort shelves	70 g C m^{-2} during July 4-8 at start of under ice bloom	1.2-4.8 $\text{g C m}^{-2} \text{d}^{-1}$ in under ice bloom	
This study	Model (1D)	Chukchi Shelf (72°N, 169°W)	30-40 $\text{g C m}^{-2} \text{yr}^{-1}$ (see Fig. 16)	Varies depending on run; see Fig. 10,15,16; Tables 7, 8	Varies depending on run; see Fig. 10,15,16; Tables 7, 8

^a Note: Satellite study doesn't include SCM-based production; Estimates this as an 7.6% (Chukchi) and 11.7% (Beaufort) underestimate of annual PP, largest error in summer; CDOM and pigment packaging may result in overestimate of 6.1% NPP

^bNote: bloom length defined as days when NPP exceeds 500 $\text{mg C m}^{-2} \text{d}^{-1}$

^cNote: Other sources cited by Lavoie et al. 2010 for estimate of regional NPP are: Carmack et al. 2004; Legendre et al. 1992; Macdonald et al. 1987, 1998; Sakshaug 2004; Subba Rao and Platt 1984; Tremblay et al. 2008.

^dNote: Hill and Cota 2005 present data from a variety of sources, including Gosselin et al. 1997, Cota et al. 1996, Springer and McRoy 1993

Table 5. Model results for light transmittance through the standard model run. Shown are the date and thickness for ice and ponds, and the resulting transmittance.

Model Run	Date	Ice thickness (m)	Pond thickness (m)	Transmittance
FYI with 30% pond (standard)	June 15	1.60 (snow: 0.10)	-	0.44%
	June 27	1.38	-	6.83%
	June 29	1.30	0.02	24.9%
	June 30	1.28	0.02	27.8%
	July 7	1.14	0.12	37.8%
	July 11	1.10	0.18	38.8%
	July 18	1.10	0.30	37.4%
	July 19	- (open water)	-	57.2%

Table 6. Model details for comparison of nitrate and chlorophyll data as shown in Figs. 9 and 10. Shown are the ice thicknesses, snow thickness, and pond thickness for the various model days shown. Peak bloom was reached on Jul 11, of 498.90 mg Chl *a* m⁻².

Date	Ice thickness (m)	Snow thickness (m)	Pond thickness (m)	Integrated Chl <i>a</i> (mg m⁻²)	Integrated POC (mg C m⁻²)
15-Jun	1.58	0.1		0.94	0.05
27-Jun	1.32	0.02		4.48	0.12
29-Jun	1.3		0.02	5.88	0.15
30-Jun	1.28		0.02	11.39	0.24
7-Jul	1.14		0.12	291.29	5.47
11-Jul	1.1		0.18	498.80	12.4
18-Jul	1.1		0.3	372.17	18.4
13-Aug	OW			380.37	17.5
12-Sep	OW			317.54	19.1
13-Oct	OW			284.56	14.0

Table 7. Results from model showing annual NPP compared to the standard model run (FYI 30% pond, shown in first column Table 1).

Model Run	Peak Bloom daily NPP, mg C m ⁻² d ⁻¹	Percent Difference in Peak NPP from Model Run	Days NPP >400 mg C m ⁻² d ⁻¹	Primary Bloom Type ^a	Peak Bloom Date and Type (Difference in days)	Annual NPP, g C m ⁻² yr ⁻¹	%NPP in UI vs. OW bloom	Percent Difference in Annual NPP from Standard Run
FYI, 0% pond	Under ice: 17.82; Open Water: 1271.75	-98.1%; +29.6%	27	OW	UI: June 28 (-9 days); OW: July 30 (+11 days)	32.8	0.3% UI; 99.7% OW	-4.66%
FYI, 10% pond	Under ice: 697.98; Open Water: 1160.41	-25.6%; +18.2%	22	MIZ	UI: July 7; OW: July 19 (0 days different)	33.8	26.1% UI; 73.9% OW	-1.84%
FYI, 30% pond (STANDARD)	Under ice: 938.19; Open Water: 981.70	n/a	18	UI and MIZ	UI: July 7; OW: July 19	34.4	30.1% UI; 69.9% OW	n/a
FYI, 50% pond	Under ice: 1011.75; Open Water: 694.75	+7.84%; -29.2%	18	UI and MIZ	UI: July 7; OW: July 19 (0 days different)	34.5	31.2% UI; 68.8% OW	0.16%
FYI, 30% pond, no zooplankton	Under ice: 952.15; Open Water: 1593.68	+1.49%; +62.3%	40	MIZ	UI: July 7; OW: July 19 (0 days different)	41.8	30.1% UI; 69.9% OW	21.3%
FYI, 30% pond, no UVR inhibition	Under ice: 959.31; Open Water: 1614.18	+2.25%; +64.4%	22	MIZ	UI: July 7; OW: July 19 (0 days different)	38.0	28.3% UI; 71.7% OW	10.3%

^aNote: MIZ: Marginal ice zone bloom, defined as a bloom that occurs within 1-2 days of ice break-up in the surface waters adjacent to the ice edge. UI: under ice bloom. OW: bloom that occurs in open water >5 days after the ice edge retreats.

Table 8. Results from model showing annual NPP in various model runs where ice cover was modified from the standard model run. Details for the ice cycles are given in Table 1.

Model Run	Annual NPP, g C m⁻² yr⁻¹	Peak Bloom daily NPP, mg C m⁻² d⁻¹	Date	Bloom length	Percent UI vs. OW
Open water (no ice)	38.1	569	May 10; OW	22	100% OW
FYI early pond, 10% pond cover	29.9	777	July 4, MIZ	12	23.2% UI; 76.8% OW
FYI early pond, 30% pond cover	30.5	619	June 20; UI	17	30.8% UI; 69.2% OW
FYI early pond, 50% pond cover	30.6	677	June 20; UI	17	32.9% UI; 67.1% OW
MYI 2m	0.84	19.0	August 10; UI	0	100% UI
MYI 5m	0.64	12.9	August 22; UI	0	100% UI

FIGURES

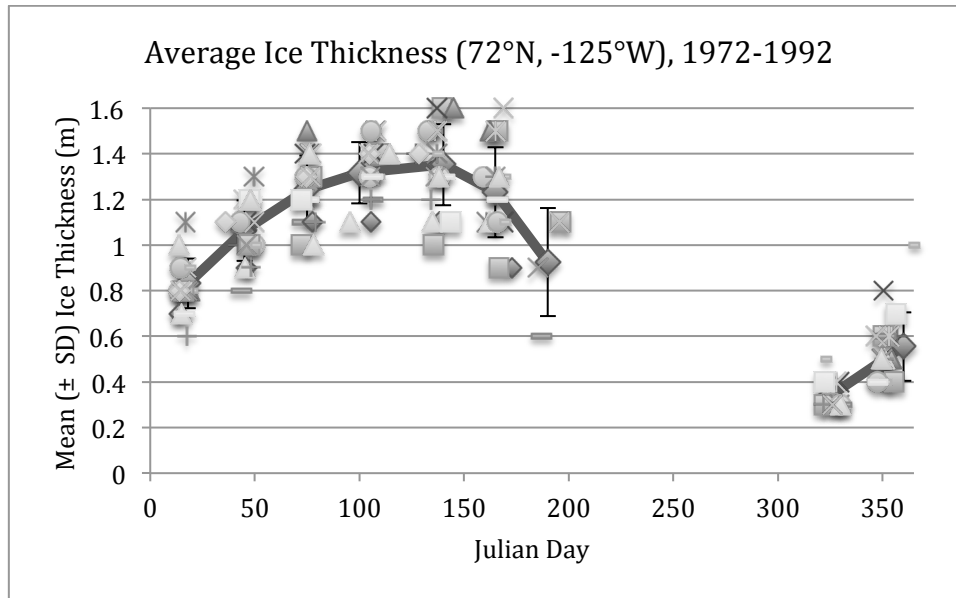


Figure 1a. Mean (\pm 1 SD) ice thickness replotted from data taken from ice auger bore holes at 72°N, -125°W in the Canadian Beaufort Sea from 1972-1992 by Environment Canada (Lindsay 2010). Data online at http://psc.apl.washington.edu/sea_ice_cdr/data_tables.html.

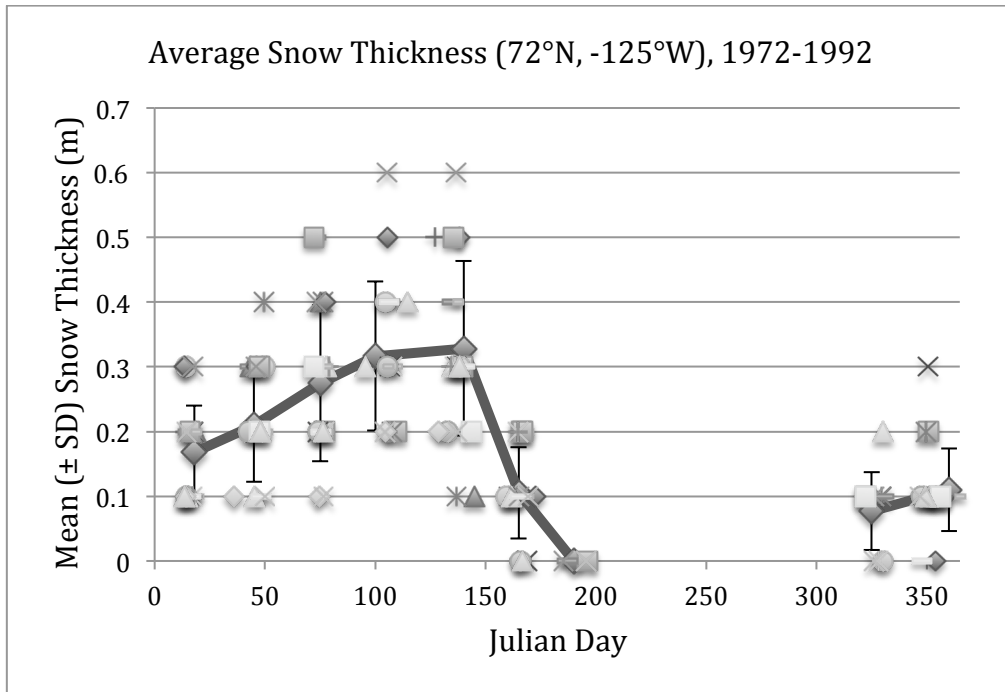


Figure 1b. Mean (± 1 SD) snow thickness replotted from data taken from ice auger bore holes measured at 72°N, -125°W in the Canadian Beaufort Sea from 1972-1992 by Environment Canada (Lindsay 2010), online at http://psc.apl.washington.edu/sea_ice_cdr/data_tables.html.

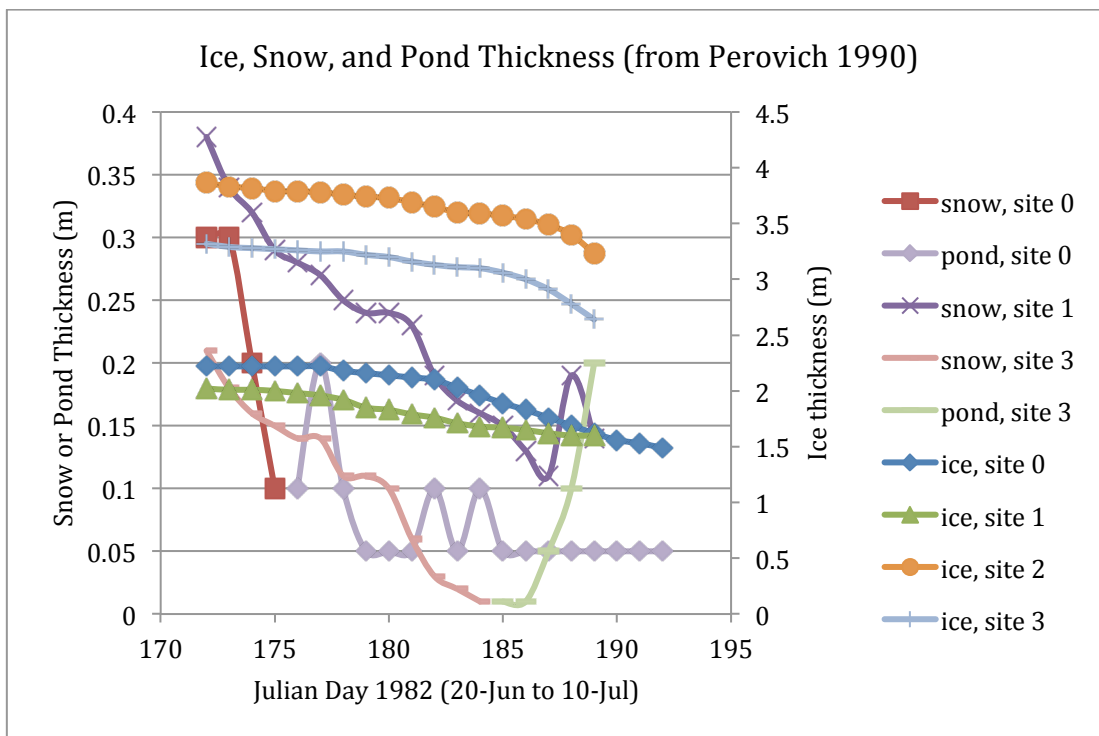


Figure 1c. Data replotted based on details presented in Perovich (1990) showing varying sea ice (right axis) and snow and pond thickness (left axis) at 4 sites in Mould Bay, Arctic Ocean. Site 0 was the main site, composed of first-year ice overlain by 0.30 m of snow early on, which melted to shallow melt ponds over the time of sampling. To illustrate the small scale spatial variability of sea ice, sites 1-3 were within 5 m of each other on a small pressure ridge (site 1: side of ridge, with snow; site 2: top of ridge, no snow; site 3: below ridge, with large pond formation) (data reproduced from Tables 2 and 3, Perovich 1990).

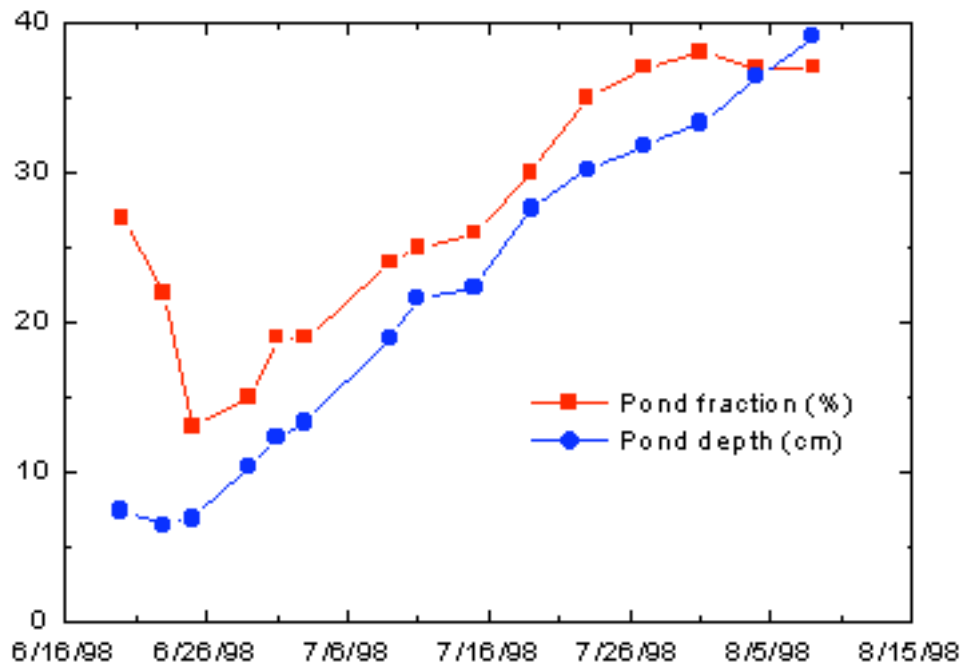


Figure 1d. Pond fraction and pond depth at the SHEBA site (Perovich et al. 2003).

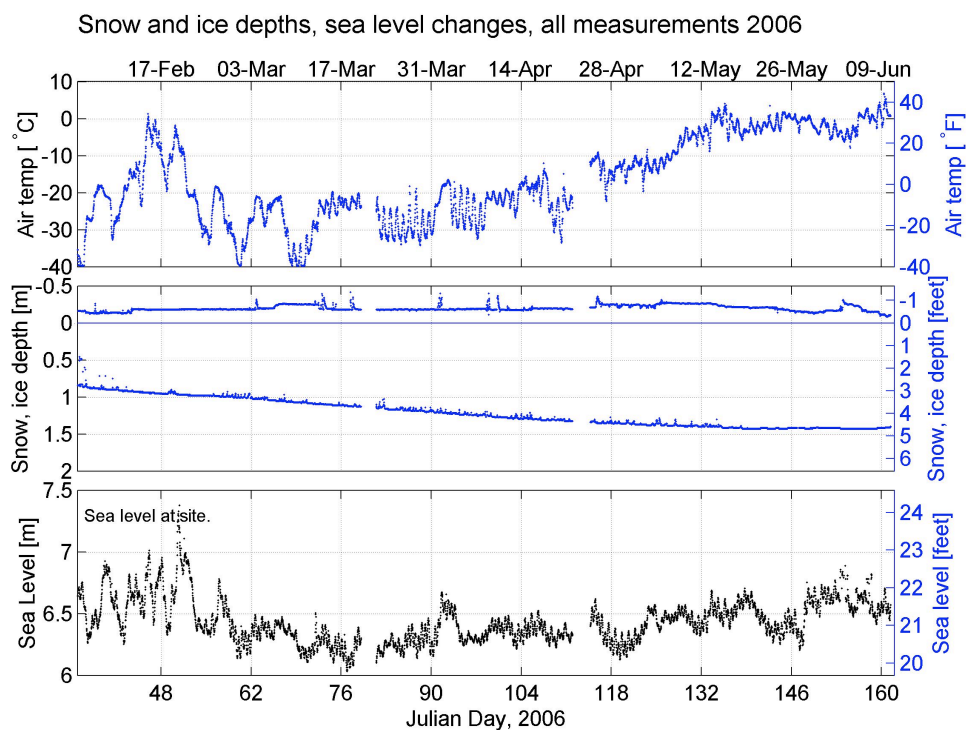


Figure 2a. Air temperatures, snow and ice depths, and sea level measured 300 m offshore in the Chukchi Sea near Barrow, AK ($71^{\circ} 22' 03''$ N, $156^{\circ} 31' 03''$ W) in 2008 by the Sea Ice Group at the Geophysical Institute of University Alaska at Fairbanks (online http://seaice.alaska.edu/gi/data/barrow_massbalance) (Druckenmiller et al. 2009).

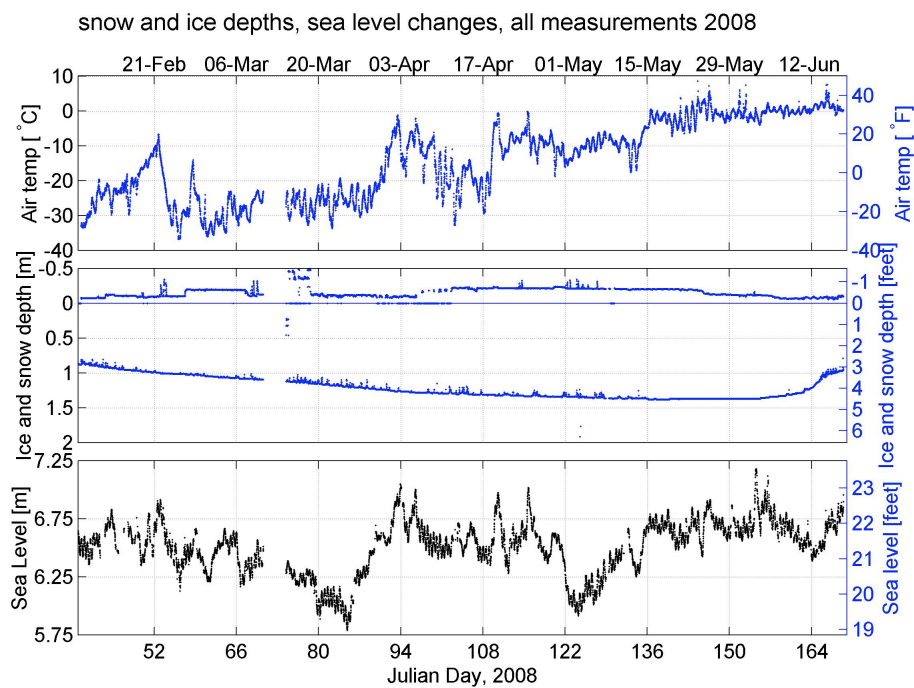


Figure 2b. Air temperatures, snow and ice depths, and sea level measured 1000 m offshore near Barrow, AK ($71^{\circ} 21' 56''$ N, $156^{\circ} 32' 39''$ W) in 2008 by the Sea Ice Group at the Geophysical Institute of University Alaska at Fairbanks (online http://seaice.alaska.edu/gi/data/barrow_massbalance) (Druckenmiller et al. 2009).

Gauge = 26

Ridge
Multi-Year Ice
Snow depth = 76 cm
Initial ice thickness = 540 cm
Maximum ice thickness = 546 cm
Final ice thickness = 322 cm
Total growth = 6 cm
Surface melt = -52 cm
Bottom melt = -166 cm
Net year = -218 cm
Start date = 10/29/97
Max ice date = 1/14/98
End date = 10/7/98

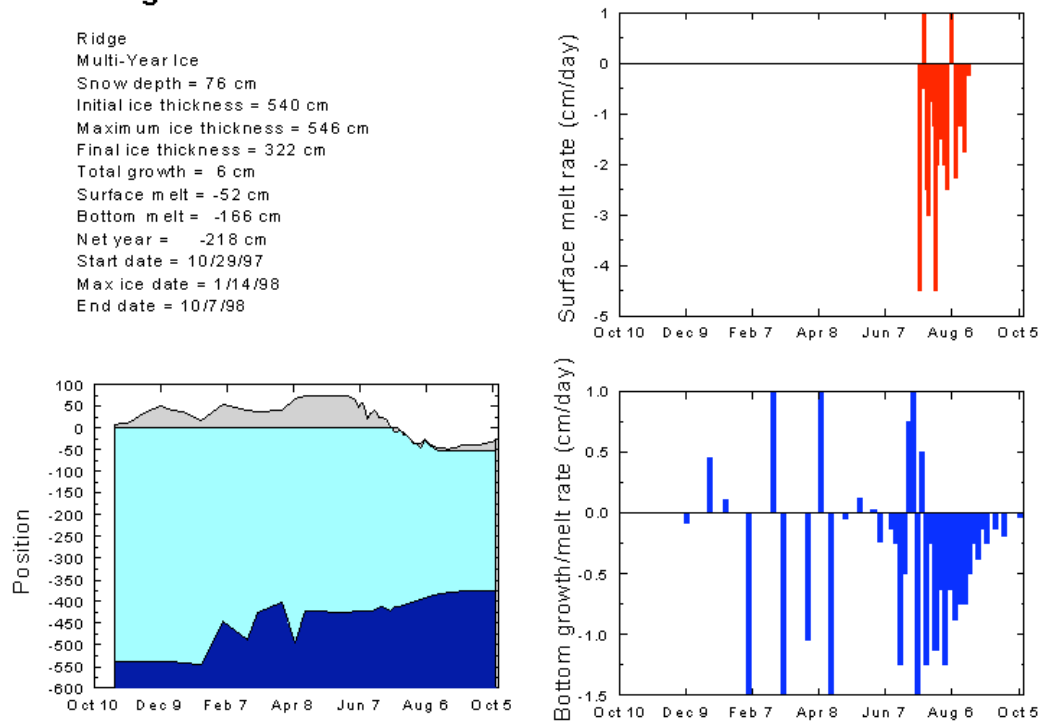


Figure 2c. Data from the SHEBA experiment showing sea ice (light blue) and snow (grey) thicknesses in MYI over the seasonal cycle (Perovich et al. 2003). Shown on the right is the rate of sea ice melt in the surface and bottom ice.

Gauge = 203

Quebec Lead
First-year Ice / Melt Pond
Snow depth = 13 cm
Initial ice thickness = 97.5 cm
Maximum ice thickness = 107 cm
Final ice thickness = 44.5 cm
Total growth = 9.5 cm
Surface melt = -53 cm
Bottom melt = -10.5 cm
Net year = 0 cm
Start date = 4/19/98
Max ice date = 6/2/98
End date = 7/4/98

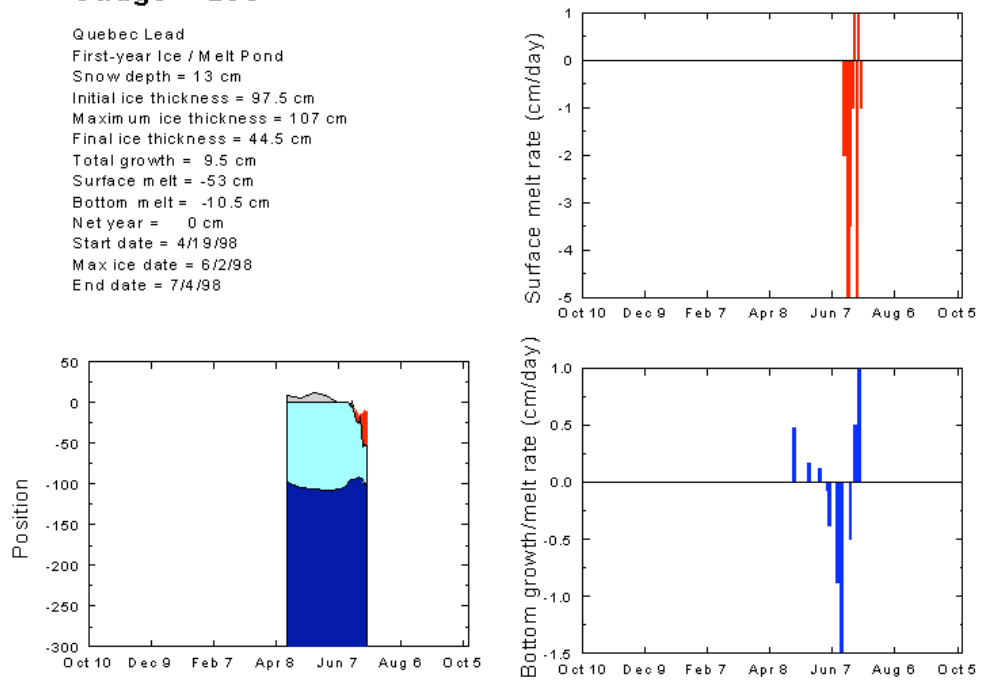


Figure 2d. Data from the SHEBA experiment showing sea ice (light blue), snow (grey), and pond thicknesses in FYI over the seasonal cycle (Perovich et al. 2003) (note: the site wasn't monitored until April 19, and ice broke up on July 4).

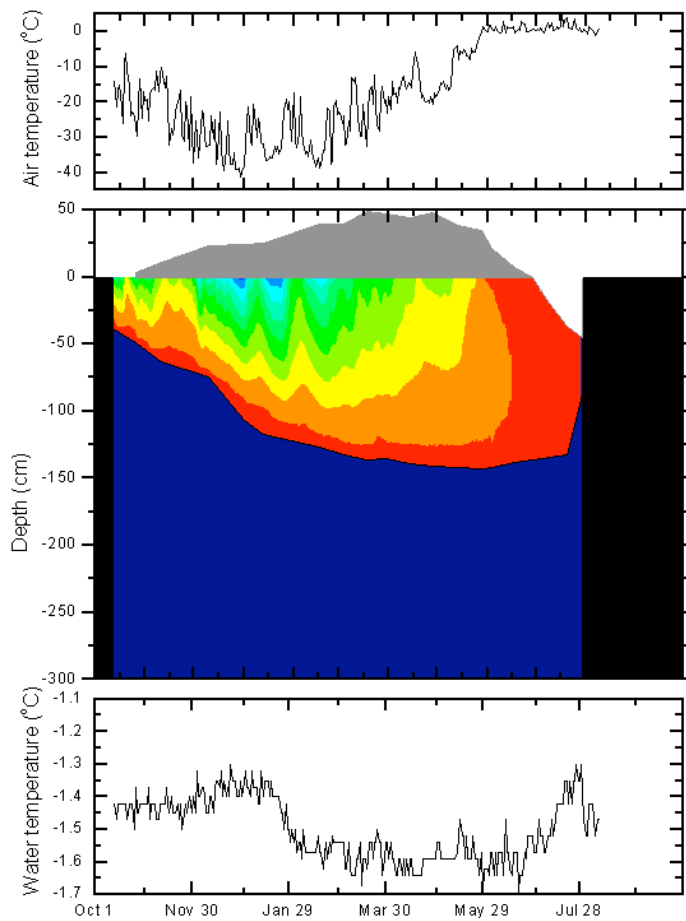


Figure 2e. Data from the SHEBA experiment showing air temperatures, ice temperatures (coldest is the blue, at -20°C ; warmest is the red, at -2°C), and water temperatures in a FYI site (Perovich et al. 2003).

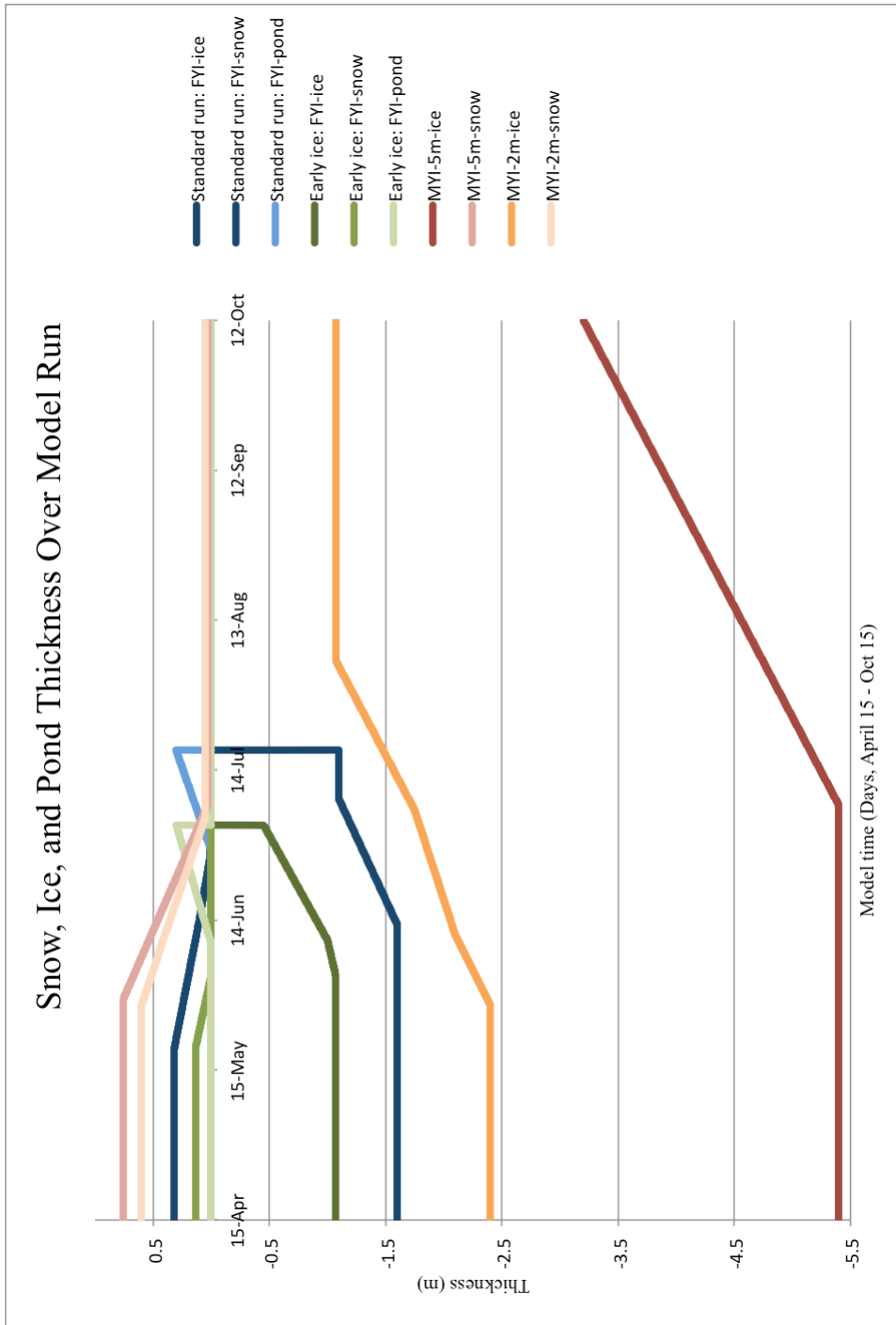


Figure 3. Plot showing modeling ice (negative values), snow and pond (positive values) thicknesses over time for the standard model runs described in Table 1. Blue: first year ice with normal ice retreat, including melt ponds (used for standard model runs). Green: first year ice with early ice retreat, including melt ponds. Orange: MYI with 2.4 m thick ice, no ponds. Red: multiyear ice 5.4 m thick, no melt ponds.

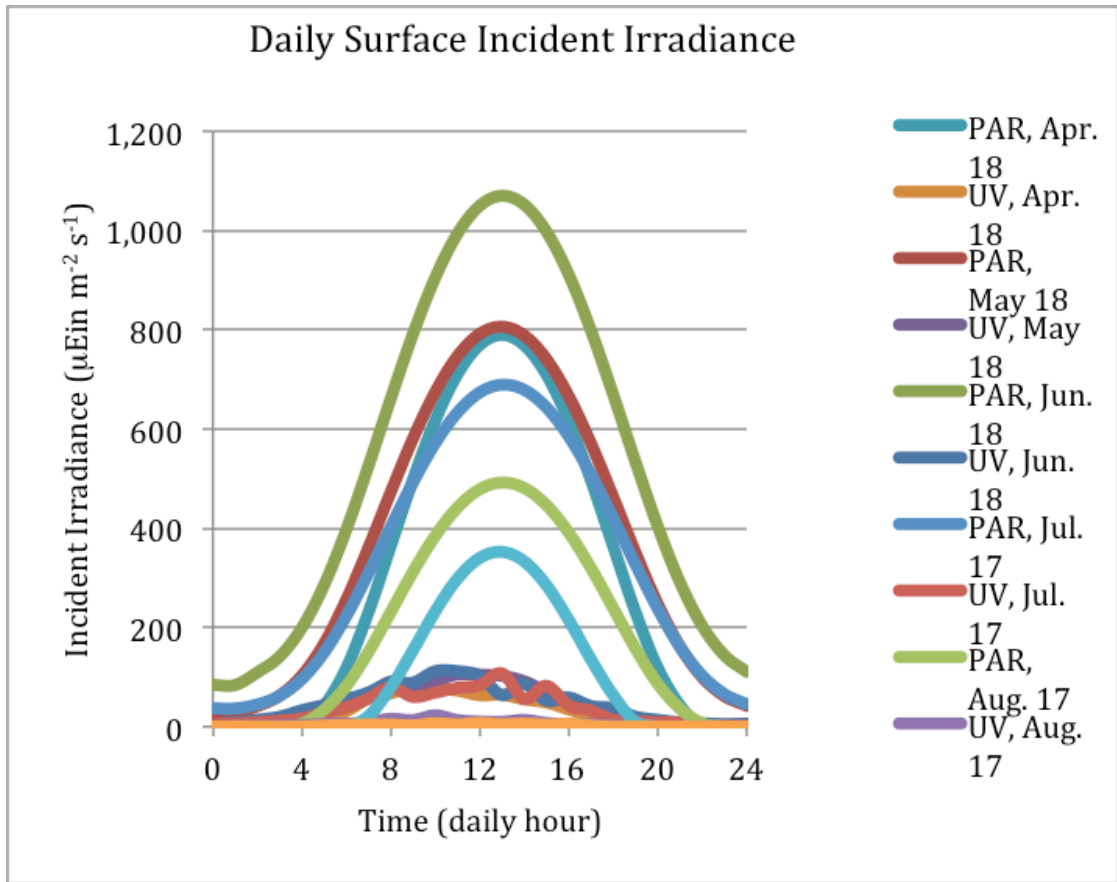


Figure 4a. Modeled daily cycle of integrated incident surface PAR (400 -700 nm) and UV (280-300) irradiance, in $\mu\text{Ein m}^{-2} \text{s}^{-1}$ for the dates shown in the year 2003. UV data was obtained in real-time (every 15 min) from the NSF Polar Programs UV Monitoring Network, online at <http://uv.biospherical.com/barrow/barrow.asp>, whereas PAR data was obtained from NCEP/NCAR reanalysis data which is then put into the Gregg and Carder (1990) atmospheric radiative transfer model with the McClain et al. (1996) correction for cloud cover.

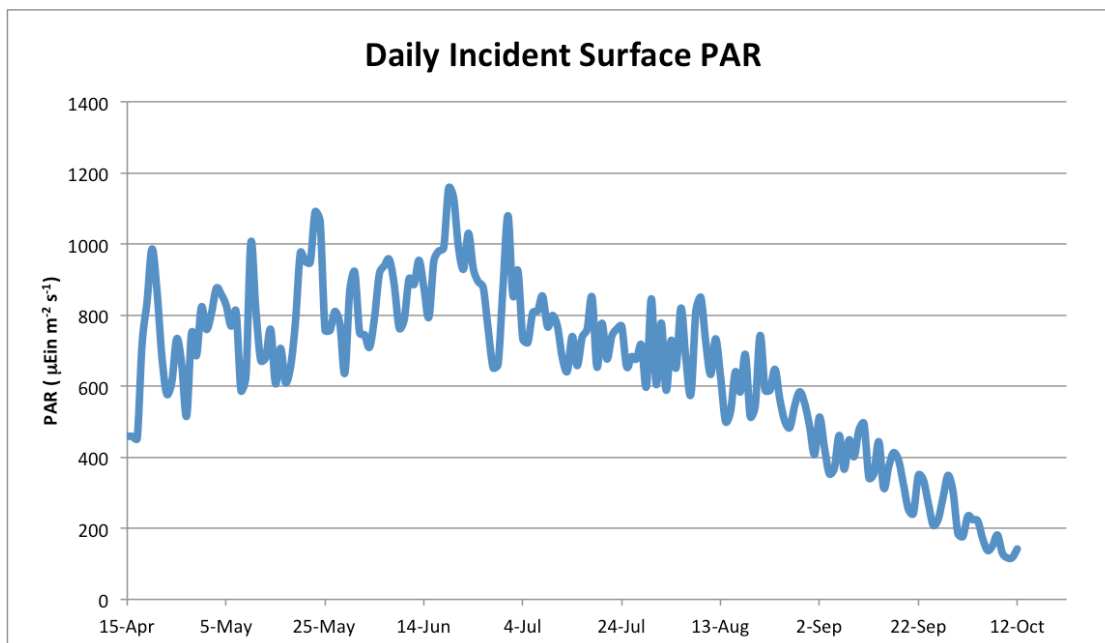


Figure 4b. Model output showing the annual cycle of daily incident surface PAR (integrated from 400-700nm) used in the model runs. PAR data was obtained from NCEP/NCAR reanalysis data which is then put into the Gregg and Carder (1990) atmospheric radiative transfer model with the McClain et al. (1996) correction for cloud cover, as described in the Methods section.

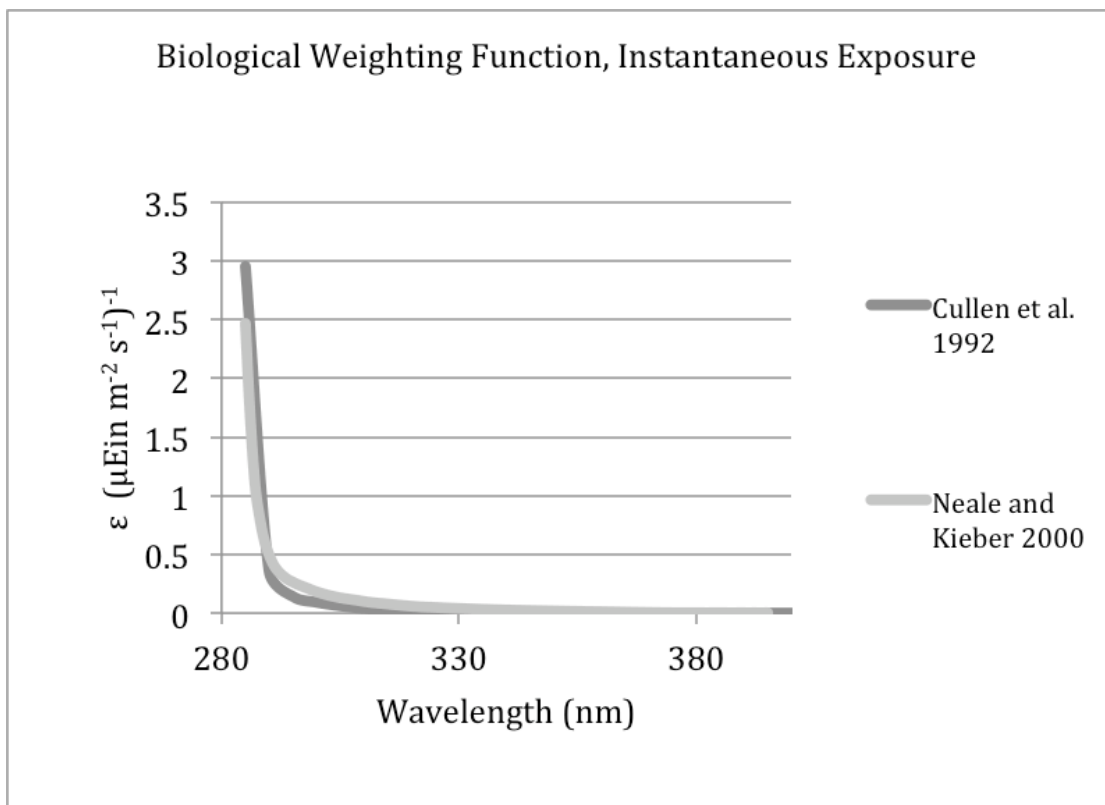


Figure 5. Biological weighting functions in units reciprocal $(\mu\text{Ein m}^{-2} \text{s}^{-1})^{-1}$ for instantaneous irradiance exposure curve. Graphs reproduced using data from Cullen et al. (1992) and Neale and Kieber (2000).

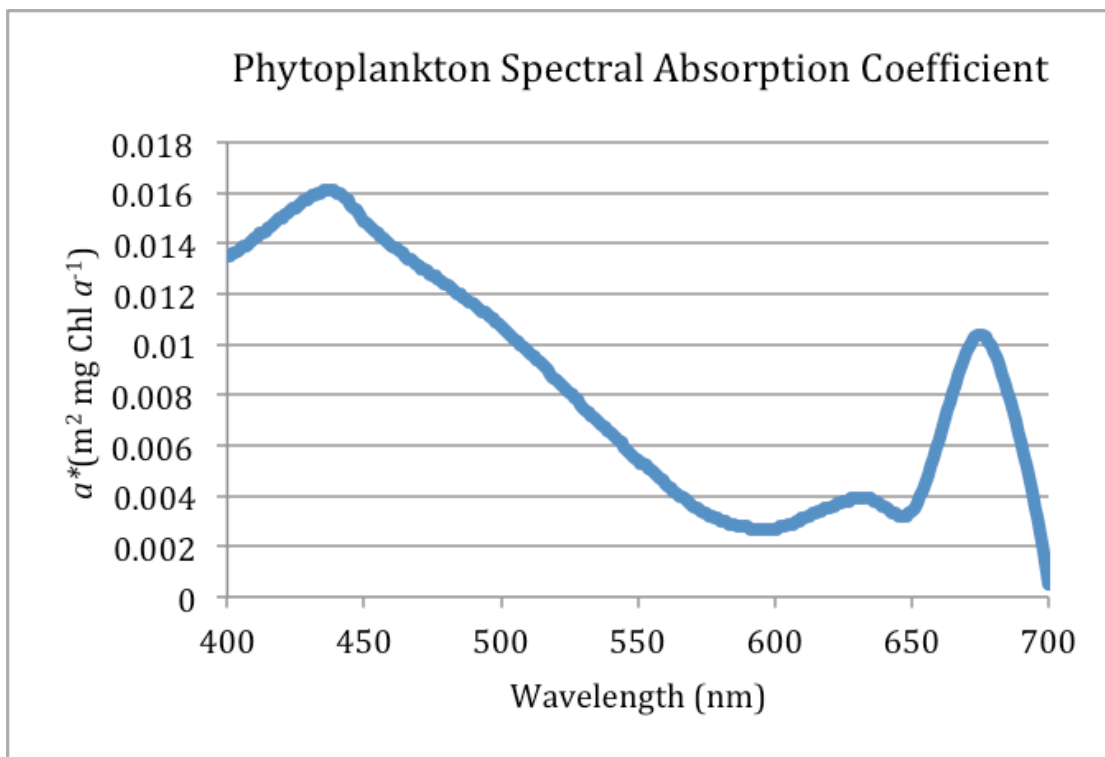


Figure 6. Phytoplankton spectral absorption coefficient, $a^*(\lambda)$, used in model runs.

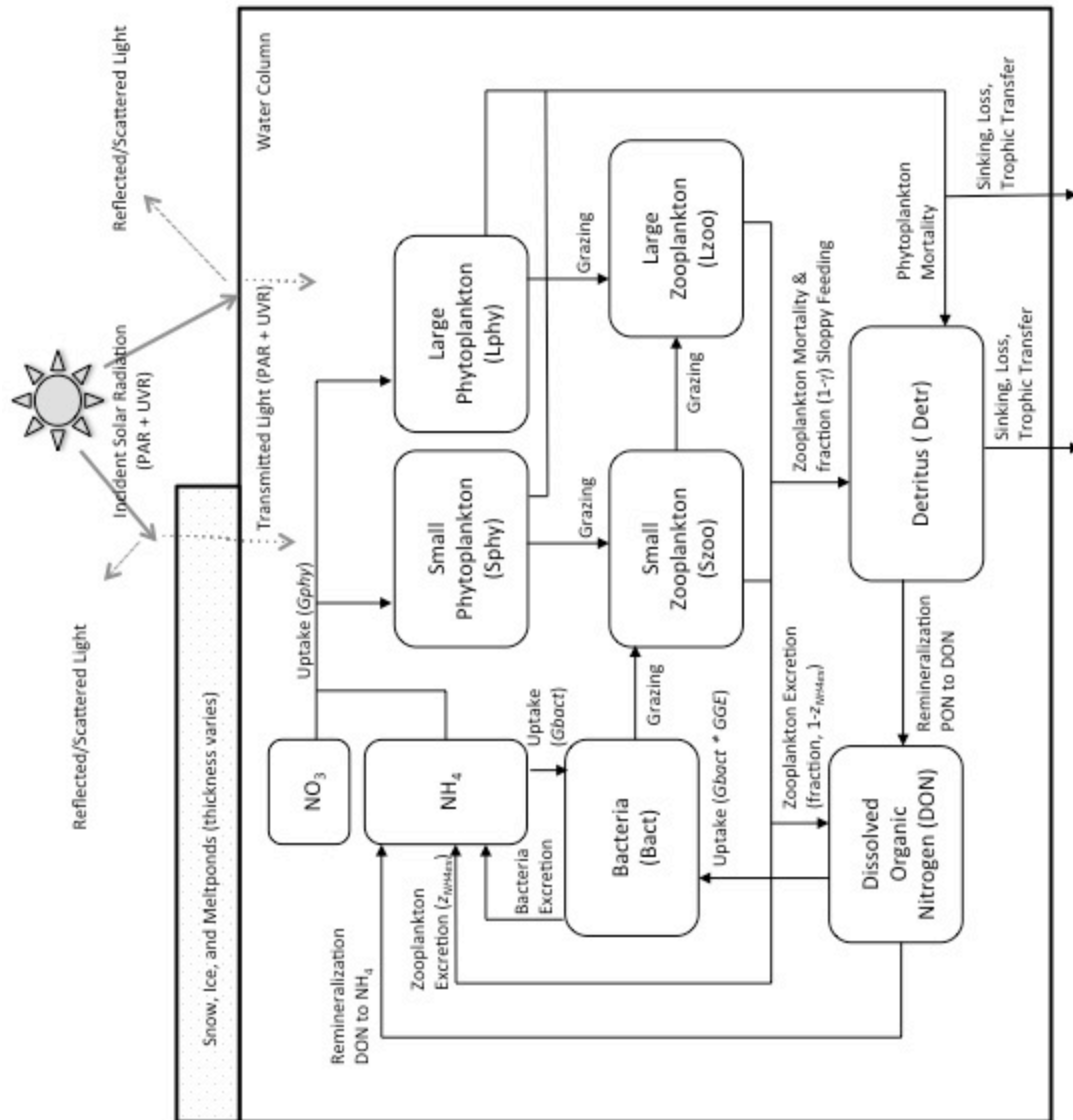


Figure 7. Conceptual diagram representing main fluxes and flows of biological model. Boxes represent the main state variables, and arrows represent the key fluxes and flows. Note that phytoplankton and detritus can sink out of the model (permanent loss), and that snow, ice, and ponde coverage varies as described in Table 1.

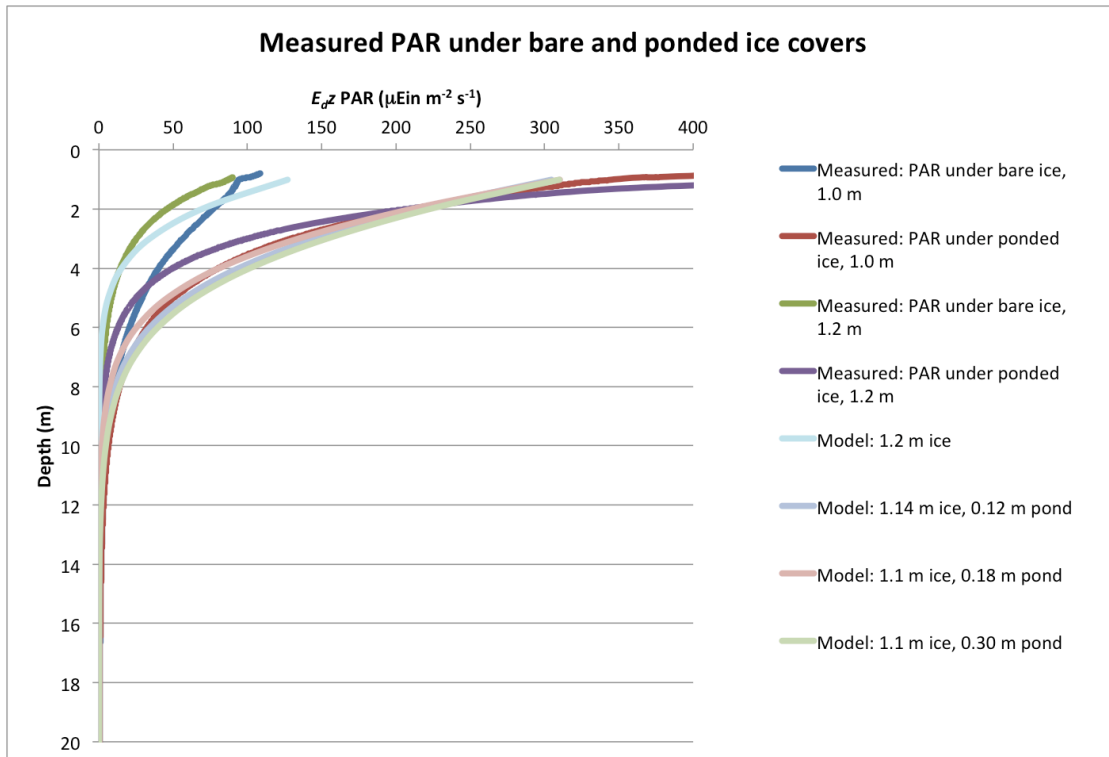


Figure 8. Modeled vs. measured PAR (400-700 nm) under bare and ponded ice covers. Measured data is from the 2011 ICESCAPE cruise, in which ice was: top two, 1.0 m thick with 25% pond coverage (dark blue: bare ice; dark red: ponded ice); ponds varied from 10-30 cm thick; second two, 1.2 m thick ice with 25% pond coverage (dark green: bare ice; dark purple: ponded ice), with ponds varying from 10-30 cm thick. Modeled data is shown in the lighter pastel colors, with light blue representing bare ice 1.2 m thick, followed by light purple as ponded ice with 0.12 m pond, light pink as 1.1 m thick ice with 0.18 m pond, and light green as 1.1 m thick ice with 0.30 m pond. All modeled data has 30% pond coverage on the ice surface.

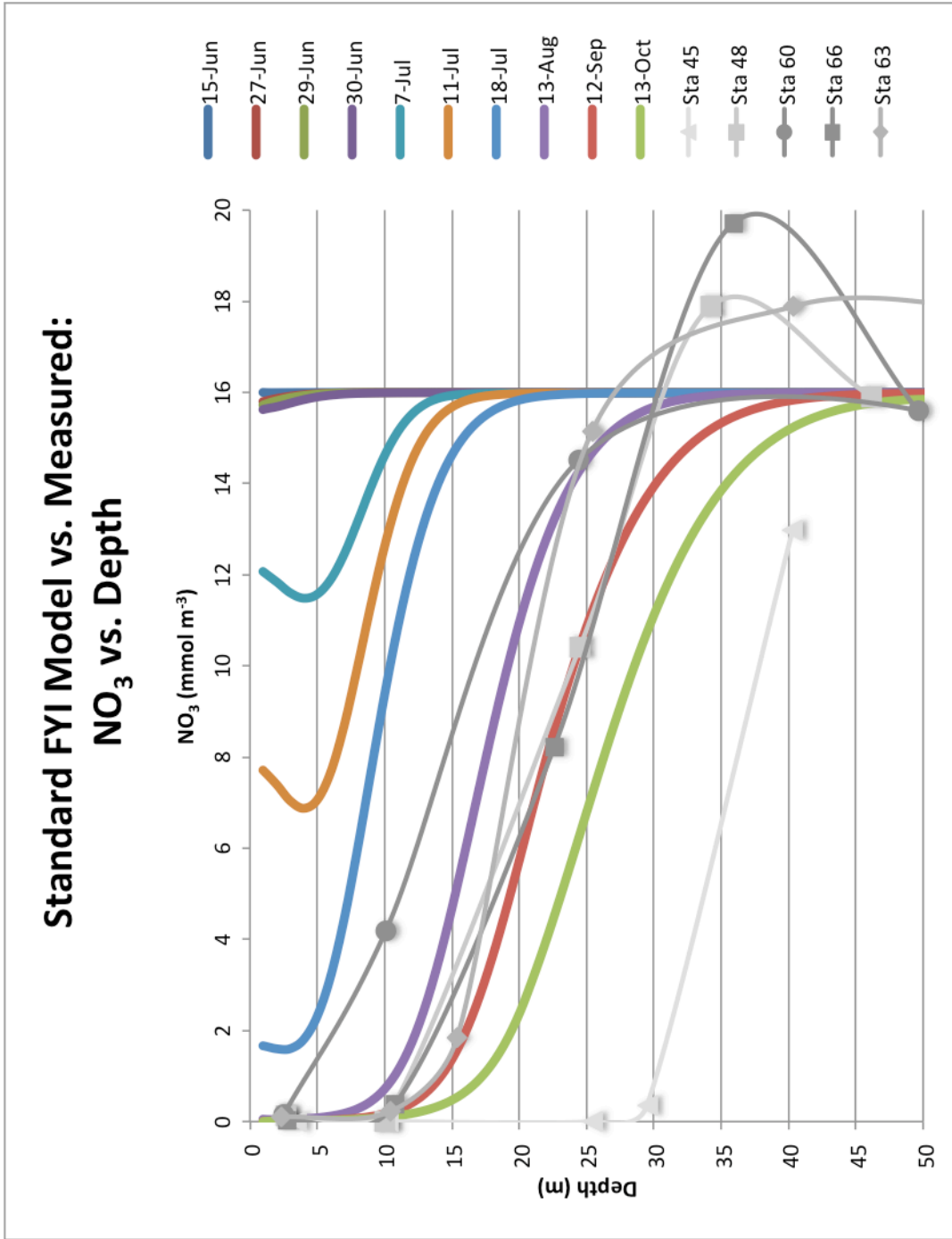


Figure 9. Measured vs. modeled nitrate (NO_3 , mmol m^{-3}) in the water column during the standard model run. Shown in the colored lines are the seasonal cycle of NO_3 at various important time periods in the model run. The grey lines with symbols show the measured NO_3 during the under ice bloom period in the ICESCAPE data.

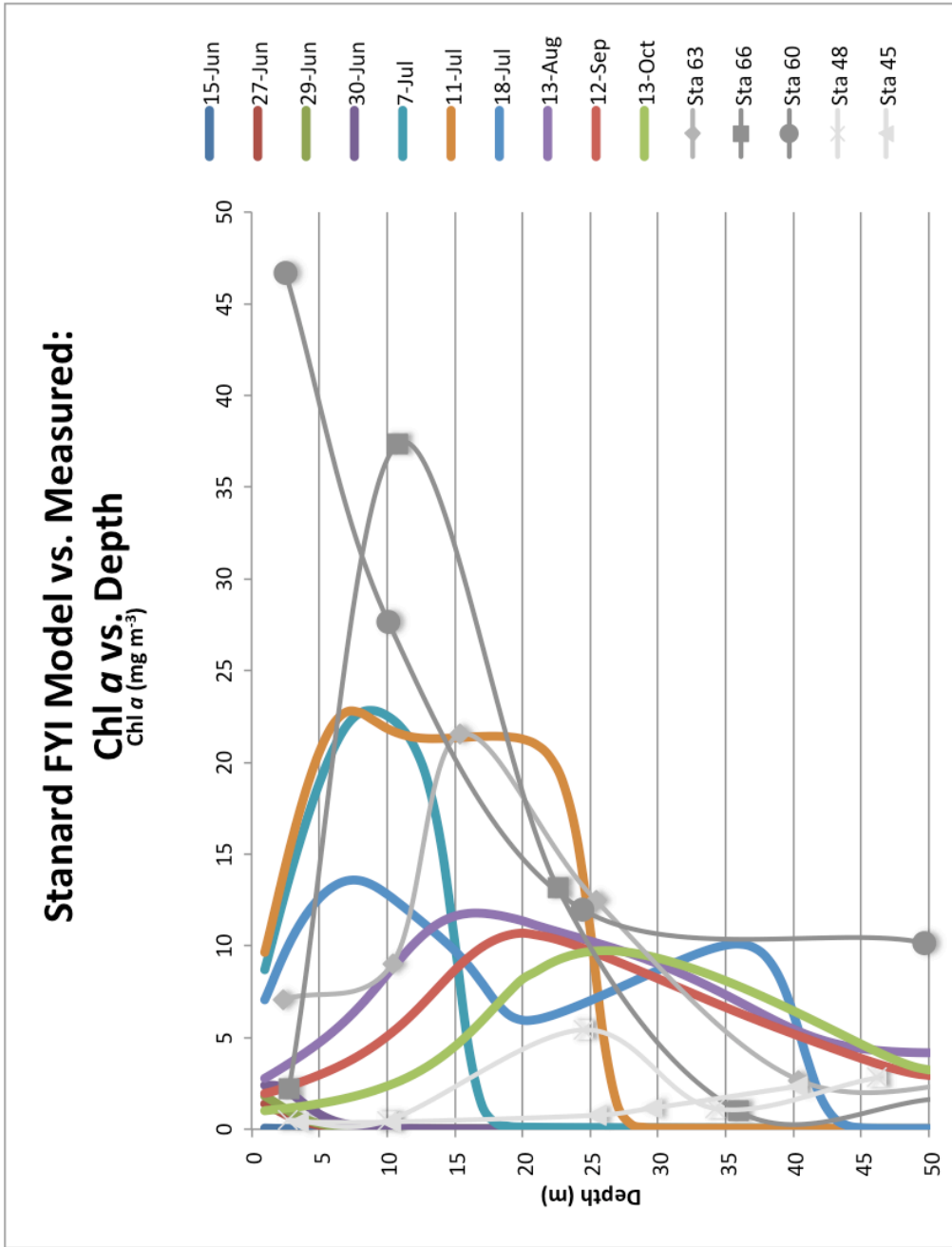


Figure 10. Measured vs. modeled chlorophyll *a* (Chl *a*, mg m⁻³) in the water column during the standard model run. Shown in the colored lines are the seasonal cycle of Chl *a* at various important time periods in the model run. The grey lines with symbols show the measured Chl *a* during the under ice bloom period in the ICESCAPE data.

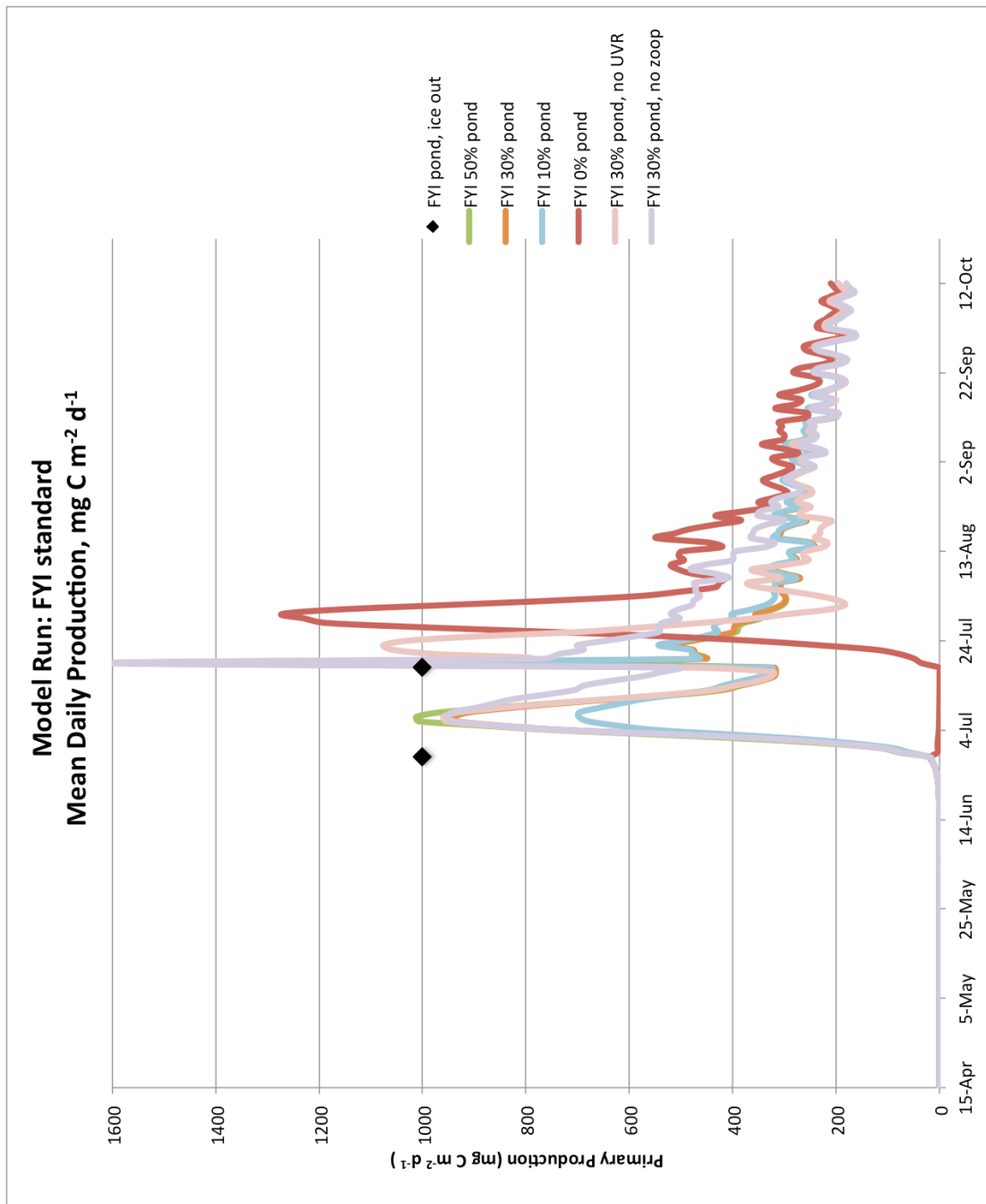
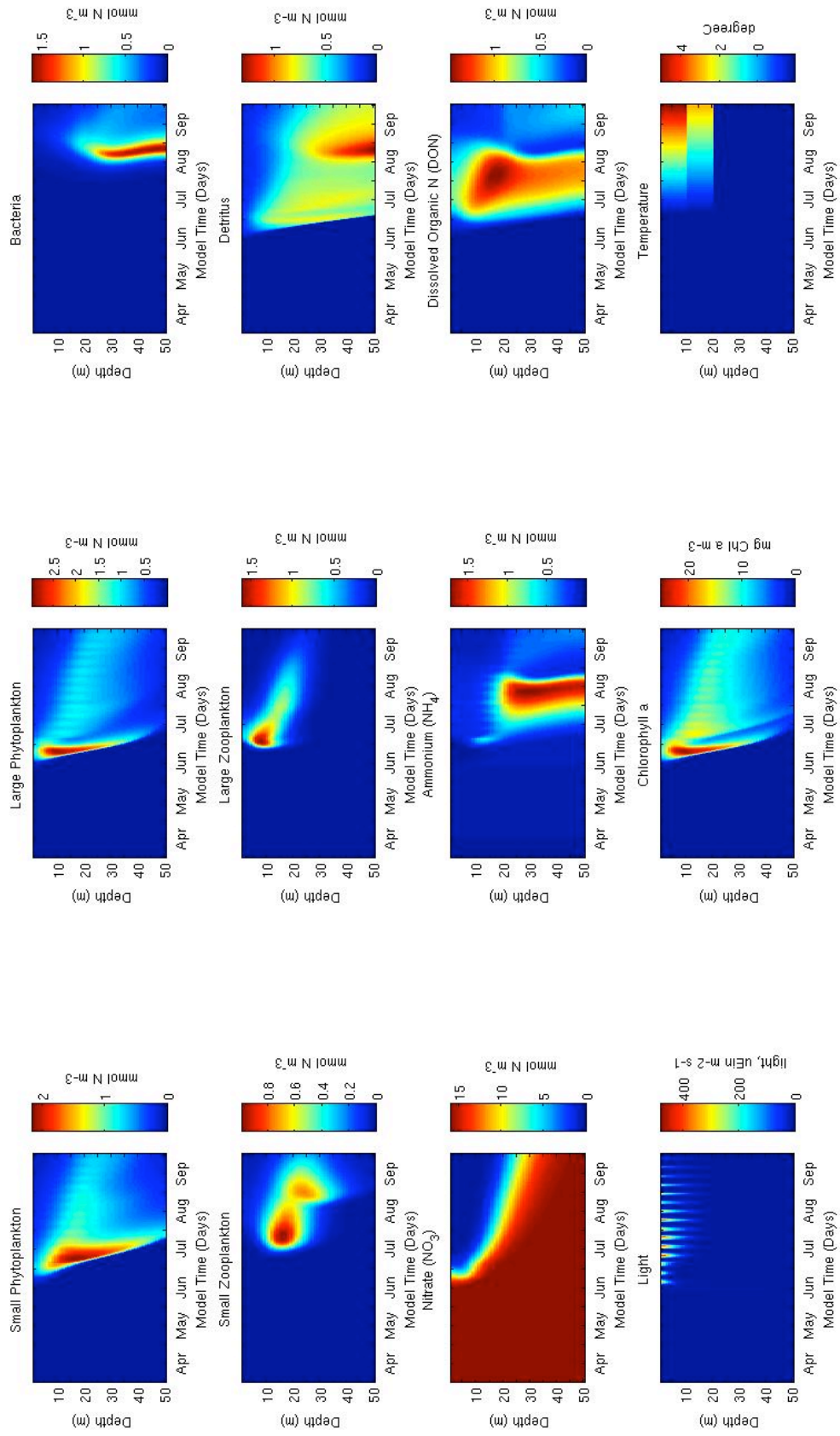


Figure 11. Daily net primary production ($\text{mg C m}^{-2} \text{d}^{-1}$) shown over the seasonal cycle for the standard model run. The black triangles indicate the day that ponds start forming and the day the ice breaks-up (thicknesses are described in Table 1).

Figure 12 (next page). Model output from standard model run, showing all model state variables. Note that the month names are on the 30 of each month, so for example “Jun” means June 30 (the model begins Apr. 15 and ends Oct. 15).



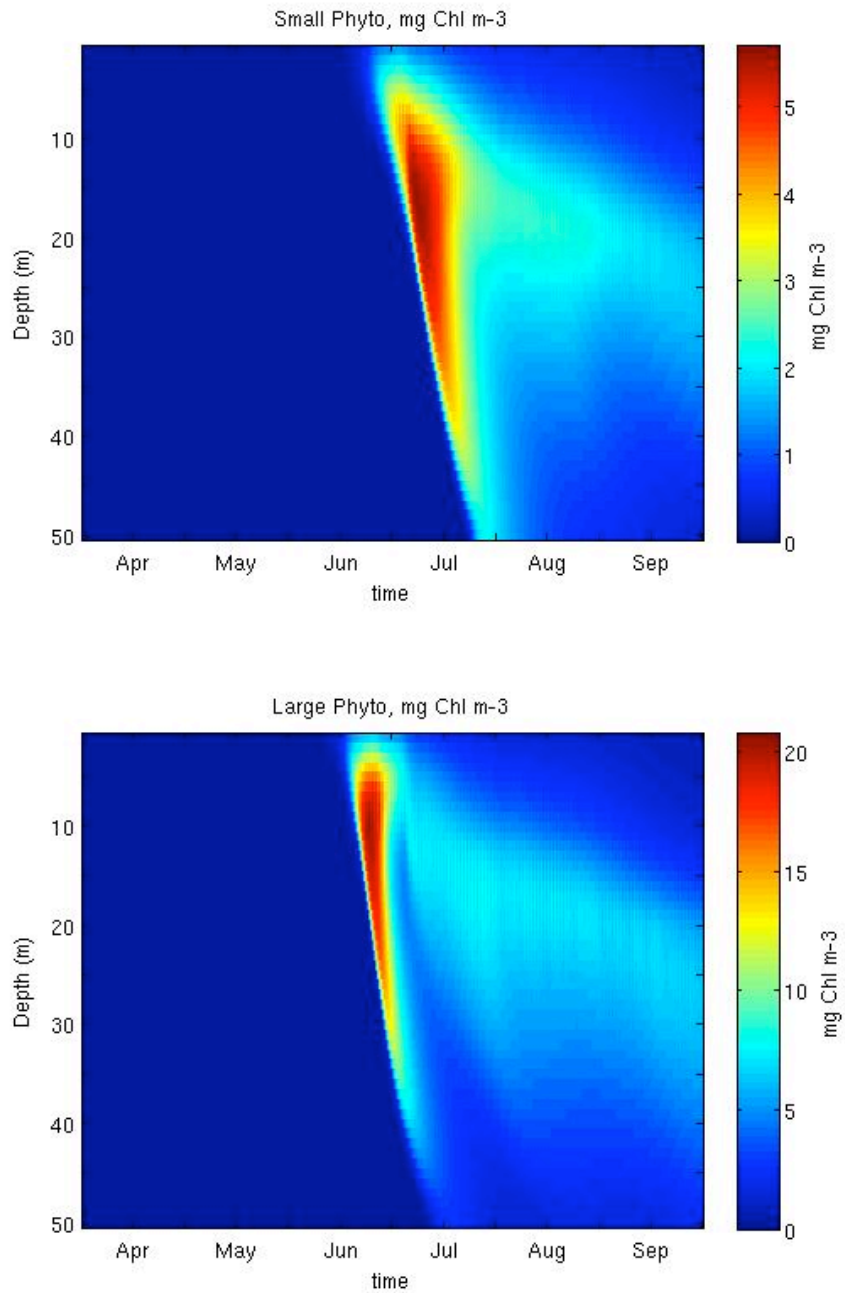


Figure 13. Results from standard model run showing state variables small (top) and large (bottom) phytoplankton in Chl *a* units. Note that the month name labels on the bottom axis are on the 30 of each month, so for example “Jun” means June 30.

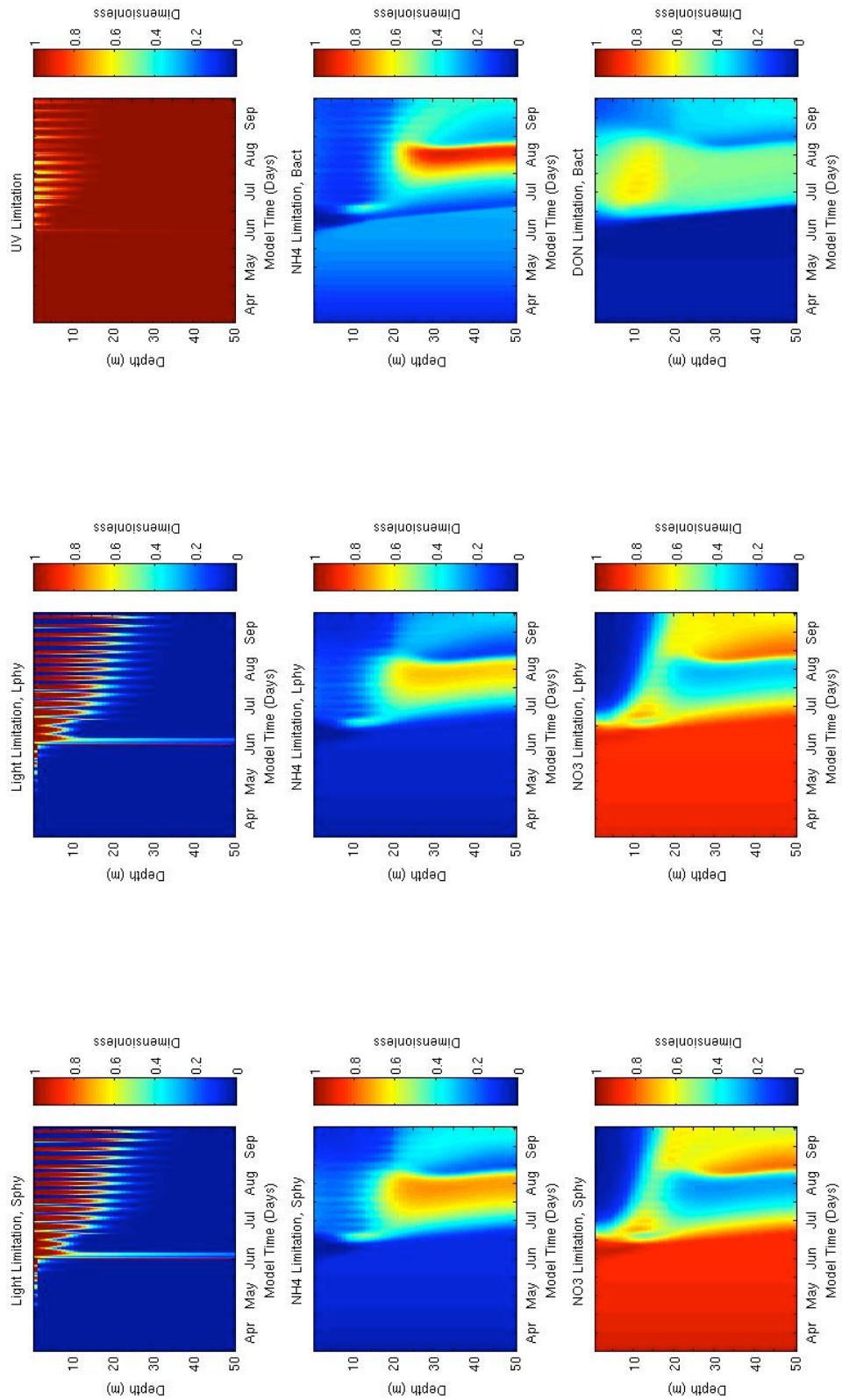


Figure 14. Model output from standard model run, showing model limitation terms.

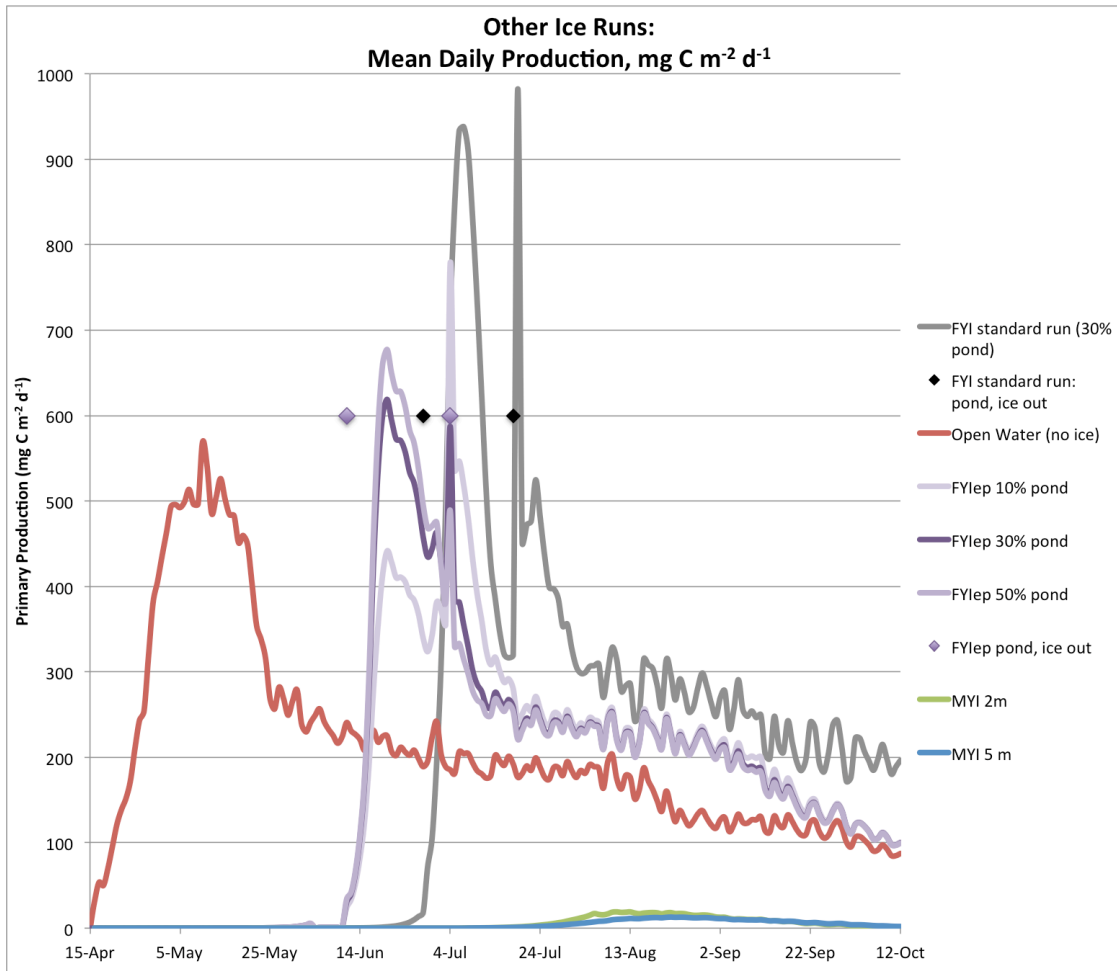


Figure 15. Daily net primary production (mg C m⁻² d⁻¹) shown over the seasonal cycle for other model runs (not the standard run, which is shown here in grey). The black diamonds indicate the day that ponds start forming and the day the ice breaks-up for the standard model run (thicknesses are described in Table 1), whereas the purple diamonds show this for the early ice and pond year model run, the results of which are shown in the various shades of purple.

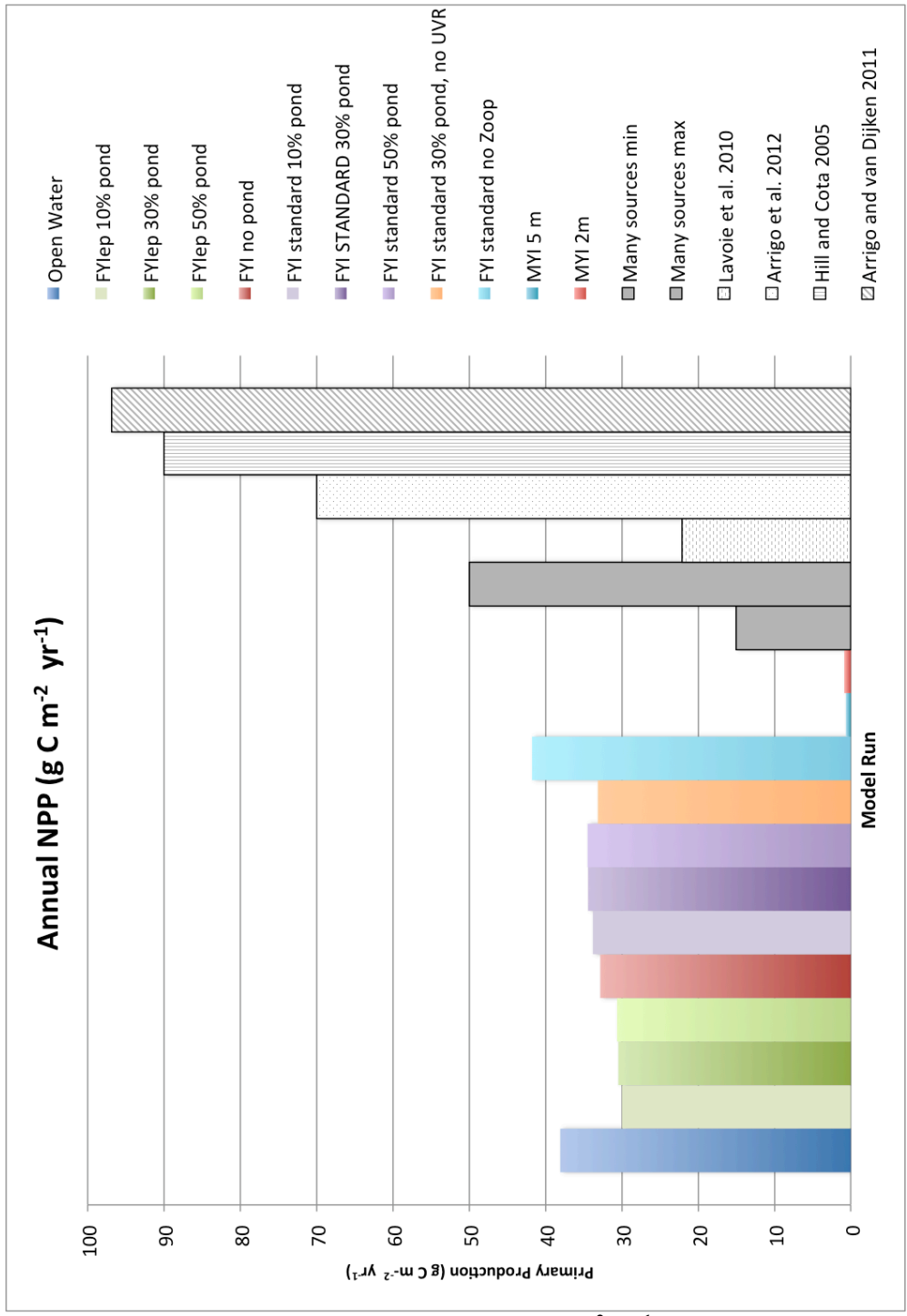


Figure 16. Annual net primary production ($\text{g C m}^{-2} \text{ yr}^{-1}$) shown for the major model runs, as compared to measured and modeled data in other studies (shown in grey). The standard model run with varying pond covers is shown here in purple, and the early pond year is shown in green shades.